Western University
Scholarship@Western

Digitized Theses

Digitized Special Collections

1991

A Numerical And Interferometric Study Of Natural Convective Heat Transfer From Divided And Undivided Vertical Channels

David Naylor

Follow this and additional works at: https://ir.lib.uwo.ca/digitizedtheses

Recommended Citation
Naylor, David, "A Numerical And Interferometric Study Of Natural Convective Heat Transfer From Divided And Undivided Vertical Channels" (1991). *Digitized Theses*. 2093.
https://ir.lib.uwo.ca/digitizedtheses/2093

This Dissertation is brought to you for free and open access by the Digitized Special Collections at Scholarship@Western. It has been accepted for inclusion in Digitized Theses by an authorized administrator of Scholarship@Western. For more information, please contact tadam@uwo.ca, wlswadmin@uwo.ca.

The author of this thesis has granted The University of Western Ontario a non-exclusive license to reproduce and distribute copies of this thesis to users of Western Libraries. Copyright remains with the author.

Electronic theses and dissertations available in The University of Western Ontario's institutional repository (Scholarship@Western) are solely for the purpose of private study and research. They may not be copied or reproduced, except as permitted by copyright laws, without written authority of the copyright owner. Any commercial use or publication is strictly prohibited.

The original copyright license attesting to these terms and signed by the author of this thesis may be found in the original print version of the thesis, held by Western Libraries.

The thesis approval page signed by the examining committee may also be found in the original print version of the thesis held in Western Libraries.

Please contact Western Libraries for further information:
E-mail: libadmin@uwo.ca
Telephone: (519) 661-2111 Ext. 84796
Web site: http://www.lib.uwo.ca/

CHAPTER 1

GENERAL REVIEW

1.1 Introduction

Natural, or free, convection is the buoyancy-induced fluid motion that results from density variations in the presence of a body force field. Natural convection is perhaps the most common cause of fluid motion. Free convective flows span from the large scale motions of weather patterns and ocean currents to the small scale flows associated with the cooling of man-made devices.

From an engineering perspective, natural convection is commonly used as a passive means of rejecting waste heat. This thesis extends the knowledge of natural convective cooling of isothermal parallel plate geometries. Early studies of isothermal parallel plates [1] were undertaken because of the need to predict the cooling of fins. At present there is a resurgence of interest in heat transfer from parallel plates because of modern applications to the cooling of electronic and computer equipment.

The intended primary application of the present research is to the air cooling of printed circuit boards (PCBs). To a large extent, the reliability of a computer chip depends upon adequate heat removal. The heat removal problem has been continuously exacerbated in the last twenty years by the trend toward larger scales of circuit integration. Increasing miniaturization has made heat transfer considerations crucial in design of electronic packaging. Typically, current devices dissipate an order of

A NUMERICAL AND INTERFEROMETRIC STUDY OF NATURAL CONVECTIVE HEAT TRANSFER FROM DIVIDED AND UNDIVIDED VERTICAL CHANNELS

by

David Naylor

Department of Mechanical Engineering
Faculty of Engineering Science

Submitted in partial fulfilment
of the requirements for the degree of
Doctor of Philosophy

Faculty of Graduate Studies
The University of Western Ontario
London, Ontario
September 1991

© David Naylor 1991

National Library of Canada
Canadian Theses Service

Ottawa, Canada
K1A 0N4

Bibliothèque nationale du Canada
Service des thèses canadiennes

The author has granted an irrevocable non-exclusive licence allowing the National Library of Canada to reproduce, loan, distribute or sell copies of his/her thesis by any means and in any form or format, making this thesis available to interested persons.

The author retains ownership of the copyright in his/her thesis. Neither the thesis nor substantial extracts from it may be printed or otherwise reproduced without his/her permission.

L'auteur a accordé une licence irrévocable et non exclusive permettant à la Bibliothèque nationale du Canada de reproduire, prêter, distribuer ou vendre des copies de sa thèse de quelque manière et sous quelque forme que ce soit pour mettre des exemplaires de cette thèse à la disposition des personnes intéressées.

L'auteur conserve la propriété du droit d'auteur qui protège sa thèse. Ni la thèse ni des extraits substantiels de celle-ci ne doivent être imprimés ou autrement reproduits sans son autorisation.

ISBN 0-315-71985-0

Canada

ABSTRACT

A numerical and experimental study has been conducted on two-dimensional laminar natural convection heat transfer in an undivided and divided vertical isothermal channel. For the divided channel configuration, an isothermal plate at the same temperature as the channel walls was located on the channel centre line. The study examined the effect of Rayleigh number, plate-to-channel length ratio, vertical plate position, and plate thickness on the heat transfer from the channel walls, the dividing plate and the channel as a whole.

Solutions to both the full elliptic and parabolic forms of the Navier-Stokes and energy equations have been obtained for Prandtl number Pr=0.7 (air). Closed form expressions were derived for the limiting case of fully developed flow in the divided channel. Experimental measurements were made in air with a Mach-Zehnder interferometer.

Positioning the plate at the bottom of the channel gave the highest average Nusselt numbers for the dividing plate and the overall channel. At low Rayleigh number, when the plate is at the bottom of the channel, extending the channel walls above the plate increased the plate heat transfer by as much as a factor of four. At higher Rayleigh number, plate average Nusselt numbers as much as two times the isolated plate Nusselt number were predicted numerically.

In the fully developed regime, a short dividing plate located at the channel inlet reduces the wall average Nusselt number by about a factor of two, compared with the undivided channel. At moderate and high Rayleigh number, the wall average Nusselt number was almost independent of both the vertical plate position and the plate-to-channel length ratio.

At low Rayleigh number, increasing the dividing plate thickness caused the plate and wall average Nusselt numbers to decrease significantly. At high Rayleigh number the effect of plate thickness was small.

Average Nusselt number correlations are presented for the dividing plate, the channel wall and the overall channel.

ACKNOWLEDGEMENTS

I would like to thank my supervisor, Dr. J.D. Tarasuk for his sound guidance, encouragement and financial support during this project.

I am also grateful to Dr. J.M. Floryan. His assistance with some of the numerical aspects of this thesis was greatly appreciated.

The author expresses appreciation to The University of Western Ontario for the financial support and lecturing experience provided during this project. Computing funds provided by The University of Western Ontario are also gratefully acknowledged.

The author wishes to thank Dr. P.H. Oosthuizen for his assistance and suggestions during the early stages of this project.

The financial support received from the Natural Sciences and Engineering Research Council of Canada is gratefully acknowledged.

Finally and above all, I wish to thank my wife, Kathryn. Her support and constant encouragement, especially during the hard times, led to the successful completion of this thesis.

TABLE OF CONTENTS

Page

CERTIFICATE OF EXAMINATION ii
ABSTRACT iii
ACKNOWLEDGEMENTS v
TABLE OF CONTENTS vi
LIST OF FIGURES ix
LIST OF TABLES xv
NOMENCLATURE xviii

CHAPTER 1 - GENERAL REVIEW

1.1 Introduction 1
1.2 Literature Review 6
1.2.1 Studies of Natural Convective Heat Transfer from Smooth Vertical Channels 8
1.2.2 Studies of Natural Convective Heat Transfer from a Single Isolated Vertical Flat Plate 17
1.2.3 Studies of the Influence of Confining Walls on Natural Convective Heat Transfer 18
1.3 Scope of the Research 24

CHAPTER 2 - NUMERICAL SOLUTION METHODS

2.1 Introduction 26
2.2 Governing Equations 26
2.3 Elliptic Solution 28
2.3.1 Grid Tests for the Undivided Channel (Elliptic Solution) 37
2.3.2 Grid Tests for the Divided Channel (Elliptic solution) 41
2.4 Parabolic Solution 45
2.4.1 Finite Difference Formulation and Method of Solution 48

CHAPTER 3 - THE FULLY DEVELOPED AND ISOLATED PLATE LIMITS

3.1 Introduction 57
3.2 Fully Developed Limit $(Ra^{*} \to 0)$ 57
3.2.1 Fully Developed Channel Average Nusselt Number 60
3.2.2 Fully Developed Plate Average Nusselt Number 65
3.2.3 Fully Developed Wall Average Nusselt Number 66
3.3 Single Isolated Plate Limit $(Ra^{*} \to \infty)$ 70
3.3.1 Isolated Plate Channel Average Nusselt Number 71
3.4 Concluding Remarks 74

CHAPTER 4 - NUMERICAL RESULTS FOR DEVELOPING NATURAL CONVECTION IN AN UNDIVIDED CHANNEL

4.1 Introduction 75
4.2 Discussion of Results 75
4.3 Concluding Remarks 96

CHAPTER 5 - NUMERICAL RESULTS FOR DEVELOPING NATURAL CONVECTION IN A PARTIALLY DIVIDED CHANNEL

5.1 Introduction 97
5.2 Divided Channel with Plate Thickness $t/b=0$ 98
5.2.1 Dividing Plate Located at Bottom of Channel - $L_i/L_c=0$, $(t/b=0)$ 99
5.2.2 Dividing Plate Located in the Middle and Top of Channel - $L_i/L_c=1-L_p/L_c$, $L_i/L_c=(1-L_p/L_c)/2$, $(t/b=0)$ 120
5.2.3 Effect of Dividing Plate Location, $(t/b=0)$ 132
5.3 Effect of Dividing Plate Thickness - $t/b\geq 0$ 138

CHAPTER 6 - EXPERIMENTAL APPARATUS, PROCEDURE AND ANALYSIS

6.1 Introduction 144
6.2 Test Section Design 145
6.3 Experimental Apparatus 156
6.4 Interferometer Alignment 159
6.5 Test Procedure 161
6.6 Interferogram Analysis 165
6.6.1 Calculation of the Local and Average Wall Nusselt Numbers 169
6.6.2 Calculation of the Local and Average Plate Nusselt Numbers 171
6.6.3 Calculation of the Channel Average Nusselt Number 175

CHAPTER 7 - PRESENTATION OF EXPERIMENTAL RESULTS

7.1 Introduction 176
7.2 Experimental Results for the Undivided Channel 176
7.3 Experimental Results for the Divided Channel 181
7.4 Reproducibility of the Experimental Data 196

CHAPTER 8 - DATA CORRELATION

8.1 Method of Data Correlation 198
8.2 Channel Average Nusselt Number Nu_c 199
8.3 Wall Average Nusselt Number Nu_w 200
8.4 Plate Average Nusselt Number Nu_p 205

CHAPTER 9 - CONCLUSIONS AND RECOMMENDATIONS

9.1 Summary and Conclusions 209
9.2 Recommendations for Future Research 213

* * * * *

APPENDIX A APPLICATION OF THE CFD CODE FIDAP 216
APPENDIX B A DIGITAL IMAGING SYSTEM FOR INTERFEROGRAM ANALYSIS 222
APPENDIX C AIR PROPERTIES 233
APPENDIX D TABULAR NUMERICAL DATA 237
APPENDIX E TABULAR EXPERIMENTAL DATA 248
APPENDIX F EXPERIMENTAL ERROR ANALYSIS 249
APPENDIX G SAMPLE EXPERIMENTAL CALCULATIONS 258

REFERENCES 263
VITA 271

LIST OF FIGURES

Figure Description Page

1.1 (a) Printed circuit board array, (b) Smooth plate model 3

1.2 Model geometry for the present study 5

1.3 Range for the natural convective cooling of electronic components (Adapted from Hannemann et al. [3]) 7

1.4 Comparison of existing numerical and experimental channel average Nusselt numbers for an undivided symmetrically heated UWT channel 12

1.5 An array of staggered plates 16

2.1 The heat transfer geometry showing the limits of the computational domain 29

2.2 The Jeffrey-Hamel flow geometry applicable to the present study 32

2.3 (a) The entire finite element grid for the undivided channel ($L_c/b=24$), (b) A close-up view of the grid in the channel entrance region 38

2.4 Finite element grids for the divided channel with a zero thickness plate ($t/b=0$, $L_p/L_c=1/3$, $L_c/b=15$), (a) $L_i/L_c=0$, (b) $L_i/L_c=1/3$, (c) $L_i/L_c=2/3$ 42

2.5 Finite element grids for the divided channel with a finite thickness plate ($L_i/L_c=0$, $L_p/L_c=1/3$, $L_c/b=15$), (a) $t/b=0.1$, (b) $t/b=0.2$, (c) $t/b=0.2$ 43

2.6 The finite difference grid for the parabolic solution 50

3.1 The heat transfer geometry showing the fully developed velocity profiles 59

3.2 Effect of length ratio L_p/L_c and blockage ratio t/b on the fully developed channel average Nusselt number (equation 3.14) 62

3.3 Effect of length ratio L_p/L_c and blockage ratio t/b on the fully developed channel average Nusselt number (equation 3.15) 64

3.4 Effect of length ratio L_p/L_c and blockage ratio t/b on the fully developed plate average Nusselt number for $L_i/b=0$ (equation 3.19) 67

3.5 Effect of length ratio L_p/L_c and blockage ratio t/b on the fully developed wall average Nusselt number for $L_1/b=0$ (equation 3.22) 69

3.6 Effect of length ratio L_p/L_c on the channel average Nusselt number for the isolated plate limit (equations 3.30 and 3.31) 73

4.1 Comparison of the streamwise velocity (V) profiles from the present elliptic solution with the work of Kettleborough, and Nakamura et al.. 78

4.2 Comparison of the temperature profiles from the present elliptic solution with the work of Kettleborough, and Nakamura et al. 79

4.3 Comparison of the channel centre line pressure distributions with that predicted by Nakamura et al.. 80

4.4 Comparison of the local Nusselt number distributions with the experimental data of Wirtz and Haag 80

4.5 Channel inlet streamline and isotherm contours from the elliptic solution for Gr=50, $L_c/b=24$, Pr=0.7 ($Ra_c^*=1.458$) . . . 83

4.6 Channel inlet streamline and isotherm contours from the elliptic solution for $Gr=10^4$, $L_c/b=24$, Pr=0.7 ($Ra_c^*=291.7$) . . . 84

4.7 Close-up view of the separated flow region for $Gr=10^4$, $L_c/b=24$, Pr=0.7 ($Ra_c^*=291.7$) 85

4.8 Streamwise velocity (V) profiles in the separated flow region for various values of Rayleigh number ($L_c/b=24$) 86

4.9 Streamwise velocity gradient at the wall in the separated flow region versus $QGr^{\frac{1}{2}}$ 87

4.10 Comparison of average Nusselt number results from the present elliptic and parabolic solutions 89

4.11 Comparison of induced flow rates from the present elliptic and parabolic solutions 90

4.12 Comparison of streamwise velocity (V) profiles from the present elliptic and parabolic solutions for $Ra_c^*=2.917$ and $Ra_c^*=291.7$ 92

4.13 Comparison of temperature profiles from the present elliptic and parabolic solutions for $Ra_c^*=2.917$ and $Ra_c^*=291.7$ 93

4.14 Comparison of centre line pressure distributions from the present elliptic and parabolic solutions 95

4.15 Comparison of local Nusselt number distributions from the present elliptic and parabolic solutions 95

5.1 Streamline and isotherm contours for the divided channel with $L_p/L_c=1/3$, $t/b=0$, and $L_i/L_c=0$, (a) $Ra_c^*=5$, (b) $Ra_c^*=10^4$ 100

5.2 Comparison of the developing velocity profiles in the divided channel at low and high Rayleigh number, $Ra_c^*=10, 10^4$, for $L_p/L_c=1/3$, $L_i/L_c=0$, $t/b=0$ 101

5.3 Comparison of the developing temperature profiles in the divided channel at low and high Rayleigh number, $Ra_c^*=10, 10^4$, for $L_p/L_c=1/3$, $L_i/L_c=0$, $t/b=0$ 102

5.4 Variation of the plate average Nusselt number (Nu_p) with Rayleigh number (Ra_p^*) for several plate length ratios and $L_i/L_c=0$, $(t/b=0)$ 105

5.5 Effect of plate length ratio L_p/L_c on the plate average Nusselt number (Nu_p) for $L_i/L_c=0$, $(t/b=0)$ 107

5.6 The plate local Nusselt number distribution for $L_i/L_c=0$ and $L_p/L_c=1/3$, $(t/b=0)$ 108

5.7 Variation of the wall average Nusselt number (Nu_w) with Rayleigh number (Ra_c^*) for several plate length ratios and $L_i/L_c=0$, $(t/b=0)$ 110

5.8 The wall local Nusselt number distribution for $L_i/L_c=0$ and $L_p/L_c=1/3$, $(t/b=0)$ 112

5.9 Variation of the channel average Nusselt number (Nu_c) with Rayleigh number (Ra_c^*) for several plate length ratios and $L_i/L_c=0$, $(t/b=0)$ 115

5.10 Variation of the dimensionless induced flow rate with Rayleigh number (Ra_c^*) for several plate length ratios and $L_i/L_c=0$, $(t/b=0)$ 116

5.11 The channel pressure distribution at several values of Rayleigh number for $L_p/L_c=1/3$ and $L_i/L_c=0$, $(t/b=0)$ 117

5.12 Variation of the plate average Nusselt number (Nu_p) with Rayleigh number (Ra_p^*) for several plate length ratios and $L_i/L_c=(1-L_p/L_c)/2$, $(t/b=0)$ 121

5.13 Variation of the plate average Nusselt number (Nu_p) with Rayleigh number (Ra_p^*) for several plate length ratios and $L_i/L_c=1-L_p/L_c$, $(t/b=0)$ 121

5.14 The plate local Nusselt number distribution for $L_i/L_c=(1-L_p/L_c)/2$ and $L_p/L_c=1/3$, $(t/b=0)$ 123

5.15 Variation of the wall average Nusselt number (Nu_w) with Rayleigh number (Ra_c^*) for several plate length ratios and $L_i/L_c=(1-L_p/L_c)/2$, (t/b=0) 124

5.16 Variation of the wall average Nusselt number (Nu_w) with Rayleigh number (Ra_c^*) for several plate length ratios and $L_i/L_c=1-L_p/L_c$, (t/b=0) 124

5.17 The wall local Nusselt number distribution for $L_i/L_c=(1-L_p/L_c)/2$ and $L_p/L_c=1/3$, (t/b=0) 126

5.18 Variation of the channel average Nusselt number (Nu_c) with Rayleigh number (Ra_c^*) for several plate length ratios and $L_i/L_c=(1-L_p/L_c)/2$, (t/b=0) 128

5.19 Variation of the channel average Nusselt number (Nu_c) with Rayleigh number (Ra_c^*) for several plate length ratios and $L_i/L_c=1-L_p/L_c$, (t/b=0) 128

5.20 The channel pressure distribution at several values of Rayleigh number for $L_p/L_c=1/3$ and $L_i/L_c=1-L_p/L_c$, (t/b=0) . 129

5.21 Streamline and isotherm contours for the divided channel with $L_p/L_c=1/3$, t/b=0, and $L_i/L_c=1-L_p/L_c=2/3$, (a) $Ra_c^*=5$, (b) $Ra_c^*=10^4$ 133

5.22 Effect of the dividing plate location on dimensionless flow rate and bulk exit temperature for $L_p/L_c=1/3$, (t/b=0) 135

5.23 Effect of the dividing plate location on the plate average Nusselt number for $L_p/L_c=1/3$, (t/b=0) 135

5.24 Effect of the dividing plate location on the wall average Nusselt number for $L_p/L_c=1/3$, (t/b=0) 137

5.25 Effect of the dividing plate location on the channel average Nusselt number for $L_p/L_c=1/3$, (t/b=0) 137

5.26 Streamline and isotherm contours for the divided channel with t/b=0.2, $L_p/L_c=1/3$, $L_i/L_c=0$, (a) $Ra_c^*=5$, (b) $Ra_c^*=10^4$ 139

5.27 Effect of the dividing plate thickness (t/b) on dimensionless flow rate for $L_p/L_c=1/3$ and $L_i/L_c=0$ 141

5.28 Effect of the dividing plate thickness (t/b) on the plate average Nusselt number for $L_p/L_c=1/3$ and $L_i/L_c=0$ 141

5.29 Effect of the dividing plate thickness (t/b) on the wall average Nusselt number for $L_p/L_c=1/3$ and $L_i/L_c=0$ 142

5.30 Effect of the dividing plate thickness (t/b) on the channel average Nusselt number for $L_p/L_c=1/3$ and $L_i/L_c=0$ 142

6.1 Cross-sectional view of the divided channel test section . . 146

6.2 Mechanical drawing of the aluminum plates that formed the isothermal channel walls 148

6.3 (a) Front and (b) back view of one channel wall assembly . 149

6.4 (a) Isometric and (b) cross-sectional views of the heat exchangers 151

6.5 Mechanical drawing of one side of the copper divider plate 152

6.6 The assembled divider plate and one thin foil heater 154

6.7 The test section in the Mach-Zehnder interferometer (L_i/L_c=0) 154

6.8 Schematic diagram of the experimental apparatus 157

6.9 Optical setup for obtaining a parallel beam 160

6.10 (a) Finite fringe condition for the unheated model, (b) Infinite fringe condition for the unheated model 162

6.11 Sketch of the divider plate showing the three sections scanned, AB, BC, CD 172

7.1 (a) Infinite fringe and (b) finite fringe interferograms of the undivided channel for Ra_c^*=92.4, L_c/b=13.8 177

7.2 Comparison of the experimental temperature profiles for the undivided channel with the numerical results of Nakamura et al., Kettleborough, and the present solution . . 179

7.3 Comparison of the experimental and numerical (elliptic) wall local Nusselt number distributions for the undivided channel 180

7.4 Comparison of (a) an infinite fringe interferogram and (b) a numerical isotherm contour plot for Ra_c^*=97.6, L_i/L_c=0, L_c/b=13.68, t/b=0.20 183

7.5 Comparison of the experimental and numerical (elliptic) local Nusselt number distributions for (a) the wall, (b) the plate. (Ra_c^*=97.6, L_p/L_c=1/3, L_i/L_c=0, t/b=0.2) 185

7.6 Interferograms showing the effect of increasing Rayleigh number with the plate located in the bottom of the channel, L_i/L_c=0, (L_p/L_c=1/3) (a) Ra_c^*=97.6, (b)Ra_c^*=874, (c) Ra_c^*=5930, (d) Ra_c^*= 874 187

7.7 Interferograms showing the effect of increasing Rayleigh number with the plate located at the top of the channel, L_i/L_c=2/3, (L_p/L_c=1/3) (a) Ra_c^*=81.4, (b)Ra_c^*=888, (c) Ra_c^*=5610, (d) Ra_c^*= 888 188

7.8 Experimental local Nusselt number distributions for (a) the plate and (b) the wall, for L_p/L_c=1/3, L_i/L_c=0 190

7.9 Experimental local Nusselt number distributions for (a) the plate and (b) the wall, for L_p/L_c=1/3, L_i/L_c=2/3 191

7.10 Comparison of the experimental and numerical plate average Nusselt numbers, L_p/L_c=1/3 194

7.11 Comparison of the experimental and numerical wall average Nusselt numbers, L_p/L_c=1/3 197

8.1 Correlation of the channel average Nusselt number (Nu_c) data for L_i/L_c=0. 202

8.2 Correlation of the wall average Nusselt number (Nu_w) data for L_i/L_c=0 204

8.3 Variation of the plate average Nusselt number (Nu_p) with plate length ratio (L_p/L_c) at $Ra_p^*=10^4$, (L_i/L_c=0, t/b=0) . . . 206

8.4 Correlation of the plate average Nusselt number (Nu_p) data for L_i/L_c=0 208

A.1 (a) Logical and (b) physical planes for the divided channel finite element mesh (corresponding to the FIDAP input file listing) 221

B.1 Schematic diagram of the image processing system. 224

B.2 (a) Section of an infinite fringe interferogram displayed on the monitor, (b) Interferogram on the monitor showing the scanned locations 227

B.3 A typical horizontal pixel intensity profile (showing three destructive fringe peaks) 228

B.4 Integrated intensity and maximum intensity fringe centre plot 229

C.1 Dynamic viscosity versus temperature for air 234

C.2 Thermal conductivity versus temperature for air 234

LIST OF TABLES

Table	Description	Page
1.1	Summary of the experimental studies of the effect of confining walls on natural convective heat transfer	20
2.1	Partial results from the elliptic solution grid tests for the undivided channel (for $Ra_c^*=291.7$, $Gr=10^4$, $L_c/b=24$, $L_p/L_c=0$)	40
2.2	Partial results from the elliptic solution grid tests for the divided channel (for $Ra_c^*=10^4$, $t/b=0$, $L_i/L_c=0$,$L_p/L_c=1/3$, $L_c/b=15$)	40
4.1	Comparison of the major data with other elliptic solutions for $Gr=1250$, $Pr=0.733$, $L_c/b=10$ ($Ra_c^*=91.625$)	76
5.1	Comparison of major data from the parabolic and elliptic solutions for $L_p/L_c=1/3$, $L_i/L_c=0$ (bottom), $t/b=0$, $Pr=0.7$	119
5.2	Comparison of major data from the parabolic and elliptic solutions for $L_p/L_c=1/3$, $L_i/L_c=(1-L_p/L_c)/2$ (middle), $t/b=0$	130
5.3	Comparison of major data from the parabolic and elliptic solutions for $L_p/L_c=1/3$, $L_i/L_c=1-L_p/L_c$ (top), $t/b=0$, $Pr=0.7$	131
7.1	Experimental and numerical average Nusselt numbers for $Ra_c^*=97.56$, $L_p/L_c=1/3$, $t/b=0.2$, $L_c/b=13.68$	184
7.2	(a) Experimental average Nusselt Number data for $L_p/L_c=1/3$, $L_i/L_c=0$ (bottom)	193
7.2	(b) Experimental average Nusselt number data for $L_p/L_c=1/3$, $L_i/L_c=1-L_p/L_c$ (top)	193
8.1	Constants and statistics for the channel Nusselt number correlation equation 8.2	201
8.2	Constants and statistics for the wall Nusselt number correlation equation 8.3	201
D.1	Numerical results from the elliptic solution (FIDAP) for the undivided channel ($L_p/L_c=0$)	237
D.2	Numerical results from the elliptic solution (FIDAP) for the divided channel, $L_p/L_c=1/3$, no blockage $t/b=0.0$, $L_c/b=15$, $Pr=0.7$, plate at the bottom of the channel $L_i/L_c=0$	238

D.3 Numerical results from the elliptic solution (FIDAP) for the divided channel, $L_p/L_c=1/3$, no blockage t/b=0.0, $L_c/b=15$, Pr=0.7, plate in the middle of the channel, $L_i/L_c=(1-L_p/L_c)/2=1/3$ 239

D.4 Numerical results from the elliptic solution (FIDAP) for the divided channel, $L_p/L_c=1/3$, no blockage t/b=0.0, $L_c/b=15$, Pr=0.7, plate at the top of the channel, $L_i/L_c=1-L_p/L_c=2/3$ 239

D.5 Numerical results from the elliptic solution (FIDAP) for the divided channel, $L_p/L_c=1/3$, 10% blockage t/b=0.1, $L_c/b=15$, Pr=0.7, plate at the bottom of the channel, $L_i/L_c=0$ 240

D.6 Numerical results from the elliptic solution (FIDAP) for the divided channel, $L_p/L_c=1/3$, 20% blockage t/b=0.2, $L_c/b=15$, Pr=0.7, plate at the bottom of the channel, $L_i/L_c=0$ 240

D.7 Numerical results from the parabolic solution for the undivided channel $L_p/L_c=0$, Pr=0.7 241

D.8 Numerical results from the parabolic solution for the divided channel (t/b=0), $L_p/L_c=2/3$ (nominal), Pr=0.7, plate at the bottom of the channel $L_i/L_c=0$ 241

D.9 Numerical results from the parabolic solution for the divided channel (t/b=0), $L_p/L_c=1/3$ (nominal), Pr=0.7, plate at the bottom of the channel $L_i/L_c=0$ 242

D.10 Numerical results from the parabolic solution for the divided channel (t/b=0), $L_p/L_c=1/10$ (nominal), Pr=0.7, plate at the bottom of the channel $L_i/L_c=0$ 242

D.11 Numerical results from the parabolic solution for the divided channel (t/b=0), $L_p/L_c=1/100$ (nominal), Pr=0.7, plate at the bottom of the channel $L_i/L_c=0$ 243

D.12 Numerical results from the parabolic solution for the divided channel (t/b=0), $L_p/L_c=2/3$ (nominal), Pr=0.7, plate in the middle of the channel $L_i/L_c=(1-L_p/L_c)/2=1/6$ 243

D.13 Numerical results from the parabolic solution for the divided channel (t/b=0), $L_p/L_c=1/3$ (nominal), Pr=0.7, plate in the middle of the channel $L_i/L_c=(1-L_p/L_c)/2=1/3$ 244

D.14 Numerical results from the parabolic solution for the divided channel (t/b=0), $L_p/L_c=1/10$ (nominal), Pr=0.7, plate in the middle of the channel $L_i/L_c=(1-L_p/L_c)/2=9/20$ 244

D.15 Numerical results from the parabolic solution for the divided channel (t/b=0), $L_p/L_c=2/3$ (nominal), Pr=0.7, plate in the top of the channel $L_i/L_c=1-L_p/L_c=1/3$ 245

D.16 Numerical results from the parabolic solution for the divided channel (t/b=0), $L_p/L_c=1/3$ (nominal), Pr=0.7, plate in the top of the channel $L_i/L_c=1-L_p/L_c=2/3$ 245

D.17 Numerical results from the parabolic solution for the divided channel (t/b=0), $L_p/L_c=1/10$ (nominal), Pr=0.7, plate in the top of the channel $L_i/L_c=1-L_p/L_c=9/10$ 246

D.18 Numerical results from the parabolic solution for the divided channel (t/b=0). Special calculations made holding Ra_p^* constant and varying the plate length ratio L_p/L_c. The plate is at the bottom of the channel $L_i/L_c=0$, and Pr=0.7 . . . 247

E.1 Experimental average Nusselt number and associated data ($L_p/L_c=1/3$, L_c=120.0mm, L_p=40.0mm , $L_{p,wet}$=42.0mm, 2t=3.5mm) 248

F.1 Summary of the sources of uncertainty in the Rayleigh number 251

NOMENCLATURE

A	amplitude of a light wave
b	half channel width
c	speed of light
C_p	contant pressure specific heat
C	constant in the isolated plate Nusselt number expression
C_1,C_2	constants in equation (8.3)
F(θ)	angular dependence of Jeffrey-Hamel flow
g	gravitational acceleration
G	specific refractivity
Gr	Grashof number, $g\beta(T_s-T_o)b^3/\nu^2$
h_c	channel average heat transfer coefficient, $H_c/((L_p+L_c)(T_s-T_o))$
h_p	plate average heat transfer coefficient, $H_p/(L_p(T_s-T_o))$
h_w	wall average heat transfer coefficient, $H_w/(L_c(T_s-T_o))$
$h_{p,y}$	plate local heat transfer coefficient
$h_{w,y}$	wall local heat transfer coefficient
H_c	total rate of heat transfer from the entire half channel
H_p	total rate of heat transfer from one side of the plate
H_w	total rate of heat transfer from one channel wall
k	thermal conductivity
L_c	channel (and wall) length
L_i	length of the channel which is undivided at the channel inlet
L_p	dividing plate length
L_c^*	dimensionless channel length (parabolic solution)
L_i^*	dimensionless length of the channel which is undivided at the channel inlet (parabolic solution)

L_p^*	dimensionless dividing plate length (parabolic solution)
$L_{p,wet}$	wetted length of the dividing plate
n	exponent for Nusselt number correlations (Chapter 8)
N	index of refraction
Nu_c	channel average Nusselt number
Nu_p	dividing plate average Nusselt number
$Nu_{p,y}$	plate local Nusselt number, $h_{p,y}b/k$
Nu_w	wall average Nusselt number
$Nu_{w,y}$	wall local Nusselt number, $h_{w,y}b/k$
p'	pressure defect, $p-p_o$
p,P	pressure and dimensionless pressure
PL	optical path length
Pr	Prandtl number, $\mu C_p/k$
q	half channel flow rate
Q_e	dimensionless half channel flow rate for the elliptic solution
Q_{p*}	dimensionless half channel flow rate for the parabolic solution
r,R	radius and dimensionless radius
R_{air}	gas constant for air
r_i,R_i	dimensional and dimensionless inlet domain radius
Ra	Rayleigh number (unmodified), Gr Pr
Ra_c^*	channel Rayleigh Number (modified), Gr Pr(b/L_c)
Ra_p^*	plate Rayleigh Number (modified), Gr Pr(b/L_p)
t	dividing plate half thickness
T,T^*	temperature and dimensionless temperature
T_b^*	bulk temperature at channel exit $(Y=L_c/b)$
T_s	surface temperature (wall or dividing plate)
T_o	ambient temperature

u,U	x velocity component and dimensionless x velocity component
U_{ref}	reference velocity scale, $U_{ref}=\alpha Pr(Gr)^{1/4}/b$
v,V	y velocity component and dimensionless y velocity component
v_r,v_θ	radial and tangential component of velocity
V_r,V_θ	dimensionless radial and tangential velocity components
x,y	cartesian coordinates
X,Y	dimensionless cartesian coordinates
$\Delta X,\Delta Y$	dimensionless grid size (parabolic solution)
z	cartesian coordinate in the direction of the light beam
Z_T	length of the test section in the direction of the light beam

Greek

α	thermal diffusivity
β	volumetric expansion coefficient
ϵ	fringe shift
η	rate of increase of grid size in the Y_{p*} direction
θ	cylindrical coordinate
λ	wavelength of light
μ	dynamic viscosity
ν	kinematic viscosity
ρ	density
σ_{rr}	radial stress component
τ	time
ϕ	phase shift between the reference beam and test beam
ψ	dimensionless stream function

Subscripts

f	evaluated at the film temperature, $(T_s+T_o)/2$
i,j	grid indices in X_{p*} and Y_{p*} directions (parabolic solution)
L	dimensionless quantity with characteristic dimension L
o	ambient value or initial value
p	value for the dividing plate
p^*	dimensionless quantity associated with the parabolic solution
ref	value for the reference beam
test	value for the test beam
w	value for the channel wall

The author of this thesis has granted The University of Western Ontario a non-exclusive license to reproduce and distribute copies of this thesis to users of Western Libraries. Copyright remains with the author.

Electronic theses and dissertations available in The University of Western Ontario's institutional repository (Scholarship@Western) are solely for the purpose of private study and research. They may not be copied or reproduced, except as permitted by copyright laws, without written authority of the copyright owner. Any commercial use or publication is strictly prohibited.

The original copyright license attesting to these terms and signed by the author of this thesis may be found in the original print version of the thesis, held by Western Libraries.

The thesis approval page signed by the examining committee may also be found in the original print version of the thesis held in Western Libraries.

Please contact Western Libraries for further information:
E-mail: libadmin@uwo.ca
Telephone: (519) 661-2111 Ext. 84796
Web site: http://www.lib.uwo.ca/

CHAPTER 1

GENERAL REVIEW

1.1 Introduction

Natural, or free, convection is the buoyancy-induced fluid motion that results from density variations in the presence of a body force field. Natural convection is perhaps the most common cause of fluid motion. Free convective flows span from the large scale motions of weather patterns and ocean currents to the small scale flows associated with the cooling of man-made devices.

From an engineering perspective, natural convection is commonly used as a passive means of rejecting waste heat. This thesis extends the knowledge of natural convective cooling of isothermal parallel plate geometries. Early studies of isothermal parallel plates [1] were undertaken because of the need to predict the cooling of fins. At present there is a resurgence of interest in heat transfer from parallel plates because of modern applications to the cooling of electronic and computer equipment.

The intended primary application of the present research is to the air cooling of printed circuit boards (PCBs). To a large extent, the reliability of a computer chip depends upon adequate heat removal. The heat removal problem has been continuously exacerbated in the last twenty years by the trend toward larger scales of circuit integration. Increasing miniaturization has made heat transfer considerations crucial in design of electronic packaging. Typically, current devices dissipate an order of magnitude more power than the devices of ten years ago. In fact, adequate heat removal may well be the limiting factor in future developments of high speed circuits [2].

Hannemann, Fox (of Digital Equipment Corporation) and Mahalingham (of Motorola Inc.) [3] state that there are three main concerns in the thermal design of electronic equipment: i) keeping the temperature of all devices below some upper limit (typically 85-100°C) as constrained by reliability factors, ii) limiting the temperature difference between critical communicating circuits, and iii) controlling thermally induced stresses; the most frequent concern is the fatigue failure of soldered joints during power cycling [4].

Heat dissipation from an *actual* PCB array is a tremendously complex phenomenon. The heat transfer from the discrete heat dissipating components on the board is not only influenced by convection to the air, but also by board conduction and by radiation exchange between the other components and the surroundings. Clearly, the actual thermal performance will be dependent upon the specific electronic packaging design.

To make this problem tractable in a general sense, PCB arrays are commonly approximated by either uniform wall temperature (UWT) or uniform heat flux (UHF) smooth plates as shown in Fig. 1.1. Indeed, many such studies of two-dimensional natural convection from smooth parallel heated plates have been published. From these studies, several practical correlations have been developed to enable design engineers to predict the thermal performance of electronic packaging [5,6,7]. In these correlations,

(a) PCB array

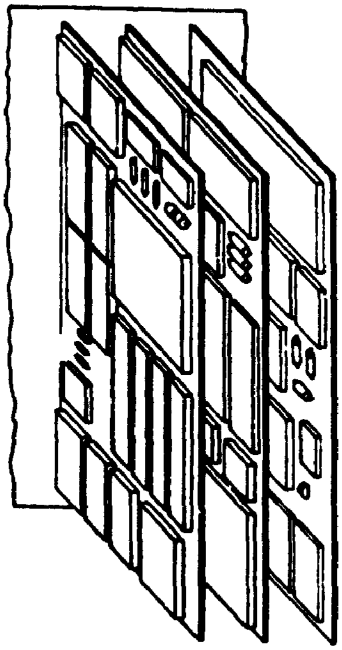

(b) Smooth plate model

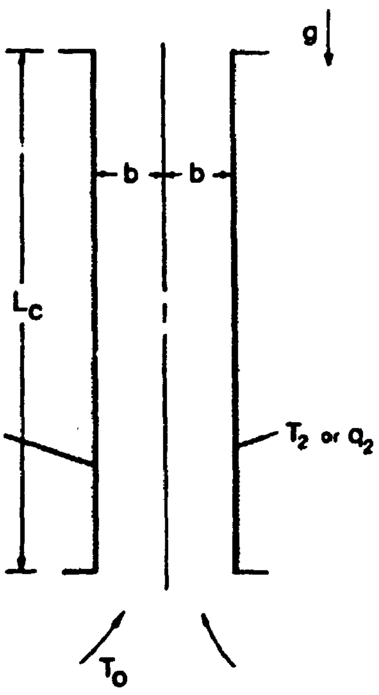
g
b
b
L_c
T_1 or q_1
T_2 or q_2
T_0

Figure 1.1: (a) Printed circuit board array and (b) Smooth plate model

factors such as edge effects, and the influence of protruding components, have not been taken into account. However, for many applications, existing parallel plate correlations can be used to suitably approximate actual PCB conditions [8,9].

Previous studies have been almost exclusively restricted to considering vertical parallel plates of equal length (as in Fig. 1.1(b)). The present study focuses on a more complex circuit board configuration. Figure 1.2 shows a schematic diagram of the model geometry. A short board of thickness 2t and length L_p is positioned on the centre line of a channel formed by two parallel boards of length L_c, spaced 2b apart. The centre board is positioned a distance L_i from the channel inlet. Both the centre board and the confining walls are heated to temperature T_s above the ambient temperature T_o. The objective of the present study is to determine if significant heat transfer enhancements, particularly for the centre board, can be obtained from the careful choice of geometric parameters (L_p, L_c, b, t, L_i).

Studies with circular cylinders [10,11,12], elliptic cylinders [13] and finned tubes [14] have demonstrated that the presence of *unheated* confining walls can enhance heat transfer because of the "chimney effect". The walls confine the heated fluid in the plume into a column, thereby increasing the buoyancy induced flow and heat transfer. The primary motivation of the present study is to determine the heat transfer enhancement that can be gained from the relative positioning of adjacent circuit boards, utilizing this same principle. Emphasis is given to the case where the short dividing board is located at the entrance of the channel (L_i=0), since this

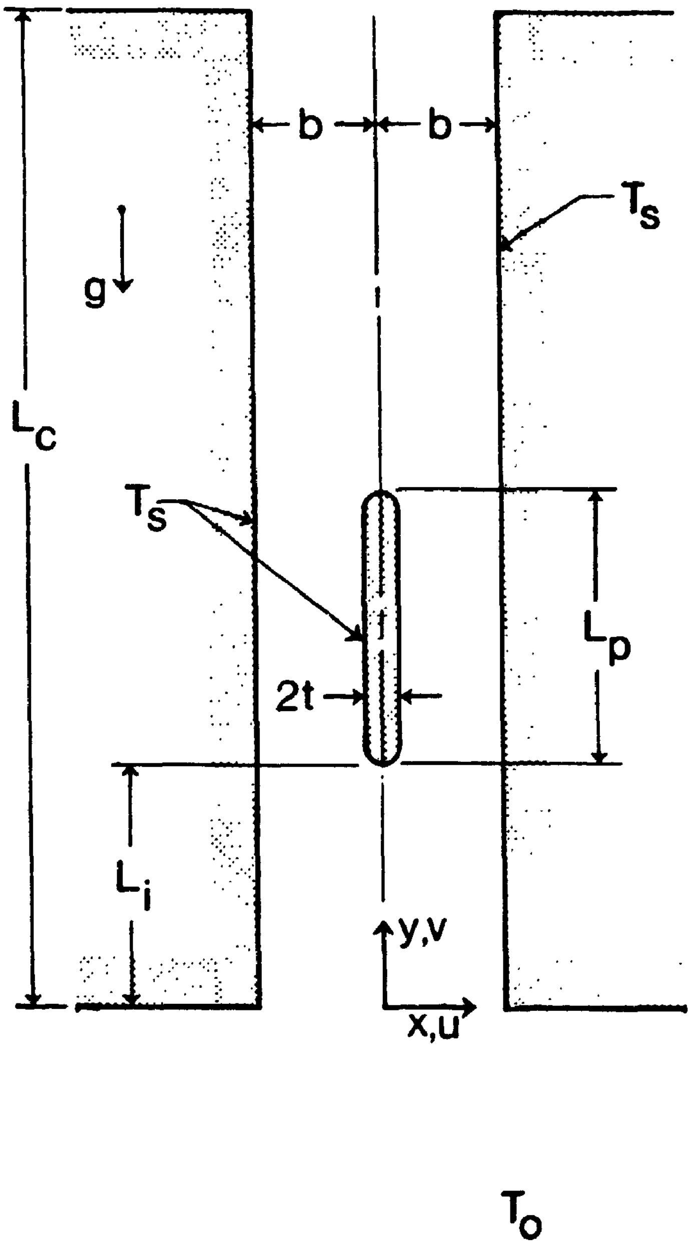
b
b
T_s
g
L_c
T_s
L_p
2t
L_i
y,v
x,u
T_o

Figure 1.2: Model geometry for the present study.

configuration is expected to yield the greatest heat transfer enhancement.

Natural convective cooling of circuit boards is preferred over forced cooling because of the lower cost, higher reliability, and lack of electromagnetic and acoustic noise. The two main parameters that govern the feasibility of natural convective cooling are the maximum chip power and the board average heat flux [15,16]. Figure 1.3 shows the "envelope" for the practical application of natural convection air cooling using standard packaging techniques (Adapted from Hannemann [15])[1]. Since a large portion of the overall thermal resistance in air-cooled electronic packages is due to convection, any increase in the external convection coefficient will result in a significant decrease in the component temperatures. Hence, convection coefficient enhancements achieved through geometric effects (such as relative board positioning) could be used to extend the range of applicability for passive cooling.

1.2 Literature Review

The geometry for the present study is a combination of two well studied geometries: i) the vertical channel, and ii) the single vertical flat plate. For this reason, the literature for natural convection from vertical channels (§1.2.1) and isolated plates (§1.2.2) will be reviewed. In addition, studies involving the influence of confining walls on free convective heat transfer will be reviewed (§1.2.3).

---

[1] Fig. 1.3 is presented for illustrative purposes only. The actual limits of applicability for natural convective cooling will be dependent upon the specific application.

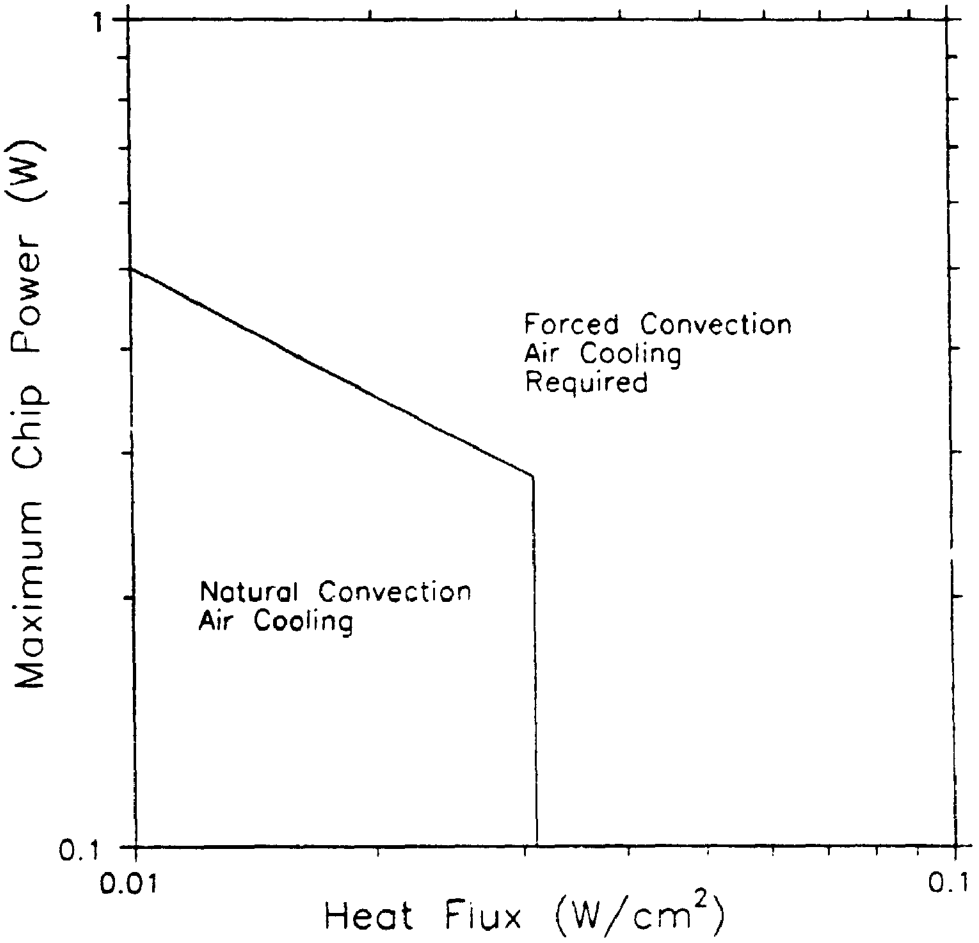

Figure 1.3: Range for the natural convective cooling of electronic components (Adapted from Hannemann et al. [3]).

1.2.1 Studies of Natural Convective Heat Transfer from Smooth Vertical Channels.

Studies of free convection from vertical channels have been undertaken mainly because of the application to the cooling of fins and electronic equipment. However, there has been additional interest in vertical channels because of the need to predict the passive solar heating of buildings via Trombe walls [17,18,19]. A brief review of studies of natural convection in vertical channels will be given here to provide the background and terminology associated with the channel geometry. Recent comprehensive reviews of natural convection in vertical channels are available in references [20,21].

The pioneering work on natural convection in vertical channels was done by Elenbaas [1] in 1942. He performed experiments using symmetrically heated, square, isothermal plates open at all edges. Combining the experimental data with theoretical analysis, Elenbaas derived the following semi-empirical correlation for the channel average Nusselt number:

$$Nu_c = \frac{h_c b}{k} = \frac{Gr Pr b}{3L_c}\left(1-e^{\frac{-35L_c}{16 Gr Pr b}}\right)^{\frac{3}{4}} \tag{1.1}$$

where, Gr is the Grashof number ($Gr=g\beta(T_s-T_o)b^3/\nu^2$) based on the half channel width (b).

Elenbaas was the first to show that the channel average Nusselt number is essentially independent of the channel aspect ratio (L_c/b) when correlated with the modified channel Rayleigh number $Ra_c^*=Gr\cdot Pr\cdot b/L_c$. Also, he showed that for large values of modified Rayleigh number, the single flat plate solution is approached (see Fig. 1.4).

The experimental results of Elenbaas are still much-quoted and are generally accepted as a reference standard. However, Sparrow and Bahrami [22] have demonstrated that Elenbaas's data are unreliable at low Rayleigh number because of variable property effects and very large corrections for extraneous heat losses. Using a naphthalene sublimation technique, Sparrow and Bahrami [22] measured average Nusselt numbers much higher than Elenbaas for $Ra_c^* < 0.625$.

Relatively few studies on the vertical channel geometry were conducted in the twenty years following Elenbaas's benchmark publication. Then, with the widespread availability of digital computer facilities, numerical studies dominated the literature in this area.

Bodoia and Osterle [23] obtained the first numerical solution of developing laminar natural convection in a symmetrically heated isothermal channel using the boundary-layer approximations. The boundary-layer form of the governing equations was solved using an explicit forward marching finite difference procedure with assumed channel inlet conditions. Bodoia and Osterle assumed a uniform velocity profile ($v=v_o$), a uniform temperature profile ($T=T_o$), and ambient pressure at the channel inlet. The overall heat transfer results were in good agreement with the experimental data of Elenbaas [1]. Also, the numerically predicted flow rates were confirmed in a later experiment by Currie and Newman [24] (for $0.036 \le Ra_c^* \le 0.35$). In addition, at low Rayleigh number, Bodoia's and Osterle's numerical data asymptotically approach the theoretical fully developed limit of:

$$Nu_c - \frac{Ra_c^*}{3} \tag{1.2}$$

The boundary-layer equations are parabolic in form. Hence, the forward marching solutions to the boundary-layer equations are often referred to as "*parabolic solutions*". In contrast, the full equations without the boundary-layer simplifications, are elliptic in form; solutions of the complete equations are commonly called full "*elliptic solutions*".

Because of the success of the original parabolic solution by Bodoia and Osterle, their basic methodology has been widely used to solve steady laminar free convective channel flows for various boundary conditions. With only slight modifications to the numerical method, developing free convection has been solved for the case of walls with unequal uniform temperature (UWT) [25,26], unequal uniform heat flux (UHF) [25,27,28], and one wall UWT/one wall adiabatic [29, 30]. Davis and Perona [31] extended the solution method to solve axisymmetric free convection in a vertical tube for UWT and UHF boundary conditions. Similarly, Pollard and Oosthuizen [32] solved free convection in a vertical tube for parabolic wall temperature and heat flux distributions. Also, Aihara [33] has used the forward marching method to study variable property effects for UWT channels. In each of the above solutions, a uniform inlet velocity profile is assumed; Aung et al. [25] noted that the uniform inlet velocity assumption makes this general solution method inaccurate for very wide channel spacings.

The most significant and widely adopted improvement to the forward marching finite difference method has been to approximate the pressure drop caused by the fluid acceleration at the channel inlet (Aihara [34]). In early studies, the pressure at the channel inlet was assumed to be equal to atmospheric pressure. Aihara [34] used a more correct inlet condition for pressure, $p-p_o=-\rho v_o^2/2$. In independent studies, Aihara [34], and Chappidi and Eno [35] have shown that the assumption of zero pressure defect results in higher predicted values of local and overall Nusselt number than those obtained with the pressure defect.

Aihara [34], and Chappidi and Eno [35] have also studied the sensitivity of the finite difference forward marching solutions to the assumed inlet velocity profile. Solutions were compared for uniform and parabolic inlet velocity profiles. At low Rayleigh number, the overall heat transfer results were insensitive to the inlet conditions. At high Rayleigh number ($Ra_c^*=10^4$), the uniform inlet velocity profile gave average Nusselt number predictions about 5% higher than the parabolic profile.

Figure 1.4 shows a comparison of the numerically predicted channel average Nusselt number (Aihara [34]) with the experimental data of Elenbaas [1], Aihara [36] and Kennard [37]. This figure clearly shows the excellent agreement between the parabolic (boundary-layer) solution and the experimental data. It is interesting that the isolated plate limit is not an upper bound; rather, the isolated plate behaviour is approached from above. For the numerical solution, Aihara obtained channel average Nusselt values almost 20% higher than for the single isolated plate. Similar high Rayleigh number behaviour was found by Sparrow and Azevedo [38] for an asymmetrically heated channel.

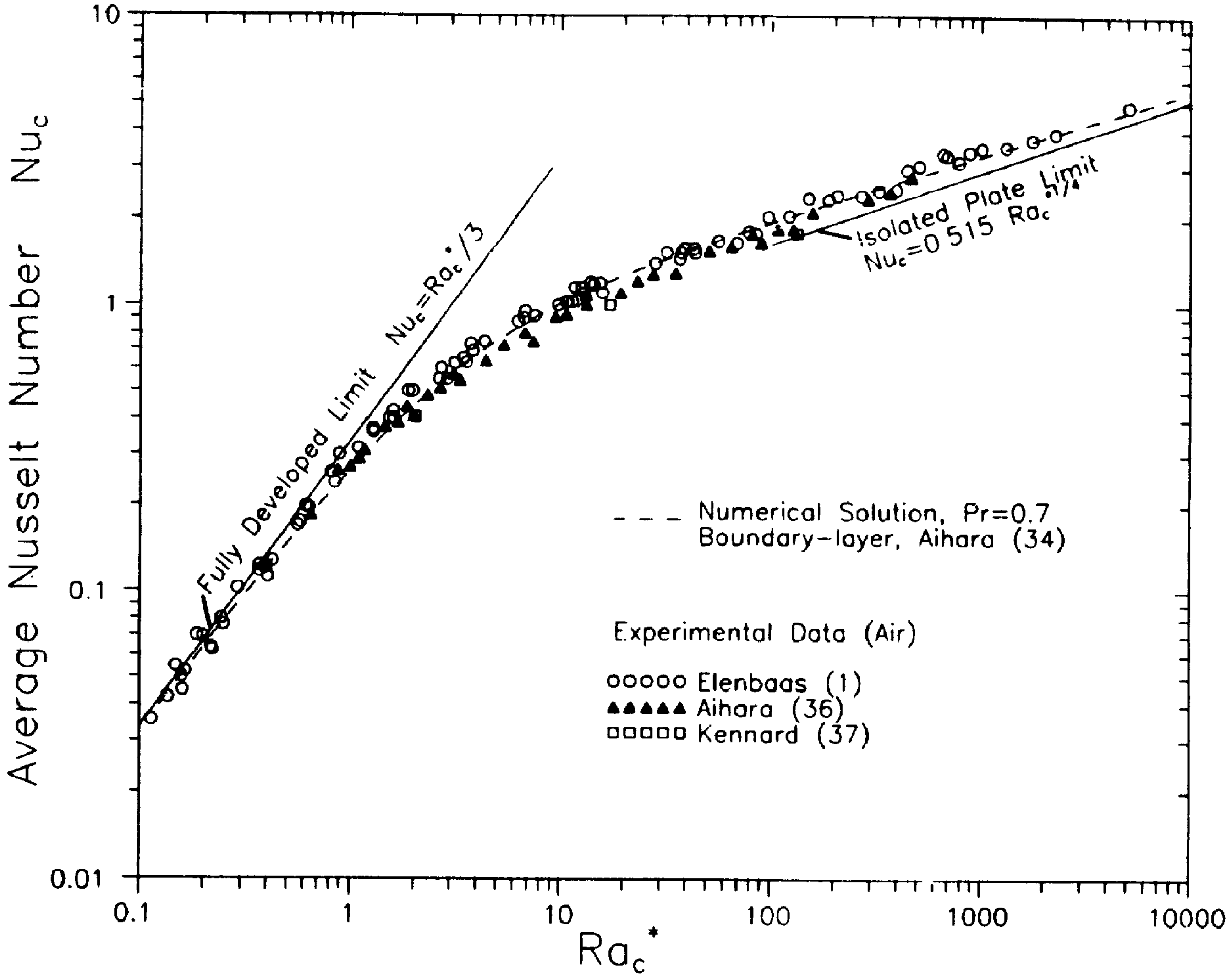

Figure 1.4: Comparison of existing numerical and experimental channel average Nusselt numbers for an undivided symmetrically heated UWT channel.

Relatively few numerical solutions to free convection in the vertical channel have been carried out without using the boundary-layer approximations. Kettleborough [39] and Nakamura et al. [40] have presented data from finite difference solutions to the full elliptic problem (for the UWT channel and Pr=0.733). Both Kettleborough and Nakamura et al. used the stream function-vorticity formulation. At the top of the channel the derivatives of temperature, vorticity, and stream function normal to the outflow boundary were set to zero. Also, in both solutions the flow domain outside the channel entrance was modelled and no assumptions were made about the velocity and temperature profiles at the channel inlet. However, the results are limited to two values of Rayleigh number ($Ra_c^*=91.625$, $Ra_c^*=0.91625$) and are in poor agreement in many aspects. Kettleborough predicts that for $Ra_c^*=91.625$ ($L_c/b=10$), fluid is drawn into the channel from the channel exit. Nakamura et al. does not predict this reverse flow.

Ramanathan et al. [7] have obtained a full elliptic solution to free convection in a UHF vertical channel for a wide range of channel aspect ratios. They found that for $L_c/b \geq 10$, the average Nusselt number is independent of channel aspect ratio and asymptotically approaches the fully developed limit at low Rayleigh number. However, for $L_c/b<10$, the data are not independent of aspect ratio at low Rayleigh number. Also, the data are significantly higher than the fully developed channel Nusselt number. They concluded that for small channel aspect ratios, vertical conduction at the channel inlet and outlet cannot be neglected. Hence, boundary-layer-type solutions will not give accurate results for short channels at low Rayleigh number.

Aung [41] has derived the limiting average Nusselt number expressions for fully developed natural convection in asymmetrically heated channels (UWT and UHF). The expressions were derived by exact analytical solution of the boundary-layer equations. As discussed above, these expressions are only valid for channels with large aspect ratios. A surprising conclusion of Aung's analysis is that for free convection in channels, the thermal developing length is shorter than or at most equal to the hydrodynamic developing length, regardless of the value of the Prandtl number.

Said and Krane [42] have studied the effect of channel blockage on natural convection from channels. In this combined numerical and interferometric study, a semi-cylindrical obstruction attached to one channel wall partially blocks the channel cross-section. Both isothermal (UWT) and uniform heat flux (UHF) conditions for the wall and semi-cylindrical obstruction were studied. Channel blockages as high as 67% of the wall spacing were considered; comparisons were made to the unblocked channel. The results indicate that an obstruction has much less effect at high Rayleigh number than low Rayleigh number. For UWT, at $Ra_c^*=0.625$ the largest obstruction reduced the channel average Nusselt number by about 40%. In contrast, at $Ra_c^*=625$, the same blockage caused only a 5% reduction in the average heat transfer.

Heat transfer enhancements produced by adding adiabatic extensions to a symmetrically heated UWT channel have been studied numerically by Oosthuizen [43]. In this study, a forward marching finite element method was used to solve the boundary-layer equations (for $Pr=0.7$). It was found that adding adiabatic extensions above the heated section increases the induced flow rate and average heat transfer because of the "chimney" effect. The average heat transfer rate can be increased by as much as 40-50%; however, very long adiabatic sections are required.

Other researchers have examined the possibility of enhancing the natural convective heat transfer by staggering the channel walls (see Fig. 1.5). Instead of a continuous smooth channel, the channel walls are divided into an array of staggered channels. The heat transfer enhancement arises from the fact that the thermal boundary-layer must reform many times in a staggered channel. Also, after each stagger, the new boundary-layer is forming in the cooler centre-line fluid from the channel below.

In an experimental study using a double staggered arrangement of UHF plates, Sobel et al. [44] observed a 38% increase in the average Nusselt number at moderate Rayleigh number. However, at low Rayleigh number, no advantage was gained from the staggered arrangement. With decreasing Rayleigh number, the high skin friction because of the staggered arrangement become the dominant effect, causing the heat transfer to be lower than for the continuous channel.

More comprehensive studies of the effect of stagger have been performed numerically by Sparrow and Prakash [45,46]. Sparrow and Prakash solved the boundary-layer equations using a standard forward-marching method for an array of UWT plates. The calculations were restricted to considering staggered channels formed by plates with no thickness. The general results are in agreement with the study of Sobel et al. [44]. It was found that heat transfer could be enhanced by stagger for $Ra_c^* > \sim 500$,

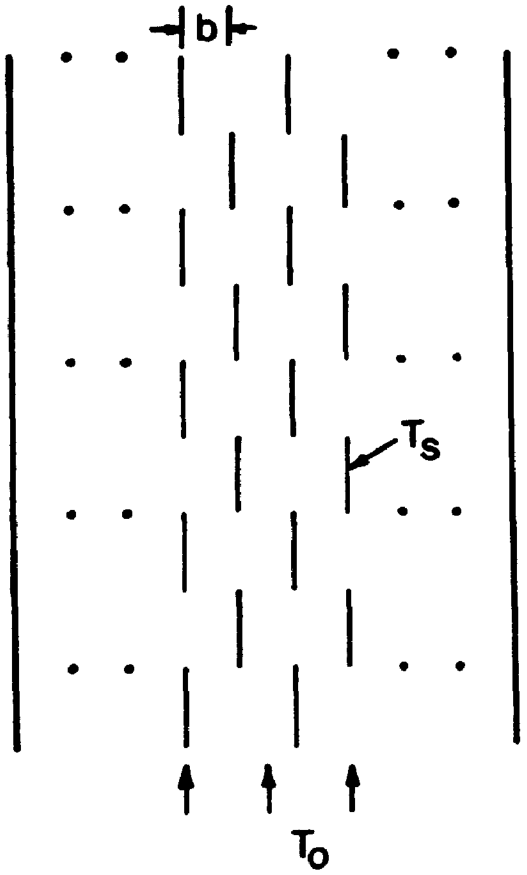

Figure 1.5: An array of staggered plates

where the modified Rayleigh number is based on the half channel width for the non-staggered configuration. Below $Ra_c^* \sim 500$, friction losses dominate. For high Rayleigh number, their results showed that the maximum enhancement, relative to the non-staggered case, was about a factor of two; however, a large number of staggers (~100) were required to achieve this level of enhancement. As a general rule, the enhancement was increased by the use of numerous short plates and short total system heights.

1.2.2 Studies of Natural Convective Heat Transfer from a Single Isolated Vertical Flat Plate

The isolated vertical flat plate is the most fundamental, and perhaps most studied, heat transfer geometry. Only a brief discussion will be given here.

In 1938, an approximate solution to the problem of laminar free convection from an isothermal vertical flat plate was obtained by Squire and Goldstein [47]. Using an integral analysis of the momentum and energy equations, the following expression for the average Nusselt number was obtained:

$$Nu_L = \frac{hL}{k} = \frac{0.677\,Pr^{\frac{1}{4}}}{(0.952+Pr)^{\frac{1}{4}}}\,Ra^{\frac{1}{4}} \qquad (1.3)$$

$$for \qquad Pr = 0.7, \quad Nu_L = 0.546\,Ra^{\frac{1}{4}}$$

This approximate solution appears in many undergraduate textbooks.

Exact solutions of the boundary-layer equations, using similarity transformations, have been obtained by Ostrach [49], and Sparrow and Gregg [50][2]. Ostrach solved the governing equations strictly for the isothermal boundary condition (UWT), whereas Sparrow and Gregg solved the more general problem of nonisothermal plates. Both solutions give the average Nusselt number for the UWT case as:

$$Nu_L = C\,Ra^{\frac{1}{4}} \tag{1.4}$$

There is slight disagreement over the value of the constant (C) for air. Ostrach obtained C=0.515 and Sparrow and Gregg get C=0.519.

Equation (1.4) with C=0.515 has been used in the present study when making comparisons to the isolated plate behaviour. Equation (1.4) is valid up to the laminar to turbulent transition, which occurs at a critical Grashof number (based on the plate length) of approximately $Gr_L=10^8-10^9$ [51].

1.2.3 Studies of the Influence of Confining Walls on Natural Convective Heat Transfer

There have been relatively few studies of the effect of confining walls on natural convective heat transfer. Those that do exist consider the effect of confining walls on heat transfer from horizontal circular, elliptic, or finned cylinders. The emphasis on heat transfer from cylinders stems from heat exchanger applications. The objective of all of these studies was to determine if the heat transfer from the cylinder could be enhanced because of the chimney effect. Also, because of the complexity of these geometries, these studies are primarily calorimetric (heat balance) experiments. Table 1.1 summarizes the existing publications on the effect of confining walls.

---

[2] An even earlier exact similarity solution was obtained by Schmidt and Beckmann [48].

One of the first studies on the effect of confining walls on natural convective heat transfer was done by Marsters and Paulus [11]. They studied the heat transfer from a vertical in-line array of ten heated horizontal cylinders confined by unheated plywood walls. Air was the test fluid. The cylinders were heated electrically to provide constant heat flux conditions, and average Nusselt number data were obtained using a heat balance method. Wall spacings of four to forty cylinder diameters (4-40D) were studied. They found that for wall spacings of forty tube diameters, the heat transfer was almost the same as with no confining walls. With decreasing wall spacing the heat transfer from the cylinders near the bottom of the array increased significantly (up to 50% for the bottom cylinder), while the heat transfer from the cylinders near the top of the array decreased. As a result, the overall heat transfer was not greatly affected by the wall spacing; the data showed a slight decrease (less than 10%) in the array average Nusselt number as the wall spacing was decreased from 40D to 4D.

In the above study, Marsters and Paulus [11] also examined the influence of the radiation properties of the unheated confining walls. Most of their experiments were done with the confining walls painted black. However, some experiments were done with the walls covered by a reflective aluminum sheet. They found that the wall radiation properties had no discernable effect on the heat transfer from the cylinder array.

Table 1.1: Summary of the experimental studies of the effect of confining walls on natural convective heat transfer.

Authors	Sketch of Geometry	Confining Wall Conditions	Cylinder Boundary Condition	Test Fluid
Marsters and Paulus [11], 1972	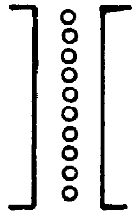 10 cylinders	unheated - plywood painted black and reflective coating (approx. adiabatic)	constant heat flux (UHF)	air $Pr \approx 0.7$
Marsters [10], 1975	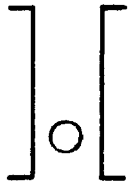 1 cylinder	unheated aluminum plate (approx. ambient temp.)	constant heat flux (UHF)	air, freon, water $0.7 \leq Pr \leq 10$
Tokura et al. [12], 1983	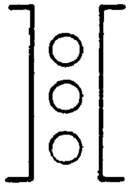 3 & 5 cylinders	unheated, bakelite plates with reflective coating (approx. adiabatic)	isothermal (UWT)	air $Pr \approx 0.7$
Sparrow et al. [14], 1986	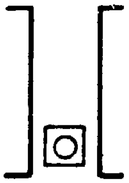 1 finned tube	unheated, insulated plywood (approx. adiabatic)	isothermal (UWT at finned tube root)	air $Pr \approx 0.7$
Yang et al. [13], 1988	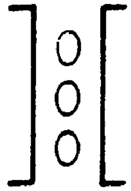 2 & 3 elliptic tubes	unheated - polished aluminum, (approx. ambient temp.)	isothermal (UWT)	air $Pr \approx 0.7$
Sparrow et al., [52], 1983	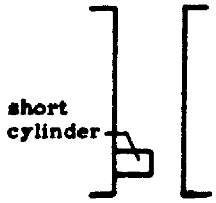 cylinder affixed to heated wall	wall with cylinder - heated and isothermal wall without cylinder - unheated, paper	isothermal (UWT)	air $Pr \approx 0.7$

After studying the array of cylinders, Marsters [10] simplified the geometry to consider a *single* cylinder confined by unheated walls. In this case, a constant heat flux cylinder was confined by walls constructed of aluminum plate (presumably at the ambient temperature). For most of the experiments, the cylinder was located six diameters from the inlet of the channel formed by the confining walls. Wall spacings ranging from two cylinder diameters (2D) to the isolated cylinder (no walls) were studied for $10 \leq Ra_D \leq 5x10^5$. Air, freon 113, and water were used as the test fluids. Marsters found that cylinder heat transfer enhancements as high as 50% could be achieved because of the presence of the confining walls. An average Nusselt number correlation was presented that includes the effects of wall spacing, channel aspect ratio, and cylinder Rayleigh number (Ra_D).

In this same study, Marsters [10] also looked at the effect of the vertical position of the cylinder. Marsters states that "as long as the heated cylinder lies within the channel formed by the walls (i.e. is not below or above the walls) its [vertical] location is of no apparent significance."

Tokura et al. [12] have also studied the heat transfer from a vertical in-line array of heated horizontal cylinders confined by unheated walls. In this study, the cylinders were isothermal and the walls were approximately adiabatic. Their study (for air) was more comprehensive and seems to have been done more carefully than the previous work of Marsters and Paulus [11]. Tokura et al. considered the effect of cylinder spacing for two different cylinder arrays in addition to the effect of wall spacing. However, the main result of Marsters and Paulus [11] remains essentially unchanged; the array average Nusselt number is relatively insensitive to wall spacing. Tokura et al. found that the array average Nusselt number increased slightly (10–15%) for some configurations, while for others the heat transfer decreased slightly.

In contrast to the results of Marsters [10] for the single cylinder, Tokura et al. [12] found that positioning the cylinder array closer to the channel inlet increased the average heat transfer. They suggest that "the reason may be that the chimney effect is promoted by setting the array in the bottom . . . because of the increase in the length of the path in which the hot air flows."

Yang et al. [13] have performed a study similar to the study by Tokura et al. [12] using an array of elliptic rather than circular cylinders. They studied vertical arrays of in-line horizontal isothermal elliptic tubes confined between walls at near ambient temperature. Air was the test fluid. Although elliptic tubes give higher heat transfer rates than circular tubes, the results are qualitatively in agreement with those of results of Tokura et al. [12]. Again, the study confirms that wall spacing does not strongly influence the total heat transfer from an array of tubes.

Sparrow et al. [14] have studied the heat transfer from a single horizontal *finned* tube confined by unheated, essentially adiabatic walls. In this study, both the walls and the finned tube were constructed to have moderately high emissivities and no attempt was made to correct for radiation losses. Rather, both the radiative and convective heat transfer components were reported together. They found that in almost all cases, in-channel positioning gave higher heat transfer rates than free-space positioning (no walls). Heat transfer enhancements as high as 2.5 times the free-space positioning were observed for some configurations because of the effect of the confining walls. In general, taller channels and smaller wall spacings gave larger enhancements. In addition, it was also found that the vertical positioning of the finned tube *strongly* influenced the enhancement due to the confining walls; again, contrary to the results of Marsters [10] (for a plane cylinder), Sparrow et al. [14] found that placing the finned tube at the bottom of the channel maximized the heat transfer.

Sparrow et al. [52] have studied a geometry that has several important similarities to the present research. They performed an experimental study of free convective heat transfer from a short horizontal cylinder in an asymmetrically heated channel. The cylinder was attached to the heated wall and partially spanned the channel gap width (see the sketch in Table 1.1). Both the heated wall and the attached cylinder were isothermal and maintained at the same temperature. They found that the heat transfer from the cylinder could be enhanced by up to 60% compared to the external flow situation (cylinder mounted on an isolated vertical UWT plate) when the cylinder was located near the bottom of the channel. At low Rayleigh number (based on the cylinder diameter, Ra_D), the cylinder heat transfer was lower than the external flow situation when the cylinder was located at the top of the channel. Also, in general it was found that small gap widths (approaching the cylinder length) gave the largest enhancements.

In this same study, Sparrow et al. [52] also examined the effect of the radiation properties of the unheated walls. They compared the cylinder heat transfer for walls with near blackbody properties and for walls with high reflectivity. Their conclusion does not agree with that of Marsters and Paulus [11]. Sparrow et al. found that black walls improved the heat transfer from the cylinder compared to reflective walls. Their explanation is that black walls have higher equilibrium temperatures than reflective walls. Hence, the elevated temperatures for the "unheated" walls augment the buoyancy force in the channel.

The above studies have investigated the effect of heated, unheated, and adiabatic confining surfaces on natural convection from horizontal cylinders. Many of the studies show that very significant heat transfer enhancements are possible due to the chimney effect. Also, from these studies, it is clear that only the most basic interactions for very simple geometries are understood. In some cases contradictory conclusions have been drawn.

1.3 Scope of the Research

The literature review shows that there has been a tremendous amount of research into natural convection from many different vertical channel geometries. However, to the author's knowledge, no study exists that considers the free convective heat transfer from a channel with a dividing plate. As discussed in section 1.1, this geometry is of significant engineering interest, especially for the cooling of electronic components. Hence, the unique contribution of this research is to delineate the laminar natural convective heat transfer characteristics of a channel, divided on the centre line by a plate.

The purpose of this study is to provide a basic understanding of the interactions between the dividing plate and the channel over a wide range of Rayleigh number and geometric parameters. For this reason, the present study is restricted to equal uniform surface temperatures (UWT) for the dividing plate and channel walls. Historically, in the heat transfer literature, UWT boundary conditions are considered first and more realistic or complex boundary conditions are studied later.

More specifically, this study will be comprised of the following:

i) Detailed comparisons will be made of the full elliptic solution and the existing boundary-layer (parabolic) solutions to natural convection in a vertical undivided UWT channel. A new approach for modelling the inlet boundary conditions will be described.

ii) Closed form expressions will be derived for the average Nusselt numbers in the divided channel for the fully developed limit ($Ra^* \to 0$).

iii) Numerical solutions (parabolic and full elliptic) will be obtained to the developing free convective flow in a divided isothermal channel. The effects of plate length ratio (L_p/L_c), vertical plate position (L_1/L_c), and channel blockage (t/b) will be shown for a wide Rayleigh number range.

iv) Experimental data for the isothermal divided channel will be obtained using a Mach-Zehnder interferometer for $L_p/L_c=1/3$. The experimental local and overall Nusselt number data will be compared with the numerical predictions. Also, qualitative comparisons will be made between the numerically predicted temperature field and the infinite fringe interferograms.

v) Average Nusselt number correlation equations for the dividing plate, the confining walls and the overall channel will be presented.

CHAPTER 2

NUMERICAL SOLUTION METHODS

2.1 Introduction

Natural convection in a divided channel has been solved numerically, both with and without the boundary-layer approximations for Pr=0.7 (air). Solution of the boundary-layer (parabolic) equations requires much less computational resources than the full elliptic problem. Furthermore, in previous studies of channel geometries, boundary-layer solutions have been in good agreement with experimental data. However, there is some concern about the accuracy of boundary-layer solutions, particularly for predicting local quantities, because of the arbitrary inlet boundary conditions. Also, the present parabolic solution is restricted to dividing plates with zero thickness (t=0). For these reasons, the full elliptic problem has also been solved.

2.2 Governing Equations

The general partial differential equations that govern the transfer of heat in a Newtonian fluid are given by Schlichting [53]. For the present study, these equations are simplified by the following assumptions: the flow in the channel is assumed to be steady, laminar, incompressible, and two-dimensional. Also, viscous dissipation is neglected and all thermophysical properties are assumed to be constant, except for density in the buoyancy term of the y-momentum equation ie., the Boussinesq approximation[1]. With these assumptions, the governing equations become:

The continuity equation:

$$\frac{\partial u}{\partial x}+\frac{\partial v}{\partial y}=0 \tag{2.1}$$

The Navier-Stokes equations:

$$\rho\left(u\frac{\partial u}{\partial x}+v\frac{\partial u}{\partial y}\right)=-\frac{\partial p}{\partial x}+\mu\left(\frac{\partial^2 u}{\partial x^2}+\frac{\partial^2 u}{\partial y^2}\right) \tag{2.2}$$

$$\rho\left(u\frac{\partial v}{\partial x}+v\frac{\partial v}{\partial y}\right)=-\frac{\partial p}{\partial y}-\rho g+\mu\left(\frac{\partial^2 v}{\partial x^2}+\frac{\partial^2 v}{\partial y^2}\right) \tag{2.3}$$

The energy equation:

$$\rho c_p\left(u\frac{\partial T}{\partial x}+v\frac{\partial T}{\partial y}\right)=k\left(\frac{\partial^2 T}{\partial x^2}+\frac{\partial^2 T}{\partial y^2}\right) \tag{2.4}$$

It is customary to define a pressure defect:

$$p'=p-p_o \tag{2.5}$$

where p_o is the pressure that would result if the temperature were the same as the ambient throughout the flow field. In other words, the pressure defect p′ is the difference between channel and the ambient pressure *at the same elevation*.

It is the density variation in the body force term of equation (2.3) that produces the fluid motion. The density variation can be approximated using the expansion:

$$\rho=\rho_o-\rho_o\beta(T-T_o) \tag{2.6}$$

where β denotes the coefficient of thermal expansion. Noting that $\partial p_o/\partial y=-\rho_o g$, the y-momentum equation (2.3) can be written as:

---

[1] Detailed discussions of the Boussinesq approximation can be found in references [55,56]. In particular, Gray and Giorgini [55] have shown the conditions under which the approximation is valid for air.

$$\rho(u\frac{\partial v}{\partial x}+v\frac{\partial v}{\partial y})=-\frac{\partial p'}{\partial y}+g\rho\beta(T-T_o)+\mu(\frac{\partial^2 v}{\partial x^2}+\frac{\partial^2 v}{\partial y^2}) \qquad (2.7)$$

2.3 Elliptic Solution

Equations (2.1, 2.2, 2.4, 2.7) have been solved without further approximation. Calculations for Pr=0.7 (air) were carried out using the finite element code FIDAP (Fluid Dynamics International, [54]). A total of 127 FIDAP runs were made during the course of this research (not including input file testing). A discussion of the application of the commercial code FIDAP to the present problem is given in Appendix A.

The computational domain for the elliptic solution is shown in Fig. 2.1. Note that for t>0, the dividing plate has rounded leading and trailing edges with radii equal to the plate half-thickness (t). Rounded edges on the plate were used to avoid the singularities associated with sharp convex corners. The corners of the channel walls were not rounded so that direct comparisons could be made with previous elliptic solutions (with sharp inlet corners) for the undivided channel (L_p=0). The flow was assumed to be symmetrical about the channel centre line. Hence, only half of the flow field was solved. In dimensional form, the centre line, plate, wall, and channel exit boundary conditions are:

$$\frac{\partial T}{\partial x}=\frac{\partial v}{\partial x}=u=0, \; for \; -r_i \leq y < L_i, \; x=0 \quad (CD) \qquad (2.8)$$

$$\frac{\partial T}{\partial x}=\frac{\partial v}{\partial x}=u=0, \; for \; (L_i+L_p) < y \leq L_e, \; x=0 \quad (EF) \qquad (2.9)$$

$$T=T_s, \; u=v=0, \; for \; L_i \leq y \leq (L_i+L_p), \; 0 \leq x \leq t \; on \; the \; plate \quad (DE) \qquad (2.10)$$

$$T=T_s, \; u=v=0, \; for \; 0 \leq y \leq L_e, \; x=b \quad (AG) \qquad (2.11)$$

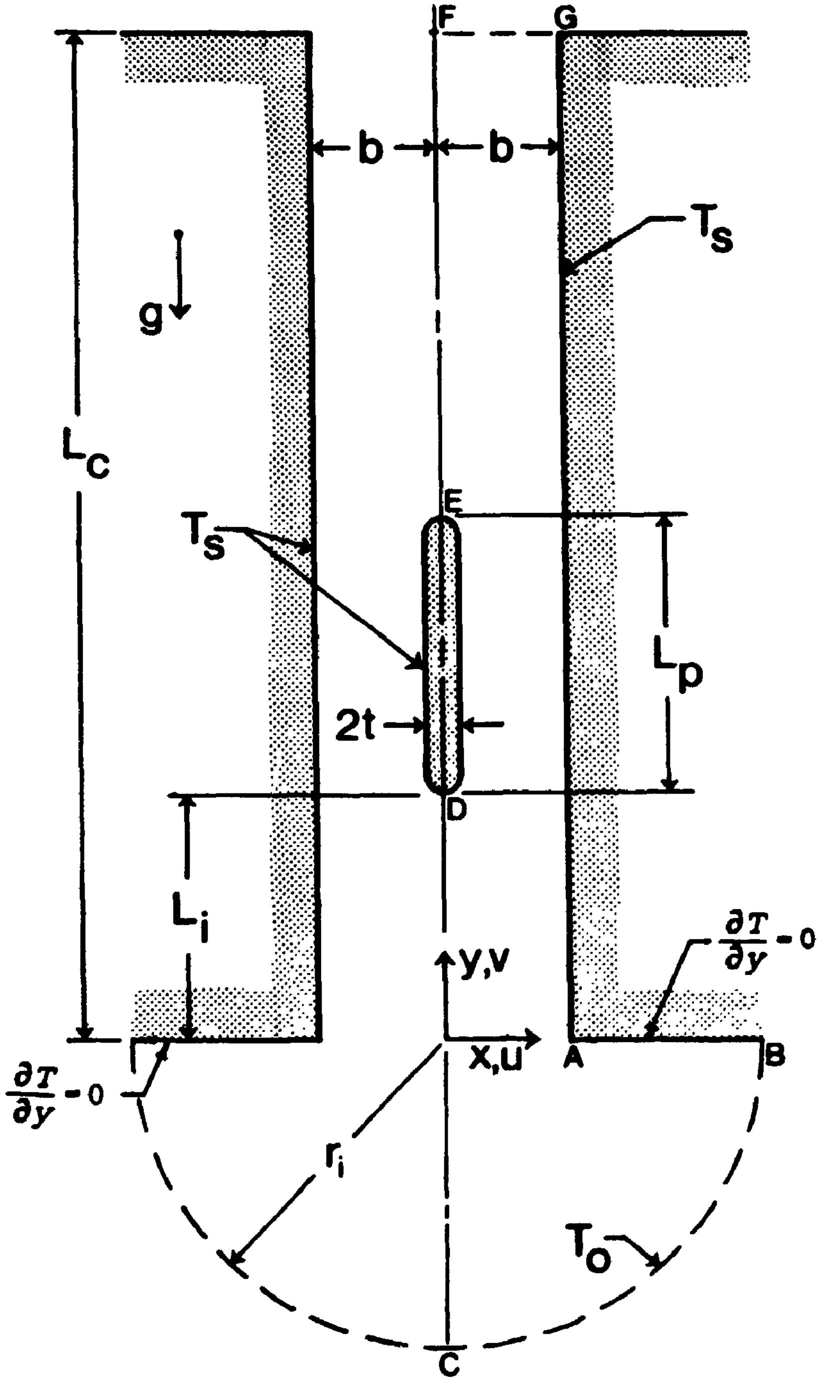
F
G
b
b
T_s
g
L_c
E
T_s
L_p
2t
D
L_i
y,v
$\frac{\partial T}{\partial y} = 0$
x,u
A
B
$\frac{\partial T}{\partial y} = 0$
r_i
T_o
C

Figure 2.1: The heat transfer geometry showing the limits of the computational domain.

$$\frac{\partial T}{\partial y} = u = v = 0, \quad for\ b < x \le r_t,\ y = 0 \quad (AB) \tag{2.12}$$

$$\frac{\partial T}{\partial y} = \frac{\partial u}{\partial y} = \frac{\partial v}{\partial y} = 0, \quad for\ 0 \le x \le b,\ y = L_e \quad (FG) \tag{2.13}$$

The derivatives of temperature and velocity normal to the channel exit have been set to zero at the upper boundary (FG). Although this condition could affect the heat transfer from the channel, it was the best assumption available short of extending the domain to consider the plume region outside the channel. Nevertheless, these exit conditions do attempt to capture the correct physics. For (Gr•Pr)>>1, convection will be much larger than conduction at the exit plane of the channel. Hence, neglecting axial conduction at the exit plane is a reasonable approximation. The derivative conditions, applied to velocity, cause the streamlines to be parallel at the exit plane. At low Rayleigh number the flow is fully developed at the exit and the traverse velocity component is near zero, consistent with the imposed exit conditions. At higher Rayleigh number, the surfaces begin to act as isolated plates and boundary-layer flow exists. For such flows, far from the leading edge the traverse velocity component is also small. Suitability of the exit boundary conditions will be discussed further when the results are presented.

In the present study, the channel inlet flow boundary conditions (BC) are non-trivial and have been given special consideration. The approach described here is entirely different from that used in previous elliptic solutions. Kettleborough [39] and Nakamura et al. [40] used boundary conditions that physically corresponded to fully developed flow entering a channel with a large sudden expansion. Kageyama and Izumi [57] used a similar approach to solve free convection between non-parallel plates.

Ramanathan et al. [7] attempted to solve the inlet and outlet boundary condition problem (for UHF plates) by enclosing the channel in a very large isothermal enclosure. This approach was only partially successful. Despite very large computational domains, enclosure effects were not entirely eliminated and corrections had to be applied for the preheating of the air entering the channel. Also, presumably because of enclosure effects, velocity and temperature fields outside the channel were not presented.

The inlet boundary conditions used in the present case are based on Jeffrey-Hamel flow as shown in Fig. 2.2. Jeffrey-Hamel flow [58] is a similarity solution of isothermal flow caused by the presence of a source or sink at the point of intersection of two walls. Solution details are given by Millsaps and Pohlhausen [59]. In the present study, converging flow caused by a sink and a wall half angle of 90° is of specific interest. The flow is purely radial and in cylindrical co-ordinates (r,θ) has the form:

$$v_r = \frac{F(\theta)}{r} \tag{2.14}$$

$$v_\theta = 0 \tag{2.15}$$

where v_r and v_θ denote the radial and tangential velocity components. The radial stress component for Jeffrey-Hamel flow is:

$$\sigma_{rr} = -p + 2\mu\frac{\partial v_r}{\partial r} = -p - 2\mu\frac{F(\theta)}{r^2} \tag{2.16}$$

At large r ($r \to \infty$), far from the sink, the pressure approaches the ambient

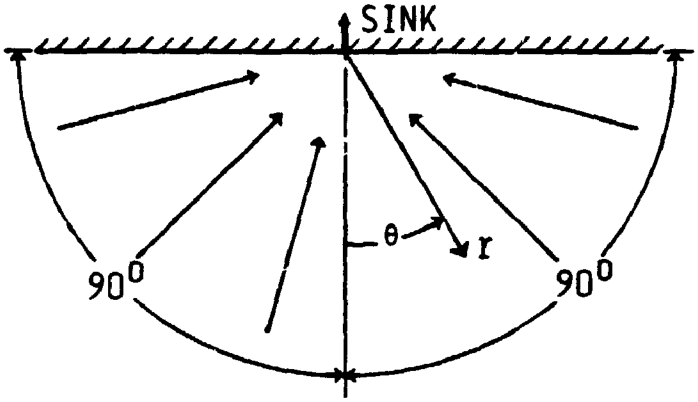
SINK
θ
r
90°
90°

Figure 2.2: The Jeffrey-Hamel flow geometry applicable to the present study.

pressure, v_r approaches zero, and the radial stress goes to zero. Hence, tangential velocity, radial stress, and temperature inlet boundary conditions can be specified as:

$$v_\theta = \sigma_{rr} = 0, \quad T = T_e, \quad as\ r \to \infty \tag{2.17}$$

On this physical basis, the above boundary conditions were imposed on a *finite* semi-circular boundary (BC). For a sufficiently large inlet domain radius (r_i), the flow at the boundary (BC) will approach Jeffrey-Hamel flow. That is, with increasing radius (r_i), the channel will induce flow at the boundary that asymptotically approaches that produced by a point sink.

Now for the elliptic solution we introduce the following dimensionless quantities:

$$X = \frac{x}{b}, \quad Y = \frac{y}{b}, \quad R = \frac{r}{b} \tag{2.18}$$

$$U = \frac{u}{U_{ref}}, \quad V = \frac{v}{U_{ref}} \tag{2.19}$$

$$T^* = \frac{(T - T_e)}{(T_s - T_e)} \tag{2.20}$$

$$P = \frac{p'b}{\mu U_{ref}} \tag{2.21}$$

$$where \quad U_{ref} = \frac{\alpha Pr Gr^{\frac{1}{2}}}{b}, \quad and \quad Gr = \frac{g\beta(T_s - T_e)b^3}{\nu^2} \tag{2.22}$$

Using the above quantities, the dimensionless governing equations become:

$$\frac{\partial U}{\partial X} + \frac{\partial V}{\partial Y} = 0 \tag{2.23}$$

$$Gr^{\frac{1}{2}}\left(U\frac{\partial U}{\partial X}+V\frac{\partial U}{\partial Y}\right)=-\frac{\partial P}{\partial X}+\left(\frac{\partial^2 U}{\partial X^2}+\frac{\partial^2 U}{\partial Y^2}\right) \tag{2.24}$$

$$Gr^{\frac{1}{2}}\left(U\frac{\partial V}{\partial X}+V\frac{\partial V}{\partial Y}\right)=-\frac{\partial P}{\partial Y}+Gr^{\frac{1}{2}}T^{*}+\left(\frac{\partial^2 V}{\partial X^2}+\frac{\partial^2 V}{\partial Y^2}\right) \tag{2.25}$$

$$Gr^{\frac{1}{2}}Pr\left(U\frac{\partial T^{*}}{\partial X}+V\frac{\partial T^{*}}{\partial Y}\right)=\left(\frac{\partial^2 T^{*}}{\partial X^2}+\frac{\partial^2 T^{*}}{\partial Y^2}\right) \tag{2.26}$$

The dimensionless boundary conditions are:

$$\frac{\partial T^{*}}{\partial X}=\frac{\partial V}{\partial X}=U=0, \quad \textit{for} \quad -R_t\leq Y<\frac{L_i}{b},\ X=0 \quad (CD) \tag{2.27}$$

$$\frac{\partial T^{*}}{\partial X}=\frac{\partial V}{\partial X}=U=0, \quad \textit{for} \quad \frac{(L_i+L_p)}{b}<Y\leq\frac{L_c}{b},\ X=0 \quad (EF) \tag{2.28}$$

$$T^{*}=1,\ U=V=0, \textit{for}\ \frac{L_i}{b}\leq Y\leq\frac{(L_i+L_p)}{b},\ 0\leq X\leq\frac{t}{b},\ \textit{on the plate}\ (DE) \tag{2.29}$$

$$T=1,\ U=V=0, \quad \textit{for}\ 0\leq Y\leq\frac{L_c}{b},\ X=1 \quad (AG) \tag{2.30}$$

$$\frac{\partial T^{*}}{\partial Y}=U=V=0, \quad \textit{for}\ 1<X\leq R_t,\ Y=0 \quad (AB) \tag{3.31}$$

$$\frac{\partial T^{*}}{\partial Y}=\frac{\partial U}{\partial Y}=\frac{\partial V}{\partial Y}=0, \textit{for}\ 0\leq X\leq 1,\ Y=\frac{L_c}{b} \quad (FG) \tag{3.32}$$

$$\textit{and}\ \ V_{\theta}=0,\quad -P+2\frac{\partial V_r}{\partial R}=0,\quad T^{*}=0, \tag{2.33}$$

$$\textit{on the semi-circular boundary}\ (BC)$$

$$\textit{where}\ \ V_r=\frac{v_r}{U_{ref}},\quad V_{\theta}=\frac{v_{\theta}}{U_{ref}} \tag{2.34}$$

These boundary conditions are not valid for low Rayleigh number. At low Rayleigh number the fluid moves with very low velocity and becomes heated by conduction far upstream from the channel inlet. The buoyancy force affects the flow at the boundary and the isothermal conditions needed for the existence of Jeffrey-Hamel flow are no longer satisfied. Based on the examination of stream function and isotherm contours in the inlet region, a conservative lower limit for which these boundary conditions are acceptable was found to be $Ra_c^* \approx 1.5$ for $L_c/b=24$ and $L_p/L_c=0$ (see Fig. 4.5).

The local heat transfer coefficients and local Nusselt numbers for the wall and plate are defined as:

$$h_{w,y}=\frac{k\frac{\partial T}{\partial x}\big|_{x=b}}{(T_s-T_o)},\qquad h_{p,y}=\frac{-k\frac{\partial T}{\partial n}\big|_{surface}}{(T_s-T_o)} \tag{2.35}$$

$$Nu_{w,y}=\frac{h_{w,y}b}{k}=\frac{\partial T^*}{\partial X}\Big|_{X=1},\qquad Nu_{p,y}=\frac{h_{p,y}b}{k}=\frac{-\partial T^*}{\partial N}\Big|_{surface} \tag{2.36}$$

where n and N are dimensional and dimensionless unit vectors normal to the plate surface.

The wall average Nusselt number was calculated by integrating the local Nusselt number distribution:

$$Nu_w=\frac{b}{L_c}\int_0^{L_c/b}\frac{\partial T^*}{\partial X}\Big|_{X=1}dY \tag{2.37}$$

Similarly, the average plate Nusselt number was calculated by integrating over the wetted length of one side of the plate ($L_{p,wet}$):

$$Nu_p=\frac{b}{L_{p,wet}}\int_0^{(L_{p,wet})/b}\frac{-\partial T^*}{\partial N}\Big|_{surface}dS \tag{2.38}$$

where dS is an incremental dimensionless distance around the wetted perimeter of the plate. Note that the wetted length of the dividing plate ($L_{p,wet}$) is slightly greater than the linear length in the y-direction (L_p) when the plate has finite thickness. For t/b=0.2 and L_p/b=5.0, the wetted length of one side of the dividing plate is $L_{p,wet}$/b=5.228.

The overall Nusselt number for the channel (plate and walls combined) was calculated using two different methods. One method used to compute the channel average Nusselt number (Nu_c) was a heat balance:

$$Nu_c = \left[Gr^{1/4} Pr \left(\frac{b}{L_c + L_{p,wet}}\right) \int_0^1 V\, T^*\, dX\right]_{Y=\frac{L_c}{b}} - \left[Gr^{1/4} Pr \left(\frac{b}{L_c + L_{p,wet}}\right) \int_0^1 V\, T^*\, dX\right]_{Y=0} + \int_0^1 \frac{\partial T^*}{\partial Y}\Big|_{Y=0}\, dX \tag{2.39}$$

The first, second, and third integrals in equation (2.39) correspond to the heat convected out of the top of the channel, the heat convected back into the channel entrance, and heat conducted out of the channel entrance. Special care was required to accurately compute the last two integrals of equation (2.39). These integrals were actually computed along a surface slightly outside the channel entrance, in order to avoid the singularity at the inlet corner. These two integrals are largest at low Rayleigh number. For the lowest Rayleigh number considered (Ra_c^*=1.458), it was found that the heat conducted out of channel entrance was equal to the heat convected back into the channel. Hence, in all cases, Nu_c was computed by:

$$Nu_c = \left[\, Gr^{1/4} Pr \left(\frac{b}{L_c + L_{p,wet}}\right) \int_0^1 V\, T^*\, dX\, \right]_{Y=L_c/b} \tag{2.40}$$

The channel average Nusselt number (Nu_{c2}) can also be calculated by averaging the wall and plate Nusselt numbers from equations (2.37) and (2.38) as:

$$Nu_{c2} = \frac{Nu_p\, L_{p,wet} + Nu_w\, L_c}{L_{p,wet} + L_c} \qquad (2.41)$$

The dimensionless half channel flow rate was calculated by:

$$Q_c = \left[\int_0^1 V\, dX \right]_{Y=L_c/b} \qquad (2.42)$$

The dimensionless bulk temperature at the channel exit was calculated by:

$$T_b^* = \left[\int_0^1 V\, T^* dX \right]_{Y=L_c/b} \Big/ \left[\int_0^1 V\, dX \right]_{Y=L_c/b} \qquad (2.43)$$

2.3.1 Grid Tests for the Undivided Channel (Elliptic Solution)

A preliminary study of natural convection in an undivided channel (L_p/L_c=0) was conducted. Figure 2.3(a) shows the entire finite element mesh for the undivided channel (for L_c/b=24). Figure 2.3(b) is a close-up view of the mesh in the channel entrance region. The "standard" mesh contained 2,456 nine node quadrilateral elements (10,033 nodes). Local interpolation functions for these elements are quadratic for velocity and temperature, and linear for pressure. The penalty formulation was used for pressure. Details of the solution method can be found in the FIDAP theoretical manual [54].

Tests were conducted on several grids to ensure that the results were independent of both grid density and the size of the inlet computational

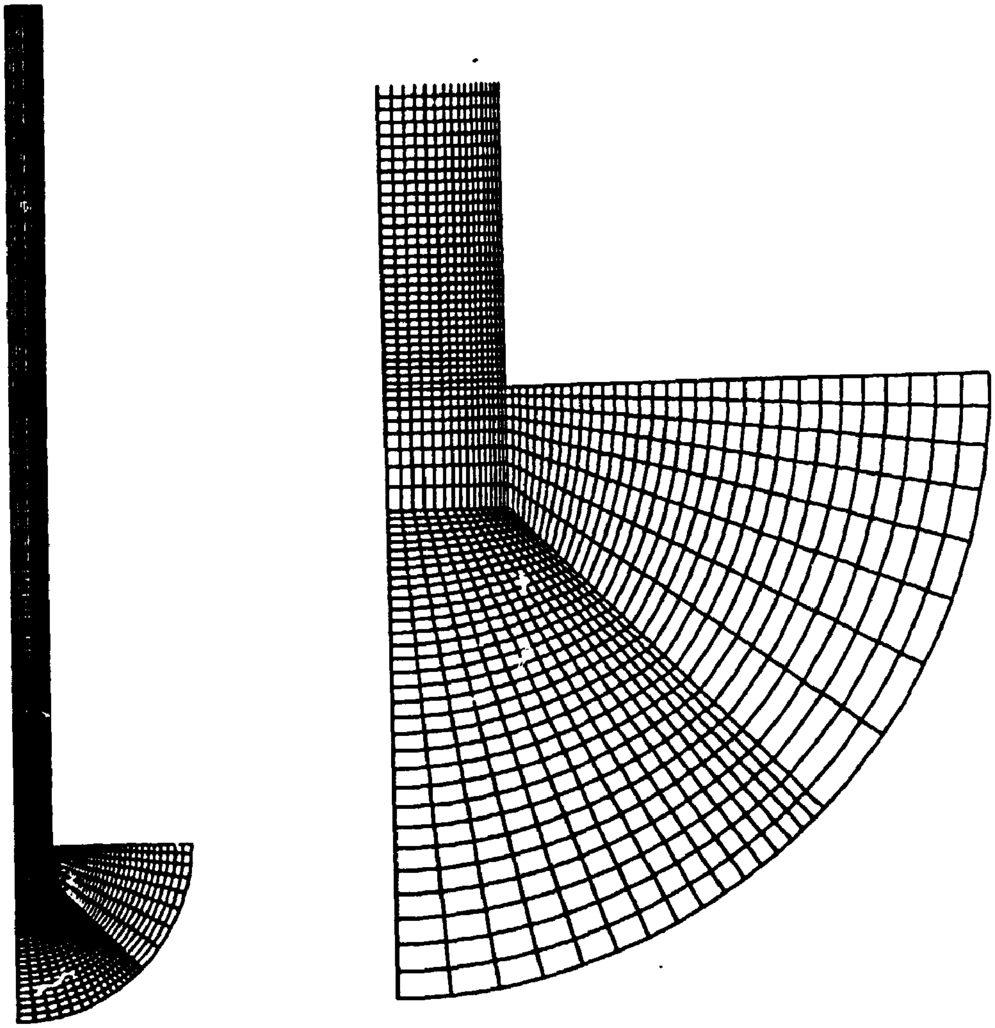

(a) (b)

Figure 2.3: (a) The entire finite element grid for the undivided channel ($L_c/b=24$), and (b) a close-up view of the grid in the channel entrance region.

domain (R_i). For all cases, the results were most grid sensitive at the upper limit of Rayleigh number, ($Gr=10^4$, $Ra_c^*=291.7$, $L_c/b=24$). Table 2.1 shows partial results from these tests. Note that for cases A, B and C, the grid density remains roughly constant and only the inlet domain radius R_i changes. In case D, the number of nodes has been increased to test the dependency of the results on grid density. When the grid density was increased from 10,033 to 14,369 nodes, the additional nodes were placed primarily in the entrance region of the channel where the increased grid density would have the most effect. Other grid tests had shown that the number of nodes in the upper portion of the channel were sufficient. So, although the total number of nodes increased only by about 43 percent, the grid density at the channel inlet region increased by a much larger amount. This approach resulted in substantial reductions in computer time, while still giving an adequate indication of the grid dependence.

Based on the grid test results, the standard grid for $L_c/b=24$ had inlet domain radius of $R_i=5$ and 10,033 nodes (2,456 elements). With this grid, the dimensionless flow rate (Q_s) is grid independent to much better than 1%. For all cases, Nu_c computed from equation (2.40) was two to three percent higher than Nu_{c2} computed using equation (2.41). Nu_c shows less grid dependence than Nu_{c2} (which tends toward Nu_c with increasing grid density). For this reason, Nu_c calculated from equation (2.40) was considered a better estimate of the channel average Nusselt number.

Grid tests also showed that the local quantities, such as local Nusselt number, were more grid dependent near the channel entrance than the exit. The local Nusselt number distributions along the channel wall (at

Table 2.1: Partial results from the elliptic solution grid tests for the undivided channel (for $Ra_c^*=291.7$, $Gr=10^4$, $L_c/b=24$, $L_p/L_c=0$).

Case	Number of Nodes	Inlet Domain Radius R_i	Average Nusselt Numbers		Flow Rate
			Nu_c	Nu_{c2}	Q_e
A	8,465	3	2.4055	2.346	2.084
B	9,249	4	2.4046	2.346	2.076
C	10,033	5	2.4040	2.345	2.073
D	14,369	5	2.4046	2.357	2.073

Table 2.2: Partial results from the elliptic solution grid tests for the divided channel (for $Ra_c^*=10^4$, $t/b=0$, $L_i/L_c=0$, $L_p/L_c=1/3$, $L_c/b=15$).

Case	# of Nodes	Inlet Radius R_i	Average Nusselt Numbers				Flow Rate
			Channel		Wall	Plate	
			Nu_c	Nu_{c2}	Nu_w	Nu_p	Q_e
A	9,003	3	6.3895	6.2621	5.2568	9.2778	1.5269
B	10,143	5	6.3856	6.2561	5.2580	9.2503	1.5115
C	14,479	5	6.3823	6.2336	5.2589	9.1578	1.5109

Ra^*=291.7, L_c/b=24) for grids with 10,033 and 14,369 nodes (R_i=5) had a maximum difference of about three percent near the leading edge. At the channel exit the difference became negligible. Despite these slight differences, the lower grid density was selected for subsequent runs since it required significantly less computing resources. A typical case with 14,369 nodes took approximately 3.9 CPU-hours on a CDC Cyber-962 mainframe computer; cases with 10,033 nodes took only 1.7 CPU-hours. For all computations, the convergence criteria were set (in the FIDAP input file) such that the calculations were carried to four digit accuracy.

It is evident from Fig. 2.3(a) that the elements near the wall in the exit region of the channel are very elongated. Highly distorted elements can cause ill-conditioning [60]. Test runs were made with double the number of nodes in the y-direction for $1/3 \leq y/L_c \leq 1$ to ensure that the elongated elements were not causing loss of accuracy. Global parameters (Nu_c, Nu_{c2}, Q_e) and local heat transfer results were unchanged to the fifth decimal place.

2.3.2 Grid Tests for the Divided Channel (Elliptic solution)

After the preliminary study of the undivided channel, the finite element grid structure was modified to have a dividing plate on the channel centre line. Calculations were done on the five different grid structures shown in Fig. 2.4 and Fig. 2.5. For these grids, the plate was located on the channel centre line and the length ratios were fixed at L_c/b=15 and L_p/b=5 (L_p/L_c=1/3). Figure 2.4 shows the grids with a zero thickness dividing plate (t/b=0) at the bottom (L_1/L_c=0), middle (L_1/L_c=(1-L_p/L_c)/2=1/3) and

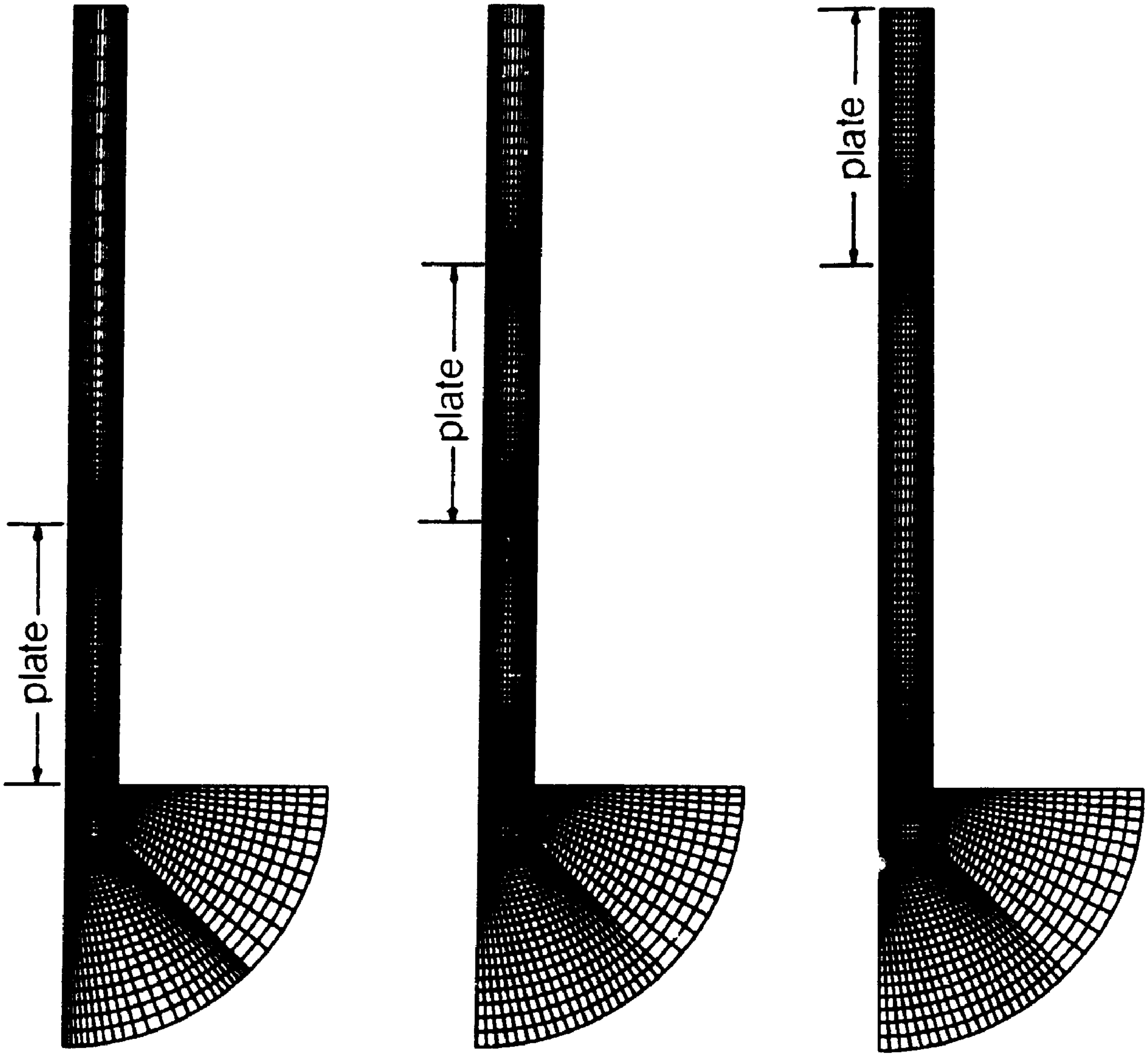

(a) L_i/L_c=0
14,479 nodes
3,576 elements

(b) L_i/L_c=1/3
15,705 nodes
3,866 elements

(c) L_i/L_c=2/3
15,567 nodes
3,831 elements

Figure 2.4: Finite element grids for the divided channel with a zero thickness plate ($t/b=0$, $L_p/L_c=1/3$, $L_c/b=15$).

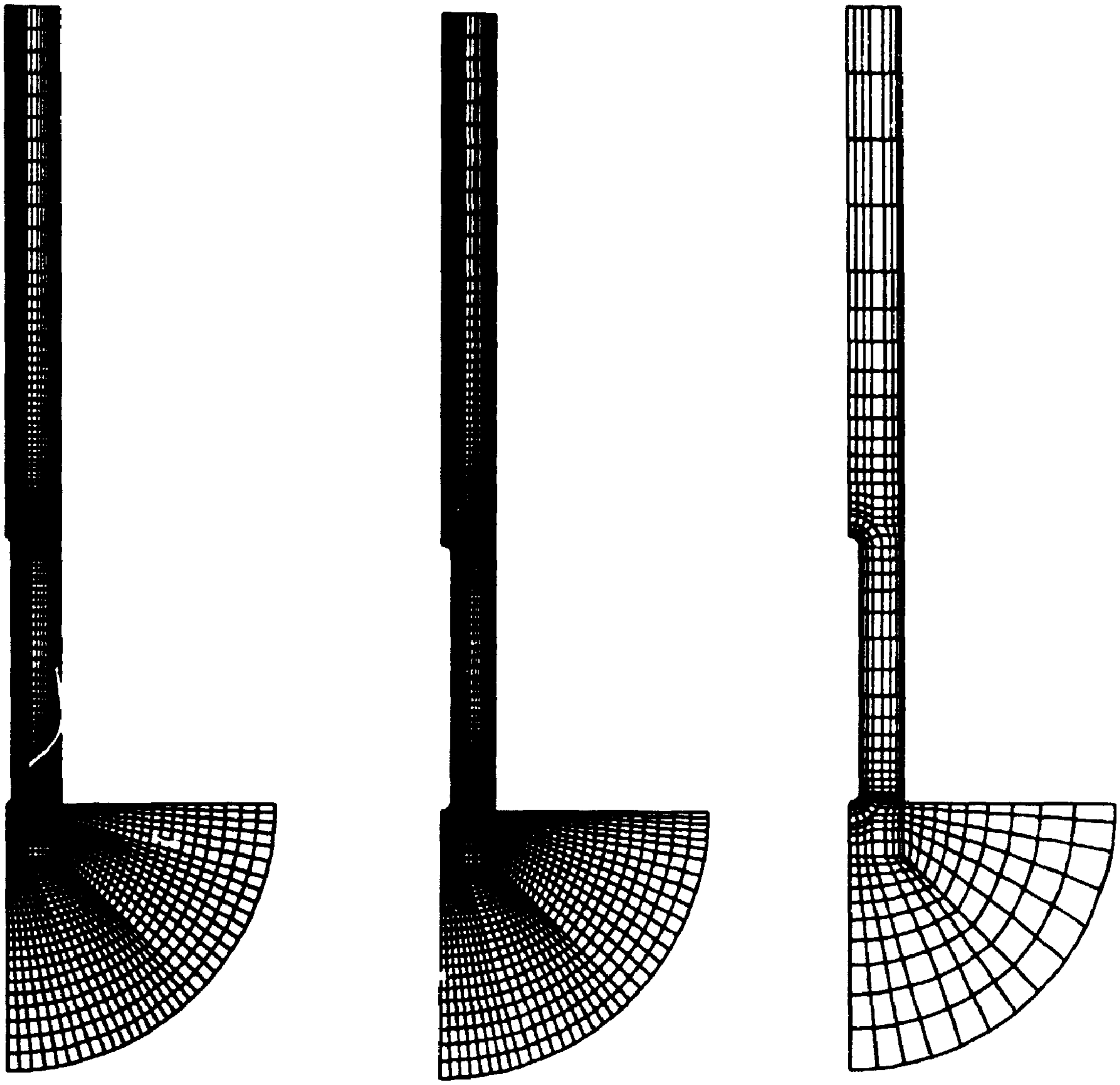

(a) t/b=0.1

14,461 nodes
3,558 elements

(b) t/b=0.2

14,461 nodes
3,558 elements

(c) t/b=0.2

2,043 nodes
562 elements

Figure 2.5: Finite element grids for the divided channel with a finite thickness plate (L_i/L_c=0, L_p/L_c=1/3, L_c/b=15).

top (L_1/L_c=1-L_p/L_c=2/3) of the channel. Figure 2.5 shows the grids for the finite thickness dividing plate located at the bottom of the channel (L_1/L_c=0), with blockage ratios of t/b=0.1, 0.2. In Fig. 2.5(c) the number of elements has been reduced in order to more clearly show the grid structure used for finite thickness dividing plates.

Again, the results were most grid dependent at the upper limit of Rayleigh number, $Ra_c^*=10^4$. Unfortunately, this causes grid testing to be very expensive and time consuming, since several calculations are required for each grid structure to get a converged solution at $Ra_c^*=10^4$. For this reason thorough grid testing was conducted only for the grid shown in Fig. 2.4(a). For this grid, a zero thickness plate (t/b=0) is located at the bottom of the channel (L_1/L_c=0). Testing was done on this particular grid because the plate heat transfer was expected to be the highest for this geometry and the plate has singularity points at its leading and trailing edges. The grid dependence of the results from the other finite element grids (Fig. 2.4(b), (c), Fig. 2.5(a), (b)) will be comparable.

Table 2.2 shows partial results from the tests for the divided channel. Note that for cases A and B, the grid density remains roughly constant and only the inlet domain radius R_1 changes. In case C, the number of nodes is increased to test the dependency of the results on grid density. The channel and wall average Nusselt numbers for cases A and C differ by much less than 1%. However, the flow rate and plate average Nusselt number is somewhat more grid sensitive; the results from cases A and C differ by slightly greater than 1%.

The local Nusselt number distributions along the channel wall for cases A and C had a maximum difference of about 5% near the leading edge; the plate local Nusselt number distributions had a maximum difference of about 3% near the leading edge. Toward the upper end of the plate and wall, the differences became negligible.

Based on the above grid testing, the finite element grids used for the divided channel calculations had an inlet domain radius of R_i=5 and about 15,000 nodes. To reduce the computation time and the expense for the divided channel study, the FIDAP processor module was installed on an ETA-10P air-cooled supercomputer. Typical runs with 14,461 nodes took only 18 CPU-minutes. (Previous similar runs on a CDC Cyber-962 took about 4 CPU-hours). Preprocessing and postprocessing was done on a CDC Cyber-962.

2.4 Parabolic Solution

The parabolic form of the governing equations is obtained by applying the boundary-layer approximations to equations (2.1, 2.2, 2.4, 2.7). Specifically, diffusion of momentum and heat in the streamwise (y) direction are neglected and the pressure is assumed to depend only on the y-coordinate ($\partial p/\partial x=0$). With these simplifications, the governing equations become:

The continuity equation:

$$\frac{\partial u}{\partial x}+\frac{\partial v}{\partial y}=0 \qquad (2.44)$$

The y-momentum equation:

$$\rho\left(u\frac{\partial v}{\partial x}+v\frac{\partial v}{\partial y}\right)=-\frac{dp'}{dy}+g\rho\beta(T-T_o)+\mu\frac{\partial^2 v}{\partial x^2} \tag{2.45}$$

The energy equation:

$$\rho c_p\left(u\frac{\partial T}{\partial x}+v\frac{\partial T}{\partial y}\right)=k\frac{\partial^2 T}{\partial x^2} \tag{2.46}$$

Equations (2.44, 2.45, 2.46) have been solved using a forward marching procedure. The computations start at the channel inlet where uniform temperature ($T=T_o$) and velocity profiles ($v=v_o$) are assumed. For the parabolic solution, the dividing plate location is specified by a change in boundary conditions on the channel centre line. Thus, the parabolic solution is restricted to modelling a dividing plate with no thickness ($t=0$). A similar technique of changing boundary conditions during the forward marching procedure has been used successfully by Oosthuizen [43], Sparrow et al. [45] and Tanda [61] to solve developing free convection in other channel configurations.

Because of symmetry about the channel centre line, only half of the flow field is solved. The boundary conditions are:

Channel inlet:

$$v=v_o,\ u=0,\ T=T_o\quad \textit{for}\ y=0,\ \ 0<x<b \tag{2.47}$$

Channel wall:

$$u=v=0,\ T=T_s\quad \textit{for}\ x=b,\ 0\le y\le L_c \tag{2.48}$$

Channel centre line:

$$\frac{\partial v}{\partial x}=\frac{\partial T}{\partial x}=u=0\quad \textit{for}\ x=0,\ 0\le y<L_l,\ (L_l+L_p)<y\le L_c \tag{2.49}$$

OR

$$T=T_s,\ u=v=0,\quad \textit{for}\ x=0,\ L_l\le y\le (L_l+L_p) \tag{2.50}$$

It is assumed that losses at the inlet are negligible so that the pressure defect at the inlet is calculated from Bernoulli's equation:

$$p'=p-p_e=\frac{-\rho v_e^2}{2} \quad \mathit{for}\ y=0 \tag{2.51}$$

Also, the top of the channel is open to atmosphere, so the pressure defect at the exit is assumed to be zero:

$$p'=p-p_e=0 \quad \mathit{for}\ y=L_c \tag{2.52}$$

Equations (2.44, 2.45, 2.46) are now expressed in terms of the following dimensionless variables:

$$X_{p^*}=\frac{x}{b}\,, \qquad Y_{p^*}=\frac{y}{bGr}\,, \tag{2.53}$$

$$U_{p^*}=\frac{ub}{\nu}\,, \qquad V_{p^*}=\frac{vb}{\nu Gr}\,, \tag{2.54}$$

$$T^*_{p^*}=\frac{T-T_e}{T_s-T_e}\,, \tag{2.55}$$

$$P_{p^*}=\frac{p'b^2}{\rho \nu^2 Gr^2} \tag{2.56}$$

Subscript "p^*" has been used to distinguish the dimensionless quantities for the parabolic solution from those of the elliptic solution. Equations (2.44, 2.45, 2.46) become:

$$\frac{\partial U_{p^*}}{\partial X_{p^*}}+\frac{\partial V_{p^*}}{\partial Y_{p^*}}=0 \tag{2.57}$$

$$U_{p^*}\frac{\partial V_{p^*}}{\partial X_{p^*}}+V_{p^*}\frac{\partial V_{p^*}}{\partial Y_{p^*}}=-\frac{dP_{p^*}}{dY_{p^*}}+\frac{\partial^2 V_{p^*}}{\partial X^2_{p^*}}+T^*_{p^*} \tag{2.58}$$

$$U_{p^*}\frac{\partial T^*_{p^*}}{\partial X_{p^*}}+V_{p^*}\frac{\partial T^*_{p^*}}{\partial Y_{p^*}}=\frac{1}{Pr}\frac{\partial^2 T^*_{p^*}}{\partial X^2_{p^*}} \tag{2.59}$$

Note that in the parabolic form, the results depend upon $Gr(b/L_c)$ and there is no separate dependence on Grashof number and aspect ratio. Therefore, the solution for a given Rayleigh number (Ra_c^*) is independent of the channel aspect ratio.

The dimensionless boundary conditions for equations (2.57, 2.58, 2.59) are:

Channel inlet:

$$V_{p^*} = V_e,\ U_{p^*} = T^*_{p^*} = 0 \quad for\ Y_{p^*} = 0,\ \ 0 < X_{p^*} < 1 \tag{2.60}$$

Channel wall:

$$U_{p^*} = V_{p^*} = 0,\ T^*_{p^*} = 1 \quad for\ X_{p^*} = 1,\ 0 \le Y_{p^*} \le L_c^* \tag{2.61}$$

Channel centre line:

$$\frac{\partial V_{p^*}}{\partial X_{p^*}} = \frac{\partial T^*_{p^*}}{\partial X_{p^*}} = U_{p^*} = 0 \quad for\ X_{p^*} = 0,\ 0 \le Y_{p^*} < L_i^*,\ \ (L_i^* + L_p^*) < Y_{p^*} \le L_c^* \tag{2.62}$$

OR

$$T^*_{p^*} = 1,\ U_{p^*} = V_{p^*} = 0, \quad for\ X_{p^*} = 0,\ \ L_i^* \le Y_{p^*} \le (L_i^* + L_p^*) \tag{2.63}$$

Pressure conditions:

$$P_{p^*} = -\frac{V_e^2}{2} \quad for\ Y_{p^*} = 0, \quad and\ P_{p^*} = 0 \quad for\ Y_{p^*} = L_c^* \tag{2.64}$$

where L_p^*, L_c^*, L_i^* are the dimensionless plate, channel, and undivided inlet lengths for the parabolic solution. The relationship to the dimensional lengths is given by equation (2.53) as:

$$L_i^* = \frac{L_i}{bGr},\ \ L_p^* = \frac{L_p}{bGr},\ \ L_c^* = \frac{L_c}{bGr} \tag{2.65}$$

2.4.1 Finite Difference Formulation and Method of Solution

An explicit forward marching finite difference procedure, similar to that described by Aung et al. [25], was used to solve the parabolic form of the equations. More sophisticated methods requiring less computing resources could have been used. However, the computing requirements for this solution are relatively small and the present method is simple to program.

Consider the finite difference grid for the half-channel flow field shown in Fig. 2.6. For uniform grid spacing in the X_{p*} direction, equations (2.57, 2.58, 2.59) can be written as the following difference equations:

y-momentum equation:

$$V_{i,j}\,\frac{V_{i,j+1}-V_{i,j}}{\Delta Y}+U_{i,j}\frac{V_{i+1,j+1}-V_{i-1,j+1}}{2\Delta X}= \\ \frac{V_{i+1,j+1}-2V_{i,j+1}+V_{i-1,j+1}}{(\Delta X)^2}-\frac{P_{j+1}-P_j}{\Delta Y}+T^*_{i,j+1} \tag{2.66}$$

Energy equation:

$$V_{i,j}\,\frac{T^*_{i,j+1}-T^*_{i,j}}{\Delta Y}+U_{i,j}\frac{T^*_{i+1,j+1}-T^*_{i-1,j+1}}{2\Delta X}= \\ \frac{1}{Pr}\left(\frac{T^*_{i+1,j+1}-2T^*_{i,j+1}+T^*_{i-1,j+1,}}{(\Delta X)^2}\right) \tag{2.67}$$

Continuity equation:

$$\frac{V_{i+1,j+1}+V_{i,j+1}-V_{i+1,j}-V_{i,j}}{2\Delta Y}+\frac{U_{i+1,j+1}-U_{i,j+1}}{\Delta X}=0 \tag{2.68}$$

The subscript "p*" has been dropped in Fig. 2.6 and in the finite difference equations for clarity.

Also, the integrated velocity profile at each step in the j-direction must equal the initially prescribed channel flow rate:

$$V_o=\int_0^1 V_{p^*}\,dX_{p^*} \tag{2.69}$$

Equation (2.69) can be written in finite difference form by application of

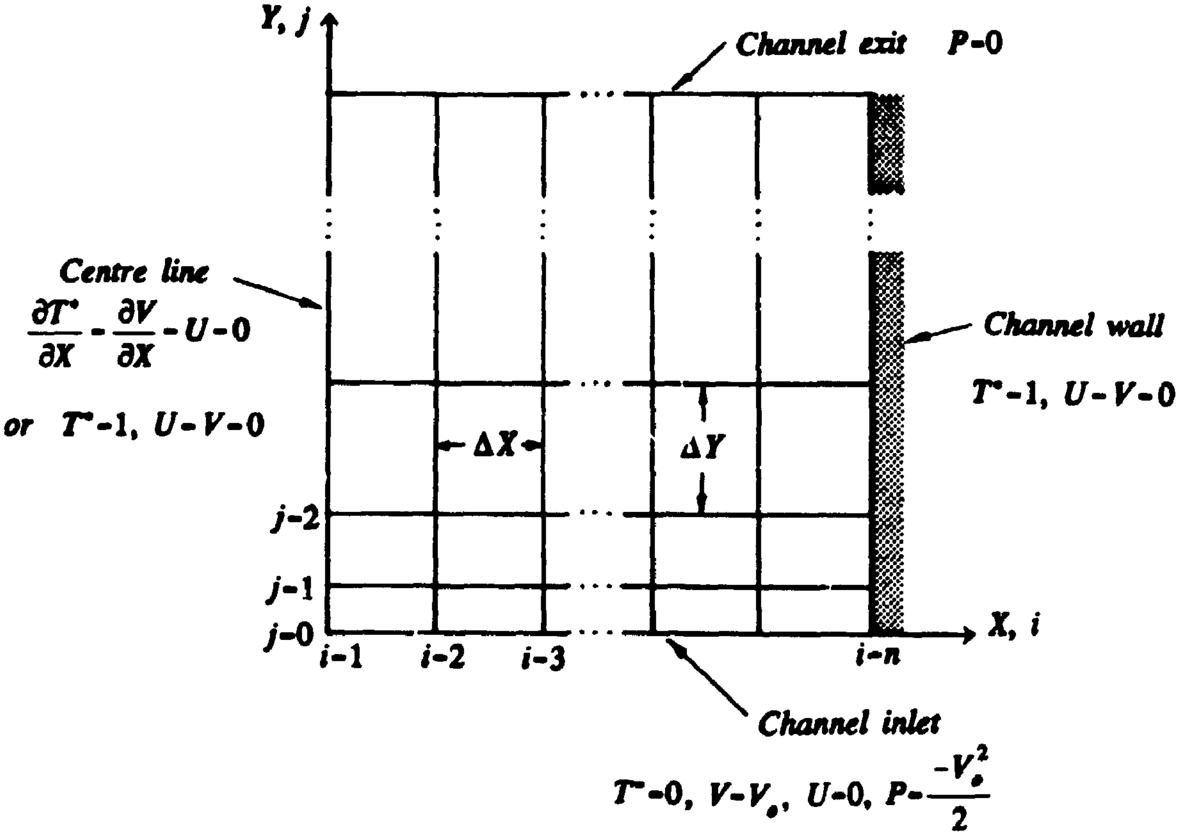
Y, j
Channel exit P=0
Centre line
$\frac{\partial T^*}{\partial X} = \frac{\partial V}{\partial X} = U = 0$
or $T^* = 1$, $U = V = 0$
Channel wall
$T^* = 1$, $U = V = 0$
ΔX
ΔY
j=2
j=1
j=0
i=1
i=2
i=3
i=n
X, i
Channel inlet
$T^* = 0$, $V = V_o$, $U = 0$, $P = \frac{-V_o^2}{2}$

Figure 2.6: The finite difference grid for the parabolic solution.

the trapezoidal rule:

$$V_o = \frac{1}{n-1}\left(\frac{V_{1,j+1}}{2} + \sum_{i=2}^{i=n-1} V_{i,j+1}\right) \qquad (2.70)$$

The forward marching procedure is applied to equations (2.66–2.70) as follows:

First, the uniform inlet velocity (V_o), the starting location of the plate (L_i^*), and the plate length (L_p^*) are specified. Then, the inlet pressure can be calculated from equation (2.64). For illustration purposes, consider the channel entrance to be undivided ($L_i^*>0$). Beginning at row j=1, with the known inlet conditions (for j=0), equations (2.66) and (2.67) are applied to points i=1, 2, ..., n-1. Equation (2.70) is applied to the entire row. This gives 2n-1 equations and 2n-1 unknowns that can be solved to give V_{p*}, T_{p*}^*, and P_{p*} at the row j=1. In the present study, the set of the simultaneous equations at each row was solved using Gaussian elimination with partial pivoting, modified slightly to take advantage of the sparseness of the coefficient matrix.

Next, the traverse component of velocity (U_{p*}) can be computed explicitly from equation (2.68), starting at either the channel wall or centre line, where U_{p*} is known ($U_{p*}=0$). However, applying equation (2.68) from only one side of the half-channel will not ensure that $U_{p*}=0$ at the other side. To overcome this problem, the traverse component of velocity (U_{p*}) was found by applying equation (2.68) in both directions, from Miyatake [30]:

$$U_{i,j+1}=\left[U_{i+1,j+1}+\frac{\Delta X}{2\Delta Y}(V_{i,j+1}-V_{i,j}+V_{i+1,j+1}-V_{i+1,j})\right]X$$
$$+\left[U_{i-1,j+1}-\frac{\Delta X}{2\Delta Y}(V_{i,j+1}-V_{i,j}+V_{i+1,j+1}-V_{i+1,j})\right](1-X) \qquad (2.71)$$

The first term in equation (2.71) (multiplied by X) was computed starting from the channel wall. The second term (multiplied by (1-X)) was computed starting from the channel centre line. Equation (2.71) satisfies the boundary conditions at X=0 and X=1, despite the discretization error in the numerical calculations.

The procedure can now be repeated for j=2, and the solution marches row by row up the half-channel. When the solution is obtained up to the desired starting location of the dividing plate ($Y_{p*}=L_i^*$), the centre line boundary conditions (2.62) are changed to boundary conditions (2.63). Similarly, at the end of the plate, the boundary conditions are changed back to (2.62). The calculations march in the Y_{p*} direction and are stopped when the pressure equals the ambient pressure ($P_{p*}=0$). Note that, for some channel configurations, the pressure in the upper portion of the channel is above ambient pressure (see Fig. 5.20). For these cases the calculations are continued until the pressure *decreases* to atmospheric pressure. Once the calculations are terminated, the dimensionless channel length is known. Then, the Rayleigh number that corresponds to the assumed inlet flow rate can be calculated from equation (2.53) as $Ra_c^*=Pr/L^*_c$.

Note that neither the exact value of Ra_c^* nor channel length (L_{c*}) can be specified directly. For the present study, solutions were required over a wide range of Rayleigh number for constant plate length ratios (L_p/L_c). For each calculation the plate length was fixed and the induced flow rate had to be adjusted by trial and error to produce the desired value of L_p/L_c; typically, several complete solutions were required to find correct induced flow rate. For the curves of constant L_p/L_c presented in Chapter 5, the induced flow rate was iterated until the corresponding L_p/L_c was within ±1% of the desired value. Also, when results were required a specific value of Rayleigh number, the induced flow rate was adjusted until a solution was obtained at the desired Ra_c^* within ±0.5 percent.

In the X_{p*} direction, 200 evenly spaced mesh points were used. In the Y_{p*} direction between 650-1,100 steps were used, depending upon the values of L_p/L_c and Ra_c^*. A progressively larger step size (after Aihara [34]) was used in Y_{p*} direction. The step size was increased by as follows:

$$\Delta Y_{j+1} = \eta \, \Delta Y_j \tag{2.72}$$

where η was a constant. However, the step size was reset to its initial starting value at the beginning and end of the dividing plate; this gave high resolution in all regions of rapid change. At the lowest Rayleigh number ($Ra_c^* \approx 0.2$), the flow develops very rapidly, so $\eta = 1.03$ was used. The value of η was decreased gradually to $\eta = 1.005$ at the highest Rayleigh number ($Ra_c^* \approx 10^4$). For each case, the initial step size ΔY_0 was selected so that there were at least 300 steps (in the Y_{p*} direction) along the length of the dividing plate. A typical case took about 8 minutes on a Sparc Station 1 (Sun 4) computer.

Tests were conducted to ensure that the results were independent of the grid size in both the X_{p*} and Y_{p*} directions. Additional calculations were done with a 50% increase in the number of steps in each direction; this results in the total number of nodes being more than doubled. Grid tests were done at the lowest, intermediate and highest values of Rayleigh number for each value of L_p/L_c and L_i/L_c studied. In all cases, the local and overall Nusselt number data from these calculations differed by less than 1%.

Using the same definitions as for the elliptic solution, the wall and plate local Nusselt numbers were calculated as:

$$Nu_{wy} = \frac{h_{wy} b}{k} = \frac{\partial T_p^*}{\partial X_p^*}\Big|_{X_p^*=1}, \qquad Nu_{py} = \frac{h_{py} b}{k} = \frac{-\partial T_p^*}{\partial X_p^*}\Big|_{X_p^*=0} \qquad (2.73)$$

The surface temperature gradients were calculated using second order one-sided difference expressions. For example, the gradient at the plate surface was calculated by:

$$\frac{\partial T_p^*}{\partial X_p^*}\Big|_{1,j} = \frac{-3T_{1,j}^* + 4T_{2,j}^* - T_{3,j}^*}{2\,\Delta X_p^*} \qquad (2.74)$$

The average Nusselt numbers for the wall and plate were calculated by integrating the local Nusselt number distributions:

$$Nu_w = \frac{1}{L_c^*}\int_0^{L_c^*} \frac{\partial T_p^*}{\partial X_p^*}\Big|_{X_p^*=1} dY_p^* \qquad Nu_p = \frac{1}{L_p^*}\int_0^{L_p^*} \frac{-\partial T_p^*}{\partial X_p^*}\Big|_{X_p^*=0} dY_p^* \qquad (2.75)$$

The channel average Nusselt number (Nu_c) was computed by integrating the heat convected across the channel exit plane as:

$$Nu_c = \frac{Pr}{L_p^* + L_c^*}\left[\int_0^1 V_p^* \cdot T_p^* \cdot dX_p^*\right]_{Y_p^* = L_c^*} \tag{2.76}$$

Also, the channel average Nusselt number (Nu_{c2}) was also calculated from the wall and plate Nusselt numbers as:

$$Nu_{c2} = \frac{Nu_p\, L_p^* + Nu_w\, L_c^*}{L_p^* + L_c^*} \tag{2.77}$$

However, the Nusselt number Nu_c was less grid dependent than Nu_{c2}. For this reason, Nu_c calculated from equation (2.76) was considered a better estimate of the channel average Nusselt number. For the parabolic solution, Nu_c and Nu_{c2} differed at most by 1.5%; typically, the difference was much less than 1%.

There is a special case when the plate is located at the channel inlet (L_i/L_c=0). For this geometry, the parabolic solution is exactly symmetrical in the divided portion of the channel. That is, the heat transferred from the plate equals the heat transferred from the wall until the end of the plate is reached. Hence, the plate average Nusselt number can also be calculated by integrating across half of the channel at the end of the plate as:

$$Nu_p = \frac{Pr}{L_p^*}\left[\int_0^{0.5} V_p^* \cdot T_p^* \cdot dX_p^*\right]_{Y_p^* = L_p^*} \tag{2.78}$$

Similarly, the wall average Nusselt number was calculated as:

$$Nu_w = \frac{Pr}{L_c^*}\left(\left[\int_0^1 V_p^* \cdot T_p^* \cdot dX_p^*\right]_{Y_p^* = L_c^*} - \left[\int_0^{0.5} V_p^* \cdot T_p^* \cdot dX_p^*\right]_{Y_p^* = L_p^*}\right) \tag{2.79}$$

The average Nusselt numbers computed from equations (2.78) and (2.79) differed by less than 1% from those calculated by integrating the local distributions (equation (2.75)). The integrals in equations (2.75, 2.76, 2.78, 2.79) were calculated numerically using the trapezoidal rule.

Comparisons of average Nusselt number, local Nusselt number, induced flow rate, exit bulk temperature and pressure were made with the published results of Aung et al. [25] and Aihara [34] for the undivided symmetrically heated UWT channel. In all cases the present calculations gave identical results. Also, it was checked that calculations for the fully divided channel ($L_p/L_c=1$) gave results identical to the fully undivided channel ($L_p/L_c=0$) after rescaling the data to account for the different half channel width.

* * * * *

Note: To avoid confusion, the results presented in the remainder of this thesis are given in terms of the dimensionless quantities used for the elliptic solution (unless otherwise noted). When comparisons are made between the parabolic and elliptic solutions, all quantities are given in terms of the elliptic dimensionless variables.

CHAPTER 3

FULLY DEVELOPED AND ISOLATED PLATE LIMITS

3.1 Introduction

At very low Rayleigh number, the flow in the channel approaches fully developed conditions throughout the entire channel. At high Rayleigh number the channel walls behave as isolated vertical flat plates. In this chapter, fully developed flow in a divided channel is solved analytically. Also, existing results in the literature for isolated flat plates are used to derive an expression for the limiting value of Nusselt number for the divided channel at high Rayleigh number. Knowledge of the upper and lower limiting behaviour not only provides insight into the convective phenomena, but is also useful for correlation purposes.

3.2 Fully Developed Limit ($Ra^* \rightarrow 0$)

Strictly, heat transfer is by pure conduction for $Ra^*=0$. However, for channels with large aspect ratios (L_c/b), fully developed conditions ($v=v(x)$, $T=T_s$) exist inside the channel at low Rayleigh number. That is, the thermal and momentum developing lengths become very short in comparison with the channel length, and the limiting condition of fully developed flow is approached. Recently, in a numerical study, Ramanathan et al. [7] have shown for channels with constant heat flux boundary conditions, that at low Rayleigh number the "fully developed" channel Nusselt number is approached when $L_c/b \geq 10$. For smaller aspect ratios ($L_c/b<10$), vertical conduction at the channel inlet and outlet cannot be neglected and the Nusselt number (for $Ra^* \to 0$) is higher than the fully developed Nusselt number. It is reasonable to assume that vertical conduction effects will also become significant for approximately $L_c/b<10$ with isothermal boundary conditions.

The model geometry is shown in Fig. 3.1. It is assumed that the flow is thermally fully developed and the velocity field is fully developed. Also, it is assumed that the "redeveloping" lengths for the velocity profile at the beginning and end of the dividing plate are small compared to the plate and channel lengths, such that:

$$v=v_1(x) \quad for \quad 0 \leq y \leq L_i^- \tag{3.1}$$

$$v=v_2(x) \quad for \quad L_i^+ \leq y \leq (L_i+L_p)^- \tag{3.2}$$

$$v=v_1(x) \quad for \quad (L_i+L_p)^+ \leq y \leq L_c \tag{3.3}$$

With these assumptions and neglecting vertical conduction, the energy equation, continuity equation, and x-momentum equation give:

$$T=T_s, \quad u=0, \quad \partial p/\partial x=0 \tag{3.4}$$

The y-momentum equation becomes:

$$-\frac{dp'}{dy}+\mu\frac{d^2v}{dx^2}+g\beta\rho(T_s-T_o)=0 \tag{3.5}$$

The buoyancy term in equation (3.5) is a constant and dp'/dy can be at most a constant since v=v(x). Hence, it is evident from equation (3.5) that the velocity profiles in both the divided and undivided sections are parabolic. Applying the boundary conditions gives:

$$v_1(x)=\frac{3q}{2b}\left(1-\frac{x^2}{b^2}\right) \tag{3.6}$$

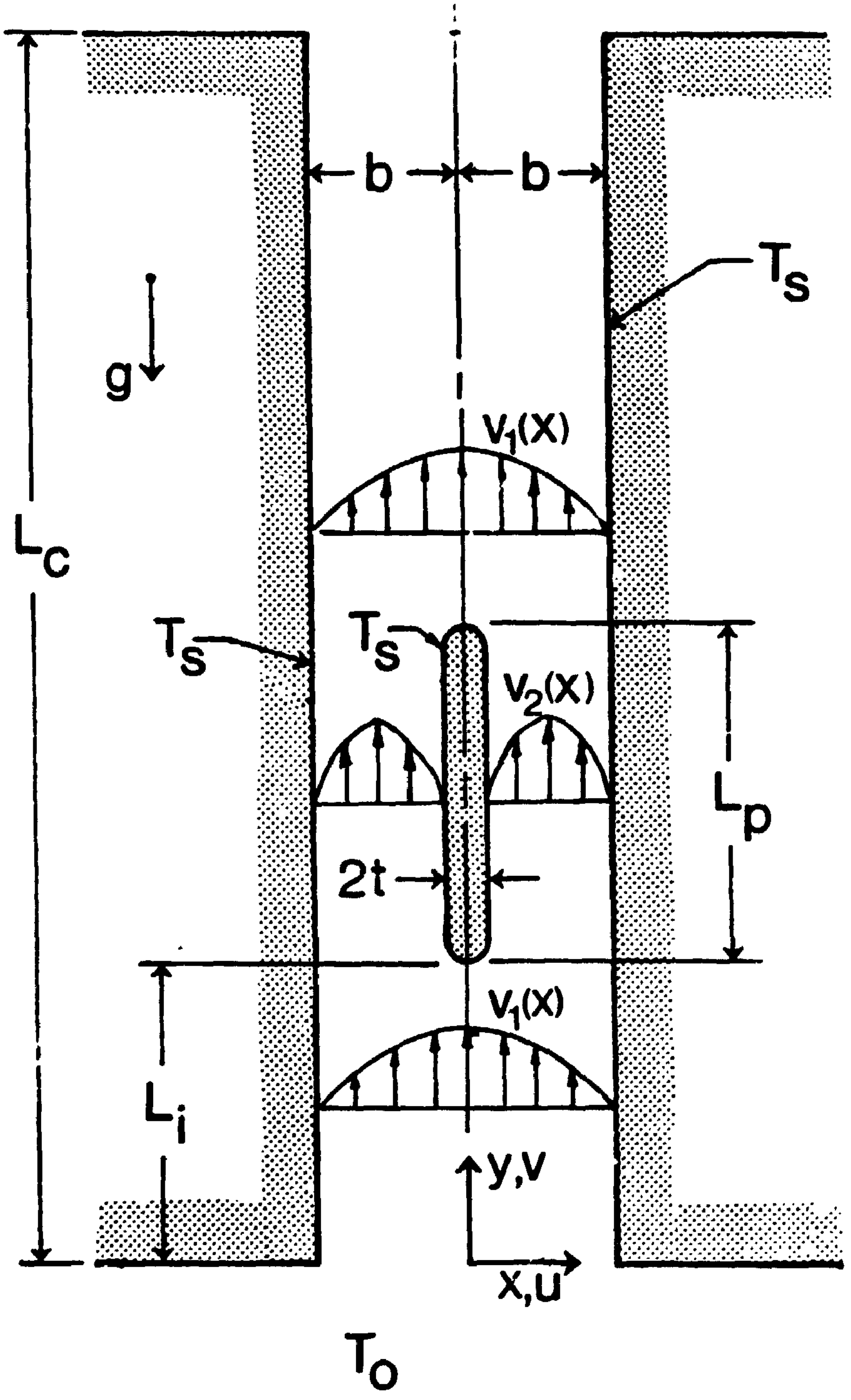
b
b
T_s
g
L_c
$V_1(X)$
T_s
T_s
$V_2(X)$
L_p
2t
$V_1(X)$
L_i
y,v
x,u
T_o

Figure 3.1: The heat transfer geometry showing the fully developed velocity profiles.

$$v_2(x) = \frac{-6q}{(b-t)^3}(x^2-bx-tx+bt) \tag{3.7}$$

where q is the half channel volume flow rate.

Substituting the appropriate velocity profile and integrating equation (3.5) with respect to y over each section of the channel gives:

$$-p'(L_i) - \frac{3q\mu L_i}{b^3} + g\beta\rho(T_s-T_o)L_i = 0 \qquad 0 \le y \le L_i^- \tag{3.8}$$

$$p'(L_i) - p'(L_i+L_p) - \frac{12q\mu L_p}{(b-t)^3} + g\beta\rho(T_s-T_o)L_p = 0 \qquad L_i^+ \le y \le (L_i+L_p)^- \tag{3.9}$$

$$p'(L_i+L_p) - \frac{3q\mu(L_c-L_i-L_p)}{b^3} + g\beta\rho(T_s-T_o)(L_c-L_i-L_p) = 0\,, \qquad (L_i+L_p)^+ \le y \le L_c \tag{3.10}$$

Note that the pressure is assumed to be equal to the ambient pressure at the channel inlet (p'(0)=0) and outlet (p'(L_c)=0). Also, it is assumed that p'(L_i^-)=p'(L_i^+) and p'$(L_i+L_p)^-$=p'$(L_i+L_p)^+$.

Equations (3.8), (3.9), and (3.10) can now be solved for the half channel flow rate:

$$q = \frac{g\beta\rho(T_s-T_o)L_c}{3\mu\left(\frac{4L_p}{(b-t)^3}+\frac{L_c-L_p}{b^3}\right)} = \frac{\nu\, Gr_b\, L_c}{3b^3\left(\frac{4L_p}{(b-t)^3}+\frac{L_c-L_p}{b^3}\right)} \tag{3.11}$$

3.2.1 Fully Developed Channel Average Nusselt Number

The total heat transfer from the half channel is:

$$H_c = \rho q C_p(T_s-T_o) \tag{3.12}$$

Neglecting the small additional area at the leading and trailing edges of the dividing plate, the channel average Nusselt number is defined as:

$$Nu_c = \frac{h_c b}{k} \quad \textit{where} \quad h_c = \frac{H_c}{(L_c + L_p)(T_s - T_o)} \tag{3.13}$$

Substituting equation (3.11) and (3.12) into (3.13) gives:

$$Nu_c = \frac{Ra_c^*}{3\left(4\left(\frac{L_p}{L_c}\right)^2 \left(\frac{b}{b-t}\right)^3 + 4\frac{L_p}{L_c}\left(\frac{b}{b-t}\right)^3 - \left(\frac{L_p}{L_c}\right)^2 + 1\right)} \tag{3.14}$$

For L_p=0, equation (3.14) gives the well known relation for the undivided channel: $Nu_c=Ra_c^*/3$. Note that the geometry of $L_p=L_c$ can be considered either a fully divided channel or two side-by-side undivided channels with b corresponding to the channel wall spacing. For $L_p=L_c$ and t=0, equation (3.14) gives an equivalent expression for the undivided channel (with b corresponding to the wall spacing): $Nu_c=Ra_c^*/24$. Thus, equation (3.14) agrees with existing expressions for the undivided channel at both limits.

Equation (3.14) can also be written in terms of Ra_p^* as:

$$Nu_c = \frac{Ra_p^* \frac{L_p}{L_c}}{3\left(4\left(\frac{L_p}{L_c}\right)^2 \left(\frac{b}{b-t}\right)^3 + 4\frac{L_p}{L_c}\left(\frac{b}{b-t}\right)^3 - \left(\frac{L_p}{L_c}\right)^2 + 1\right)} \tag{3.15}$$

Equation (3.14) is plotted in Fig. 3.2 to show the effect of L_p/L_c and t/b on the fully developed channel Nusselt number. It can be seen from Fig. 3.2 that for a channel with fixed geometric parameters (L_c, b) and temperature difference such that Ra_c^* is constant, the undivided configuration (L_p/L_c=0) gives the highest channel Nusselt number. In the fully developed regime, the dividing plate causes extra viscous resistance

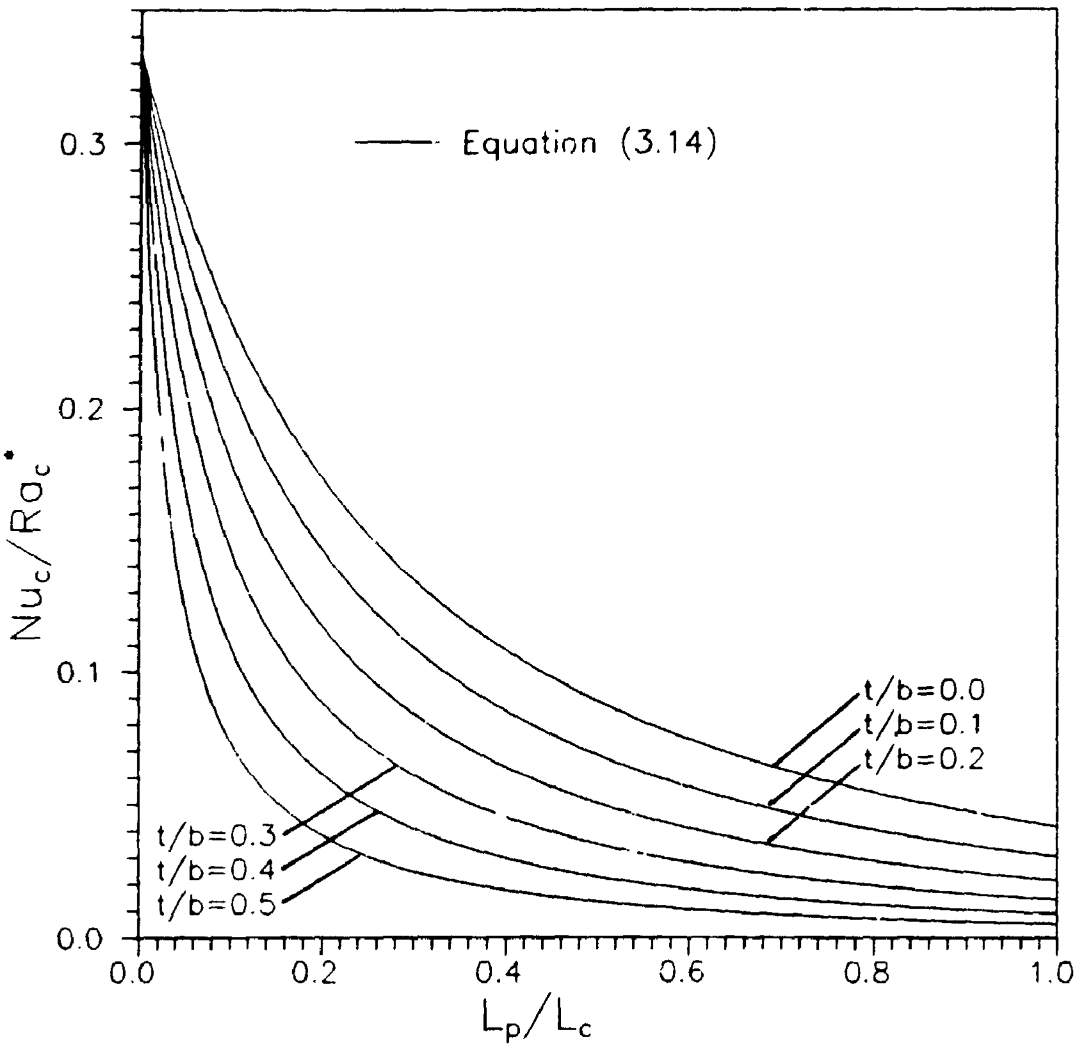

Figure 3.2: Effect of length ratio L_p/L_c and blockage ratio t/b on the fully developed channel average Nusselt number (equation 3.14).

and does not contribute any additional buoyancy force. Also, the dividing plate introduces additional surface area. Hence, adding a dividing plate on the channel centre line causes the Nusselt number to decrease for all values of L_p/L_c and t/b. For t/b=0, Nu_c decreases by a factor of eight from $L_p/L_c=0$ (undivided channel) to $L_p/L_c=1$ (fully divided channel). As expected, the channel Nusselt number decreases with increasing blockage (t/b). Note that in the fully developed regime, Nu_c is independent of the plate location in the channel.

Equation (3.15), shown in Fig. 3.3, has a maximum value in the range $0<L_p/L_c<1$ for every value of fixed plate thickness, $0\leq t/b<1$. The value of L_p/L_c that maximizes equation (3.15) was determined numerically for several values of t/b and the locus of these points is shown in Fig. 3.3.[1] Note that for larger plate thicknesses, the maximum occurs at lower values of L_p/L_c. For t/b=0, the maximum value was calculated to five decimal plates as:

$$\left(\frac{Nu_c}{Ra_p^*}\right)_{max}=0.04466 \quad at \quad \frac{L_p}{L_c}=0.57735 \qquad (3.16)$$

Consider a channel with fixed spacing (b) and temperature, divided by a zero thickness plate of fixed finite length (L_p), such that Ra_p is constant. Figure 3.3 shows that for this channel, extending the channel walls beyond $L_p/L_c=1$ to $L_p/L_c\approx0.58$ will give about a seven percent increase in Nu_c. The Nusselt number increases because the longer column of heated fluid induces a larger flow rate i.e., the chimney effect. Beyond $L_p/L_c\approx0.58$, viscous resistance and the additional surface area cause Nu_c decrease to

---

[1] A closed form expression was obtained using the symbolic manipulation language MAPLE [62]. However, it was too complex to be of practical use.

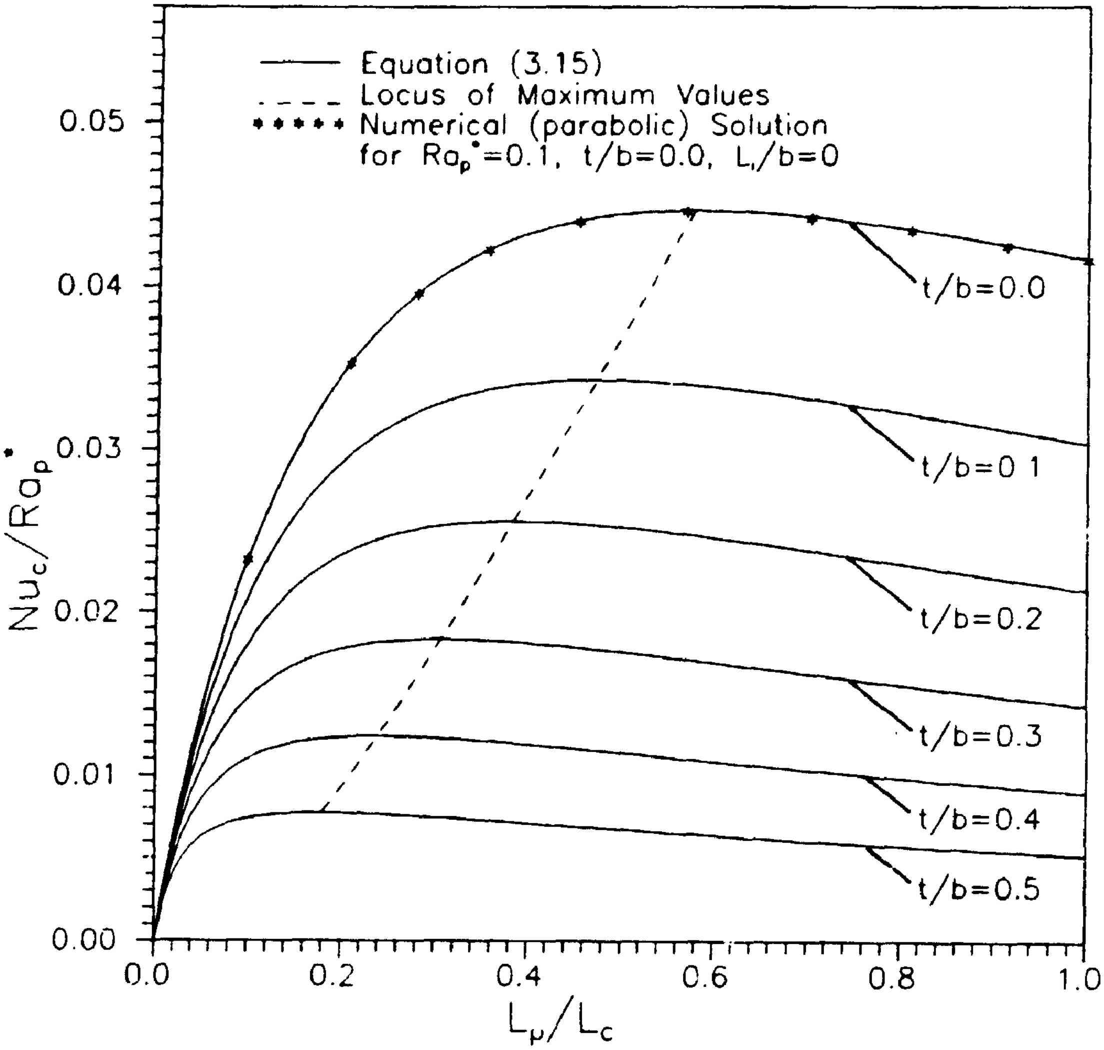

Figure 3.3: Effect of length ratio L_p/L_c and blockage ratio t/b on the fully developed channel average Nusselt number (equation 3.15).

zero as $L_c \to \infty$. Numerical results from the parabolic solution in the fully developed regime are also shown in Fig. 3.3 (for $Ra_p^* = 0.1$, $t/b = 0$, $L_i/b = 0$). The numerical data verify the closed form expression (3.15) for $t/b = 0$.

3.2.2 Fully Developed Plate Average Nusselt Number

For fully developed conditions, the plate Nusselt number (Nu_p) is highly dependent upon the location of the plate in the channel. For analysis, two separate cases must be considered:

Case 1: $L_i = 0$

For $L_i = 0$, the flow is divided by the plate starting at the channel inlet. In this case, half of the total heat transfer will come from the dividing plate because of symmetry. Practically, since the thermal developing length (L_T) will always be greater than zero, this implies that the temperature field must be fully developed at the end of the plate i.e., $L_p \geq L_T$. With this assumption, the heat transfer from the plate (H_p) is:

$$H_p = \frac{1}{2}\,\rho q C_p (T_s - T_o) \qquad (3.17)$$

The plate average Nusselt number is defined as:

$$Nu_p = \frac{h_p b}{k} \quad \text{where} \quad h_p = \frac{H_p}{L_p (T_s - T_o)} \qquad (3.18)$$

Noting that q is given by equation (3.11), and substituting equation (3.17) into (3.18) gives:

$$Nu_p = \frac{Ra_p^*}{6\left(4\frac{L_p}{L_c}\left(\frac{b}{b-t}\right)^3 - \frac{L_p}{L_c} + 1\right)} = \frac{Ra_c^* \frac{L_c}{L_p}}{6\left(4\frac{L_p}{L_c}\left(\frac{b}{b-t}\right)^3 - \frac{L_p}{L_c} + 1\right)} \quad \begin{array}{l} L_p \neq 0 \\ L_i = 0 \end{array} \tag{3.19}$$

Equation (3.19) is shown in Fig. 3.4. Consider a channel with fixed channel width (b) and temperature, divided by a plate of fixed finite length (L_p) such that Ra_p is constant. Figure 3.4 shows that for this channel, extending the channel walls above the plate ($L_p/L_c<1$) will significantly increase the plate Nusselt number because of the chimney effect. In fact, for t/b=0, in the limit as the walls are extended an infinite distance above the plate ($L_p/L_c \to 0$), the plate Nusselt number increases by a factor of 4. As would be expected, increasing t/b lowers the plate Nusselt number because of blockage effects. Again, the numerical results from the parabolic solution validate the analytical expression for t/b=0.

Case 2: $L_i>0$

If the flow is thermally fully developed when it reaches the plate, the plate Nusselt number will be zero, i.e $Nu_p=0$ for $L_i \geq L_T$, where L_T denotes the thermal developing length. This is true for all values of Rayleigh number. In the fully developed limit as $Ra_p^* \to 0$ and $Ra_c^* \to 0$, the thermal developing length also goes to zero. Hence, in the fully developed limit:

$$Nu_p=0 \text{ for } L_i>0 \tag{3.20}$$

3.2.3 Fully Developed Wall Average Nusselt Number

For fully developed conditions the wall Nusselt number (Nu_w) is dependent upon the location of the plate in the channel. Again, the analysis is done

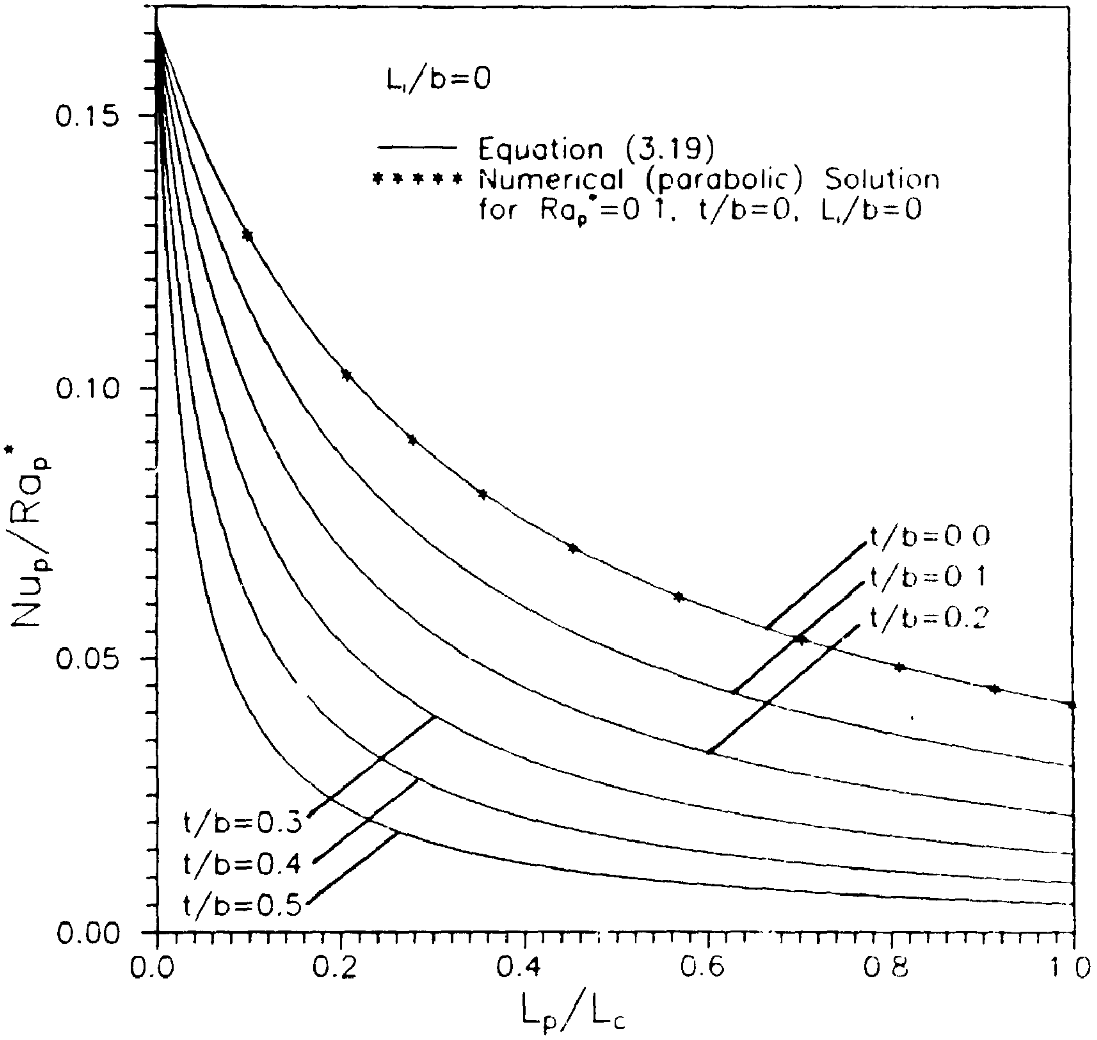

Figure 3.4: Effect of length ratio L_p/L_c and blockage ratio t/b on the fully developed plate average Nusselt number for $L_i/b=0$ (equation 3.19).

for two separate cases:

Case 1: $L_i=0$

When $L_i=0$, half of the heat transferred to the fluid comes from the wall because of symmetry, provided that the temperature field is fully developed at the end of the plate ($L_p \geq L_T$). The wall Nusselt number is defined as:

$$Nu_w = \frac{h_w b}{k} \quad \text{where} \quad h_w = \frac{H_w}{L_c(T_s - T_o)} \tag{3.21}$$

Using the same analysis as for the dividing plate gives:

$$Nu_w = \frac{Ra_c^*}{6\left(4\frac{L_p}{L_c}\left(\frac{b}{b-t}\right)^3 - \frac{L_p}{L_c} + 1\right)} = \frac{Ra_p^* \frac{L_p}{L_c}}{6\left(4\frac{L_p}{L_c}\left(\frac{b}{b-t}\right)^3 - \frac{L_p}{L_c} + 1\right)} \quad \begin{matrix} L_p \neq 0 \\ L_i = 0 \end{matrix} \tag{3.22}$$

Equation (3.22) is shown in Fig. 3.5. Consider a channel with fixed channel width (b) and temperature, divided by a plate of fixed finite length (L_p) such that Ra_p is constant. Equation (3.22) shows that extending the channel walls such that $L_p/L_c<1$ causes the fully developed wall Nusselt number to decrease for all values of plate thickness t/b. Although the chimney effect increases the channel flow rate and wall heat transfer, the associated increase in the wall length (L_c) is sufficient to reduce the wall average Nusselt number. Again, the numerical results validate the analytical expression for t/b=0.

Case 2: $L_i>0$

As already discussed, if $L_i>0$ the heat transfer from the plate is zero in

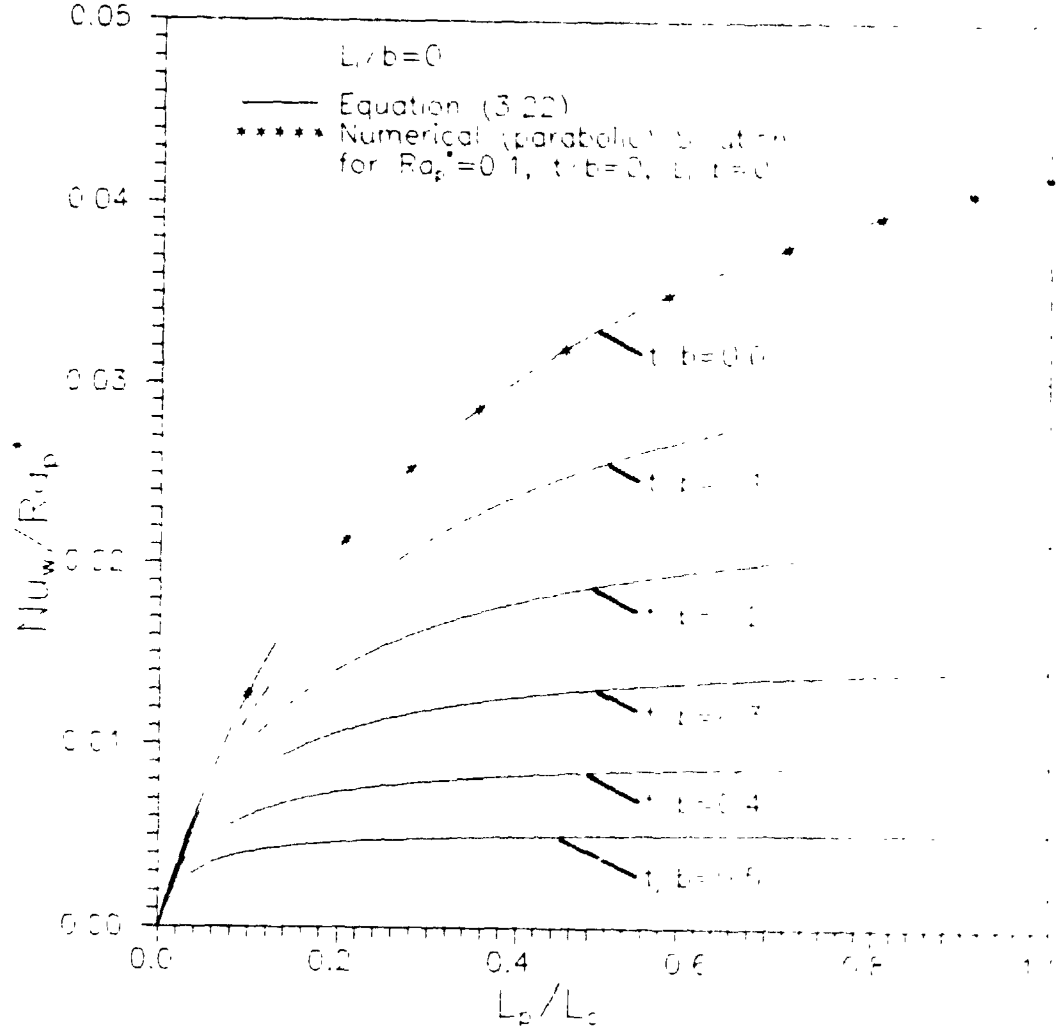

Figure 3.5: Effect of length ratio L_p/L_c and blockage ratio t/b on the fully developed wall average Nusselt number for L_i/b=0 (equation 3.22).

the fully developed limit. Hence, all of the heat transferred to the fluid comes from the wall. Using the same method as used previously gives:

$$Nu_w = \frac{Ra_c^*}{3(4\frac{L_p}{L_c}(\frac{b}{b-t})^3 - \frac{L_p}{L_c} + 1)} = \frac{Ra_p^* \frac{L_p}{L_c}}{3(4\frac{L_p}{L_c}(\frac{b}{b-t})^3 - \frac{L_p}{L_c} + 1)} \quad \begin{matrix} L_p \neq L_c \\ L_t > 0 \end{matrix} \qquad (3.23)$$

Equation (3.23) is identical to equation (3.22) except for a factor of two.

The above analysis predicts that the effect of plate thickness (t/b) is large at low Rayleigh number; even ten percent blockage (t/b=0.1) causes a significant reduction in heat transfer in the fully developed regime. At higher Rayleigh number, the influence of blockage will diminish. Hence, "worst case" estimates of the reduction in heat transfer because of blockage can be obtained from the above analysis.

3.3 Single Isolated Plate Limit ($Ra^* \to \infty$)

Experimental studies of the isothermal vertical channel [1,36,38] have shown that at high Rayleigh number ($Ra_c^* \to \infty$), the heat transfer behaviour of the channel approaches that of two isolated flat plates. The similarity solution by Ostrach [49] for a single isothermal vertical plate gives:

$$Nu_L = C(Gr_L Pr)^{1/4} \qquad (3.24)$$

where C=0.515 for a Prandtl number of Pr=0.7. In equation (3.24), the Nusselt and Grashof numbers are defined as:

$$Nu_L = \frac{hL}{k}, \qquad Gr_L = \frac{g\beta(T_w - T_o)L^3}{\nu^2} \tag{3.25}$$

Changing the characteristic length in the equations (3.24) and (3.25) from plate length "L" to the plate spacing "b" gives:

$$Nu = \frac{hb}{k} = C\left(Gr_b Pr \frac{b}{L}\right)^{1/4} \tag{3.26}$$

Note that the heat transfer coefficient (h) is independent of the plate spacing "b", as must be the case for an isolated plate. Also note that $Nu_L \rightarrow \infty$ as $L \rightarrow \infty$ in equation (3.24) whereas, using the conventional "channel" Nusselt number definition in equation (3.26), $Nu \rightarrow 0$ as $L \rightarrow \infty$.

3.3.1 Isolated Plate Channel Average Nusselt Number

Now consider a channel with a dividing plate as shown in Fig. 3.1. At high Rayleigh number ($Ra_c^* \rightarrow \infty$, $Ra_p^* \rightarrow \infty$) the divided channel will behave like three isolated flat plates: two isolated plates of length L_c and one isolated plate of length L_p. Small plate thicknesses (t/b) will have no effect on heat transfer at high Rayleigh number. Using equation (3.26), the total heat transfer (H_c) from channel wall and plate in the half channel is:

$$H_c = \frac{Ck(T_w - T_o)}{b}\left(Ra_p^{*1/4} L_p + Ra_c^{*1/4} L_c\right) \tag{3.27}$$

$$\text{where} \quad Ra_p^* = Gr_b Pr \frac{b}{L_p} \quad \text{and} \quad Ra_c^* = Gr_b Pr \frac{b}{L_c} \tag{3.28}$$

The channel average Nusselt number is defined as:

$$Nu_c = \frac{h_c b}{k} \quad \text{where} \quad h_c = \frac{H_c}{(L_p + L_c)(T_w - T_o)} \tag{3.29}$$

Substituting equation (3.27) into (3.29) gives:

$$Nu_c = C\,Ra_c^{*\,1/4}\left(\frac{(\frac{L_p}{L_c})^{3/4}+1}{\frac{L_p}{L_c}+1}\right) \tag{3.30}$$

Equation (3.30) can be written in terms of Ra_p^* as:

$$Nu_c = C\,Ra_p^{*\,1/4}\left(\frac{(\frac{L_p}{L_c})^{1/4}+\frac{L_p}{L_c}}{\frac{L_p}{L_c}+1}\right) \tag{3.31}$$

Equations (3.30) and (3.31) have been plotted in Fig. 3.6. Equation (3.30) has a maximum value in the range $0<L_p/L_c<1$. The value of L_p/L_c that maximizes equation (3.30) was determined analytically using the symbolic manipulation language MAPLE [62]. Unfortunately, the resulting expression was too complex to be of practical use and hence, was evaluated to five decimal places as:

$$\left(\frac{Nu_c}{C Ra_c^{*\,1/4}}\right)_{max} = 1.08302 \quad at \quad \frac{L_p}{L_c} = 0.22998 \tag{3.32}$$

Equation 3.30 shows that for a channel with fixed channel length (L_c) and temperature difference such that Ra_c^* is constant, the addition of a small "dividing" plate with L_p/L_c =0.23 will produce about an eight percent increase in the channel average Nusselt number. This maximum value is caused by the fact that the short plate has a greater average heat transfer coefficient than the channel walls. Therefore, the *channel* average Nusselt number increases.

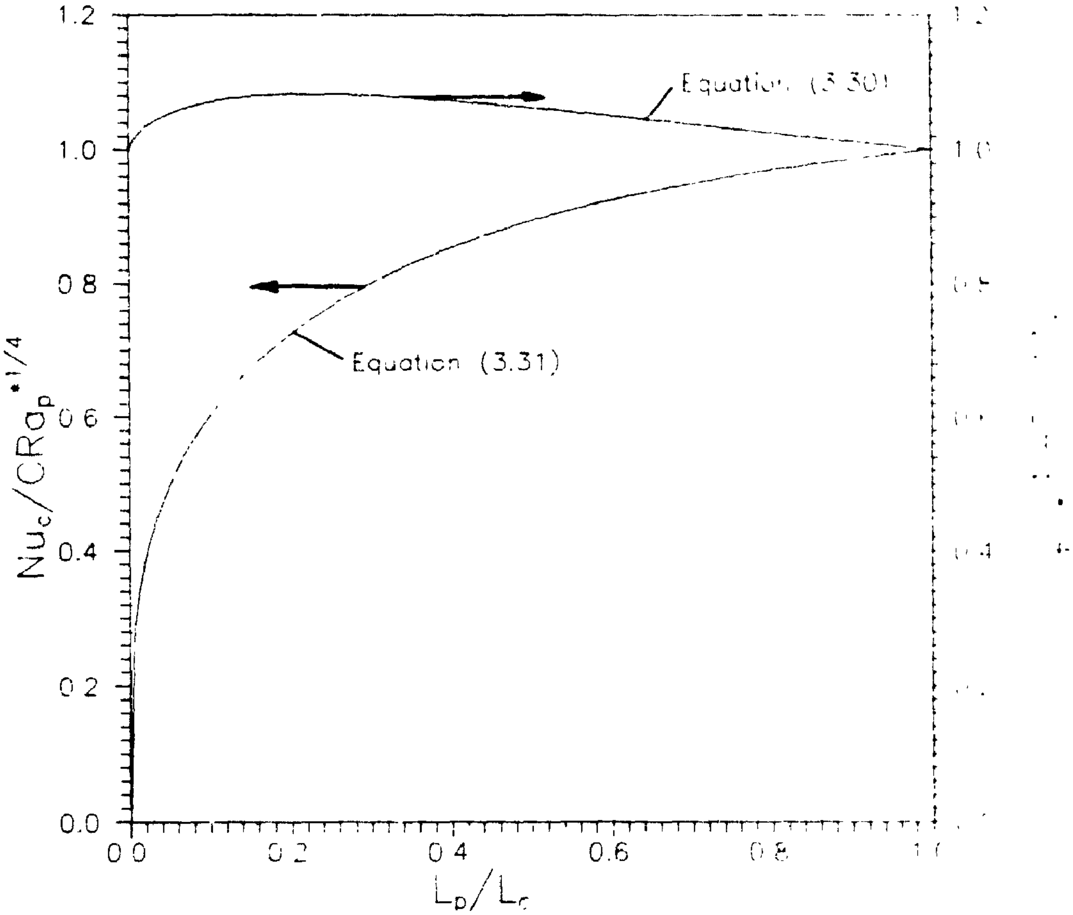

Figure 3.6: Effect of length ratio L_p/L_c on the channel average Nusselt number for the isolated plate limit (equations 3.30 and 3.31).

Equation (3.31) shows that for a channel with fixed plate length (L_p) and temperature difference such that Ra_p^* is constant, increasing the channel wall length (L_c) causes the channel average heat transfer to decrease. In the limit as $L_p/L_c \rightarrow 0$, which corresponds to infinitely long channel walls ($L_c \rightarrow \infty$), the channel average Nusselt number is zero ($Nu_c \rightarrow 0$). The channel average Nusselt number approaches zero as $L_c \rightarrow \infty$ because the *wall* Nusselt number approaches zero. Since Nu_c represents an "area averaged" Nusselt number of the wall and plate (and the wall area is infinite), Nu_c also approaches zero.

3.4 Concluding Remarks

In this chapter, closed form expressions for the channel, wall and plate average Nusselt numbers at the fully developed and isolated plate limits have been derived. Although useful in themselves, the primary value of these expressions is for correlation purposes. When a process varies smoothly between two well defined limiting solutions, data between these limits can be correlated easily and accurately using the method of Churchill and Usagi [63]. Correlations utilizing these expressions are presented in Chapter 8.

CHAPTER 4

NUMERICAL RESULTS FOR DEVELOPING NATURAL CONVECTION IN AN UNDIVIDED CHANNEL

4.1 Introduction

As a preliminary study to the divided channel problem, developing natural convection in a channel without a dividing plate has been solved. In this chapter, the results of a full elliptic solution are presented for Pr=0.7, $1.5 \le Ra_c^* \le 3{,}500$, $L_c/b=10$, 17, 24. The parabolic solution (of Aihara [34]) for the isothermal vertical channel has been reproduced so that detailed comparisons could be made with the elliptic solution. Comparisons of the elliptic and approximate boundary-layer results for the undivided channel show the applicability and limitations of boundary-layer-type solutions.

4.2 Discussion of Results

As discussed in the literature review, there are two elliptic solutions (using finite difference methods) for the isothermal channel in the literature: those of Kettleborough [39] and Nakamura et al. [40] (hereafter, Nakamura). Each considered only two Grashof numbers (Gr=12.5, 1,250), an aspect ratio $L_c/b=10$ and a Prandtl number Pr=0.733. The results from these studies are in poor agreement in many aspects. Table 4.1 shows a comparison of the present results with these two solutions for Gr=1250. The present work is in closer agreement with Nakamura than Kettleborough. However, the close agreement with the average Nusselt number predicted

Table 4.1: Comparison of major data with other elliptic solutions for Gr=1[illegible] 733, $L_c/b=10$ ($Ra_c^*=91.625$).

Author	Average Nusselt Numbers Nu_c	 Nu_{c2}	Flow Rate Q_e	Exit Bulk Temperature T_b^*
Kettleborough [39], (1972)	2.38	2.75	2.079	0.442
Nakamura et al. [40] (1982)	1.877	1.814	1.358	0.533
Present Elliptic Solution	1.867	1.802	1.439	0.501
Present Parabolic Solution	1.899	1.900	1.478	0.499

by Nakamura is somewhat coincidental since the temperature and velocity profiles are not in close agreement as will be shown later.

Figure 4.1 shows a comparison of the streamwise velocity profiles from the present elliptic solution with those predicted by Kettleborough and by Nakamura. Again, the present work is closer to that of Nakamura, although significant disagreement does exist. Kettleborough predicts reverse flow in the channel with fluid being drawn deep into the channel from the channel exit. This was not found in the present study nor in the study by Nakamura.

A comparison of the developing temperature profiles with those predicted by Kettleborough and by Nakamura is displayed in Fig. 4.2. The present work is not in agreement with either of the other two solutions. Although the agreement with both solutions is fair at the channel inlet, very large differences exist closer to the exit. It is likely coincidental that the exit temperature profile (y/b=10) of the present solution is in close agreement with Kettleborough's since the temperature profiles closer to the channel entrance and the exit velocity profiles are vastly different.

Figure 4.3 shows a comparison of the channel centre line pressure distributions predicted by the present elliptic and parabolic solutions compared to the results of Nakamura. For the parabolic solution the inlet pressure is assumed to be $p'=-\rho v_o^2/2$, where v_o is the assumed uniform inlet velocity. The present elliptic solution shows fair agreement with the parabolic pressure distribution; the maximum difference is about 11% and occurs quite close to the location of minimum pressure. The pressure

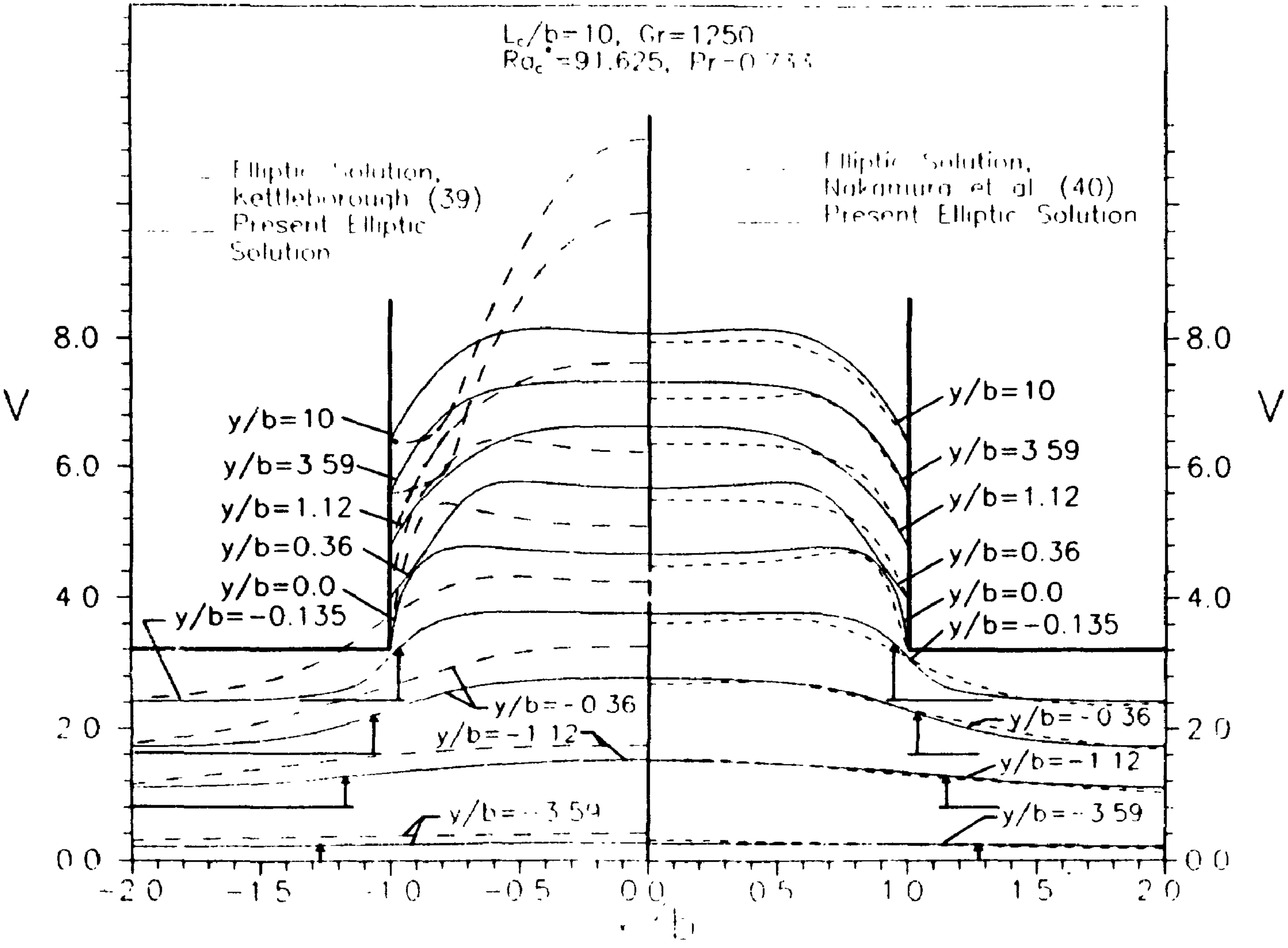

Figure 4.1: Comparison of the streamwise velocity (V) profiles from the present elliptic solution with the work of Kettleborough, and Nakamura et al..

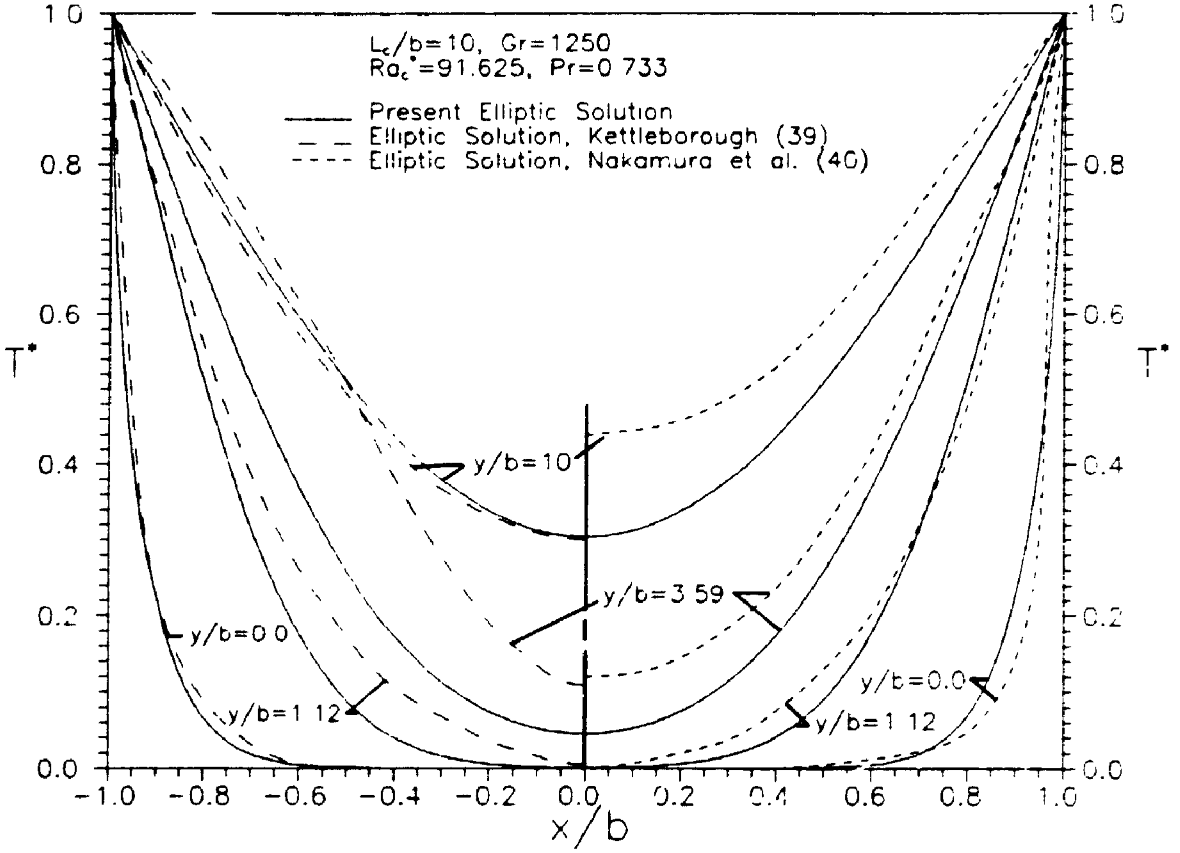

Figure 4.2: Comparison of the temperature profiles from the present elliptic solution with the work of Kettleborough, and Nakamura et al..

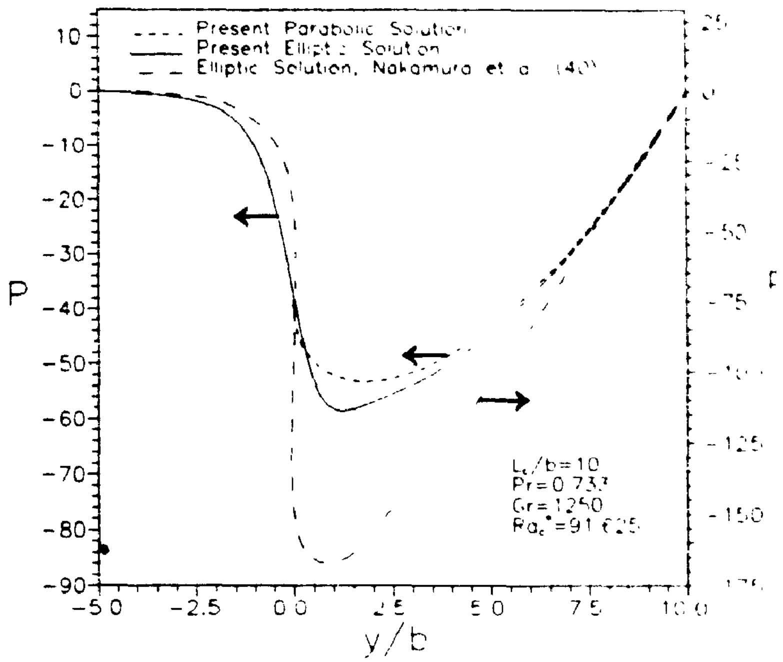

Figure 4.3: Comparison of the channel centre line pressure distributions with that predicted by Nakamura et al..

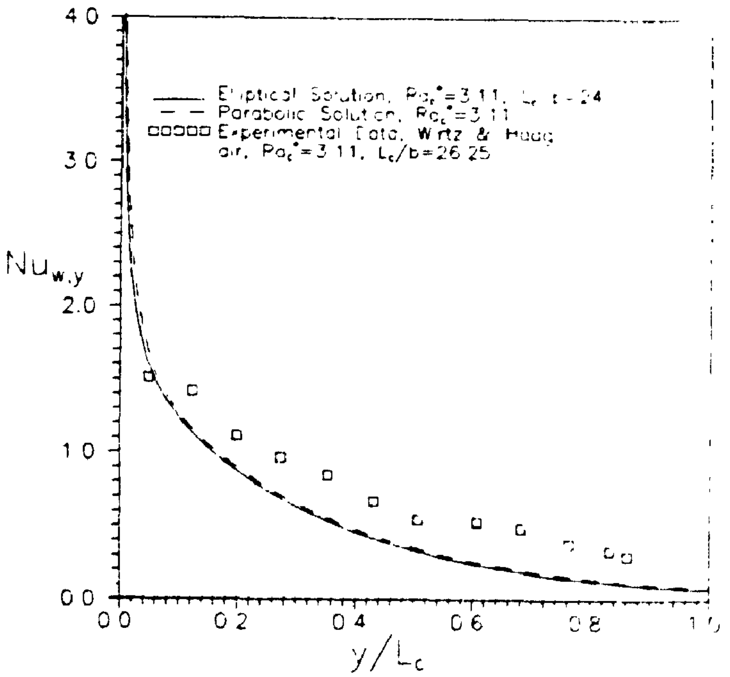

Figure 4.4: Comparison of the local Nusselt number distributions with the experimental data of Wirtz and Haag.

distribution presented by Nakamura is many times lower than that found by either of the present methods (note the different axis scales). The channel inlet pressure (y/b=0.0) is reported by Nakamura to be about five times lower than that of the parabolic solution, whereas the centre line inlet pressure found by the present elliptic solution (P=-37.4) is only about 3% different from the parabolic solution (P=-38.6). Nakamura does not explain the large discrepancy between the obtained inlet pressure and that predicted by Bernoulli's equation. Hence, it is likely that the present elliptic results more closely represent the actual channel pressure.

Figure 4.4 shows a comparison of the present data with the experimental local Nusselt distribution measured in air by Wirtz and Haag [64]. The experimental data are for $Ra_c^*=3.11$ and $L_c/b=26.25$. It should be noted that the aspect ratio for the elliptic solution is slightly different ($L_c/b=24$) and the parabolic results are independent of aspect ratio. Although the general trend of the local heat transfer distributions are the same, both of the numerical predictions are much lower than the experimental data, particularly toward the top of the channel. In fact, the maximum discrepancy between the results is about 100% at the channel exit. The difference may be due to the difference in the boundary conditions at the channel inlet. In Wirtz's and Haag's model the channel walls were formed by two 6mm thick copper plates. These plates were not bevelled at the channel inlet, so the air was likely preheated before entering the channel. It should also be mentioned that the average Nusselt number given by Wirtz and Haag is about 20% higher than the experimental values given by Elenbaas [1]. Unfortunately, these were the only experimental local heat transfer data available in the literature for the symmetrically heated isothermal channel.

Figures 4.5 and 4.6 show the elliptic solution streamline and isotherm contours of the inlet region for Gr=50, 10^4, $L_c/b=24$, (Ra_c^*=1.458, 291.7). At low Rayleigh number the induced velocities are low and the flow enters the channel smoothly. Also, due to the low velocities, the non-zero isotherms extend well outside the channel inlet and preheat the incoming air. At high Rayleigh number, fluid velocities are sufficiently high that the flow separates from the wall and there is a small eddy on the channel wall near the leading edge. A close-up view of the separated flow region is shown in Fig. 4.7. Dots are shown at each nodal point to illustrate the grid density in the vicinity of the eddy. The fluid re-attachment occurs at about y/b=0.78, as determined from the wall shear stress distribution. To the author's knowledge, flow separation at the inlet has not been predicted by any previous study of natural convection in vertical channels.

Figure 4.8 shows how the streamwise velocity profile near the centre of the separation region (y/b=0.24) evolves with Rayleigh number. It is evident from Fig. 4.8 that the velocity profile evolves slowly over a wide range of Rayleigh number and the separation eddy strengthens and gets wider with increasing Rayleigh number.

Additional elliptic solutions were obtained for aspect ratios of $L_c/b=10$, 17 so that the onset of inlet flow separation could be correlated. For $L_c/b=10$, separation occurs at Gr≈8,200, $Ra_c^*\approx570$ as determined from the wall shear stress distribution. For $L_c/b=17$, separation occurs at Gr≈2,900, $Ra_c^*\approx120$ and for $L_c/b=24$, separation occurs at Gr≈1,700, $Ra_c^*\approx50$. Fig. 4.9 shows an

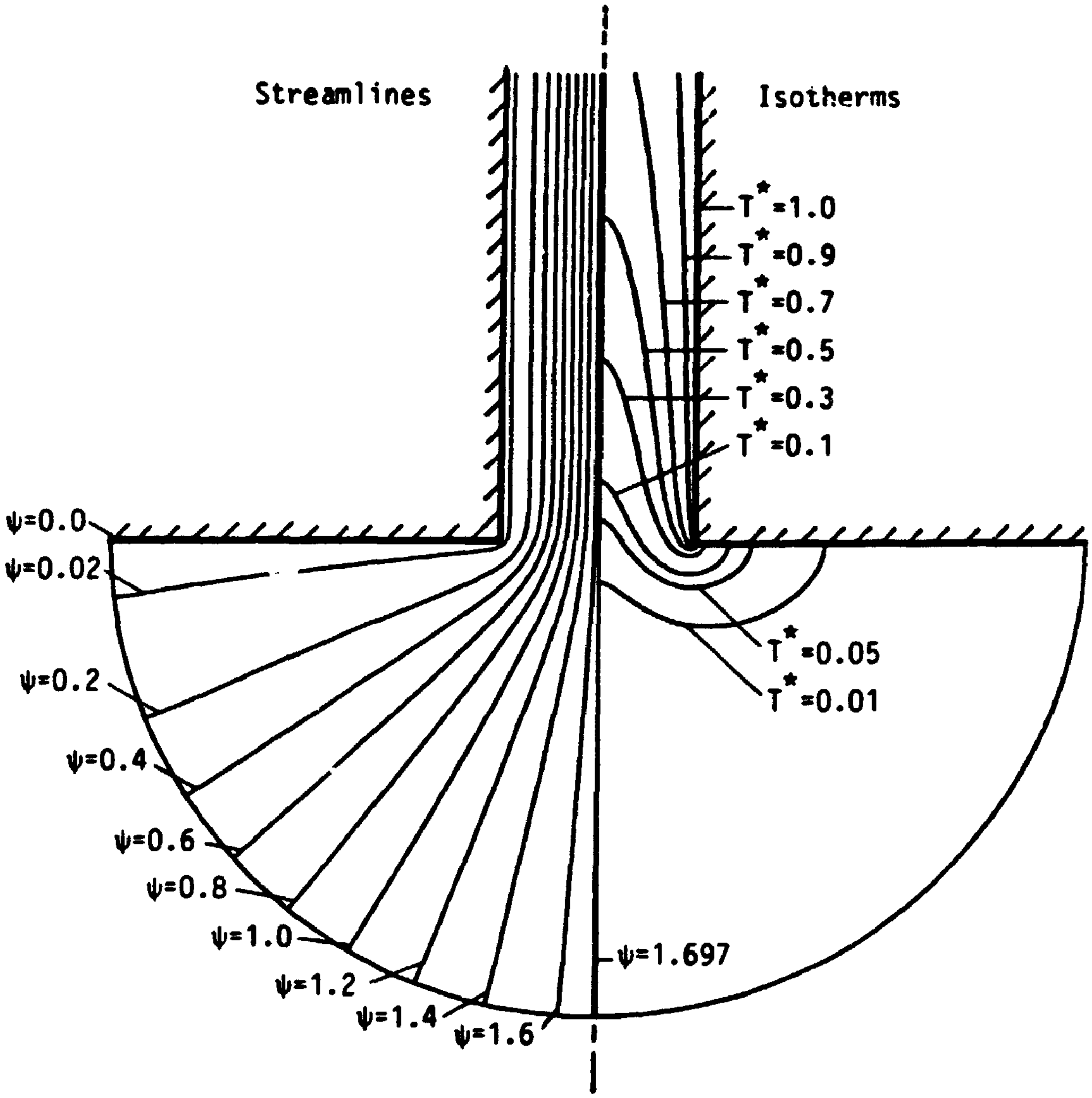
Streamlines
Isotherms
T*=1.0
T*=0.9
T*=0.7
T*=0.5
T*=0.3
T*=0.1
T*=0.05
T*=0.01
ψ=0.0
ψ=0.02
ψ=0.2
ψ=0.4
ψ=0.6
ψ=0.8
ψ=1.0
ψ=1.2
ψ=1.4
ψ=1.6
ψ=1.697

Figure 4.5: Channel inlet streamline and isotherm contours from the elliptic solution for Gr=50, $L_{\text{℄}}/b=24$, Pr=0.7, $(Ra_{\text{℄}}^{*}=1.458)$.

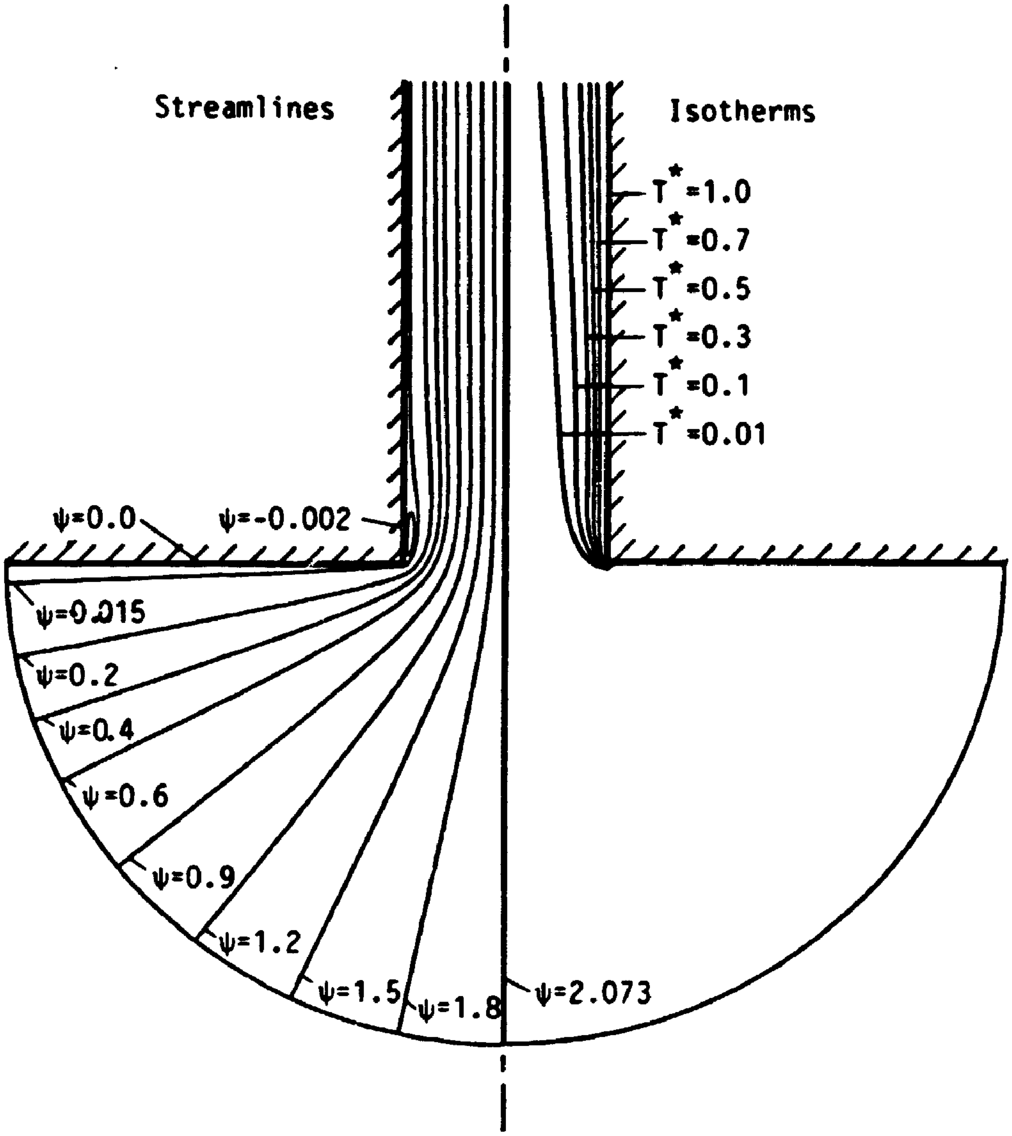

Figure 4.6: Channel inlet streamline and isotherm contours from the elliptic solution for $Gr=10^4$, $L_c/b=24$, $Pr=0.7$, $(Ra_c^*=291.7)$.

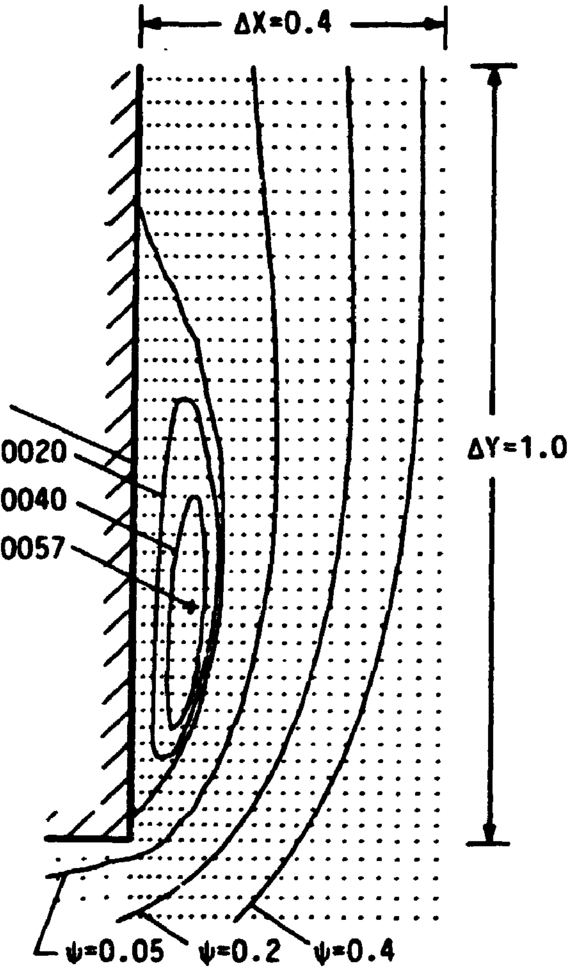
ΔX=0.4
ΔY=1.0
ψ=0.0
ψ=-0.0020
ψ=-0.0040
ψ=-0.0057
ψ=0.05
ψ=0.2
ψ=0.4

Figure 4.7: Close-up view of the separated flow region for $Gr=10^4$, $L_c/b=24$, $Pr=0.7$, $(Ra_c^*=291.7)$.

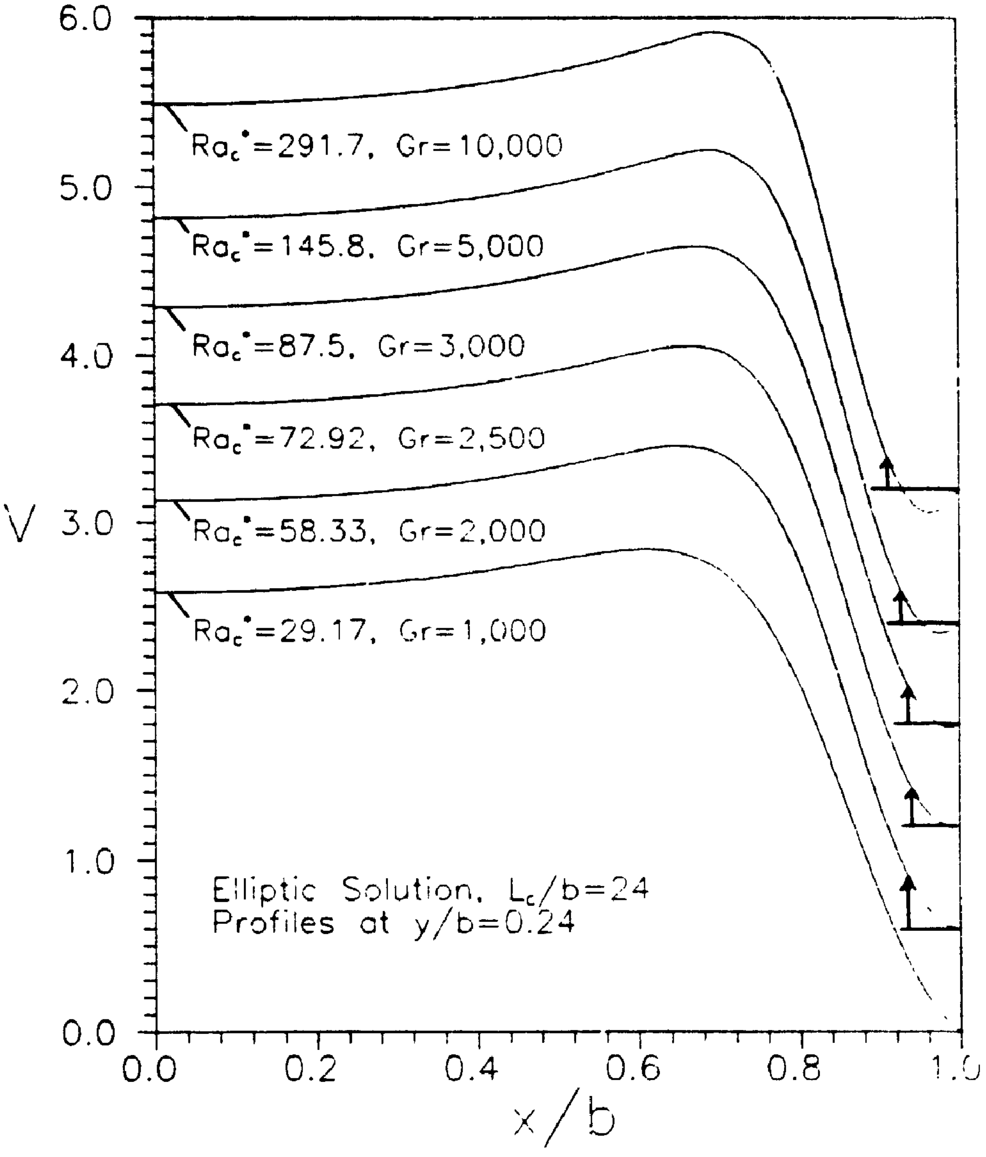

Figure 4.8: Streamwise velocity (V) profiles in the separated flow region for various values of Rayleigh number, (L_c/b=24).

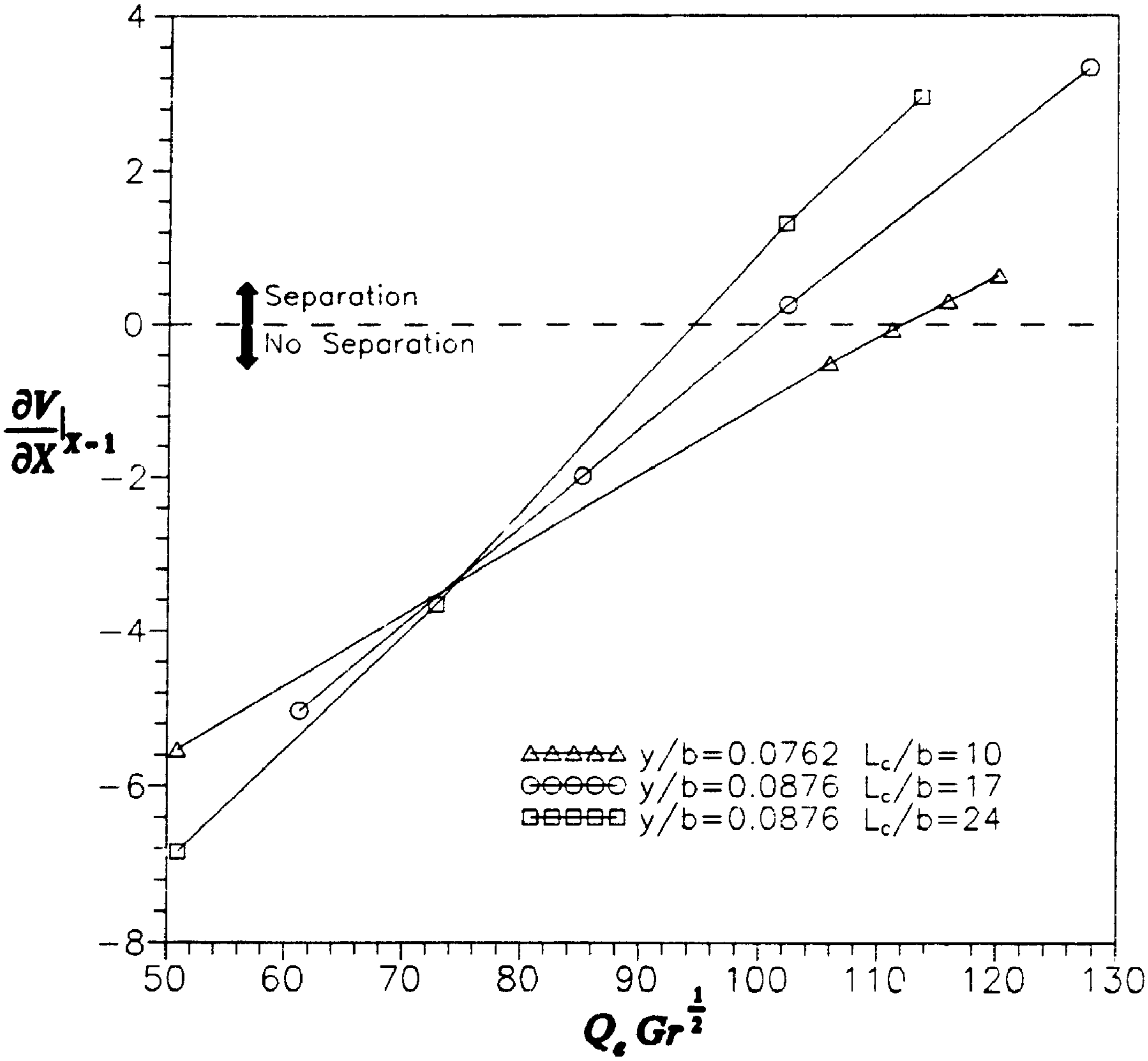

Figure 4.9: Streamwise velocity gradient at the wall in the separated flow region versus $QGr^{\frac{1}{2}}$.

attempt to correlate the onset of separation ($\partial V/\partial X|_{x=1}=0$) with dimensional channel flow rate. (Note that dimensional channel flow rate (q) is proportional to $Q_e Gr^{1/2}$). Velocity gradients at the wall were taken at several values of y/b near the channel entrance and the results were insensitive to the specific location chosen. Data at only one value of y/b (for each aspect ratio) are shown for clarity. This parameter is quite successful in predicting separation; separation occurs within a twenty percent range of $Q_e Gr^{1/2}$ for all three channel aspect ratios. Buoyancy effects can explain the slight delay of separation for channels with lower aspect ratios. Low aspect ratio channels require higher temperatures than large aspect ratio to obtain the same dimensional flow rate. This higher heating causes larger buoyancy forces at the wall which act to oppose separation. Hence, slightly greater flow rates are required to induce separation in short channels.

The behaviour of average Nusselt number (Nu_c) with Rayleigh number for both of the present solutions is displayed in Fig. 4.10. The asymptotic limits for low and high Ra_c^* are also shown. The parabolic and elliptic solutions are in excellent agreement at low Ra_c^* and at higher Ra_c^* they differ by about 3%. As discussed in the literature review (see Fig. 1.4), the experimental data of Elenbaas [1] and Aihara [36] are in good agreement with the parabolic solution over the range given in Fig. 4.10. Hence, the close agreement of the two solutions gives confidence in the present elliptic results.

A comparison of the parabolic and elliptic channel flow rates is shown in Fig. 4.11. The results are in good agreement over a wide range of

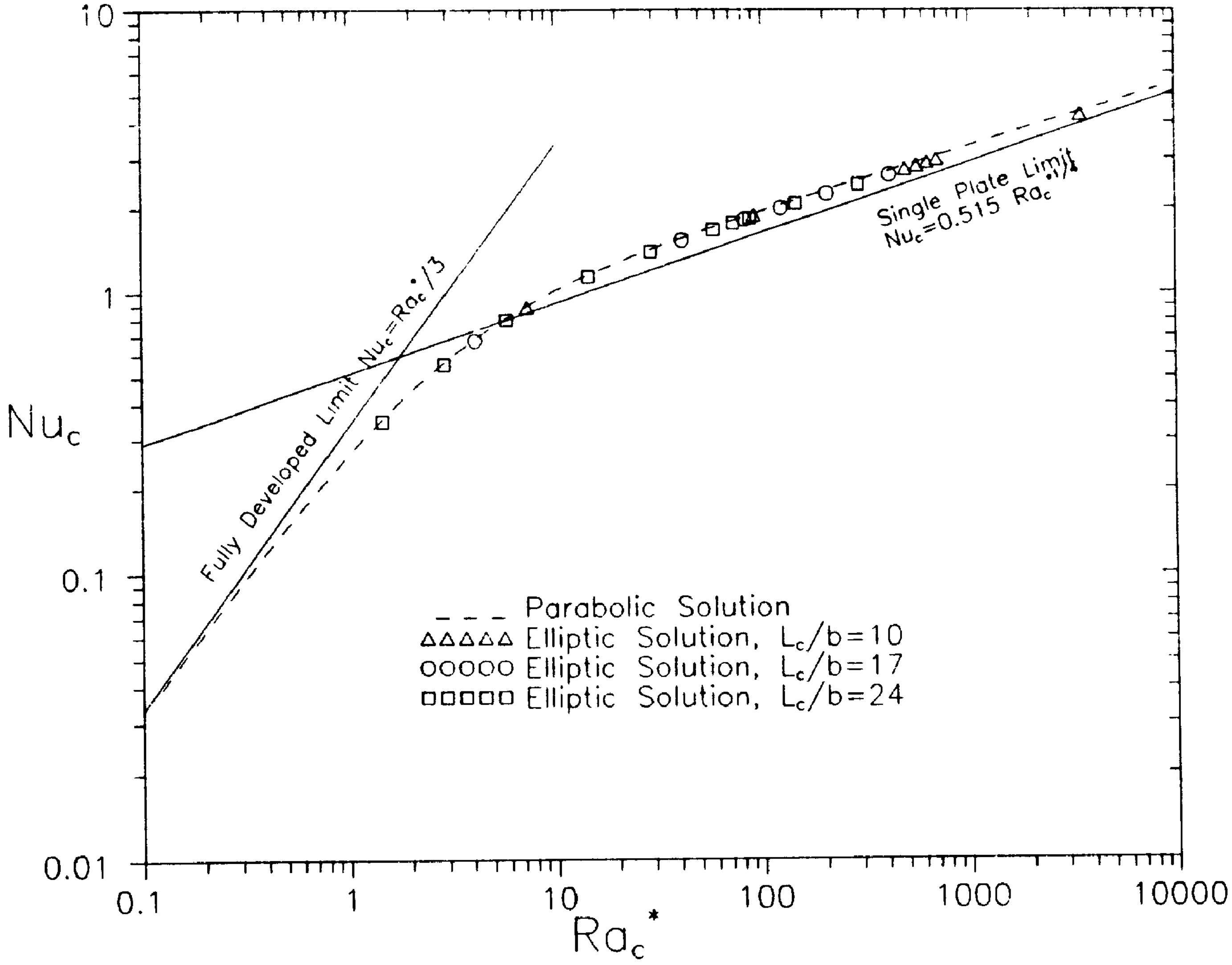

Figure 4.10: Comparison of average Nusselt number results from the present elliptic and parabolic solutions.

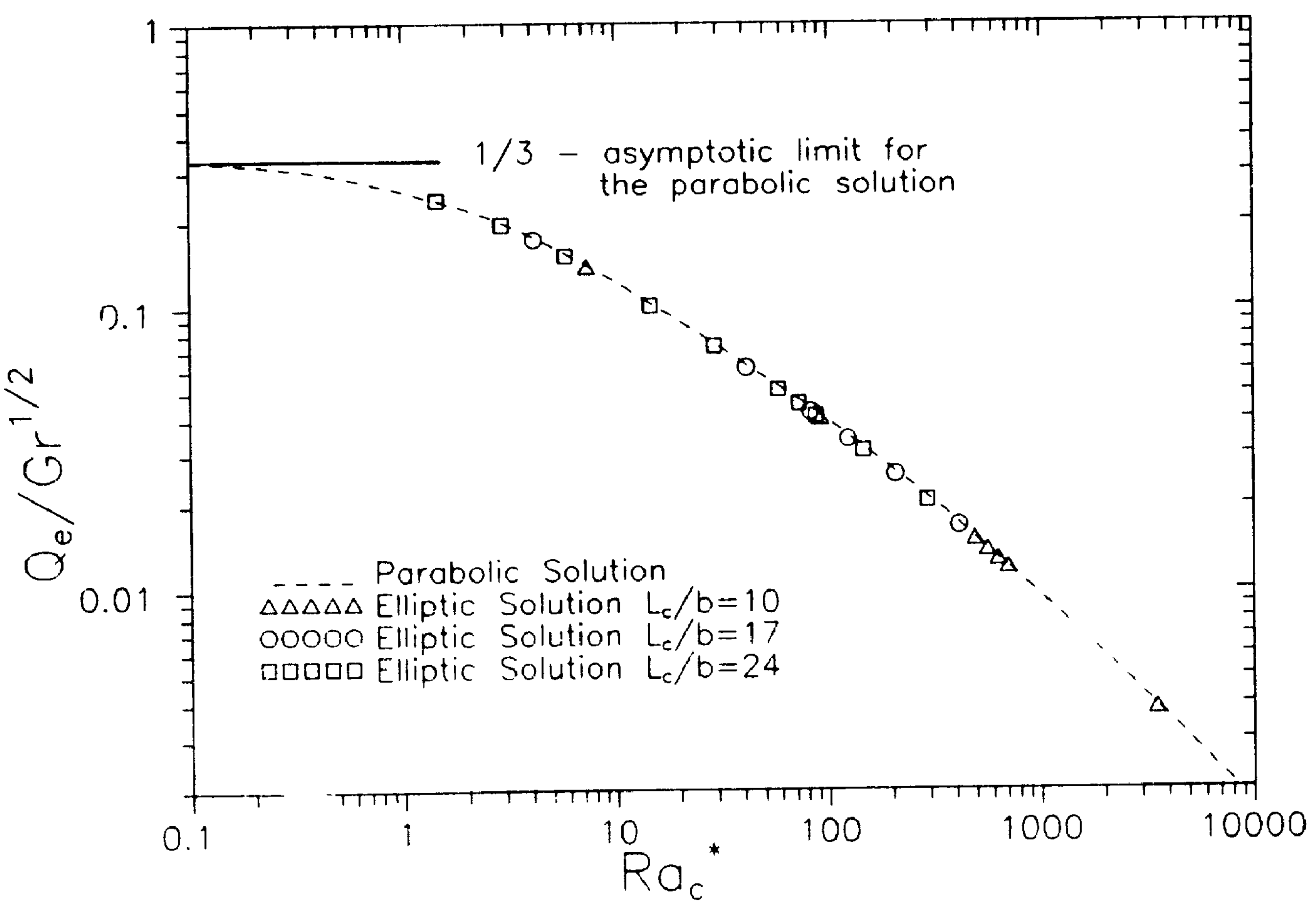

Figure 4.11: Comparison of induced flow rates from the present elliptic and parabolic solutions.

Rayleigh number for $L_c/b=10$, 17, 24.

Figures 4.12 and 4.13 show comparisons of the developing velocity and temperature profiles for $Ra_c^*=2.917$ and $Ra_c^*=291.7$. For the elliptic solution ($L_c/b=24$), the developing velocity profiles outside the channel are also presented; for the parabolic solution the assumed inlet profiles ($y/b=0$) are uniform. In both figures, the parabolic profiles differ substantially from the elliptic profiles near the entrance. However, these differences diminish as the flow proceeds toward the channel exit. Exit velocity and temperature profiles ($y/b=24$) are in close agreement. Considering the large differences near the channel entrance, it is somewhat surprising that the overall heat transfer and induced flow rate are in good agreement. These figures clearly show how insensitive the parabolic solution is to the assumed inlet conditions. It is also clear from these figures that derivative boundary conditions used at the channel exit for the elliptic solution are quite acceptable at $Ra_c^*=2.917$; however, at $Ra_c^*=291.7$ the velocity and temperature profiles are still developing and these conditions are less suitable.

There are several features of the developing velocity profiles predicted by the elliptic solution that have not been seen previously. The velocity profiles shown in Fig. 4.12 for $Ra_c^*=291.7$ ($L_c/b=24$) show rather an unusual evolution. The inlet profile ($y/b=0$) has a maximum velocity near the wall. At this location, the fluid is being drawn into the channel by the negative pressure gradient and the maximum velocity is produced by the additional buoyancy force which acts only close to the wall. The profile at $y/b=0.3$ clearly shows the reverse flow in the separated region near the wall. Here

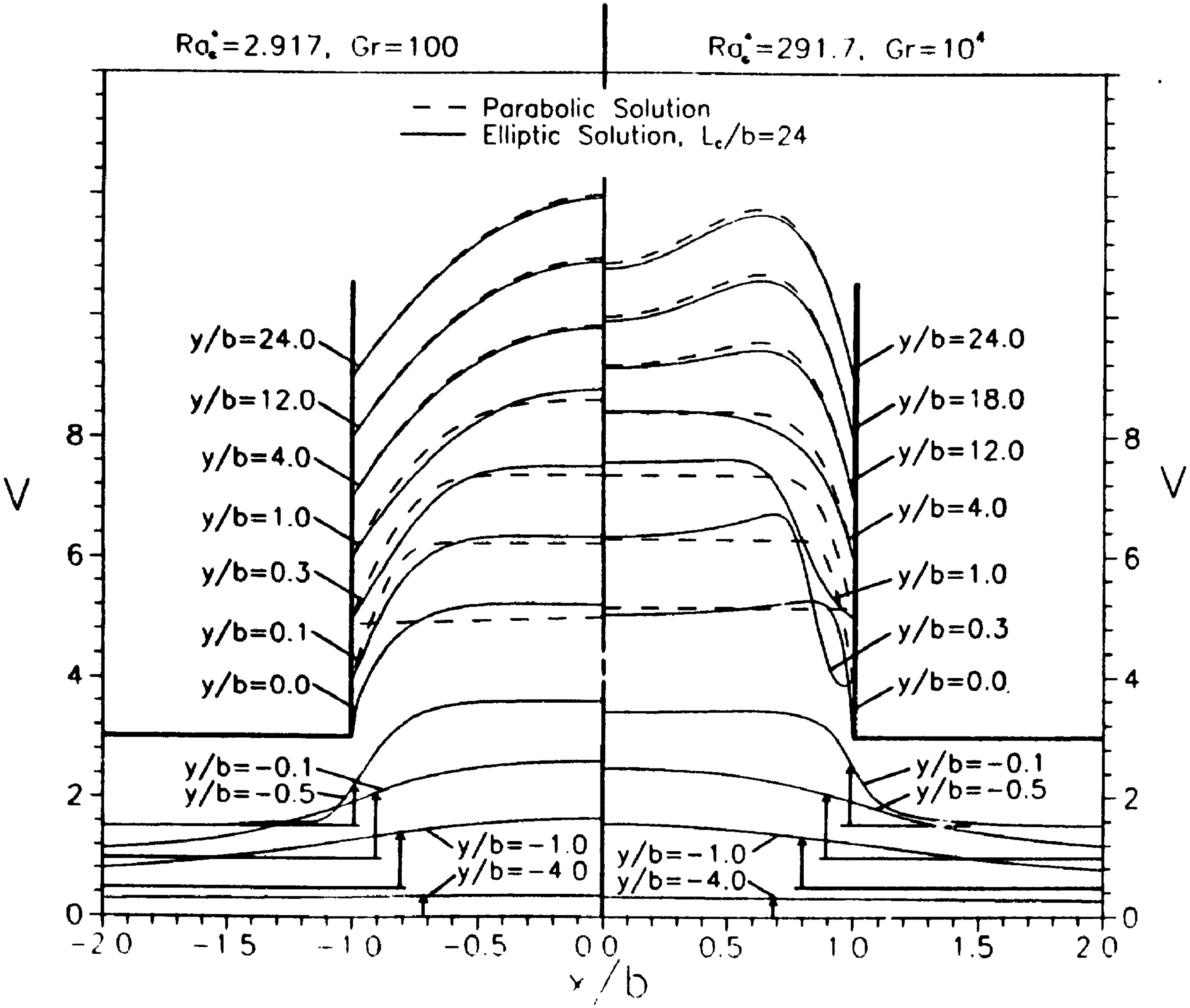

Figure 4.12: Comparison of streamwise velocity (V) profiles from the present elliptic and parabolic solutions for Ra^*=2.917 and Ra_c^*=291.7.

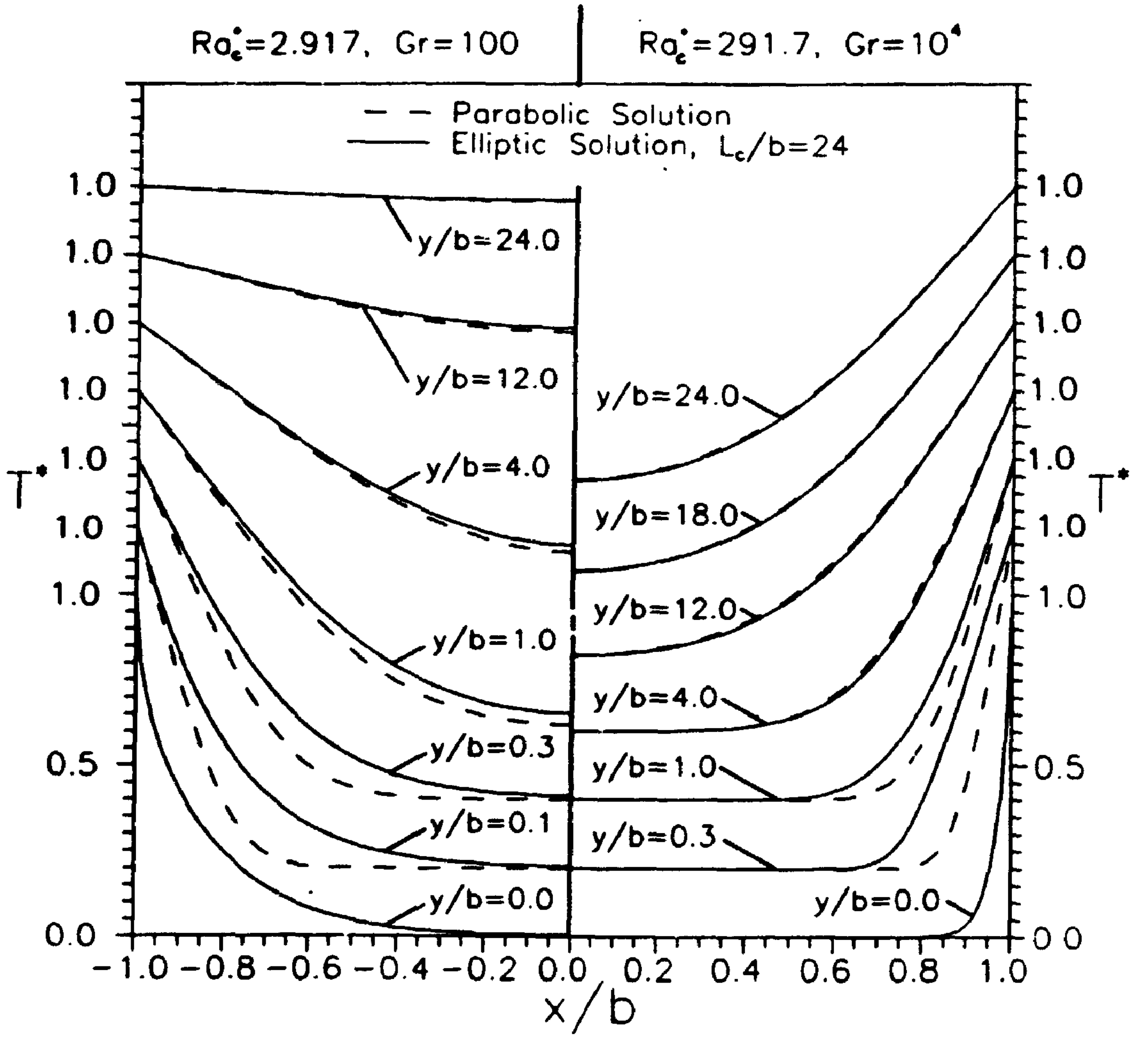

Figure 4.13: Comparison of temperature profiles from the present elliptic and parabolic solutions for $Ra_c^*=2.917$ and $Ra_c^*=291.7$.

the location of maximum velocity shifts away from the wall because of the presence of the separated flow. The next profile (y/b=1.0) is beyond the reattachment point; however, the flow near the wall is still recovering as evident by the low velocity gradient at the wall. At y/b=1.0, the location of maximum velocity is almost outside the thermal boundary-layer (see Fig. 4.13). The maximum at this location is a remnant from separation and is not buoyancy induced. Hence, the peak velocity diminishes to compensate for the buoyancy driven recovery of the flow closer to the wall. At y/b=4.0 the location of maximum velocity shifts to the centre line due to this compensation for the increasing flow near the wall. Farther up the channel ($y/b \geq 12$) the buoyancy driven flow near the wall dominates and the maximum velocity reappears near the wall. The peak velocity strengthens and shifts toward the centre line as the thermal boundary-layer penetrates farther across the channel.

The channel centre line pressure distributions for various values of Rayleigh number are displayed in Fig. 4.14. At low Rayleigh number, the parabolic and elliptic solutions are in fair agreement throughout the channel. However, at higher Rayleigh number there is a large difference near the channel entrance, which is due to entrance flow effects. At high Ra_c^* the fluid separation at the entrance has a "venturi" effect on the mainstream flow and causes a local reduction in pressure. Since the parabolic solution does not detect the inlet flow separation, it predicts higher pressures. Again, contrary to results presented by Nakamura et al. [40], it was found that the inlet pressure assumption ($p=-\rho v^2/2$) used in the parabolic solution is a reasonable approximation over a wide range of Rayleigh number.

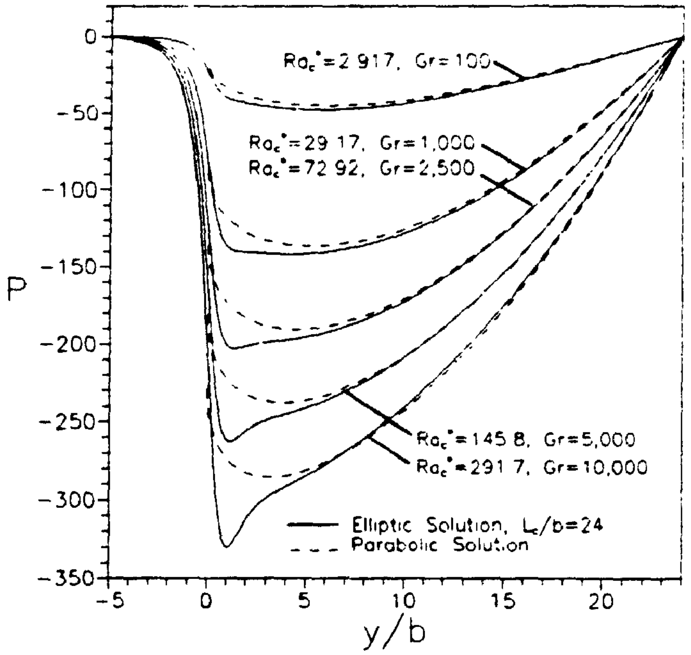

Figure 4.14: Comparison of centre line pressure distributions from the present elliptic and parabolic solutions.

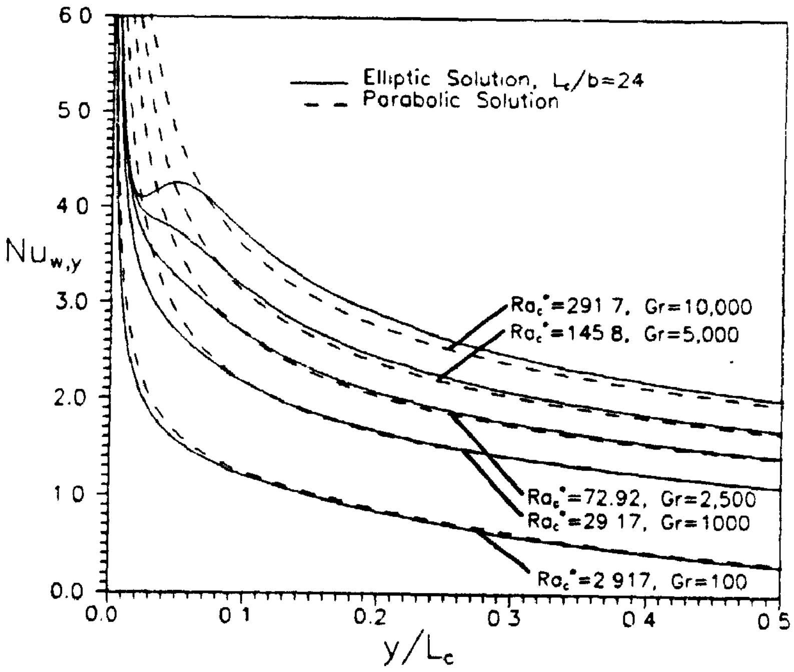

Figure 4.15: Comparison of local Nusselt number distributions from the present elliptic and parabolic solutions.

The fluid separation at the channel entrance has a adverse effect on local heat transfer. Figure 4.15 shows the local Nusselt number ($Nu_{w,y}$) distributions in the lower half of the channel for various values of Rayleigh number. At $Ra_c^*=2.917$, the fluid does not separate, and the local heat transfer distributions predicted by the parabolic and elliptic solutions are in good agreement. At higher Rayleigh number, the discrepancy near the leading edge becomes large due to the fluid separation. The recirculating eddy predicted by the elliptic solution has an insulating effect on the channel wall. For $Ra_c^*=291.7$, the elliptic solution shows a pronounced local minimum in $Nu_{w,y}$ near the entrance. At this location, the parabolic solution predicts a local Nusselt number that is 65% higher than the elliptic solution.

4.3 Concluding Remarks

Detailed comparisons of the parabolic and elliptic solutions show that an elliptic solution is necessary to get accurate local quantities, such as local heat transfer, near the channel entrance[1]. However, global quantities predicted by the elliptic and parabolic solutions (such as total flow and average Nusselt number) are in good agreement. Also, the present elliptic solution is not in agreement with previous elliptic solutions. The close agreement of the present elliptic and parabolic solutions casts doubt on the validity of the results of Nakamura et al. [40] and Kettleborough [39].

The results of this chapter have been published as a full paper in the ASME Journal of Heat Transfer (Naylor et al. [65]).

---

[1] Closer agreement with the parabolic solution would be expected for an elliptic solution with a rounded channel inlet.

CHAPTER 5

NUMERICAL RESULTS FOR DEVELOPING NATURAL CONVECTION IN A PARTIALLY DIVIDED CHANNEL

5.1 Introduction

Boundary-layer and full elliptic solutions to developing natural convection in a partially divided isothermal vertical channel have been obtained (for Pr=0.7). For practical reasons, the numerical calculations were restricted to the range of variables of most interest. For the parabolic (boundary-layer) solution, the range of variables considered was as follows:

Channel Rayleigh Number $0.1 \le Ra_c^* \le 10^4$
Plate Length Ratio $L_p/L_c = 0, 1/10, 1/3, 2/3, 1$
Plate Thickness $t/b = 0$
Vertical Plate Position $L_i/L_c = 0, (1-L_p/L_c)/2, 1-L_p/L_c$

The approximate parabolic solution requires much less computing resources than the full elliptic solution. Also, as shown in Chapter 4, the parabolic solution gives reasonable predictions for the overall Nusselt number. For this reason, most of the calculations presented in this chapter were made using the boundary-layer equations.

The full elliptic solution was obtained using the finite element code FIDAP [54]. From the results presented in Chapter 4, it is clear that a full elliptic solution is needed in order to get accurate local quantities near the leading and trailing edges of the plate, as well as near the channel entrance. For the full elliptic solution, the range of variables considered was as follows:

Channel Rayleigh Number $5.0 \leq Ra_c^* \leq 10^4$

Plate Length Ratio $L_p/L_c = 1/3$ (with $L_c/b=15$, $L_p/b=5$)

Plate Thickness $t/b= 0, 0.1, 0.2$

Vertical Plate Position $L_i/L_c= 0, (1-L_p/L_c)/2, 1-L_p/L_c$

The dividing plate was located on the channel centre line for all calculations. The three vertical locations of the plate, listed above, correspond to the bottom ($L_i/L_c=0$), middle ($L_i/L_c=(1-L_p/L_c)/2$), and top ($L_i/L_c=1-L_p/L_c$) of the channel. Most of the calculations were done with the plate located at the bottom of the channel ($L_i/L_c=0$), because this configuration was expected to give the highest heat transfer.

Initially in this chapter, a channel divided by a plate of zero-thickness ($t/b=0$) is studied (§5.2). Of course, any real dividing plate will have a finite thickness. In Section 5.3, the effect of small plate thicknesses ($t/b\leq 0.2$) is incorporated into the general understanding obtained in Section 5.2.

5.2 The Divided Channel with Plate Thickness t/b=0

The results for a zero-thickness plate show the limiting channel behaviour in the absence of blockage ($t/b \to 0$). Data for each vertical plate position are presented in Sections 5.2.1 and 5.2.2. Then in Section 5.2.3, the results for each vertical plate position are compared for one fixed plate length ratio ($L_p/L_c=1/3$). From the behaviour of the zero-thickness plate, most of the geometric influences on heat transfer are delineated.

5.2.1 Dividing Plate Located at Bottom of Channel - $L_i/L_c=0$, $(t/b=0)$

As will be shown in this chapter, the heat transfer from the dividing plate and the overall channel is the highest when the plate is located at the bottom of the channel. For this reason, the data for this geometry are likely of most practical engineering interest and are presented in the most detail.

Streamline and isotherm contours from the elliptic solution for a partially divided channel with a plate length ratio $L_p/L_c=1/3$ are shown in Fig. 5.1 ($L_i/L_c=0$, $t/b=0$). The appearance of the streamlines is similar to that of the undivided channel discussed in Chapter 4. At low Rayleigh number ($Ra_c^*=5$, Fig. 5.1(a)) the flow enters the channel smoothly, whereas separation occurs at the channel inlet for high Rayleigh number ($Ra_c^*=10^4$, Fig. 5.1(b)). For $L_p/L_c=1/3$, $L_c/b=15$, $L_i/L_c=0$, the elliptic solution predicts that separation occurs between $100 \leq Ra_c^* \leq 200$, as determined from the wall shear stress distribution. At $Ra_c^*=10^4$, the thermal boundary-layers look similar to those of isolated flat plates; however, the boundary-layers merge well before the channel exit. Also, the adverse effect of separation on the local heat transfer at the channel inlet can be seen from the isotherm contours.

Figures 5.2 and 5.3 show comparisons of the developing velocity and temperature profiles in the partially divided channel at low and high Rayleigh number: $Ra_c^*=10$, 10^4 ($L_p/L_c=1/3$, $L_i/L_c=0$, $t/b=0$). For the elliptic

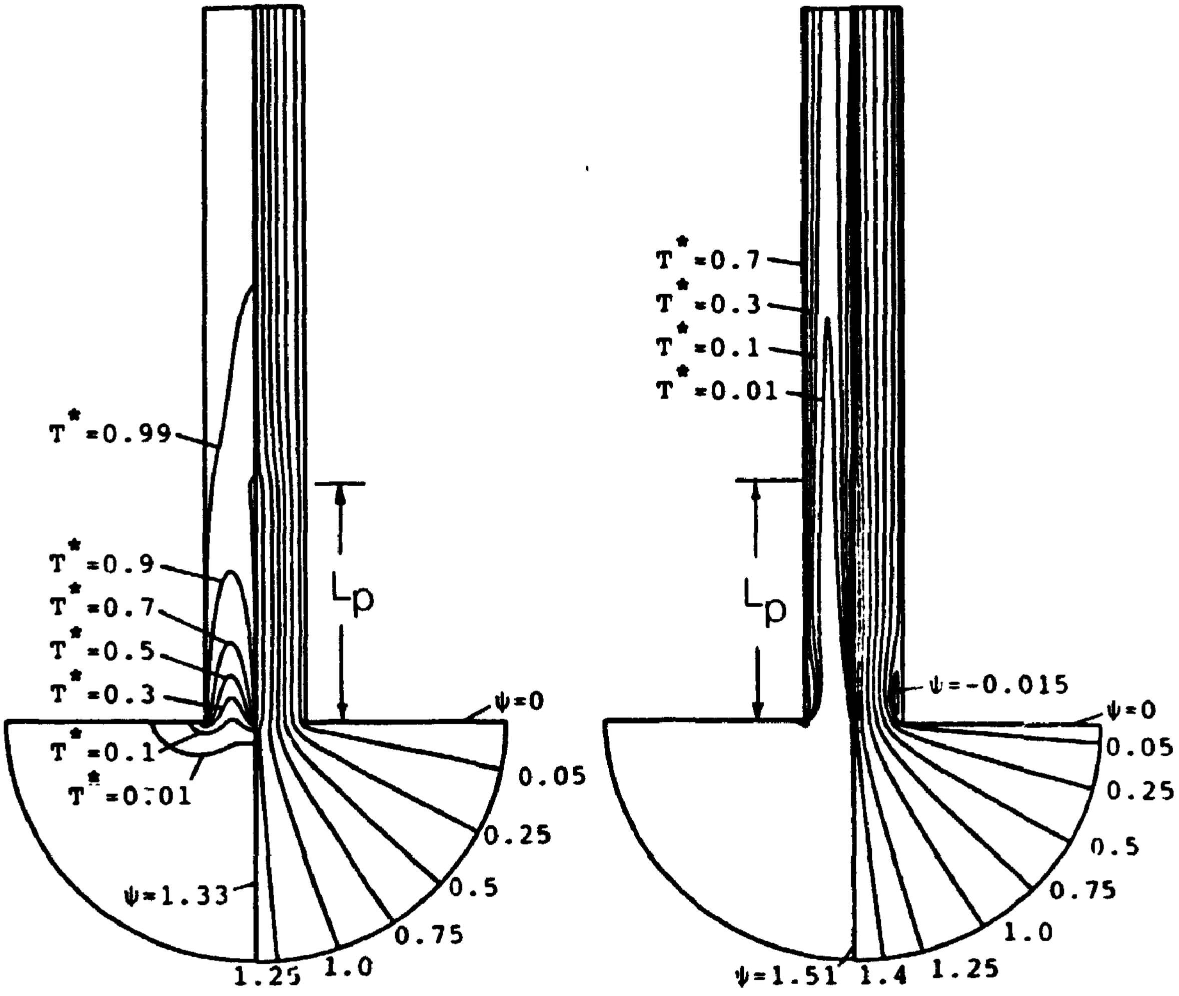

(a) $Ra_c^*=5$ **(b) $Ra_c^*=10^4$**

Figure 5.1: Streamline and isotherm contours for the divided channel with $L_p/L_c=1/3$, $t/b=0$, and $L_1/L_c=0$, (a) $Ra_c^*=5$, (b) $Ra_c^*=10^4$.

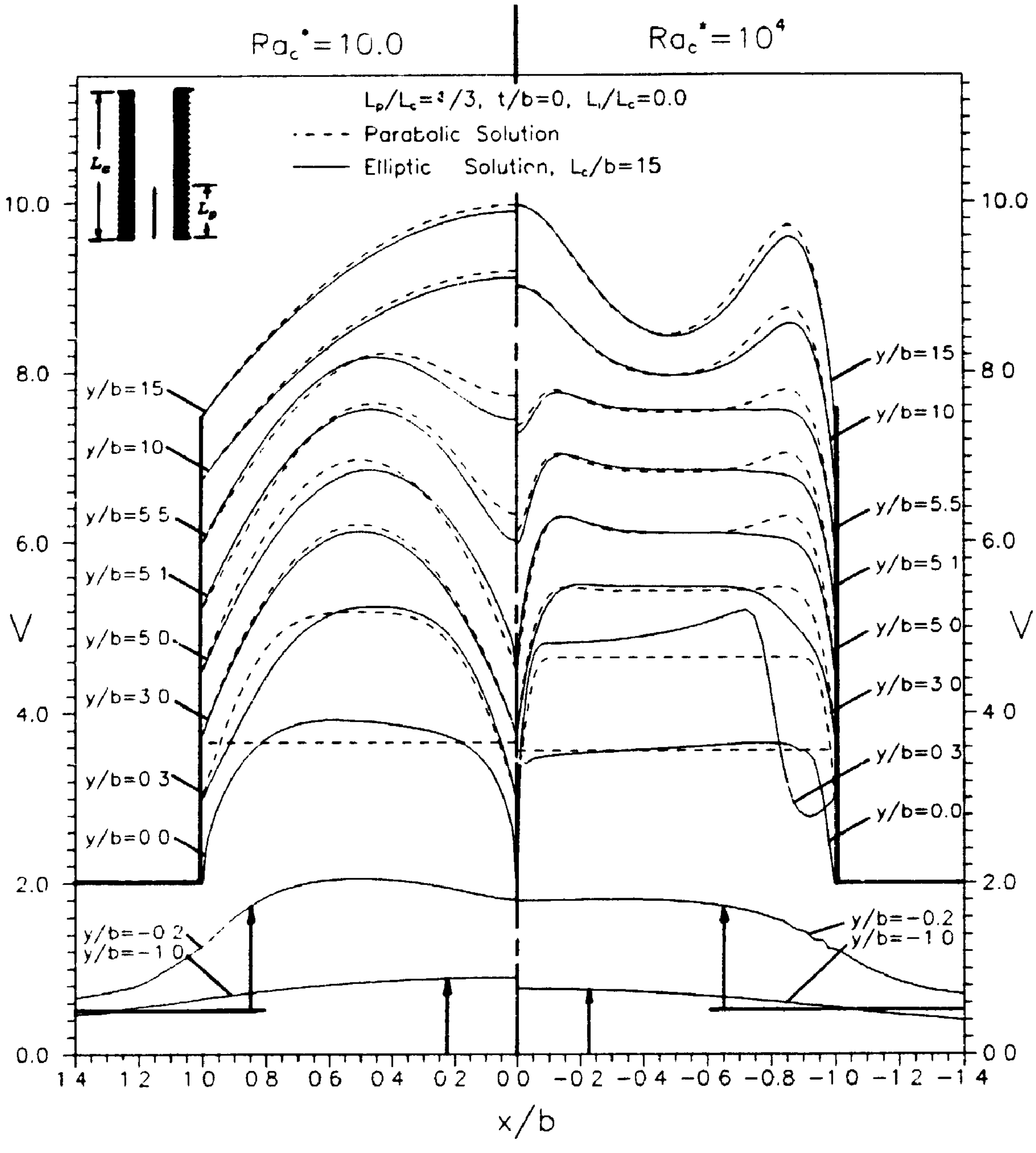

Figure 5.2: Comparison of the developing velocity profiles in the divided channel at low and high Rayleigh number, $Ra_c^*=10$, 10^4, for $L_p/L_c=1/3$, $L_i/L_c=0$, $t/b=0$.

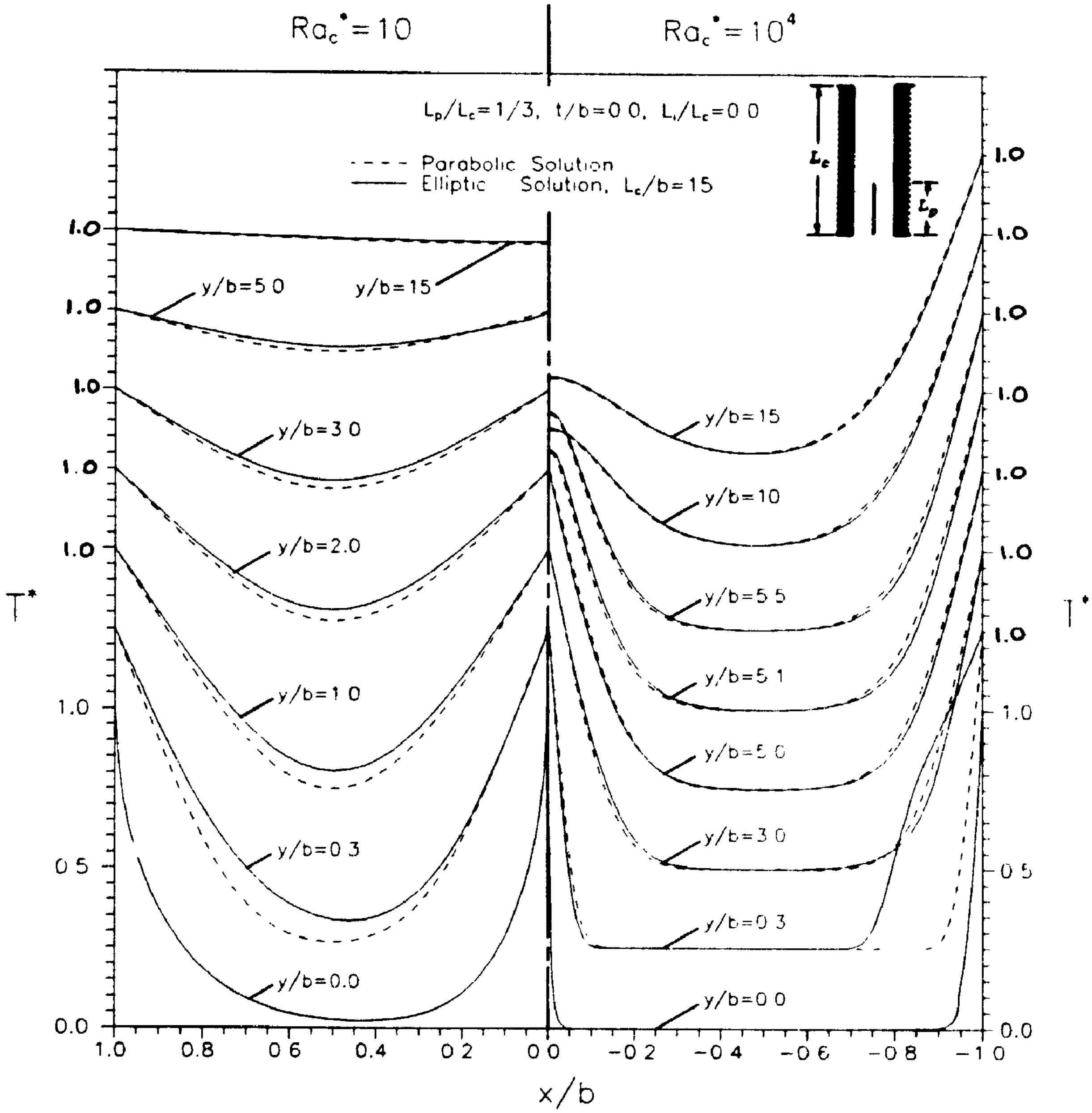

Figure 5.3: Comparison of the developing temperature profiles in the divided channel at low and high Rayleigh number, Ra_c^*=10, 10^4, for L_p/L_c=1/3, L_i/L_c=0, t/b=0.

solution, the velocity profiles outside the channel are also presented; for the parabolic solution the inlet profiles (y/b=0) are assumed to be uniform. The behaviour is similar to that for the undivided channel presented in Chapter 4; the parabolic solution differs substantially from the elliptic solution near the entrance and is in close agreement toward the channel exit. Note that because of the nature of the parabolic solution, the velocity and temperature profiles are perfectly symmetrical about the half-channel centre line, up to the end of the dividing plate (y/b=5). In contrast, the temperature and velocity profiles from the elliptic solution show substantial asymmetry at the channel entrance, particularly at high Rayleigh number because of separation.

The developing velocity profiles for $Ra_c^*=10^4$ shown in Fig. 5.2 show several interesting features. Strong reverse flow in the separated flow region near the channel entrance (y/b=0.3) is clearly shown. At the end of the plate (y/b=5.0), the velocity is a maximum near the plate because of the locally high buoyancy force in the plate's thermal boundary-layer. Similarly, near the channel exit, high local buoyancy forces produce a maximum velocity near the channel wall and a global maximum velocity in the plume above the plate.

Beyond the channel entrance, the temperature profiles from both solution methods are in excellent agreement at both high and low Rayleigh number (see Fig. 5.3). At $Ra_c^*=10$, the temperature field is almost fully developed ($T^*=1.0$) by the end of the dividing plate (y/b=5). At $Ra_c^*=10^4$, the temperature profile is still developing at the channel exit plane. In fact, the temperature of the fluid near the channel centre line above the plate decreases toward the channel exit; heat is transferred from the hot plume above the plate to the cooler fluid near the centre of the half-channel.

The variation of dividing plate average Nusselt number (Nu_p) with plate Rayleigh number (Ra_p^*) for several plate length ratios is shown in Fig. 5.4 ($t/b=0$). The close agreement of the parabolic and elliptic solutions for $L_p/L_c=1/3$ gives confidence in the accuracy of both numerical results. At low Rayleigh number, the plate Nusselt number approaches the closed form expression for the fully developed Nusselt number (equation 3.19). With increasing Rayleigh number, average Nusselt numbers well above those for a single isolated plate are predicted. For example, the plate Nusselt number for $L_p/L_c=1/10$ is about two times higher than the isolated plate Nusselt number at $Ra_p^*=100$.

In Fig. 5.4 it can be seen that the length of the channel walls greatly influences the heat transfer from the plate. Consider a channel with a dividing plate of fixed length. For this channel, Fig. 5.4 shows that extending the channel walls above the plate (decreasing L_p/L_c), while holding Ra_p^* constant, gives substantial heat transfer enhancement for the plate over the full range of Rayleigh number. For $L_p/L_c=1/10$, at low Rayleigh number there is a 300% increase in plate Nusselt number compared to $L_p/L_c=1$; at $Ra_p^*=10^4$ there is approximately a 55% enhancement for $L_p/L_c=1/10$ compared to $L_p/L_c=1$. Extension of the channel walls beyond $L_p/L_c=1/10$ is of little practical significance. However, calculations were made for $L_p/L_c=1/100$ to confirm that the numerical results approach a fully developed limit close to that for $L_p/L_c=0$ for small plate length ratios.

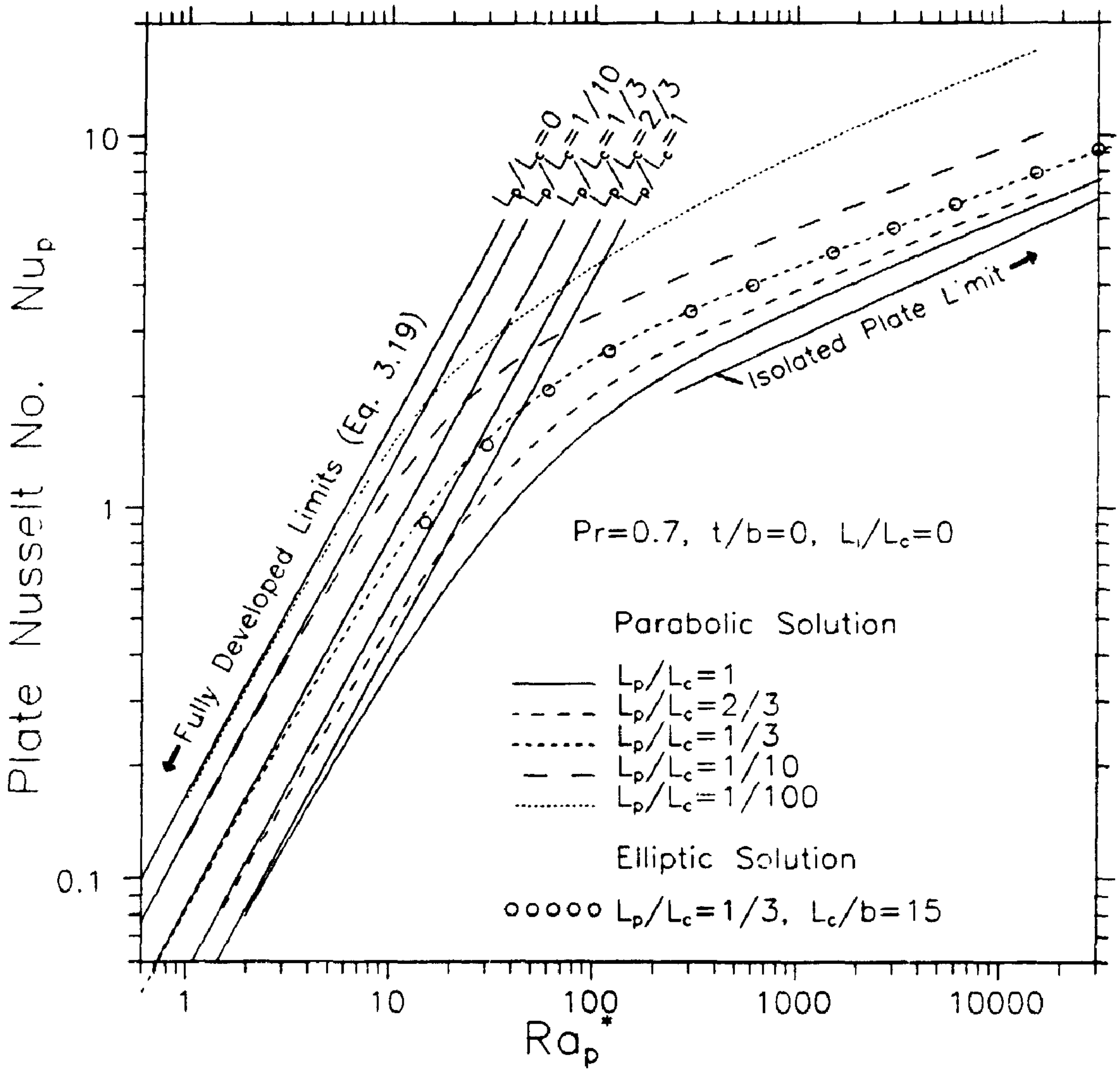

Figure 5.4: Variation of the plate average Nusselt number (Nu_p) with Rayleigh number (Ra_p^*) for several plate length ratios and $L_i/L_c=0$, (t/b=0).

Quantifying the heat transfer enhancement for the dividing plate was a large part of the motivation for this study. For this reason, additional calculations were made to clarify the plate average Nusselt number behaviour. For the parabolic equations, calculations were made holding Ra_p^* constant and varying the plate length ratio over the range $1/10 \leq L_p/L_c \leq 1$ for $L_i/L_c=0$, $(t/b=0)$. Calculations were done for $Ra_p^*=10^{-1}$, 10^2, 10^4. The results are shown in Fig. 5.5. Note that the plate Nusselt number has been normalized by dividing by the Nusselt number when the plate and channel walls are the same length ($L_p/L_c=1$). Again, consider a channel with a dividing plate of fixed length. This figure shows that extending the channel walls above the plate (decreasing L_p/L_c) causes the largest chimney effect at low Rayleigh number i.e., at the fully developed limit. With increasing Rayleigh number, the heat transfer enhancement caused by the chimney effect diminishes. In the limit as $Ra_p^* \rightarrow \infty$, the plate and confining walls act as isolated plates and there is no enhancement.

Figure 5.6 shows a comparison of the plate local Nusselt number distributions from the elliptic and parabolic solutions for $L_p/L_c=1/3$ at several values of Rayleigh number ($L_i/L_c=0$, $t/b=0$). At low Rayleigh number, the distributions predicted by both numerical methods are in excellent agreement. At high Rayleigh number, the results differ substantially because of flow separation at the channel inlet. For the elliptic solution, there is a separated flow region next to the wall at the channel inlet (see Fig. 5.1(b)). The separated flow reduces the cross-section for the flow at the entrance, causing the fluid velocity near the leading edge of the dividing plate to be higher than in the absence of separation. The higher velocities cause increased heat transfer near the

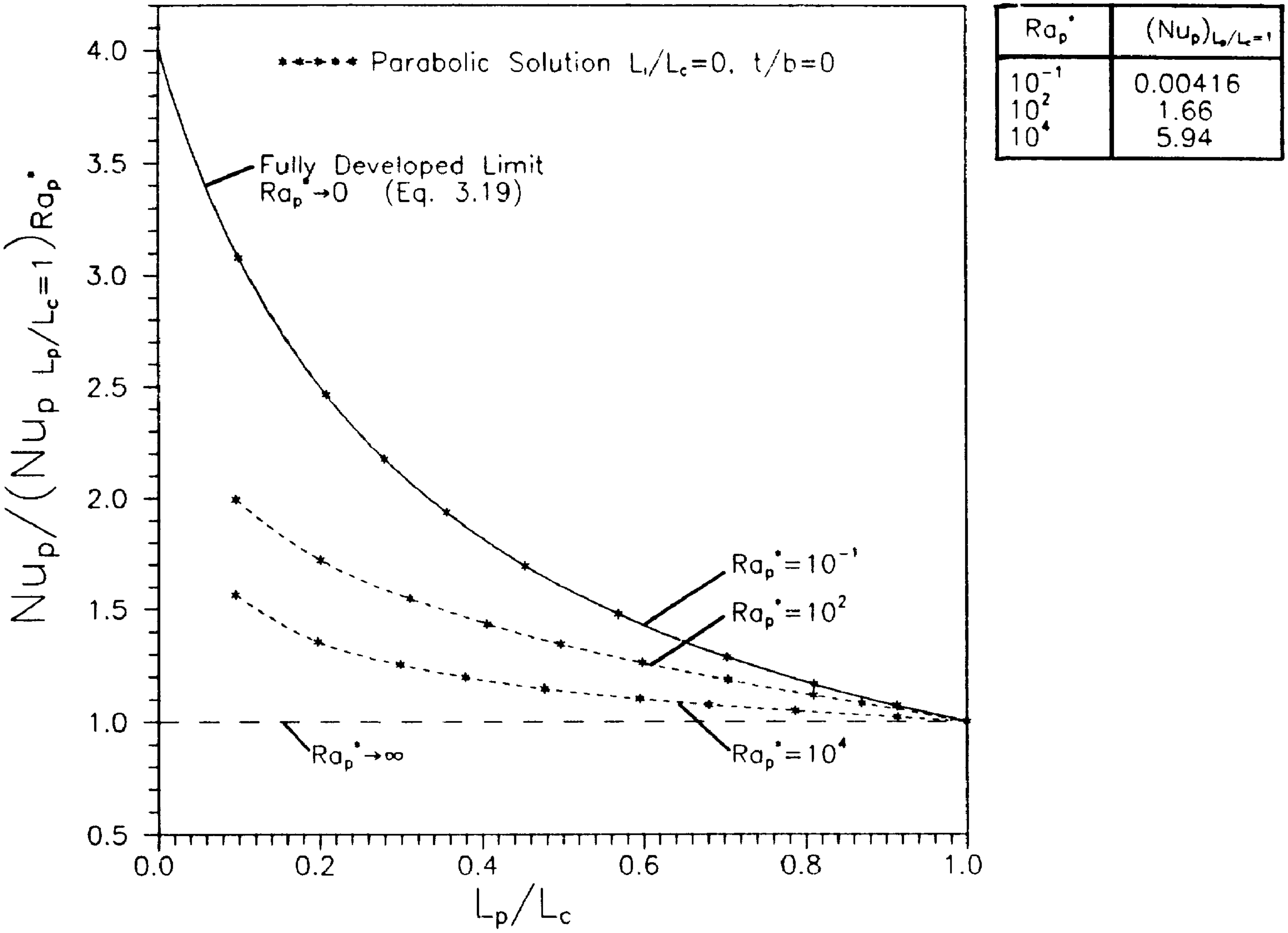

Ra_p^*	$(Nu_p)_{L_p/L_c=1}$
10^{-1}	0.00416
10^2	1.66
10^4	5.94

Figure 5.5: Effect of plate length ratio L_p/L_c on the plate average Nusselt number (Nu_p) for $L_i/L_c=0$, ($t/b=0$).

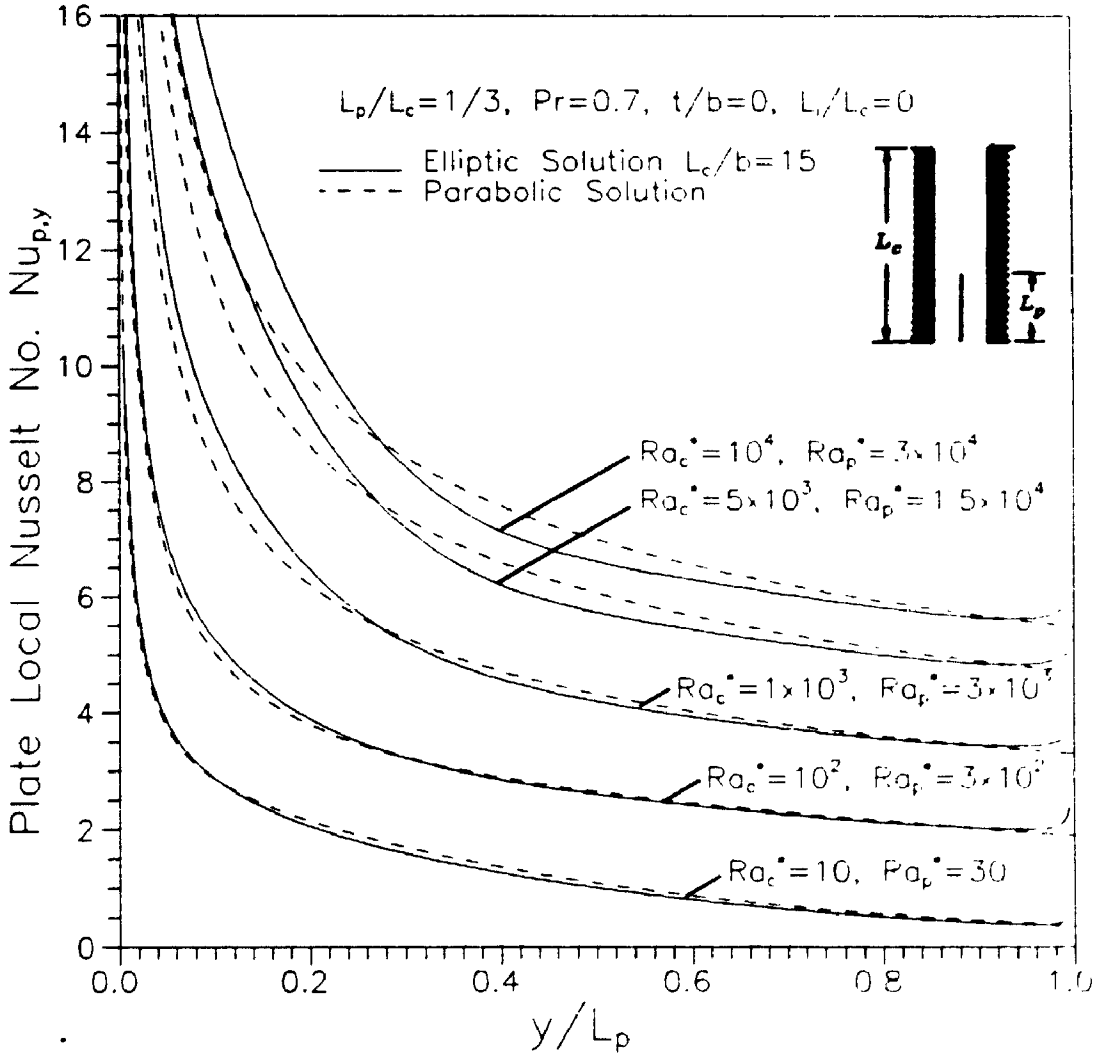

Figure 5.6: The plate local Nusselt number distribution for $L_i/L_c=0$ and $L_p/L_c=1/3$, (t/b=0).

leading edge of the plate for the elliptic solution.

Although a minor effect, it is interesting that the elliptic solution predicts that the plate local Nusselt number increases slightly near the trailing edge of the plate. The slight increase in heat transfer in this region can be explained by examining the streamline contours shown in Fig. 5.1. It can be seen that the streamlines are disturbed by the undivided section of the channel *upstream* of the end of the plate. The streamlines start to bend toward the channel centre line just before the end of the plate. As the fluid moves toward the centre line, it brings cool fluid closer to the plate surface, causing the plate local Nusselt number to increase. The parabolic solution cannot predict this phenomena; by the nature of the approximate equations, downstream changes cannot affect the upstream solution.

Figure 5.7 shows the variation of the average wall Nusselt number with channel Rayleigh number for several plate length ratios (L_i/L_c=0, t/b=0). At high Rayleigh number, the wall Nusselt number is only weakly dependent upon the plate length ratio. By a small margin, the plate length ratio L_p/L_c=1 gives the highest Nusselt number at $Ra_c^*=10^4$. The behaviour is completely opposite at low Rayleigh number; the Nusselt number is highly dependent upon the plate length ratio and L_p/L_c=1 gives the *lowest* Nusselt number. The wall Nusselt number predicted by the elliptic solution (for L_p/L_c=1/3) is in fair agreement with the parabolic data. Both sets of data have the same trend; however, the elliptic solution gives wall Nusselt numbers about ten percent lower than the parabolic solution.

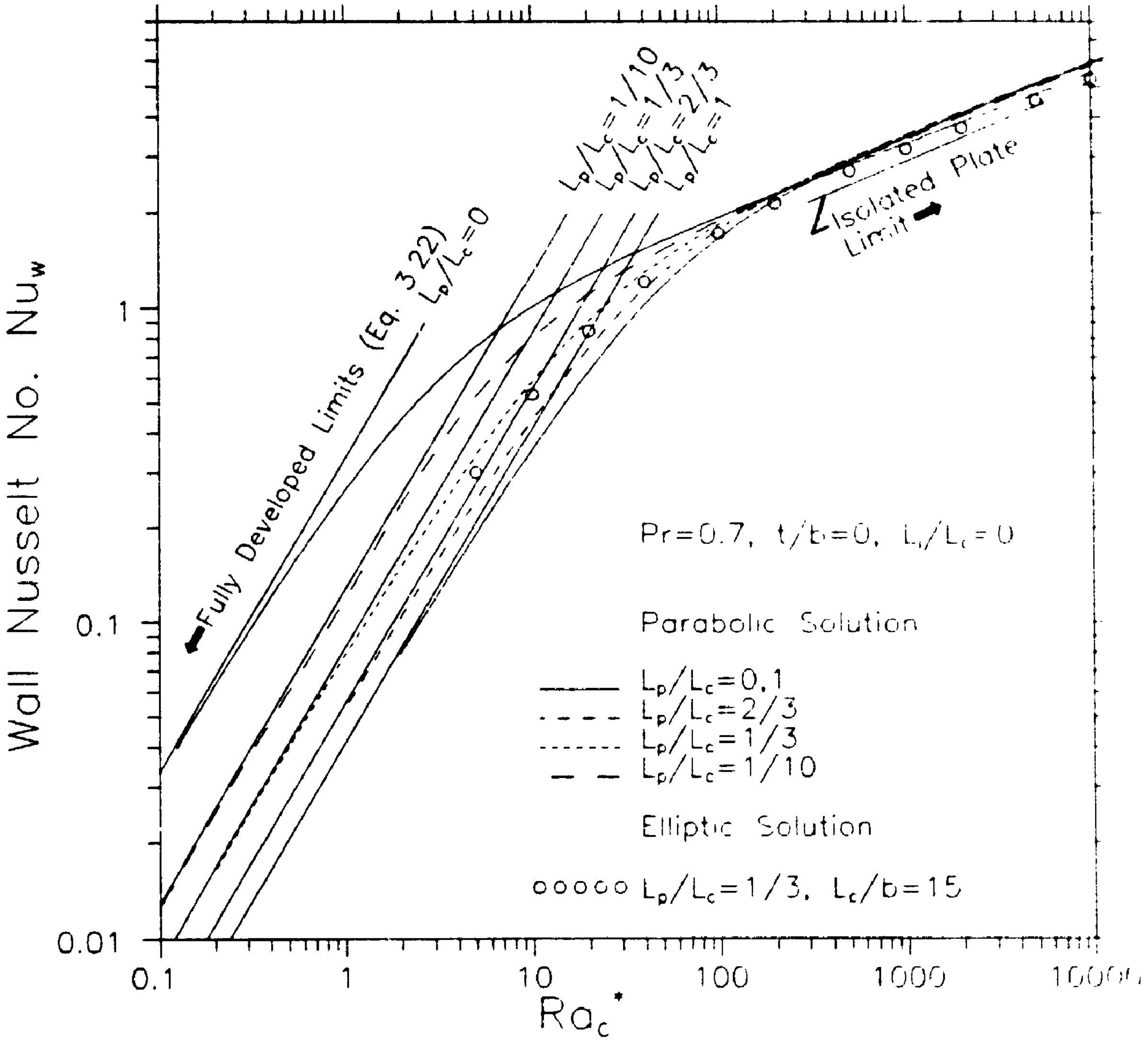

Figure 5.7: Variation of the wall average Nusselt number (Nu_w) with Rayleigh number (Ra_c^*) for several plate length ratios and $L_i/L_c=0$, (t/b=0).

An important feature shown in Fig. 5.7 is the large decrease in the wall Nusselt number for L_p/L_c=1/10 compared to the undivided channel (L_p/L_c=0) at low Rayleigh number. The decrease can be explained as follows: if the dividing plate length is greater than or equal to the thermal developing length, then approximately one half of the heat transfer will be contributed by the dividing plate and the heat transfer from the channel walls will decrease proportionately. At low Rayleigh number the flow becomes thermally fully developed within a short distance from the channel inlet. As a result, even a short dividing plate will cause the wall Nusselt number to be reduced by about a factor of two at low Rayleigh number.

Figure 5.8 shows a comparison of the wall local Nusselt number distributions from the elliptic and parabolic solutions for L_p/L_c=1/3 at several values of Rayleigh number (L_i/L_c=0, t/b=0). Again, at low Rayleigh number the flow does not separate at the inlet and both numerical predictions are in close agreement. Similar to the undivided channel (Chapter 4), the flow separation in the partially divided channel has an adverse effect on the wall local heat transfer. For $Ra_c^* \geq 10^3$, there is a pronounced minimum in the local heat transfer distribution near the channel inlet. With increasing Rayleigh number, the separated flow gets stronger and larger causing the local minimum value of Nusselt number to decrease. At $Ra_c^*=10^4$, the local Nusselt number is about four times lower than predicted by the parabolic solution.

In Fig. 5.8, each wall Nusselt number distribution predicted by the parabolic solution has a discontinuity at the location of the end of the plate, y/L_c=1/3. For L_i/L_c>0, similar discontinuities also occur at the

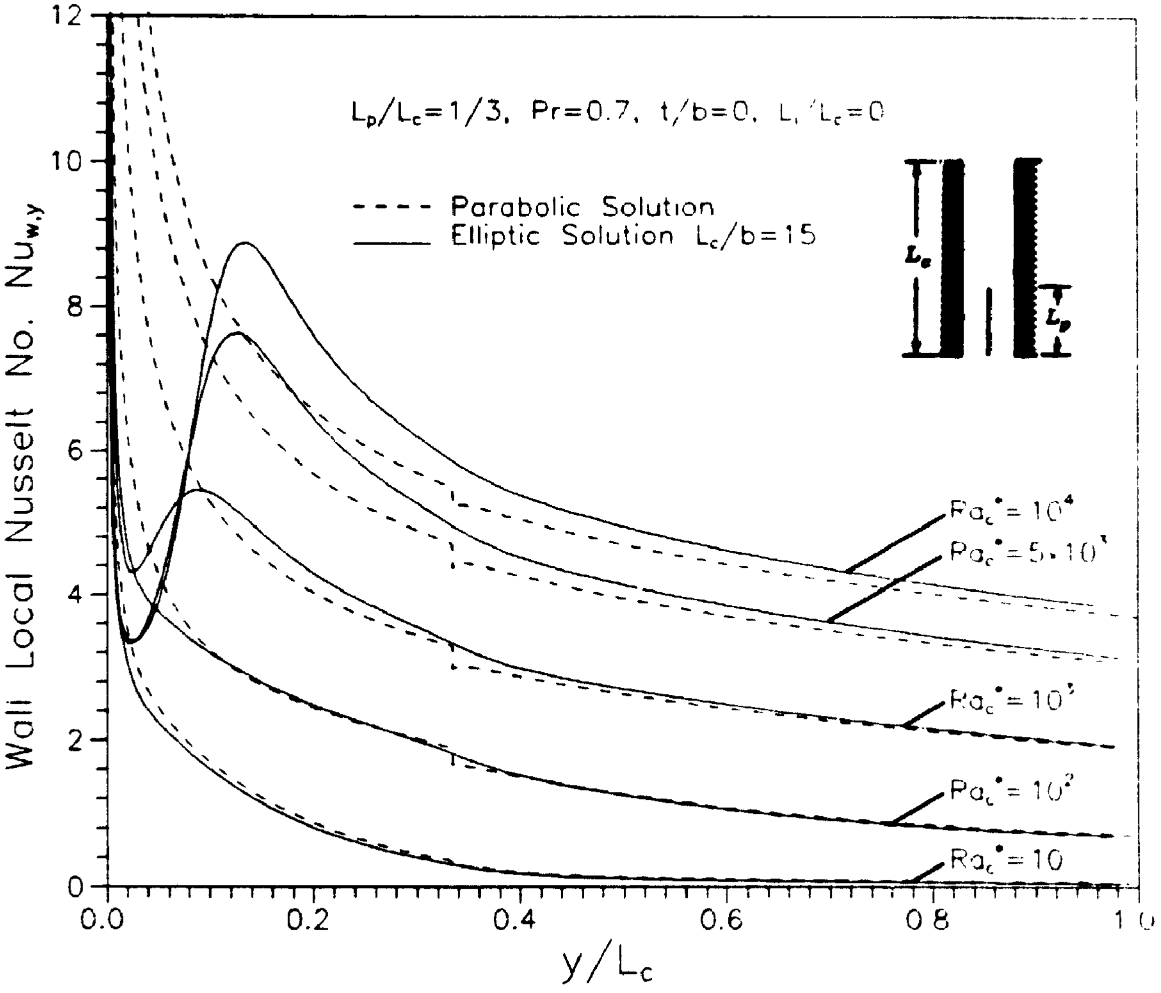

Figure 5.8: The wall local Nusselt number distribution for $L_i/L_c=0$ and $L_p/L_c=1/3$, $(t/b=0)$.

location of the leading edge of the plate (see Fig. 5.17). Several checks, including hand calculations for low grids, were performed to confirm that the discontinuity was not caused by a programming error. It was concluded that the discontinuity is caused by the singularity at the end of the plate and the nature of the approximate parabolic equations. The parabolic equations are solved using a forward marching method. Hence, downstream changes cannot influence the upstream solution. During the forward marching procedure, when the end of the plate is reached, the temperature, no-slip, and impermeability boundary conditions on the plate are changed to symmetry boundary conditions on the channel centre line. This instantaneous change in boundary conditions causes the numerical discontinuity in local heat transfer. For the same reason, an instantaneous change in pressure gradient also occurs (see Fig. 5.11 and Fig. 5.20). Within about two steps in the y direction from the end of the plate, the numerical solution rapidly adjusts for the newly imposed boundary conditions.

Although the numerical results from the parabolic solution are not accurate close to the singularity points, the results downstream recover the correct flow and temperature field characteristics. This is confirmed by the comparison of the temperature and velocity profiles with the elliptic solution (Fig. 5.2, Fig. 5.3) and also by the fact that the average Nusselt numbers are in close agreement with the elliptic solution. Further, it has been checked by numerical integration that the total fluid momentum and bulk temperature are continuous at the leading and trailing edge of the plate for the parabolic solution.

The variation of the overall channel Nusselt number and induced flow rate with channel Rayleigh number is shown in Fig. 5.9 and Fig. 5.10 (L_i/L_c=0, t/b=0). Again, the numerical data approaches the closed form expressions for fully developed flow. The fully developed channel Nusselt number and flow rate are independent of the vertical position of the dividing plate. At low Rayleigh number, the buoyancy force is maximized because the dimensionless bulk fluid temperature is approximately T^*=1.0 throughout the channel. Hence, the induced flow rate and heat transfer decreases with increasing L_p/L_c because of the higher viscous resistance in the divided section of the channel. Also, the additional surface area of the dividing plate causes a further reduction in the channel average Nusselt number. Contrary to the low Rayleigh number behaviour, at $Ra_c^*=10^4$ the undivided channel (L_p/L_c=0) gives the *lowest* Nusselt number. At high Rayleigh number, the addition of a dividing plate increases the bulk fluid temperature in the channel. The higher bulk temperature causes a greater induced flow rate (see Fig. 5.10) and therefore greater heat transfer. Note also that the isolated plate Nusselt number for the divided channel is a function of the plate length ratio and is described by equation (3.30) (see Chapter 3, Section 3.3). For the specific plate length ratios considered, L_c/L_c=1/3 gave the highest average channel Nusselt number at $Ra_c^*=10^4$.

Channel pressure distributions for the elliptic and parabolic solutions are shown in Fig. 5.11 (for L_p/L_c=1/3 L_i/L_c=0, t/b=0). The pressure distributions have been taken along a line half way between the plate and the channel wall (x/b=0.5). These pressure distributions are very similar to those of the undivided channel (see Fig. 4.14). Notice that the parabolic solution gives a discontinuity in the pressure gradient. For the elliptic

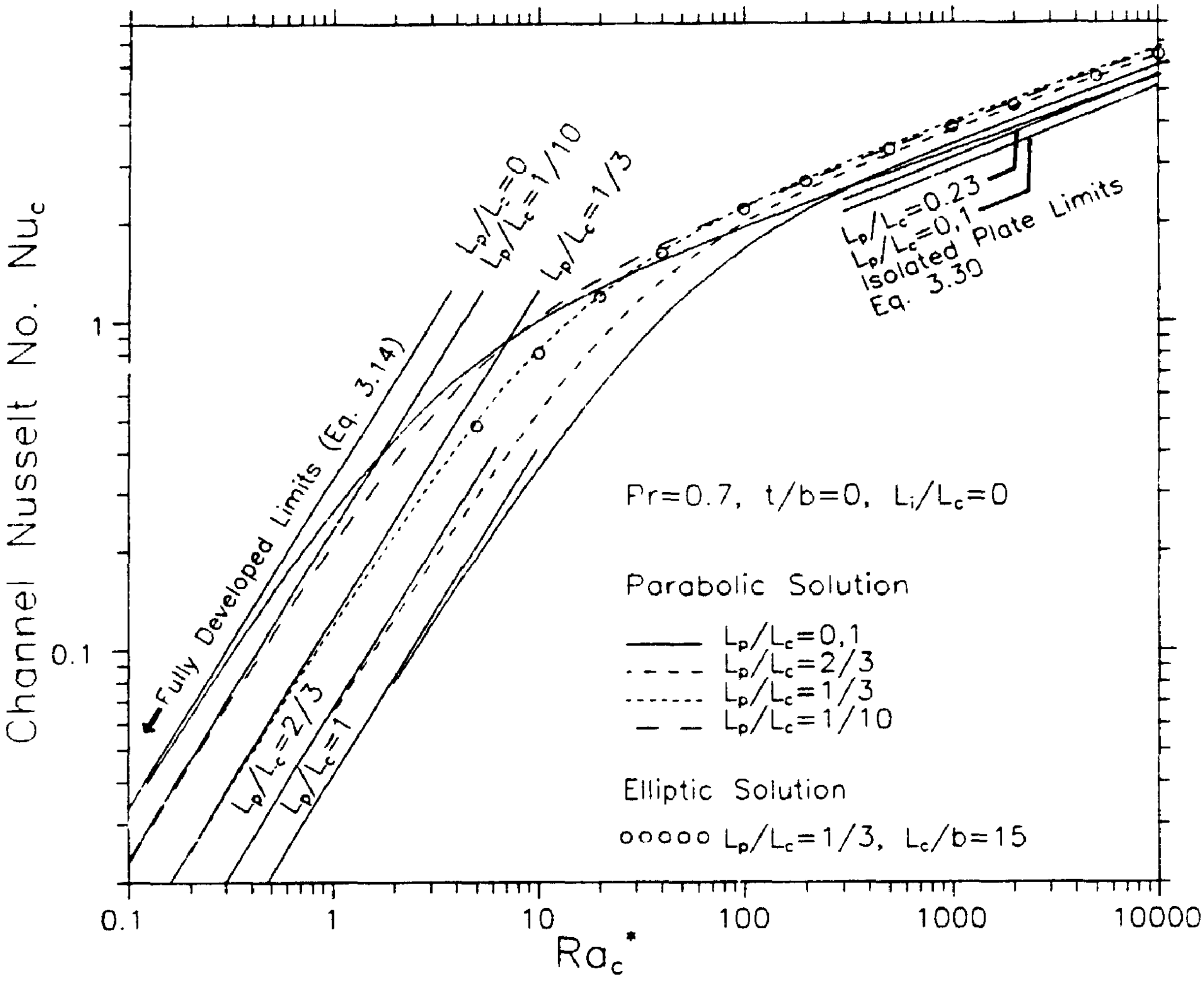

Figure 5.9: Variation of the channel average Nusselt number (Nu_c) with Rayleigh number (Ra_c^*) for several plate length ratios and $L_i/L_c=0$, ($t/b=0$).

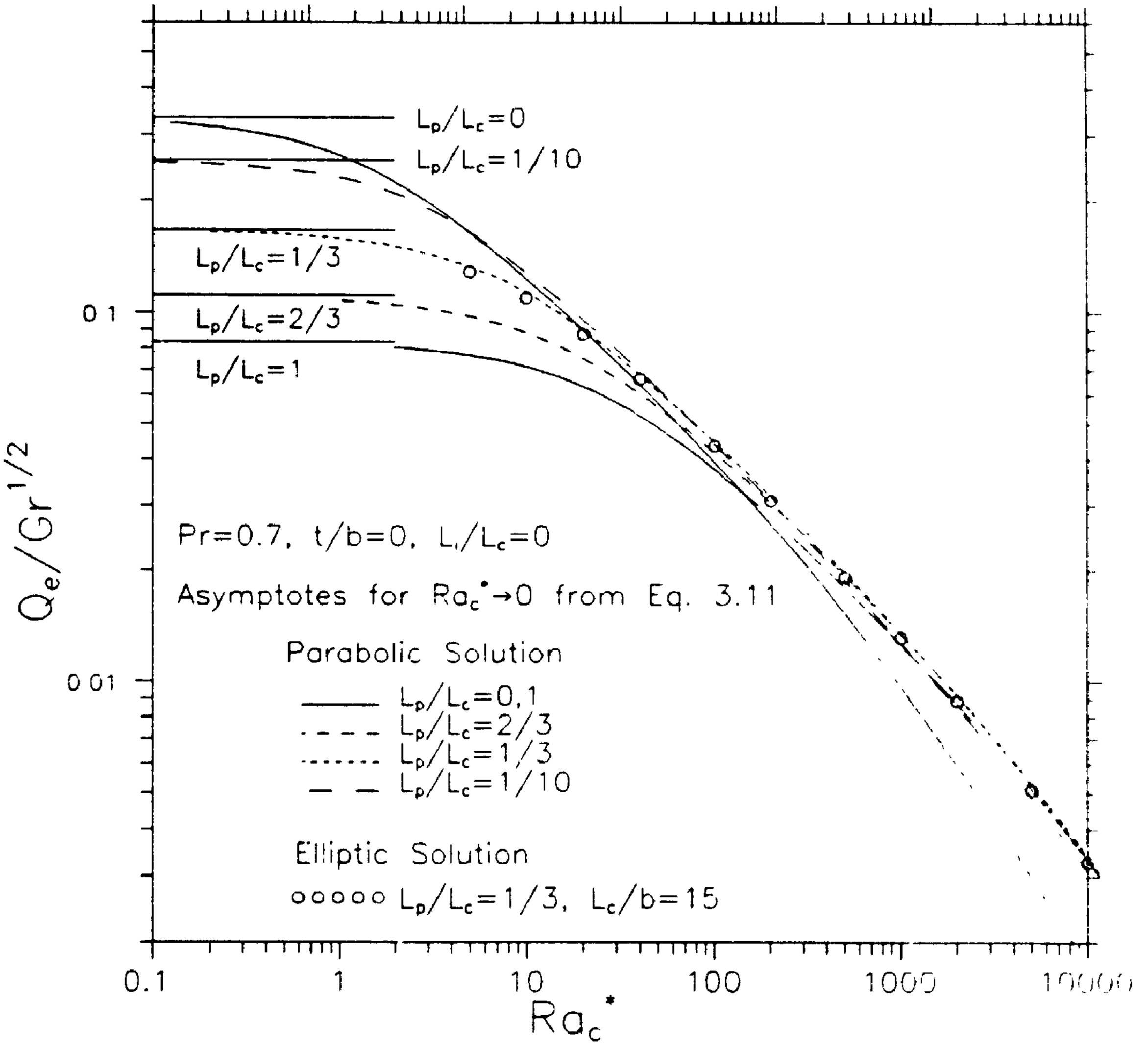

Figure 5.10: Variation of the dimensionless induced flow rate with Rayleigh number (Ra_c^*) for several plate length ratios and $L_i/L_c=0$,(t/b=0).

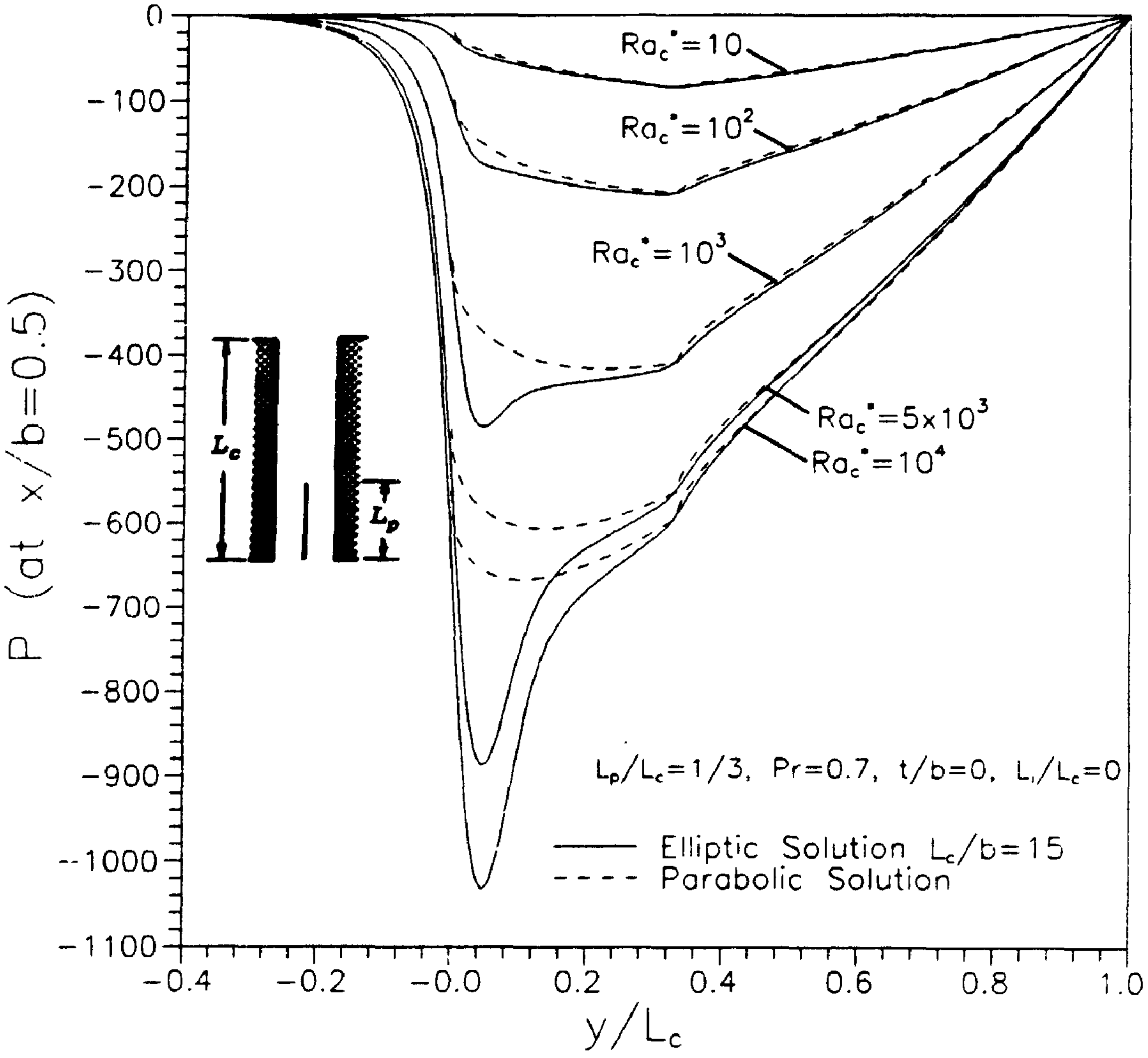

Figure 5.11: The channel pressure distribution at several values of Rayleigh number for $L_p/L_c=1/3$ and $L_i/L_c=0$,(t/b=0).

solution, the flow upstream of the end of the plate senses the change in boundary conditions so that the change in pressure gradient occurs smoothly. Except at low Rayleigh number, the pressure just inside the channel entrance is much lower for the elliptic solution. As mentioned in Chapter 4, at high Ra^* the fluid separation at the entrance has a "venturi" effect on the mainstream flow and causes a local reduction in pressure. Since the parabolic solution does not detect the inlet flow separation, it predicts higher pressures near the inlet. With the exception of the pressure near the separated region, the distributions are in excellent agreement.

Table 5.1 shows a comparison of the major data from the parabolic and elliptic solutions for $L_p/L_c=1/3$, $L_i/L_c=0$, $t/b=0$. The agreement of the two solutions is typically within five percent for the plate average Nusselt number, the channel average Nusselt number and induced flow rate. The wall average Nusselt numbers predicted by the elliptic solution are about ten percent lower than those from the parabolic solution; the difference at high Rayleigh number may, in part, be caused by separation at the inlet for the elliptic solution; separation reduces the heat transfer near the channel inlet. A more complete listing of the numerical data is given in Appendix D.

In summary, the results show that careful consideration must be given to the Rayleigh number range in order to achieve heat transfer enhancements from geometric effects. For example, consider adding a dividing plate at the entrance of a previously undivided channel. As shown in Fig. 5.7 and Fig. 5.9, at low Rayleigh number the addition of the plate severely reduces

Table 5.1: Comparison of major data from the parabolic and elliptic solutions for $L_p/L_c=1/3$, $L_i/L_c=0$ (bottom), t/b=0, Pr=0.7.

Plate Average Nusselt Number - Nu_p

Ra_c^*	Ra_p^*	Parabolic Soltn Nu_p	Elliptic Soltn Nu_p	% Difference
5	15	0.9792	0.9127	6.8
10	30	1.5350	1.4762	3.8
100	300	3.4006	3.3883	0.36
1,000	1,000	5.6539	5.6531	0.014
5,000	15,000	7.8968	7.9529	-0.71
10,000	30,000	9.0711	9.1578	-0.96

Wall Average Nusselt Number - Nu_w

Ra_c^*	Ra_p^*	Parabolic Soltn Nu_w	Elliptic Soltn Nu_w	% Difference
5	15	0.3389	0.3008	11.2
10	30	0.5874	0.5316	9.5
100	300	1.8384	1.7248	6.2
1,000	1,000	3.4678	3.1738	8.5
5,000	15,000	5.0523	4.5088	10.7
10,000	30,000	5.9254	5.2589	11.2

Channel Average Nusselt Number - Nu_c

Ra_c^*	Ra_p^*	Parabolic Soltn Nu_c	Elliptic Soltn Nu_c	% Difference
5	15	0.4990	0.4820	3.4
10	30	0.8244	0.8020	2.7
100	300	2.2290	2.1978	1.4
1,000	1,000	4.0145	3.8848	3.2
5,000	15,000	5.7635	5.4975	4.6
10,000	30,000	6.7119	6.3823	4.9

Half Channel Induced Flow Rate ($Q_p=Q_s/Gr^{1/4}$)

Ra_c^*	Ra_p^*	Parabolic Soltn Q_p	Elliptic Soltn Q_p	% Difference
5	15	0.13347	0.12887	3.4
10	30	0.11315	0.10966	3.1
100	300	0.44630E-1	0.43516E-1	2.5
1,000	1,000	0.13563E-1	0.13146E-1	3.1
5,000	15,000	0.52745E-2	0.51001E-2	3.3
10,000	30,000	0.33658E-2	0.32640E-2	3.0

the heat transfer from the walls and channel as a whole. However, as shown in Fig. 5.7, above $Ra_c^* \approx 200$ the channel wall Nusselt number is almost independent of L_p/L_c, i.e., the wall heat transfer is independent of the presence of a dividing plate. So, for $Ra_c^*>200$, plate average Nusselt numbers well above the single isolated plate limit can be achieved without adversely affecting the heat transfer from the confining walls.

5.2.2 Dividing Plate Located in the Middle and Top of the Channel - $L_1/L_c=1-L_p/L_c$, $L_1/L_c=(1-L_p/L_c)/2$, (t/b=0)

The results for the plate in the middle and top of the channel are presented in less detail than those for the plate in the bottom of the channel. Average Nusselt number trends are of primary interest. Only the most illustrative local data are presented graphically. Data not shown are available from the author upon request.

Figures 5.12 and 5.13 show the variation of the plate average Nusselt number (Nu_p) with plate Rayleigh number (Ra_p^*) for $L_1/L_c=(1-L_p/L_c)/2$, and $L_1/L_c=1-L_p/L_c$, (t/b=0). In both figures there is close agreement of the parabolic and elliptic solutions for $L_p/L_c=1/3$. The plate average Nusselt number trends are much different from the trends when the plate is located in the bottom of the channel (see Fig. 5.4). At low Rayleigh number only the data for $L_p/L_c=1.0$ approaches a limiting fully developed asymptote. Also, extending the channel walls, while holding L_p and Ra_p^* constant, *decreases* the plate heat transfer at low Ra_p^*. This rapid decrease in the plate heat transfer for $L_p/L_c<1.0$ at low Rayleigh number can be understood by considering the thermal developing length. At low

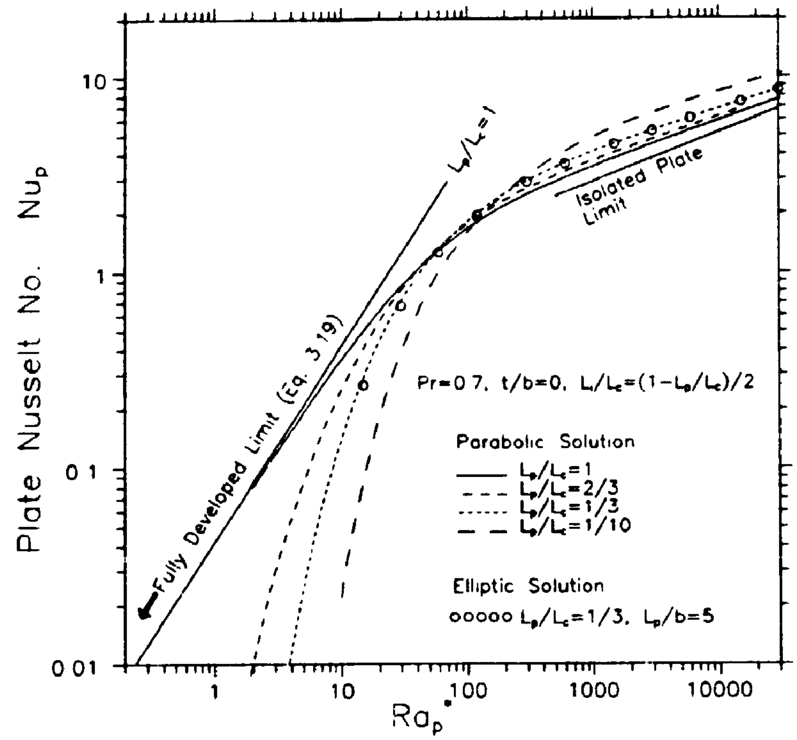

Figure 5.12: Variation of the plate average Nusselt number (Nu_p) with Rayleigh number (Ra_p^*) for several plate length ratios and $L_i/L_c=(1-L_p/L_c)/2$,($t/b=0$).

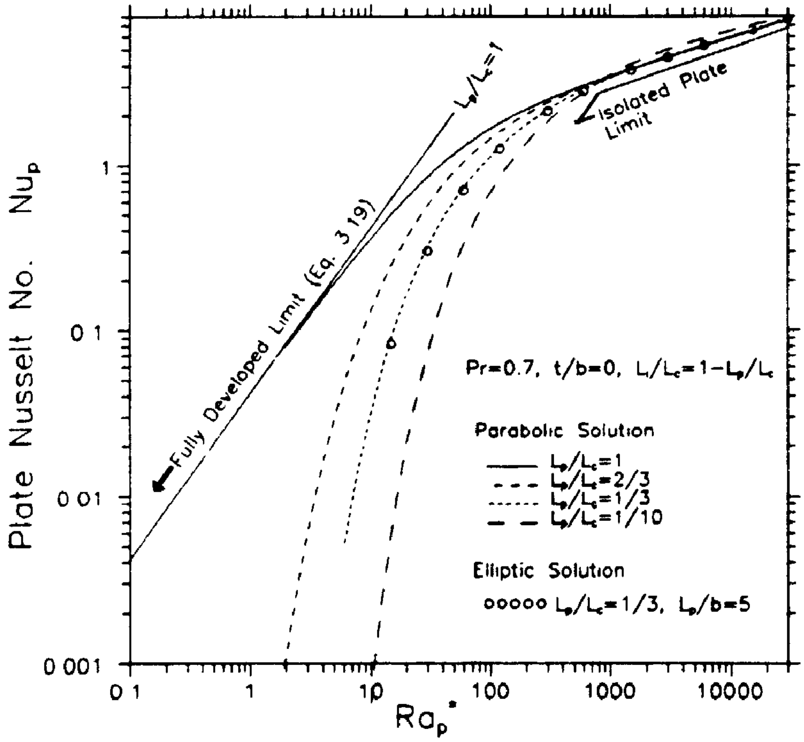

Figure 5.13: Variation of the plate average Nusselt number (Nu_p) with Rayleigh number (Ra_p^*) for several plate length ratios and $L_i/L_c=1-L_p/L_c$,($t/b=0$).

Rayleigh number, extending the channel walls causes the flow to be more thermally developed when it reaches the plate. Eventually, as the walls are extended further, the flow becomes thermally fully developed before reaching the leading edge of the plate and the heat transfer from the plate drops rapidly to almost zero.

Figure 5.14 shows a comparison of the plate local Nusselt number distributions from the elliptic and parabolic solutions for $L_p/L_c=1/3$ and $L_i/L_c=(1-L_p/L_c)/2$, at several values of Rayleigh number (t/b=0). Unlike the plate local Nusselt data for the case of $L_i/L_c=0$ (Fig. 5.6), the elliptic and parabolic solutions are in very close agreement over the entire range of Rayleigh number. Note that the differences near the leading edge of the plate are substantially smaller than for $L_i/L_c=0$. The plate local Nusselt number distributions predicted by the elliptic and parabolic solutions were also in close agreement when the plate was located at the top of the channel. This supports the supposition that the large differences between the two solution methods for $L_i/L_c=0$ (shown in Fig. 5.6) can be attributed to the influence flow separation at the inlet. It may be concluded that the parabolic solution will give accurate predictions of the plate local Nusselt number provided the plate is not near the channel inlet.

Figures 5.15 and 5.16 show the behaviour of the wall average Nusselt number (Nu_w) with channel Rayleigh number (Ra_c^*) for $L_i/L_c=(1-L_p/L_c)/2$, and $L_i/L_c=1-L_p/L_c$, (t/b=0). In both figures, the wall average Nusselt number predicted by the elliptic solution for $L_p/L_c=1/3$ is in fair agreement with the parabolic solution. Both sets of data have the same trend; however, the elliptic solution gives wall Nusselt numbers between five and

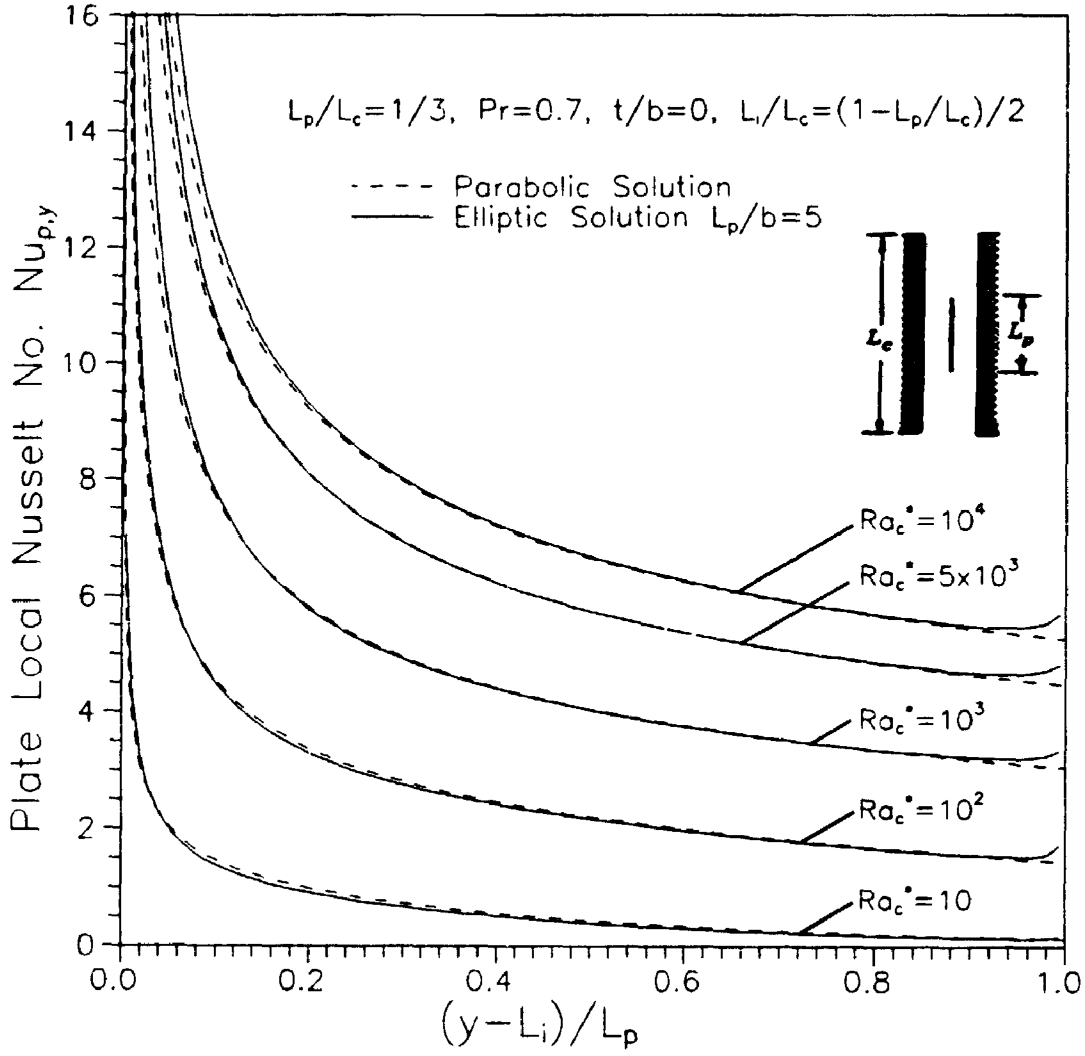

Figure 5.14: The plate local Nusselt number distribution for $L_i/L_c=(1-L_p/L_c)/2$ and $L_p/L_c=1/3$, (t/b=0).

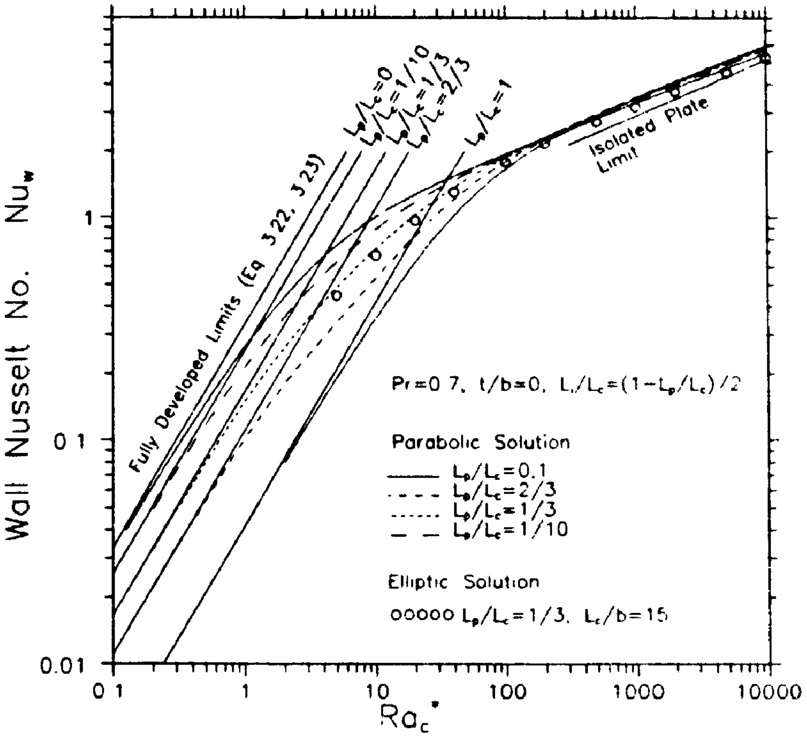

Figure 5.15: Variation of the wall average Nusselt number (Nu_w) with Rayleigh number (Ra_c^*) for several plate length ratios and $L_i/L_c=(1-L_p/L_c)/2$,(t/b=0).

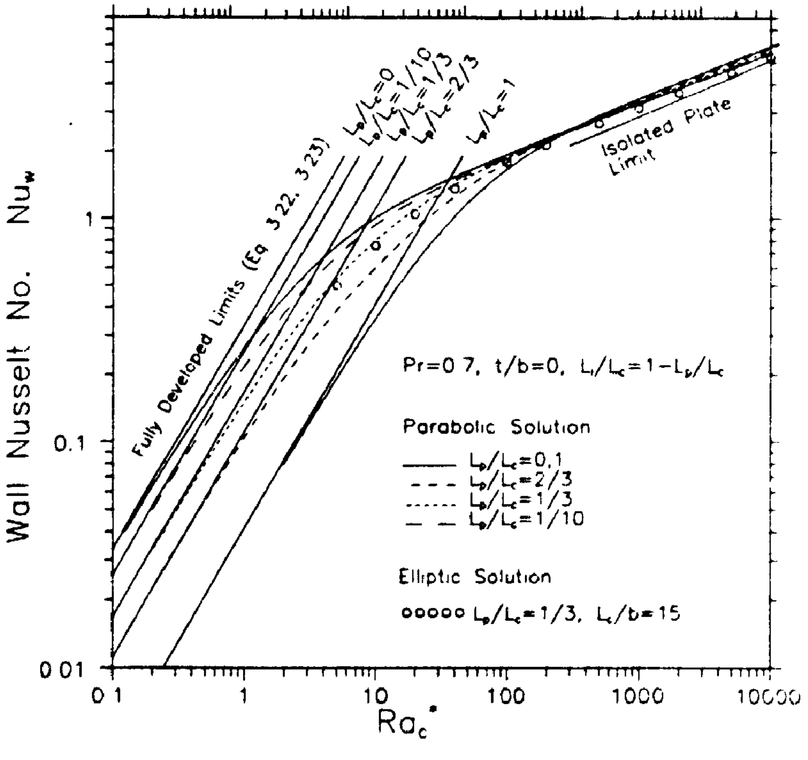

Figure 5.16: Variation of the wall average Nusselt number (Nu_w) with Rayleigh number (Ra_c^*) for several plate length ratios and $L_i/L_c=1-L_p/L_c$,(t/b=0).

nine percent lower than the parabolic solution. With the plate in either vertical position, at high Rayleigh number the wall Nusselt number is only weakly dependent upon the plate length ratio. At $Ra_c^*=10^4$, $L_p/L_c=1.0$ gives a Nusselt number that is only about six percent higher than for $L_p/L_c=0.0$. At low Rayleigh number the wall Nusselt number is highly dependent upon the plate length ratio. Again, the wall Nusselt numbers approach the fully developed limits (equations 3.22, 3.23). An interesting feature of the low Rayleigh number behaviour is the disproportionate reduction in the wall Nusselt number from $L_p/L_c=2/3$ to $L_p/L_c=1.0$. This decrease is only partially caused by viscous resistance and can be explained as follows: at low Rayleigh number the flow becomes thermally fully developed within a short distance from the channel inlet. If the dividing plate is much shorter than the channel length ($L_p<<L_c$), then the flow will be fully developed before reaching the plate and the plate heat transfer will be almost zero. However, in the limit as $L_p/L_c \to 1$, approximately one half of the heat transfer will be contributed by the dividing plate. As a result, the heat transfer from the plate reduces the wall Nusselt number by approximately a factor of two.

Figure 5.17 shows a comparison of the wall local Nusselt number distributions from the elliptic and parabolic solutions for $L_p/L_c=1/3$ at several values of Rayleigh number for the plate in the middle of the channel ($L_1/L_c=(1-L_p/L_c)/2$, $t/b=0$). Again, at low Rayleigh number, the elliptic solution is in close agreement with the parabolic solution, except that the discontinuities are smoothed. The results show that the wall heat transfer rises slightly near the location of the leading edge of the plate and falls slightly near the trailing edge of the plate. The slight variations

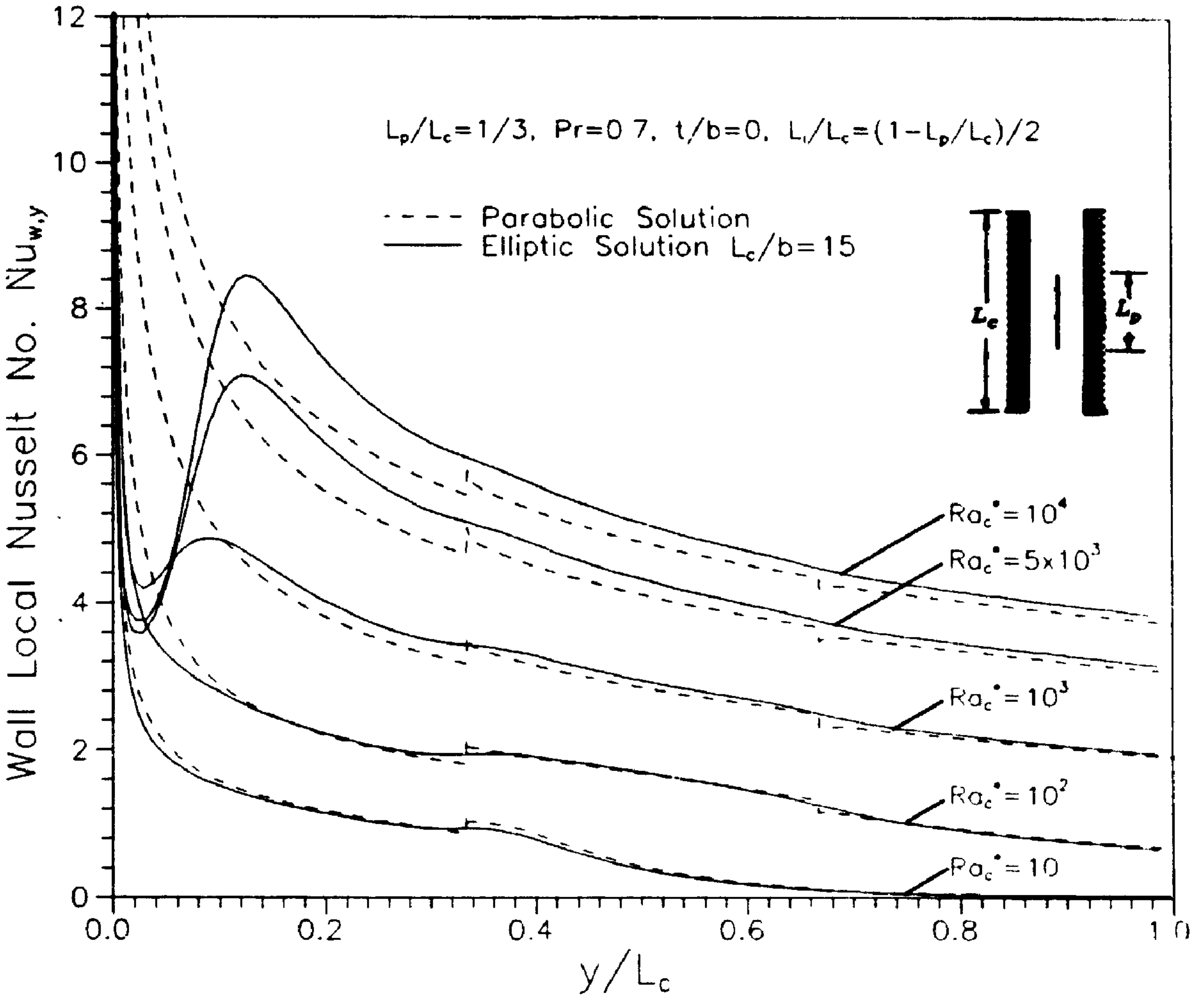

Figure 5.17: The wall local Nusselt number distribution for $L_i/L_c=(1-L_p/L_c)/2$ and $L_p/L_c=1/3$, (t/b=0).

of the wall heat transfer can be explained by considering the traverse (u) component of velocity. At the leading edge of the plate a momentum boundary-layer begins to develop on the zero-thickness dividing plate; accordingly, the x-component of velocity (u) is positive across the entire channel. This traverse component of velocity brings cooler fluid from the centre regions of the channel closer to the wall, causing the heat transfer to increase slightly. Similarly, at the trailing edge of the dividing plate the traverse component of velocity is negative across the entire channel. Hence, cooler fluid is pushed away from the wall, causing the wall heat transfer to decrease slightly.

Figures 5.18 and 5.19 show the variation of the channel average Nusselt number (Nu_c) with channel Rayleigh number (Ra_c^*) for $L_i/L_c=(1-L_p/L_c)/2$, and $L_i/L_c=1-L_p/L_c$, (t/b=0). Comparison with the results for the plate in the bottom of the channel (Fig. 5.9) shows that the general trends of the data are similar. However, when the plate is located higher in the channel, curves of fixed plate length ratio (L_p/L_c) are slightly lower than when the plate is located at the channel inlet. This effect is discussed further in Section 5.2.3.

The channel axial pressure distributions for $L_p/L_c=1/3$ with the plate in the top of the channel are shown in Fig. 5.20. Notice that the pressure decreases near the leading edge of the plate. Temporary, the high skin friction at the leading edge causes a negative pressure gradient. It is also interesting to note that at low Rayleigh number, the pressure in the upper portion of the channel is *above* the ambient pressure. At low Rayleigh number, the dividing plate contributes additional viscous

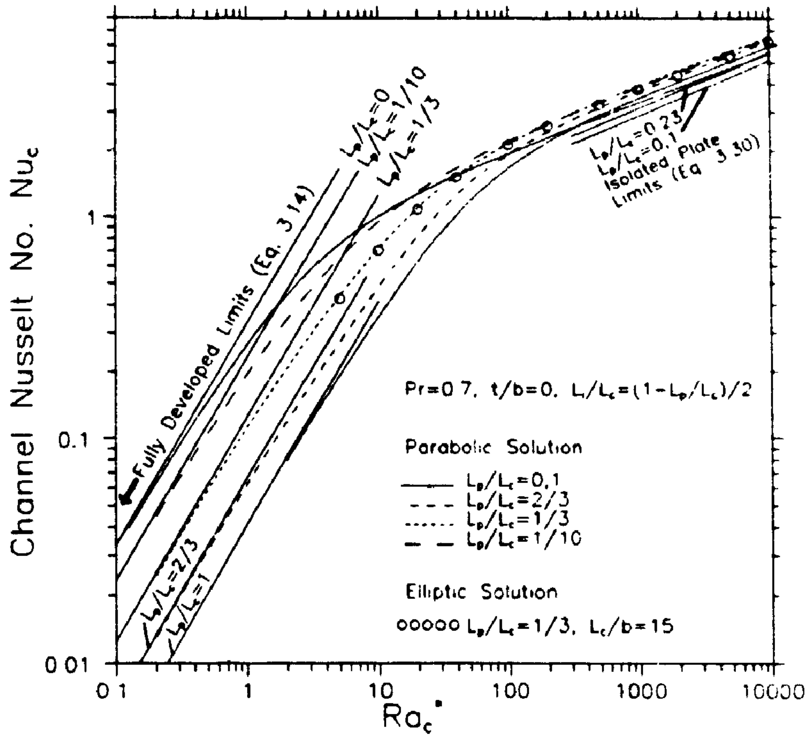

Figure 5.18: Variation of the channel average Nusselt number (Nu$_c$) with Rayleigh number (Ra$_c$*) for several plate length ratios and $L_i/L_c=(1-L_p/L_c)/2$, $(t/b=0)$.

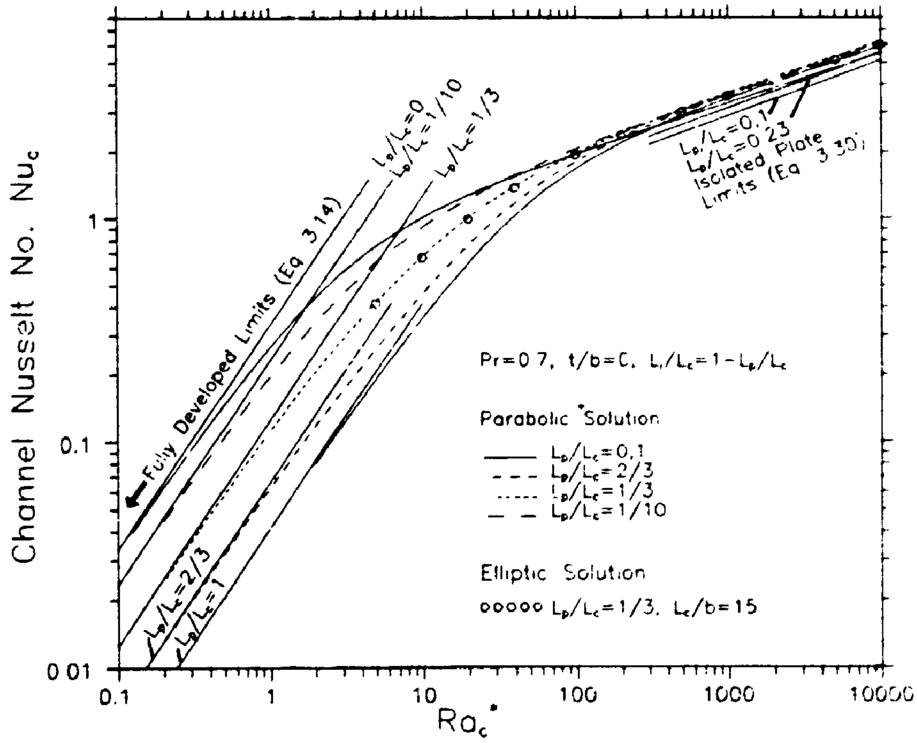

Figure 5.19: Variation of the channel average Nusselt number (Nu$_c$) with Rayleigh number (Ra$_c$*) for several plate length ratios and $L_i/L_c=1-L_p/L_c$, $(t/b=0)$.

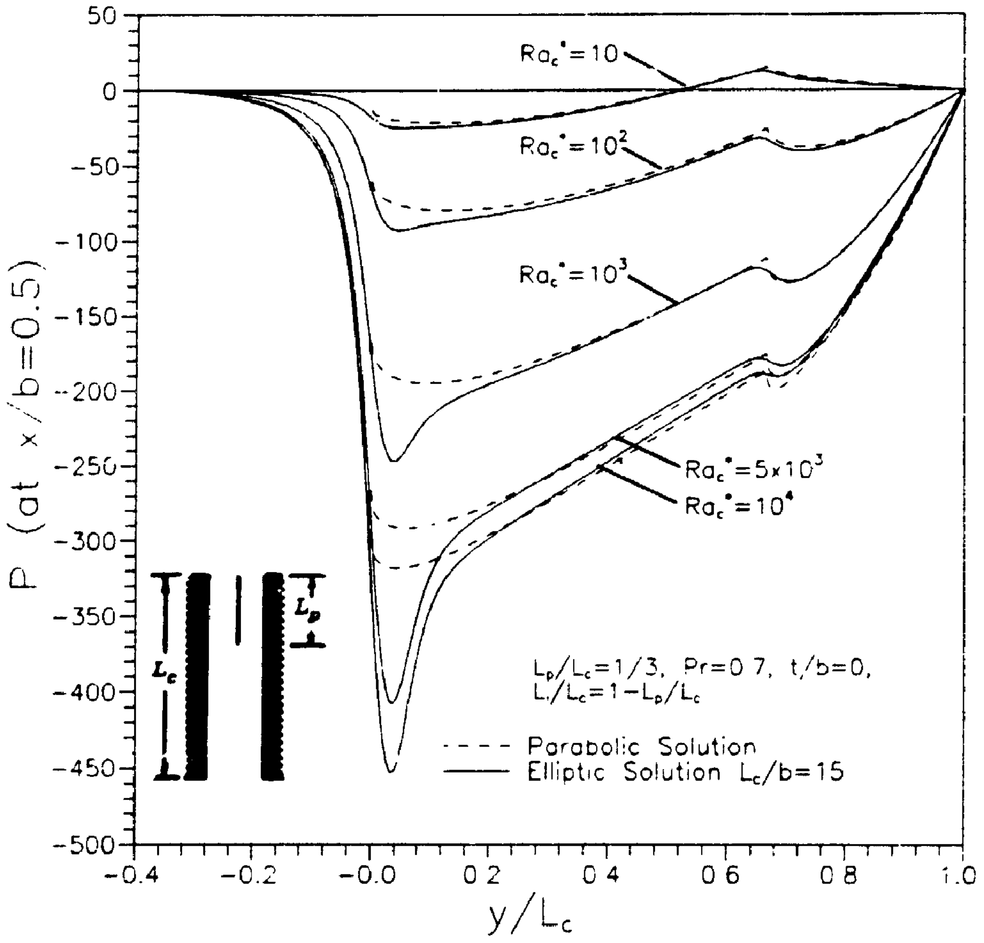

Figure 5.20: The channel pressure distribution at several values of Rayleigh number for $L_p/L_c=1/3$ and $L_i/L_c=1-L_p/L_c$, $(t/b=0)$.

Table 5.2: Comparison of major data from the parabolic and elliptic solutions for $L_p/L_c=1/3$, $L_i/L_c=(1-L_p/L_c)/2$ (middle), $t/b=0$.

Plate Average Nusselt Number - Nu_p

Ra_c^*	Ra_p^*	Parabolic Soltn Nu_p	Elliptic Soltn Nu_p	% Difference
5	15	0.2924	0.2647	9.5
10	30	0.7191	0.6712	6.6
100	300	2.9094	2.8743	1.2
1,000	1,000	5.2828	5.2446	0.72
5,000	15,000	7.3718	7.3983	-0.36
10,000	30,000	8.4942	8.5263	-0.38

Wall Average Nusselt Number - Nu_w

Ra_c^*	Ra_p^*	Parabolic Soltn Nu_w	Elliptic Soltn Nu_w	% Difference
5	15	0.4870	0.4487	7.9
10	30	0.7251	0.6775	6.6
100	300	1.8808	1.7866	5.0
1,000	1,000	3.4328	3.1748	7.5
5,000	15,000	4.9821	4.5270	9.1
10,000	30,000	5.8368	5.2968	9.3

Channel Average Nusselt Number - Nu_c

Ra_c^*	Ra_p^*	Parabolic Soltn Nu_c	Elliptic Soltn Nu_c	% Difference
5	15	0.4372	0.4256	2.7
10	30	0.7229	0.7058	2.4
100	300	2.1458	2.1154	1.4
1,000	1,000	3.9118	3.7809	3.3
5,000	15,000	5.6217	5.3631	4.6
10,000	30,000	6.5447	6.2369	4.7

Half Channel Induced Flow Rate ($Q_p=Q_e/Gr^{*}$)

Ra_c^*	Ra_p^*	Parabolic Soltn Q_p	Elliptic Soltn Q_p	% Difference
5	15	0.11673	0.11365	2.6
10	30	0.97887E-1	0.95391	2.5
100	300	0.40036E-1	0.39104E-1	2.3
1,000	1,000	0.12280E-1	0.11912E-1	3.0
5,000	15,000	0.47301E-2	0.45727E-2	3.3
10,000	30,000	0.29932E-2	0.28989E-2	3.1

Table 5.3: Comparison of major data from the parabolic and elliptic solutions for $L_p/L_c=1/3$, $L_1/L_c=1-L_p/L_c$ (top), $t/b=0$, $Pr=0.7$.

Plate Average Nusselt Number - Nu_p

Ra_c^*	Ra_p^*	Parabolic Soltn Nu_p	Elliptic Soltn Nu_p	% Difference
5	15	0.08946	0.08244	7.8
10	30	0.3194	0.2997	6.2
100	300	2.1635	2.1182	2.1
1,000	1,000	4.5091	4.4952	0.31
5,000	15,000	6.6331	6.5829	-4.0
10,000	30,000	7.7104	7.7049	-0.07

Wall Average Nusselt Number - Nu_w

Ra_c^*	Ra_p^*	Parabolic Soltn Nu_w	Elliptic Soltn Nu_w	% Difference
5	15	0.5354	0.4996	6.7
10	30	0.7973	0.7545	5.4
100	300	1.8729	1.7904	4.4
1,000	1,000	3.3234	3.1279	5.9
5,000	15,000	4.9746	4.5124	9.3
10,000	30,000	5.7059	5.2976	7.1

Channel Average Nusselt Number - Nu_c

Ra_c^*	Ra_p^*	Parabolic Soltn Nu_c	Elliptic Soltn Nu_c	% Difference
5	15	0.4217	0.4155	1.5
10	30	0.6762	0.6659	1.5
100	300	1.9464	1.9195	1.4
1,000	1,000	3.6408	3.5462	2.6
5,000	15,000	5.3233	5.1322	3.6
10,000	30,000	6.2300	6.0119	3.5

Half Channel Induced Flow Rate ($Q_p=Q_e/Gr^{\frac{1}{4}}$)

Ra_c^*	Ra_p^*	Parabolic Soltn Q_p	Elliptic Soltn Q_p	% Difference
5	15	0.11261	0.11103	1.4
10	30	0.91329E-1	0.89934E-1	1.5
100	300	0.34713E-1	0.34090E-1	1.8
1,000	1,000	0.10345E-1	0.10093E-1	2.4
5,000	15,000	0.38988E-2	0.37885E-2	2.8
10,000	30,000	0.24448E-2	0.23817E-2	2.6

resistance and almost no additional buoyancy force. Hence, the pressure must be above the ambient pressure before reaching the plate's leading edge in order to push the fluid past the restriction caused by the dividing plate.

Tables 5.2 and 5.3 show a comparison of major data from the parabolic and elliptic solutions for $L_p/L_c=1/3$, $L_i/L_c=(1-L_p/L_c)/2$ and $L_i/L_c=1-L_p/L_c$, (t/b=0). The agreement of the two solutions is typically better than five percent for the plate Nusselt number, the channel Nusselt number and induced flow rate. The wall Nusselt number agreement is not as close. A more complete tabular listing of the numerical data is given in Appendix D.

5.2.3 Effect of Dividing Plate Location, (t/b=0)

Results for the dividing plate in the bottom, middle and top of the channel have been presented in the Sections 5.2.1 and 5.2.2. However, the results are given in separate graphs for each plate position, making comparison difficult. In this section the data are compared for the dividing plate in each vertical position with one fixed plate length ratio, $L_p/L_c=1/3$.

Figure 5.21 shows streamline and isotherm contours at low and high Rayleigh number from the elliptic solution with the plate in the top of channel for $L_p/L_c=1/3$, (t/b=0). Comparing the streamline patterns for this configuration with those for the plate located in the bottom of the channel (Fig. 5.1) shows only minor differences. However. the effect of plate position on the temperature field can be seen to be quite dramatic.

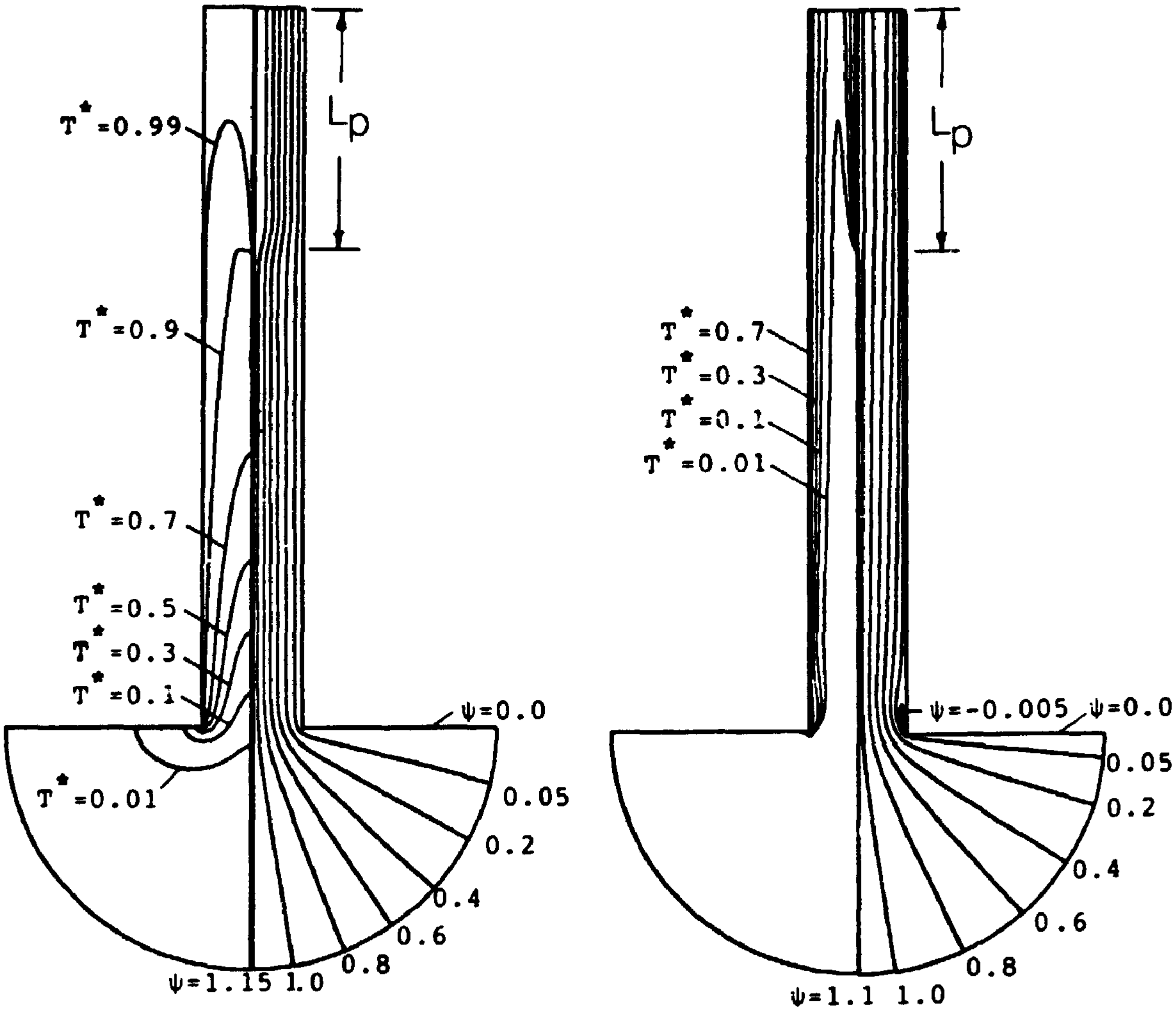

(a) $Ra_c^*=5$

(b) $Ra_c^*=10^4$

Figure 5.21: Streamline and isotherm contours for the divided channel with $L_p/L_c=1/3$, t/b=0, and $L_i/L_c=1-L_p/L_c=2/3$, (a) $Ra_c^*=5$, (b) $Ra_c^*=10^4$.

Comparing Fig. 5.1 and Fig. 5.21, it can be seen that the average fluid temperature at any elevation in the channel is higher when the plate is located at the bottom of the channel. Hence, simply by inspecting the isotherm contour plots, it could be expected that the buoyancy induced flow and overall heat transfer will be higher when the plate is in the bottom of the channel.

Figure 5.22 shows the behaviour of the dimensionless flow rate (Q_p) and exit bulk temperature (T_b^*) with channel Rayleigh number (Ra_c^*) for each plate position[1]. At low Rayleigh number, the fully developed induced flow rate is independent of the plate location. For $Ra_c^*>0$, the largest flow rate occurs when the plate is at the channel entrance ($L_i/L_c=0$), and decreases as the plate moves from the bottom to the top of the channel. At $Ra_c^*=10^4$, the induced flow rate is about thirty seven percent higher when the plate is in the bottom of the channel than when the plate is at the top. As previously mentioned, it is evident from the temperature contour plots that the average fluid temperature in the channel is the highest when the plate is at the bottom. This implies that the average buoyancy force is the largest when the plate is at the bottom. The higher average buoyancy force induces a larger flow rate.

Figure 5.23 shows the variation of the plate average Nusselt number (Nu_p) with plate Rayleigh number (Ra_p^*) for each plate position. At low Rayleigh number there is a strong influence of plate position on the plate Nusselt number. For $L_i/L_c>0$, the Nusselt number decreases very rapidly with

---

[1] Note that the parabolic and elliptic dimensionless flow rates are related as: $Q_p = Q_e/Gr^*$

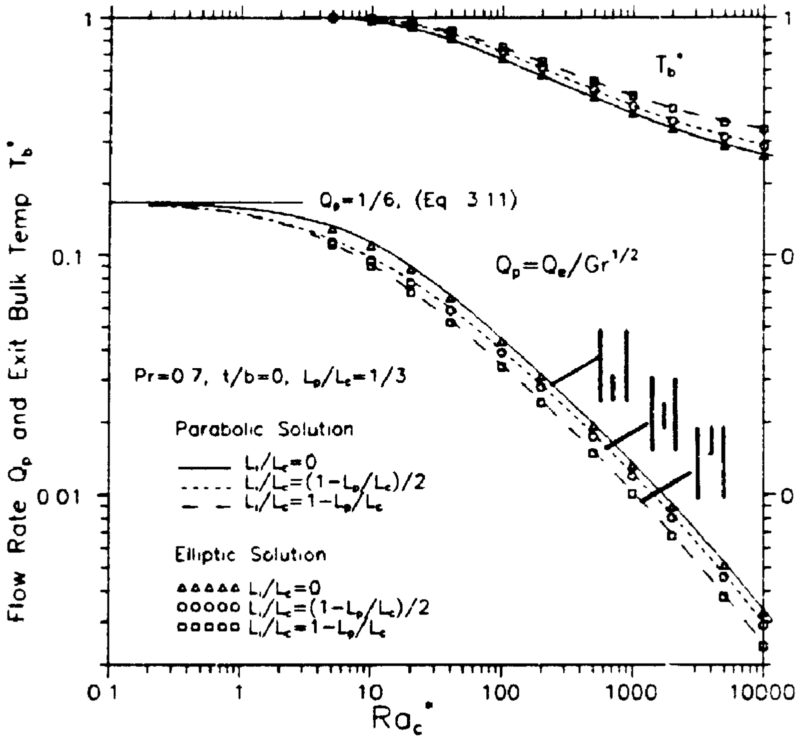

Figure 5.22: Effect of the divider plate location on dimensionless flow rate and bulk exit temperature for $L_p/L_c=1/3$,(t/b=0).

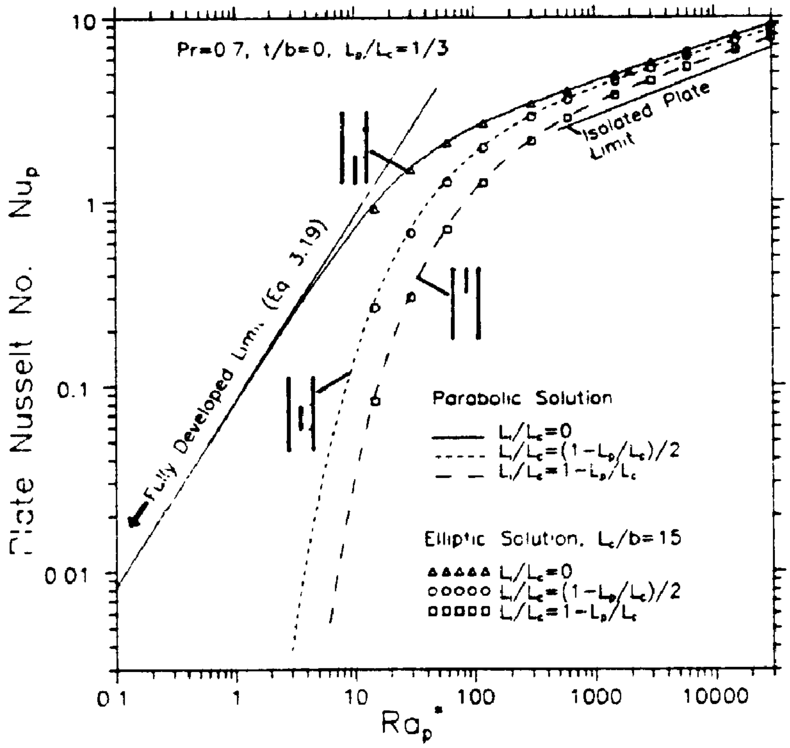

Figure 5.23: Effect of the divider plate location on the plate average Nusselt number for $L_p/L_c=1/3$,(t/b=0).

decreasing Rayleigh number because of the shortening thermal developing length (as discussed in Section 5.2.2). At high Rayleigh number the plate Nusselt number is much less dependent on the vertical location of the plate. At $Ra_p^*=3x10^4$, the Nusselt number for the plate located at the bottom of the channel ($L_i/L_c=0$) is about twenty percent higher than for the plate located at the top of the channel ($L_i/L_c=1-L_p/L_c=2/3$).

Figure 5.24 shows the variation of the wall average Nusselt number (Nu_w) with channel Rayleigh number (Ra_c^*) for each plate position. At low Rayleigh number the wall Nusselt number for $L_i/L_c=0$ is one half the value for $L_i/L_c>0$ for reasons explained in Section 5.2.2. However, the lack of dependence on plate location at high Ra_c^* is very interesting. Although the induced flow rate is larger when the plate is in the bottom of the channel (which would tend to increase the wall heat transfer), the bulk fluid temperature is higher (which tends to decrease the wall heat transfer). These effects counteract each other for $Ra_c^*>200$, causing the wall Nusselt number to be almost independent of the plate position.

The effect of the plate position on the channel average Nusselt number (Nu_c) is shown in Figure 5.25. Positioning the plate at the bottom of the channel ($L_i/L_c=0$) produces the greatest heat transfer over the entire range of Rayleigh number. However, the channel average Nusselt number is only weakly dependent upon the plate's vertical position; at $Ra_c^*=10^4$, the channel Nusselt number for $L_i/L_c=0$ is only seven percent higher than for $L_i/L_c=1-L_p/L_c$. Since the wall average Nusselt number is almost independent of the plate position at high Ra_c^*, this increase in the channel average Nusselt number can be attributed solely to the additional heat

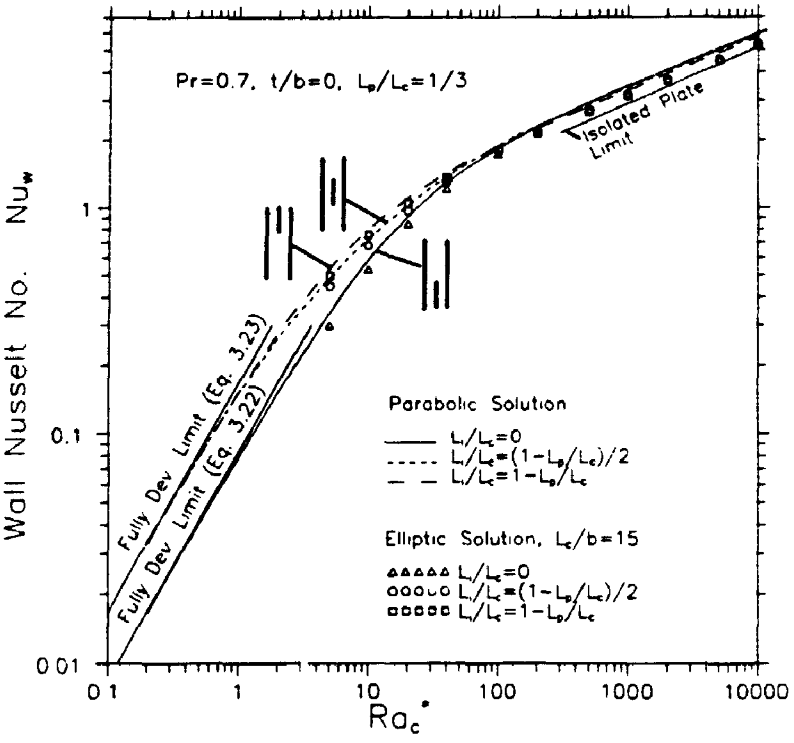

Figure 5.24: Effect of the divider plate location on the wall average Nusselt number for L_p/L_c=1/3,(t/b=0).

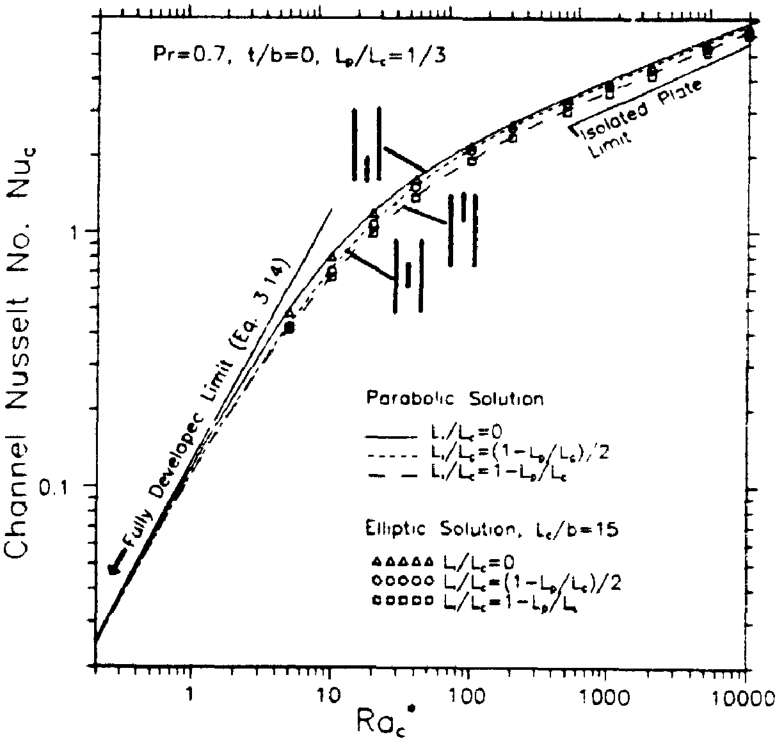

Figure 5.25: Effect of the divider plate location on the channel average Nusselt number for L_p/L_c=1/3,(t/b=0).

transfer from the plate.

5.3 Effect of Dividing Plate Thickness - $t/b \geq 0$

The previous sections have shown the influence of plate length ratio (L_p/L_c) and vertical plate position (L_i/L_c) on the heat transfer from the channel walls, the dividing plate and the channel as a whole. This section shows the influence of slight blockage caused by a finite thickness dividing plate ($0 \leq t/b \leq 0.2$).

Additional cases were run with dividing plate thicknesses of $t/b=0.1$ and $t/b=0.2$ for a fixed plate length ratio ($L_p/L_c=1/3$) and with the plate in the bottom of the channel ($L_i/L_c=0$). The parabolic solution is limited to $t/b=0$. Hence, only the full elliptic solutions could be obtained for finite plate thicknesses.

Figure 5.26 shows streamline and isotherm contours from the elliptic solution for a partially divided channel with a plate length ratio $L_p/L_c=1/3$ and thickness $t/=0.2$, ($L_i/L_c=0$). The behaviour is similar to that of the divided channel with $t/b=0$ (Fig. 5.1). At low Rayleigh rumber ($Ra_c^*=10$, Fig. 5.26(a)), the flow enters the channel smoothly. Separation occurs on the wall at the channel inlet at higher Rayleigh number ($Ra_c^*=10^4$, Fig. 5.26(b)). The elliptic solution predicts that increasing the plate thickness delays the onset of separation at the channel inlet. With twenty percent blockage ($t/b=0.2$) separation occurs between $200 \leq Ra_c^* \leq 500$, as compared to $100 \leq Ra_c^* \leq 200$ for zero blockage ($t/b=0$). This result is not surprising since blockage reduces the induced flow rate in this range of Rayleigh number;

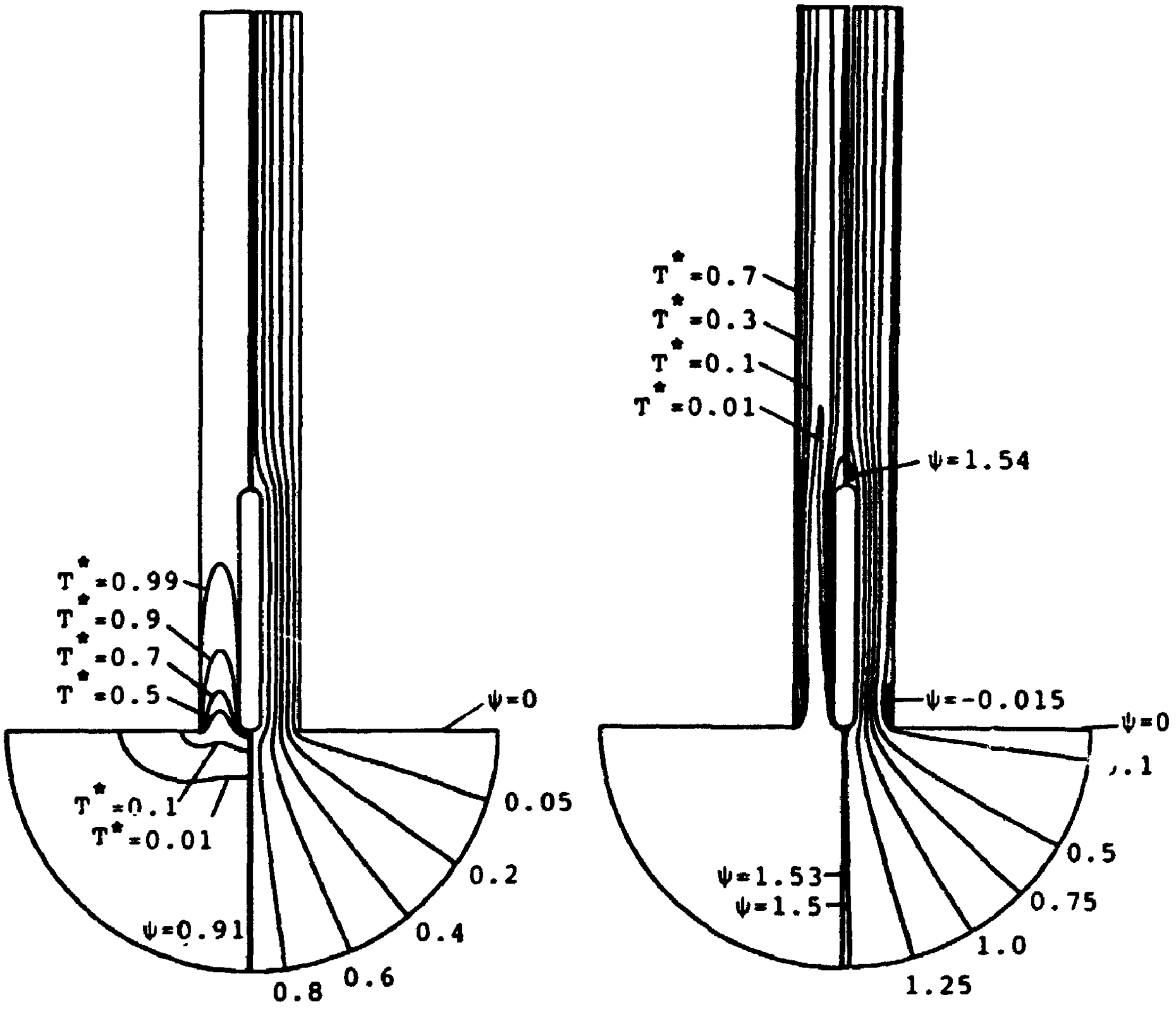

(a) $Ra_c^*=5$

(b) $Ra_c^*=10^4$

Figure 5.26: Streamline and isotherm contours for the divided channel with $t/b=0.2$, $L_p/L_c=1/3$, $L_i/L_c=0$, (a) $Ra_c^*=5$, (b) $Ra_c^*=10^4$.

separation has been previously shown to correlate with flow rate (see Chapter 4). For finite thickness dividing plates, flow separation also occurs at the top of the dividing plate. For $L_p/L_c=1/3$, $L_p/b=5$, $L_i/L_c=0$, and $t/b=0.2$, the elliptic solution predicts that separation occurs between $10 \leq Ra_c^* \leq 20$, as determined from the plate shear stress distribution.

Figures 5.27, 5.28, 5.29 and 5.30 show the variation of flow rate (Q_p) and Nusselt numbers (Nu_p, Nu_w, Nu_c) with Rayleigh number for zero, ten and twenty percent channel blockage ($t/b=0$, 0.1, 0.2). As would be expected, increasing blockage (t/b) causes a reduction in the induced flow rate and Nusselt numbers at low Rayleigh number. Note that the data from the elliptic solution (for $t/b>0$) appear to be approaching the fully developed asymptotes derived in Chapter 3. At $Ra_c^*=5$, for $L_p/L_c=1/3$ and $L_i/L_c=0$, twenty percent blockage of the channel cross-section ($t/b=0.2$) causes a thirty percent reduction in the plate and channel average Nusselt numbers. In the fully developed limit, the maximum reduction is predicted to be 38.8 percent.

At high Rayleigh number, small plate thicknesses have almost no effect on the channel's thermal behaviour since the dividing plate and walls act as isolated plates. The induced flow rate and Nusselt numbers are almost independent of the channel half width (b), so small changes in the effective channel width caused by blockage has very little effect. There is, however, a small secondary effect to be considered. A dividing plate with finite plate thickness ($t/b>0$) has a slightly larger wetted length than a plate of zero-thickness ($t/b=0$) with the same length in the y-direction (L_p/b). The extra wetted length is associated with the rounded leading

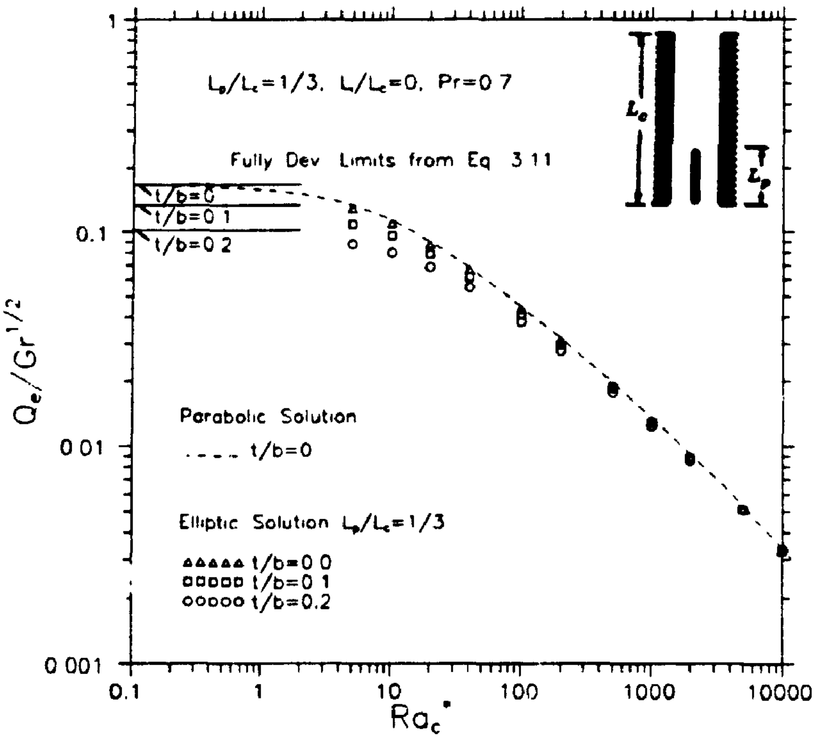

Figure 5.27: Effect of the divider plate thickness (t/b) on dimensionless flow rate for L_p/L_c=1/3 and L_i/L_c=0.

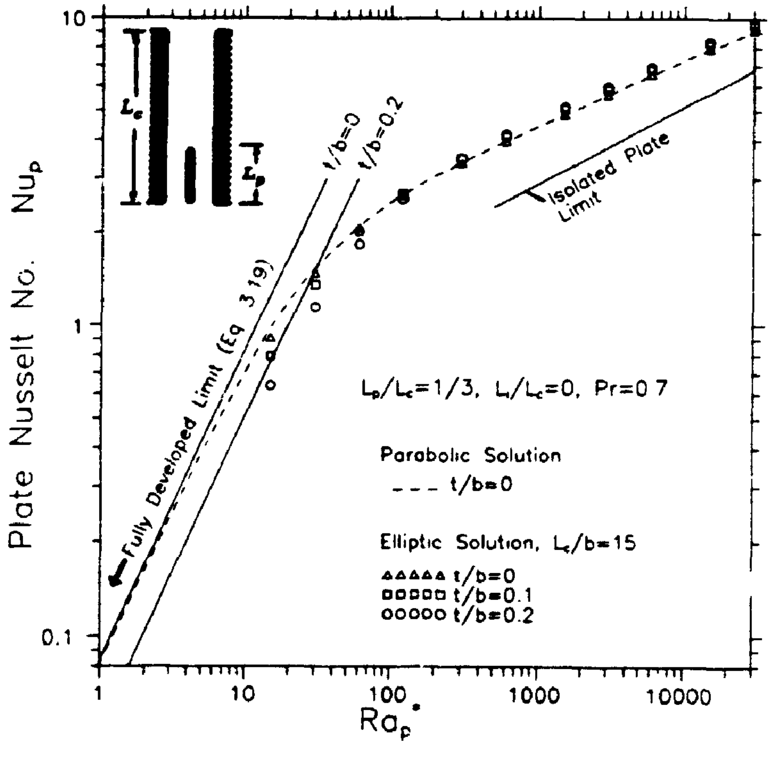

Figure 5.28: Effect of the divider plate thickness (t/b) on the plate average Nusselt number for L_p/L_c=1/3 and L_i/L_c=0.

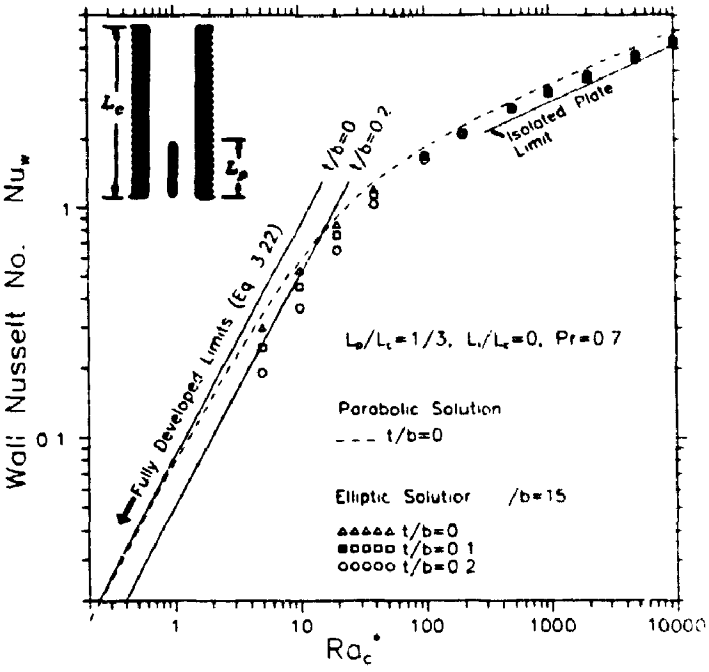

Figure 5.29: Effect of the divider plate thickness (t/b) on the wall average Nusselt number for $L_p/L_c=1/3$ and $L_i/L_c=0$.

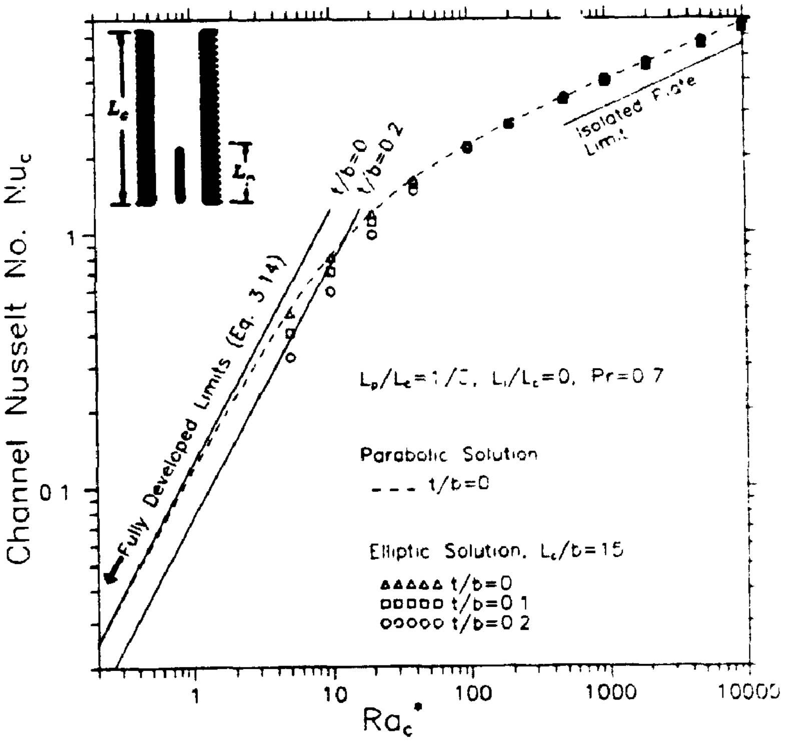

Figure 5.30: Effect of the divider plate thickness (t/b) on the channel average Nusselt number for $L_p/L_c=1/3$ and $L_i/L_c=0$.

and trailing edges. The plate with thickness t/b=0.1 has 2.3 percent more wetted length than the zero-thickness plate (for $L_p/b=5$, $L_p/L_c=1/3$). Similarly, the plate with thickness t/b=0.2 has 4.6 percent more wetted length than the zero-thickness plate. Consequently, at high Rayleigh number, the channel with twenty percent blockage (t/b=0.2) has a slightly higher induced flow and heat transfer than the channel with t/b=0 and t/b=0.1 (see Fig. 5.27, 5.28, 5.29, and 5.30). However, the extra wetted length is a relatively minor effect for t/b≤0.2 and can be neglected for most practical purposes. For example, at $Ra_c^*=10^4$, the plate, wall and overall channel average Nusselt numbers for t/b=0.2 are only about three to five percent higher than for t/b=0.

CHAPTER 6

EXPERIMENTAL APPARATUS, PROCEDURE AND ANALYSIS

6.1 Introduction

A Mach-Zehnder interferometer was used to visualize and measure the free convective temperature field in an isothermal divided channel. Using interferometry, the entire temperature field can be recorded simultaneously and non-intrusively. From the temperature field, local as well as overall heat transfer coefficients can be obtained for comparison with the numerical predictions. An additional advantage of interferometry is that radiation does not influence the fluid temperature measurement when the heat transfer medium (such as air) is transparent to thermal radiation [66]. Only the convective component of heat transfer is measured and corrections for radiation are not necessary.

The output of the interferometer is the optically integrated refractive index field, which can be "calibrated" to give the temperature field. Since the interferometer integrates the temperature field in the direction of the light beam, it is best suited to measurements of two-dimensional fields such as the present study. However, it should be noted that interferometry can also be applied to three-dimensional and axisymmetric fields [67,68,69].

This chapter describes the construction details of the test section, the experimental procedure and the interferometric analysis for the experiment.

6.2 Test Section Design

A cross-sectional diagram of the divided channel test section is shown in Fig. 6.1. The height of the channel was L_c=120.00 ± 0.05mm. This length was chosen to be as long as possible without exceeding working height of the interferometer test beam. With the height of the channel established, the dividing plate length was selected to give a length ratio of exactly $L_p/L_c=1/3$ i.e., L_p=40.00 ± 0.05mm. This length ratio coincides with the ratio used in most of the numerical calculations.

The length of the test section in the direction of the test beam (Z_T) is crucial design parameter. The considerations in choosing this length were as follows:

i) The length must be chosen to produce sufficient interference fringes in the Rayleigh number range of interest. Decreasing the model length in the direction of the beam will reduce the total fringe shift for a fixed surface-to-ambient temperature difference.

ii) The test section must be long enough to make end effects small so that the temperature field is essentially two-dimensional.

iii) The length must be kept to a minimum to reduce refraction effects.

iv) A high degree of surface flatness is easier to attain for shorter models. Improved flatness will allow more accurate alignment of the interferometer test beam with the model.

v) Thin foil resistance heaters to be used in the dividing plate were available in a limited number of lengths.

Based on these considerations, a test section length of Z_T=25.91 ± 0.01cm was selected. For this length and air as the test fluid, each fringe shift corresponds to a temperature difference of about ΔT=3C°.

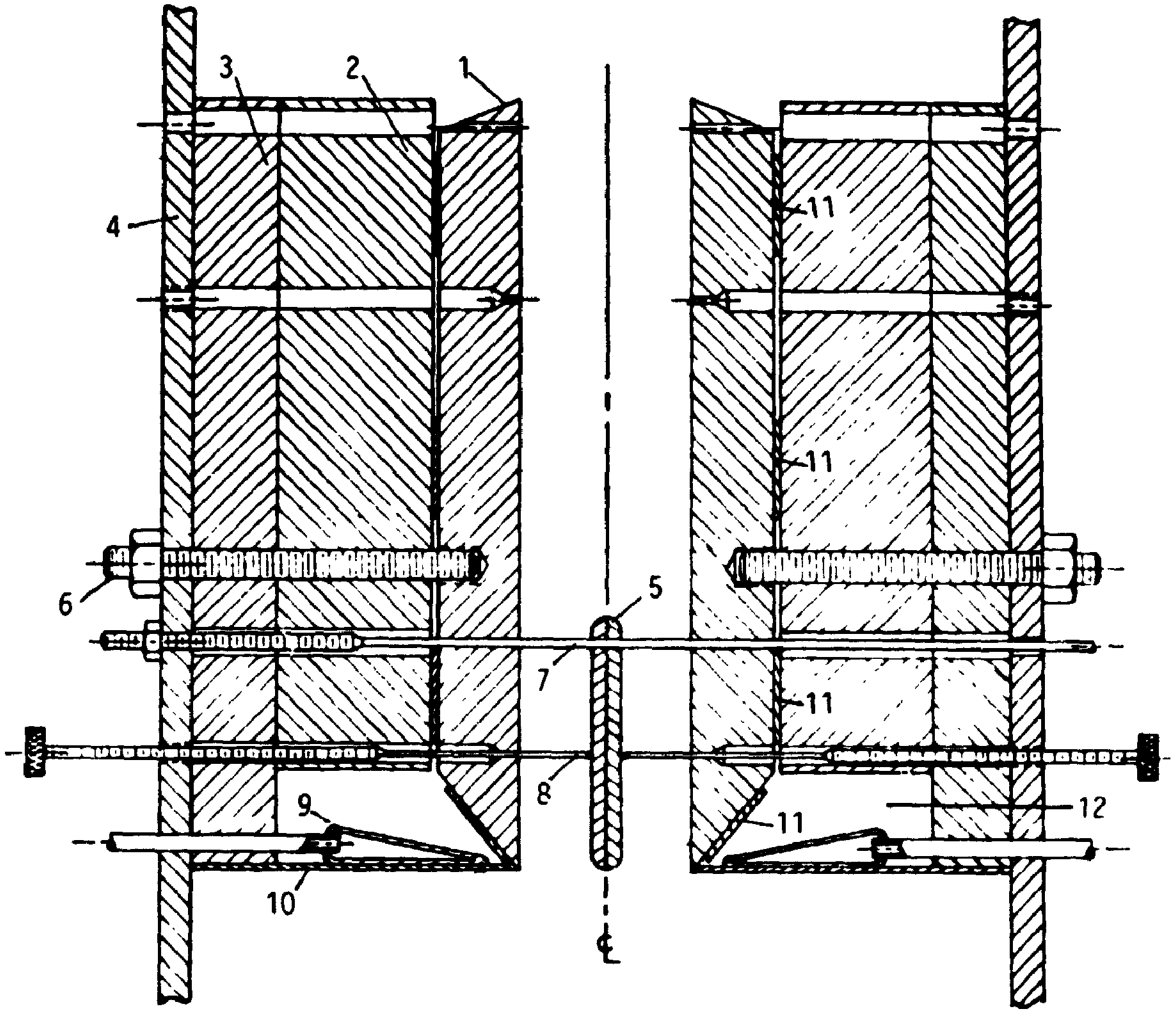

1. aluminum plate 1.27cm thick
2. polystyrene insulation
   2.54cm thick
3. plywood 1.27cm thick
4. 5x5x0.48cm aluminum angle
5. copper divider plate
6. nylon threaded rod 6.35mm dia.
7. plate support wire 1.2mm dia.
8. plate locating pin 0.53mm dia.
9. heat exchanger
10. phenolic sheet 0.8mm thick
11. electric heaters
    (4 per wall)
12. air gap

Figure 6.1: Cross-sectional view of the divided channel test section.

The main component of each wall assembly was a precision machined aluminum plate. A mechanical drawing of one of the plates is shown in Fig. 6.2. For clarity, only the locations of thermocouple holes are shown. Two plates, identical to the one shown in Fig. 6.2, formed the isothermal channel and were machined from 12.7mm thick aluminum tooling plate. Tooling plate is much flatter than standard aluminum plate; after machining, both of the aluminum plates were measured to be flat to within 0.0254mm.

Nine copper-constantan (40 gauge) thermocouples were installed in each wall of the channel. The thermocouple locations are shown in Fig. 6.2. For all experiments, the nine thermocouples read the same to within 0.5C°, which is about 2.4 percent of the overall temperature difference.

The construction of each wall assembly was identical (see Fig. 6.1). The aluminum plate was insulated on the back surface by a 2.54cm layer of polystyrene (styrofoam SM^{TM}) and a 1.27cm sheet of plywood. The polystyrene, wood and aluminum plate were held together by six nylon rods that were threaded into the back surface of the aluminum plate. To support the assembly, a 37cm length of 5x5x0.48cm angle aluminum was attached to both ends of each wall. Photographs of the front and back of one wall assembly are shown in Fig. 6.3. Note that directly above and below the wall assembly, a portion of the angle bracket was removed so that the flow of air into the channel was not obstructed. Four nylon threaded rods were used to connect the two wall assemblies at the top and bottom of each angle bracket. The thread rods held the walls at a fixed distance apart and allowed the spacing (2b) to be easily adjusted.

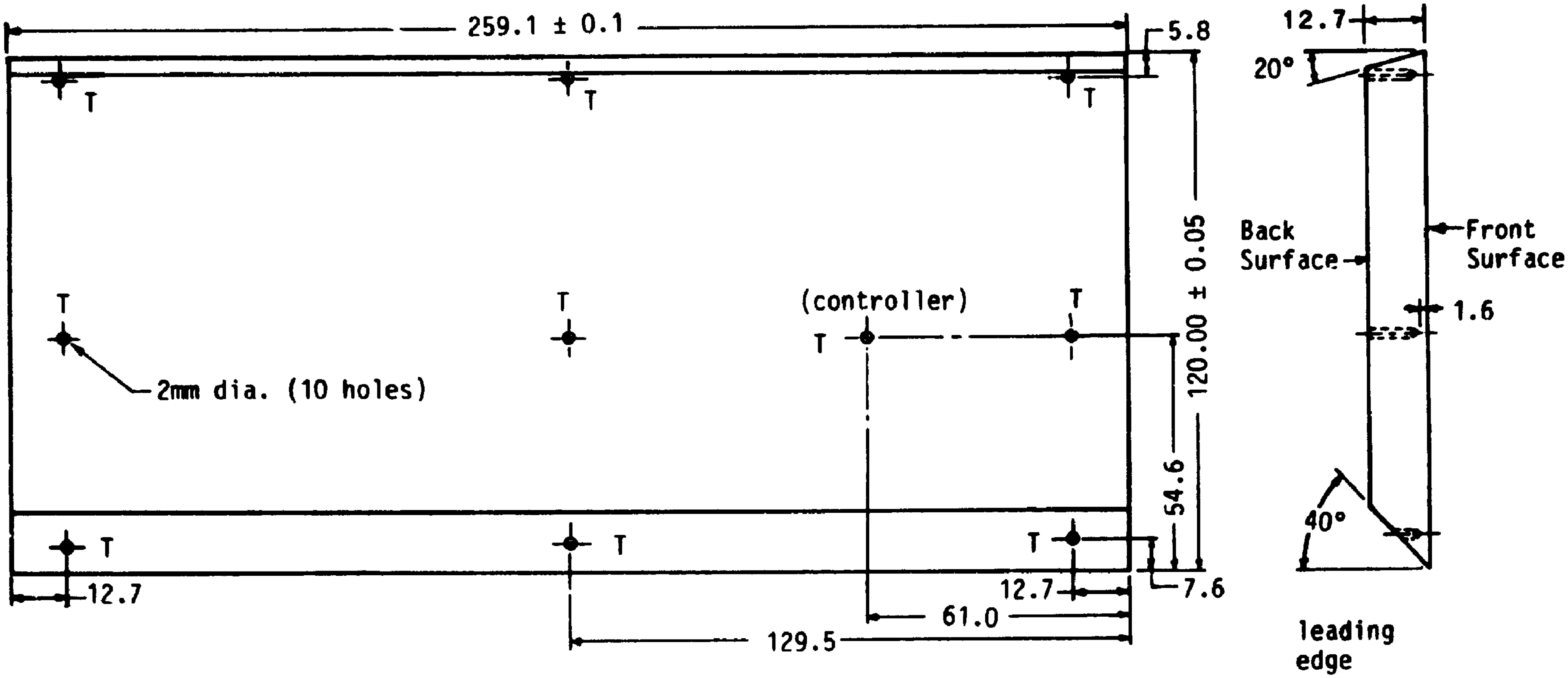
259.1 ± 0.1
5.8
12.7
20°
T
T
T
Back Surface
Front Surface
120.00 ± 0.05
T
T
(controller)
T
T
1.6
2mm dia. (10 holes)
54.6
40°
T
T
T
12.7
12.7
7.6
61.0
129.5
leading edge

"T" - marks the location of thermocouple holes

Dimensions are in millimeters

Figure 6.2: Mechanical drawing of the aluminum plates that formed the isothermal channel walls.

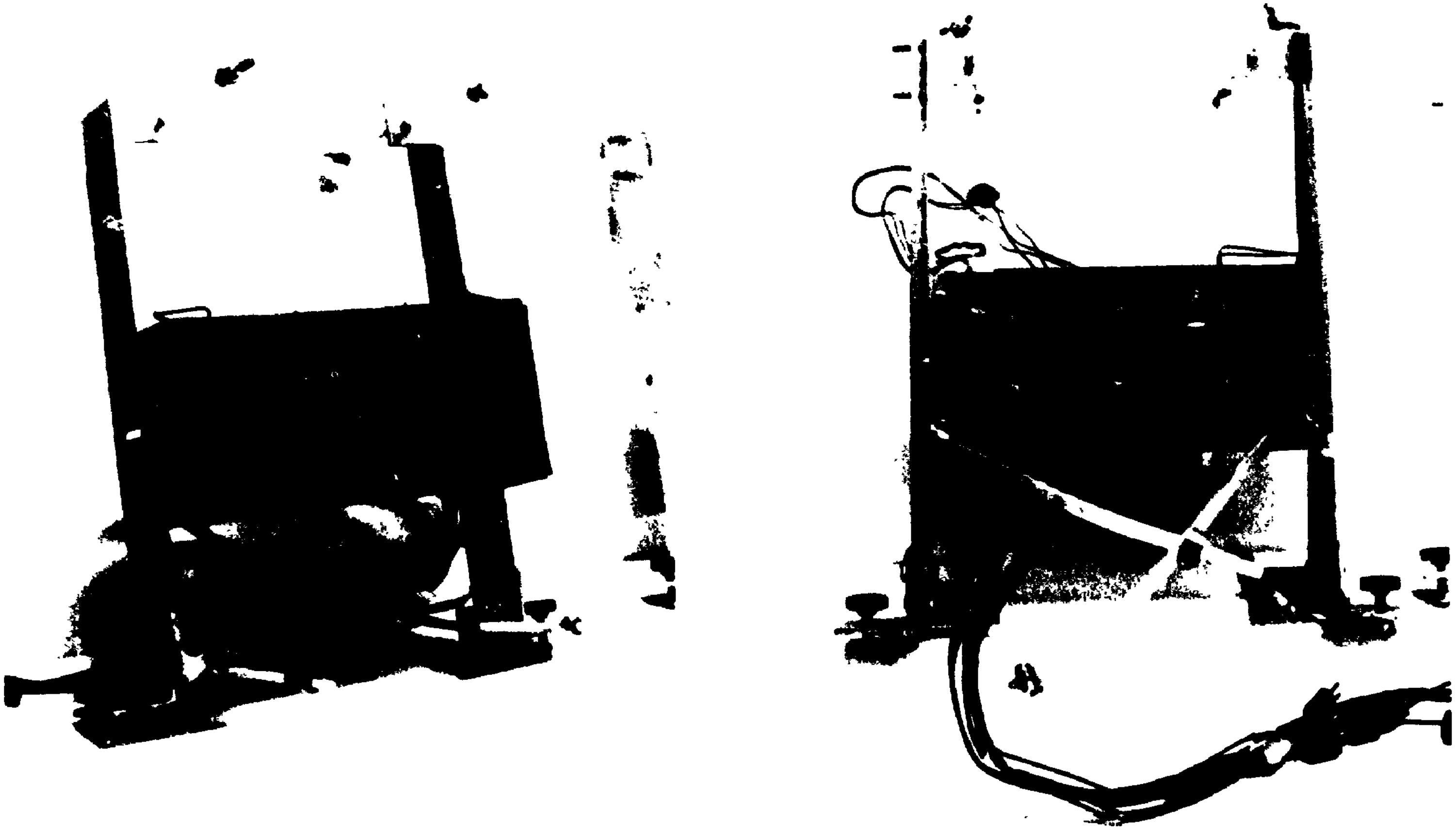

(a) Front view

(b) Back view

Figure 6.3: (a) Front and (b) back view of one channel wall assembly.

Each wall was heated by four electric strip heaters (manufactured by Minco Products Inc.). The heaters were affixed to the back surface of the aluminum plate using aluminum foil tape. Each heater had dimensions 25.5x2x0.04cm and a resistance of about 60 ohms. The location of each strip heater is shown in Fig. 6.1 (item #11).

Preliminary tests showed that there was significant heating of the horizontal surfaces near the channel inlet. To reduce the pre-heating of the air entering the channel, small heat exchangers were installed in each wall assembly to cool the phenolic sheet near the channel inlet (see item #9 in Fig. 6.1). An isometric and cross-sectional drawing of one heat exchanger is shown in Fig. 6.4. The single-pass heat exchangers were constructed by bending and soldering 0.8mm thick copper sheet. Water at room temperature was supplied to the heat exchangers. In the operating Rayleigh number range of the test model, maintaining the horizontal surfaces at room temperature is almost equivalent to maintaining an adiabatic condition.

The dividing plate was machined from two pieces of 259.1x40.0x1.59mm copper plate. Despite somewhat poorer machining properties, copper was used instead of aluminum because of its higher thermal conductivity. Figure 6.5 is a mechanical drawing of one side of the copper plate. Only one side of the dividing plate is shown in Fig. 6.5 because the machining for both sides was almost identical. Both the top and the bottom of the plate were machined to have a radius of 1.59mm. Shallow grooves (0.5mm deep) for thermocouples were machined near each end and in the middle of *one* side of the plate. The thin foil heaters installed between the two

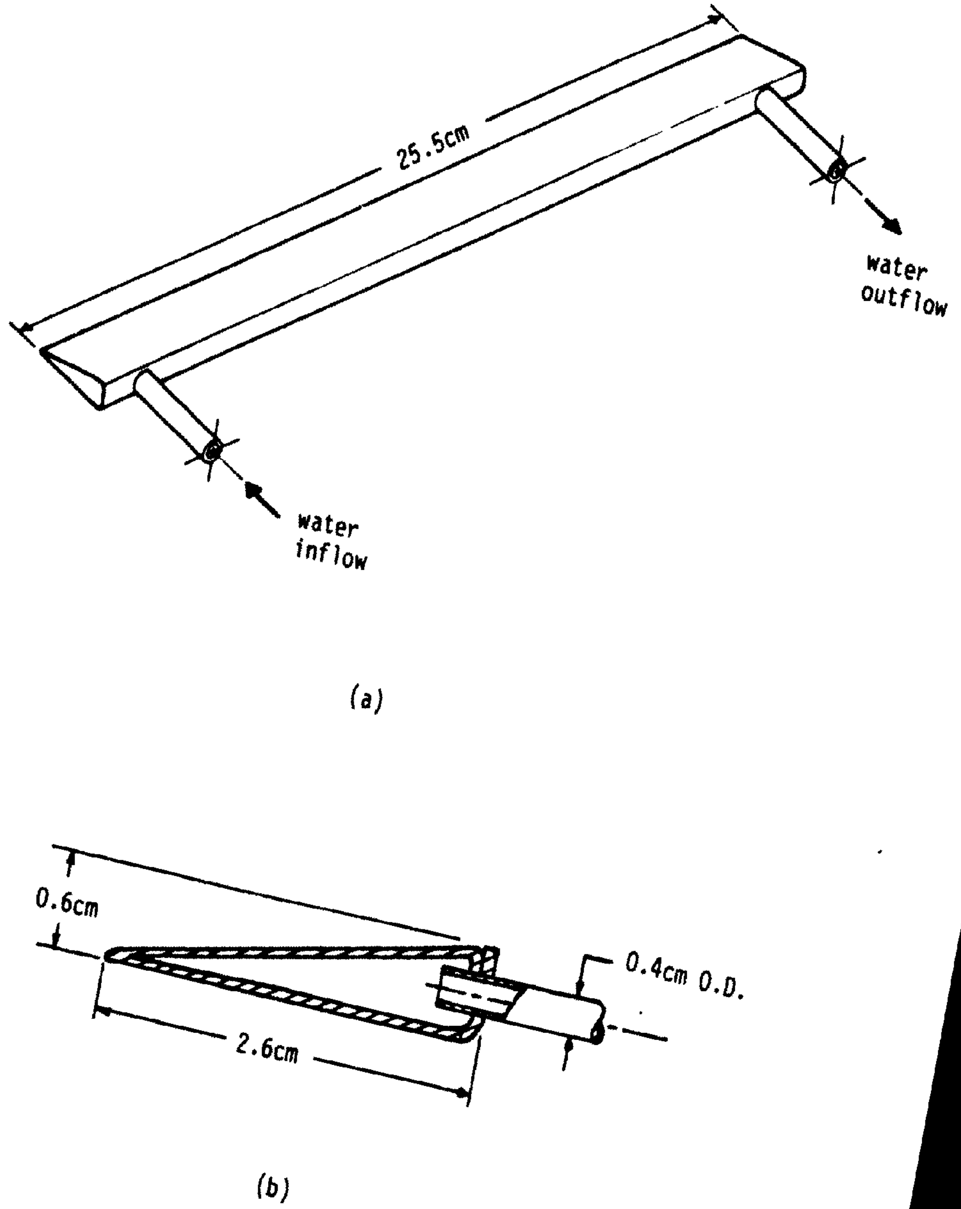
25.5cm
water outflow
water inflow
0.6cm
2.6cm
0.4cm O.D.

(a)

(b)

Figure 6.4: (a) Isometric and (b) cross-sectional views of the heat exchangers.

Note: Plate is shown thicker than actual model so that details are clearer.

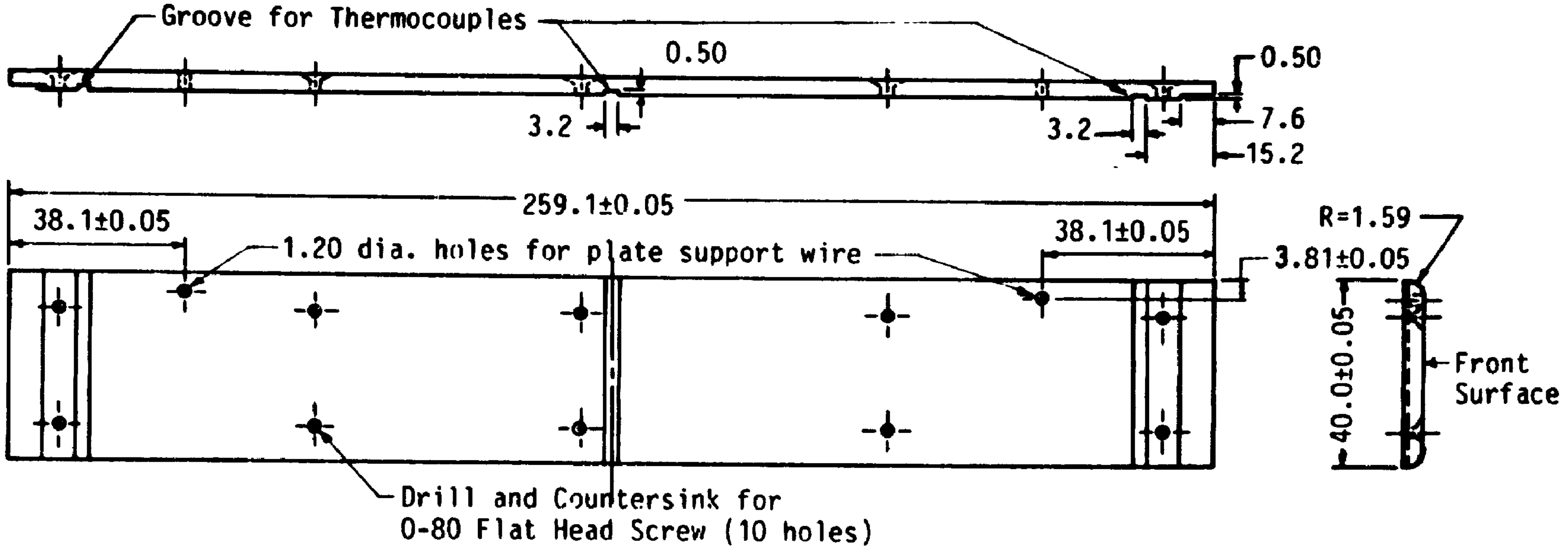
Groove for Thermocouples
0.50
3.2
3.2
0.50
7.6
15.2
259.1±0.05
38.1±0.05
38.1±0.05
1.20 dia. holes for plate support wire
3.81±0.05
R=1.59
40.0±0.05
Front Surface
Drill and Countersink for
0-80 Flat Head Screw (10 holes)

Dimensions are in millimeters

Figure 6.5: Mechanical drawing of one side of the copper divider plate.

machined plates were slightly thicker at each end because of the wire connections. To allow for the increased thickness, a small amount of material was milled from the inside surface at each end of both plates. Ten flat head screws were used to assemble the two halves of the dividing plate. Care was taken to ensure that the screws were countersunk below the surface. After assembly, the plate thickness was measured to be 2t=3.50±0.04mm over the entire surface.

Four thin foil electric heaters (manufactured by Minco Products Inc.) were installed in the middle of the dividing plate. Each foil resistance heater had dimensions 26x0.6x0.016cm, was insulated with Kapton™, and had a resistance of about 50 ohms. A photograph of the fully assembled dividing plate and a single thin foil heater is shown in Fig. 6.6. The lead wires to the heaters at each end of the plate show the location of each heater.

As shown in Fig. 6.1, the dividing plate was supported in the channel at each end by a 1.2mm diameter steel music wire. The music wire was attached to a piece of threaded steel rod so that the plate position could be finely adjusted. At each end of the channel, fine positioning pins (0.53mm dia.) were provided on both sides of the plate. These pins stabilized the lower portion of the plate and enabled the plate to be accurately positioned in the centre of the channel. Using these adjustments, the plate could be centrally positioned in the channel within 0.1mm. Holes were drilled in the walls so that the plate could be installed at both the bottom (L_1/L_c=0) and the top (L_1/L_c=2/3) of the channel.

Nine copper-constantan (24 gauge) thermocouples were installed in the

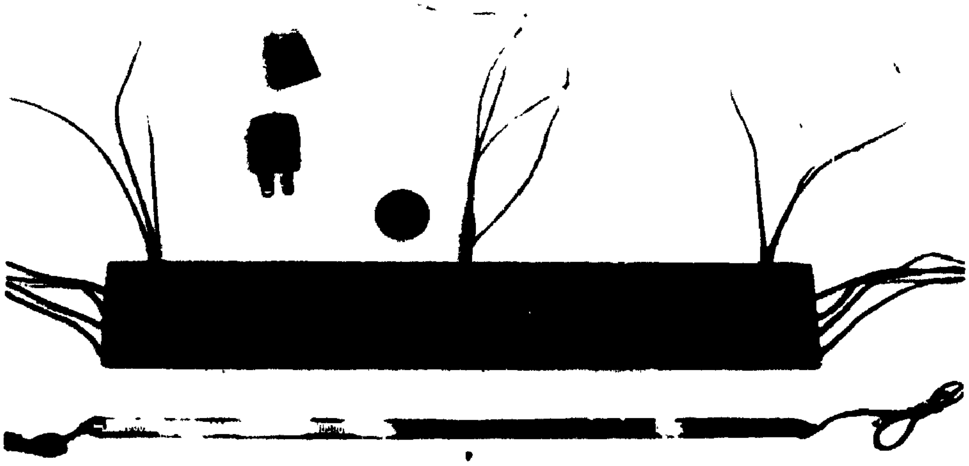

Figure 6.6: The assembled divider plate and one thin foil heater.

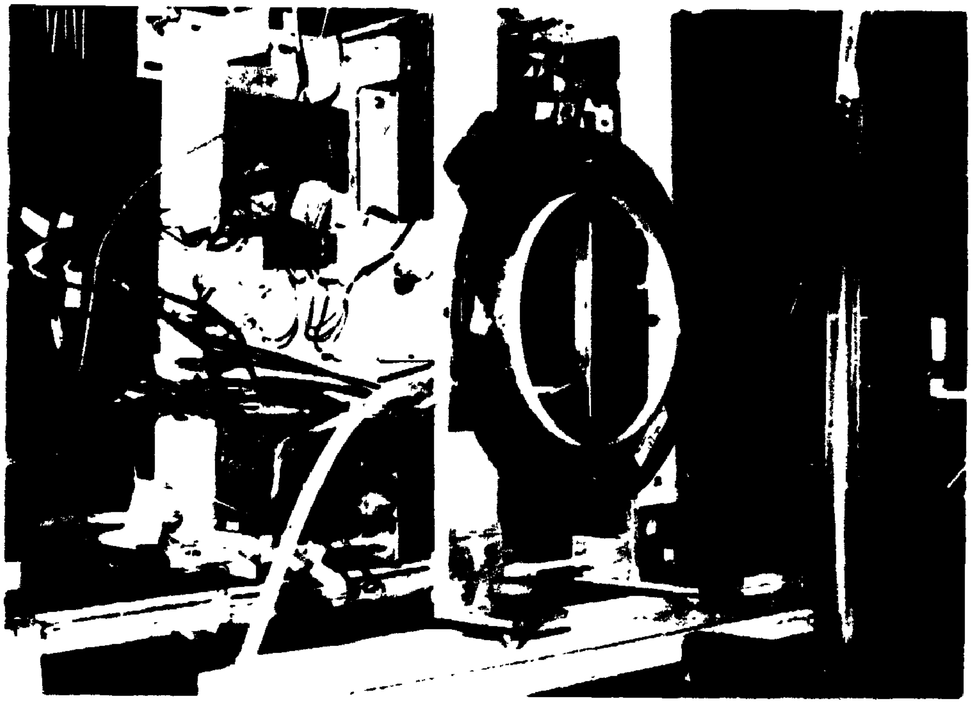

Figure 6.7: The test section in the Mach-Zehnder interferometer (L_i/L_c=0).

plate. The thermocouple tips were positioned at the top, middle and bottom of the thermocouple grooves shown in Fig. 6.5. Care was taken to ensure that the thermocouple tips were not directly beneath the resistance heating elements. Thermocouple leads were brought out of the top of the plate and up the centre line of the channel (see Fig. 6.10). For all experiments, the plate was isothermal to within 0.4C°.

Undulations and bowing of the dividing plate would reduce the accuracy of locating the surface on the interferograms. After installing the heating elements and thermocouples, the flatness of the plate assembly was measured on a machinist's stone. It was found to be flat to within ±0.15mm over its entire length.

The junctions of the fine thermocouples (24 gauge) installed in the dividing plate were made by soldering the tips under a magnifying glass. Although these thermocouples are very fragile, this method provided a robust tip that did not separate during installation. The tips of the 40 gauge thermocouples used to measure the wall, ambient, and water temperature were jointed using a spot welder.

Before assembling the test model, the wall and dividing plate surfaces were polished using commercially available aluminum and copper cleaners. Polished surfaces aid in aligning the beam with the test section; also, dust particles are removed that would scatter light and make the surface difficult to locate on the interferograms. To a small extent, polishing reduces the radiative heat exchange by lowering the emissivity, and the lower heat transfer promotes isothermal conditions.

Heat conducting paste (Omegatherm 201, Omega Engineering Inc.) was used in several locations to reduce the thermal contact resistance. Each electric strip heater in the wall and dividing plate assemblies was coated with paste during installation The holes in the walls and the grooves in the dividing plate were packed with the heat conducting paste prior to inserting the thermocouples. Also, paste was spread on the bottom of both heat exchangers to reduce the air gap between the copper and the phenolic sheet.

The fully assembled model is shown in the interferometer in Fig. 6.7. In this photograph, the dividing plate is located at the bottom of the channel ($L_i/L_c=0$). Each end of the test section was sealed off with a 15.2cm diameter optical window. The windows prevent entrainment of air into the sides of the channel. Both windows were 2.54cm thick, parallel to 5 arc seconds and optically flat to within $\lambda/16$ of helium-neon laser light.

6.3 Experimental Apparatus

The test section and associated instrumentation was integrated with a 20cm (8 inch) mirror Mach-Zehnder interferometer. A schematic layout of the experimental apparatus is given in Fig. 6.8. The interferometer was initially designed by Tarasuk [70] and operated with the test and reference beams in the same horizontal plane. Recently, using the same optical components, Papple [71] has modified the setup such that the reference beam and test beam are in the same *vertical* plane. Either configuration would suffice for the present study. For convenience, Papple's [71] modified setup was used.

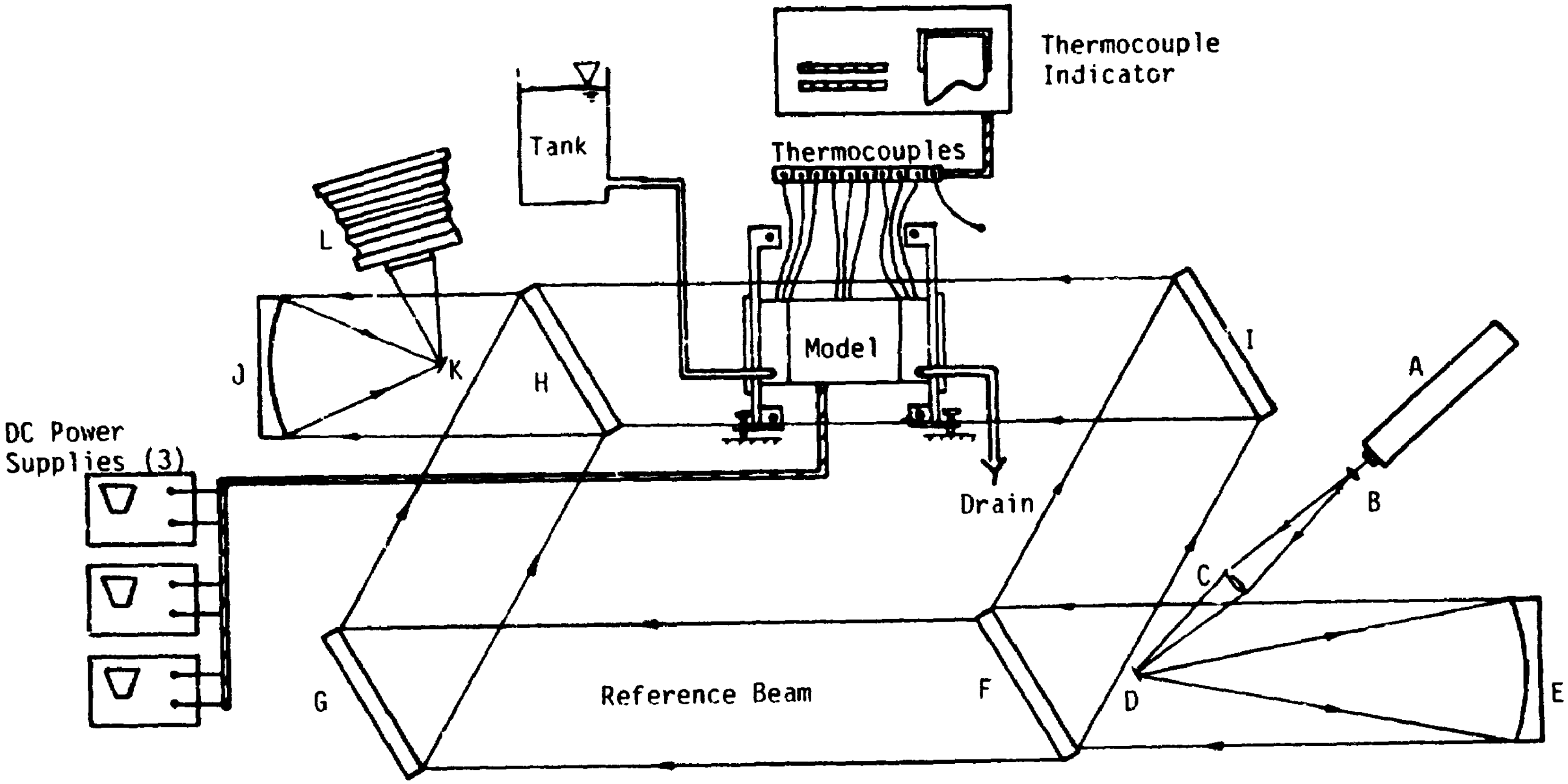
Thermocouple Indicator
Tank
Thermocouples
L
Model
J
K
H
I
A
DC Power Supplies (3)
Drain
B
C
G
Reference Beam
F
D
E

A - Helium-Neon laser
B - expanding lens
C - condensing lens
D - 5mm dia. flat mirror

E - 20cm parabolic mirror focal length 162.5cm
F,H - 20cm beamsplitters
G,I - 20cm flat mirrors

J - 20cm spherical mirror focal length 78.7cm
K - 10mm flat mirror
L - camera

Figure 6.8: Schematic diagram of the experimental apparatus.

The model surface temperatures, as well as the ambient and cooling water temperatures were recorded by a Doric Digitrend 220 data logger. The resolution of the data logger was 0.1C°. The thermocouples were connected in absolute mode, as opposed to differential mode. Prior to installing the thermocouples in the test section, they were checked at the ice point and boiling point of distilled water. All the thermocouples read correctly at the ice point and about 0.2C° low at the boiling point.

Two shielded thermocouples, located near the channel entrance, were used to measure the ambient air temperature (T_0). For all experiments, the two thermocouples gave the same temperature within 0.1C°.

The power input to each wall of the channel and to the centre plate was controlled from three separate direct current power supplies. It was not possible to get each surface at exactly the same average temperature. Typically, the average temperature of both walls and the dividing plate was within 0.3C° (≈ 1.4% of the overall temperature difference). The maximum difference for all experiments was not greater than 0.5C° (≈2.4% of the overall temperature difference).

A 15 litre tank supplied cooling water to the heat exchangers installed in the channel walls. The tank was situated approximately 2 meters above the drain so that the required flow (≈0.3 litres/min) could be achieved by gravity. To approximate adiabatic conditions, it was desired to maintain the horizontal surfaces near the channel inlet at room temperature. For this reason, the water supplied from the tank was always within 1C° of room temperature.

Interference fringe patterns were recorded using a Calumet 10cmx12.5cm view camera with the lens removed. The film used to photograph the interference patterns was Polaroid 10cmx12.5cm Land film, type 55 (positive/negative). The film negatives were used for analysis purposes since they have greater resolution (150-160 lines per mm) than the film positives.

6.4 Interferometer Alignment

The interferometer rests on three air bags, which partially isolate the optics from building vibrations. Prior to any test, the interferometer was levelled by adjusting the pressure in these air bags.

Once level, the interferometer optics were aligned. The first step in the alignment is to ensure that the expanded beam is collimated when it leaves parabolic mirror E (see Fig. 6.8). If collimating lenses B and C focus the laser to a point at small mirror D, beam parallelism results if the small mirror D is exactly at the focal point of the parabolic mirror E. The technique used to obtain the position of mirror D is illustrated in Fig. 6.9. With beamsplitter F temporarily removed, mirror G was rotated to be perpendicular to the beam. Then, mirror D was located by trial and error such that the light reflecting off mirror G would refocus exactly back at mirror D. If mirror D was not at the focal point, the returning beam would focus at a different location on the centre line. Once collimation was achieved, the focal point was marked so that it could be checked before all subsequent experiments. The procedure given by Tarasuk [70] was used for the remainder of the alignment.

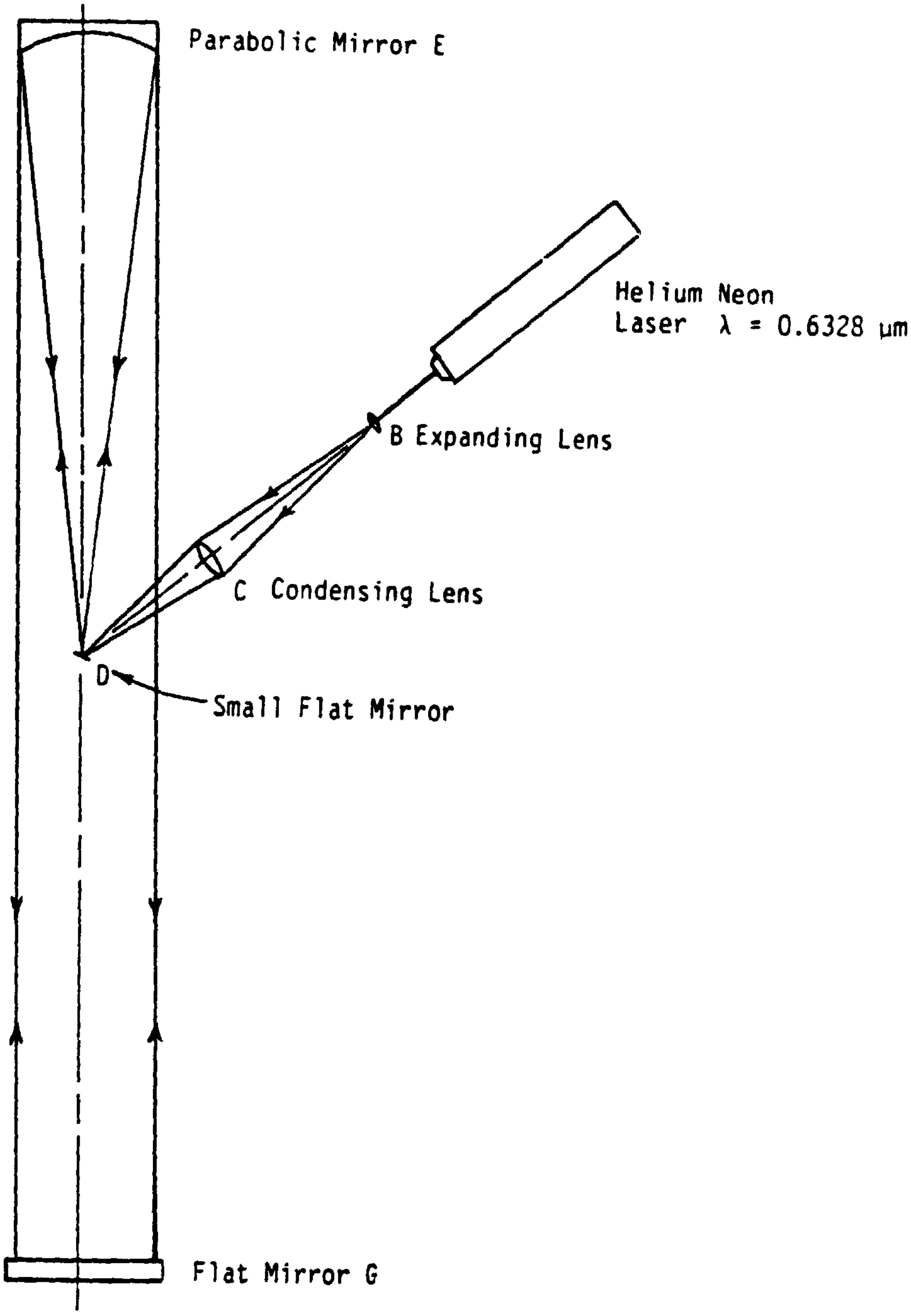
Parabolic Mirror E
Helium Neon
Laser λ = 0.6328 μm
B Expanding Lens
C Condensing Lens
D
Small Flat Mirror
Flat Mirror G

Figure 6.9: Optical setup for obtaining a parallel beam

As an aside, it should be noted that shear plate collimation testers are now commercially available (from Melles-Griot Corp. [72]). These testers allow fast, accurate beam collimation without the above procedure. Also, there is the added convenience that collimation can be confirmed in seconds, prior to each new experiment. For this reason, it is recommended to use a collimation tester in the future, rather than the above method.

When the alignment is completed, visible "finite (wedge) fringes" appear in the output of the interferometer. Figure 6.10(a) is a photograph of the unheated model showing these finite fringes. Note that the shadows of mirrors D and K appear in the output. Once finite fringes were obtained, these fringes were spread apart by rotating mirror G to the extent that the output field was almost entirely light or dark. Complete constructive or destructive interference of the output beam is called the "infinite fringe" condition and is a consequence of the nearly perfect parallelism of the recombining beams at beamsplitter H. A typical infinite fringe condition with the model unheated is shown in Fig. 6.10(b). Note that the infinite fringe setting is not perfect; in Fig. 6.10(b), there is about one full fringe shift over the field of view. Only minor adjustments of the optics were required to maintain alignment after the initial setup.

6.5 Test Procedure

A total of 12 experiments were performed. The range of variables covered is summarized below:

L_p/L_c = 0, 1/3

L_i/L_c = 0, 2/3

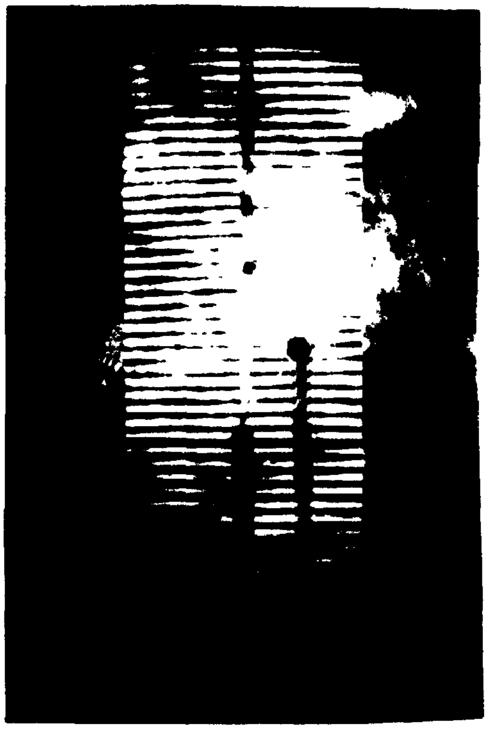

(a) Finite fringe condition

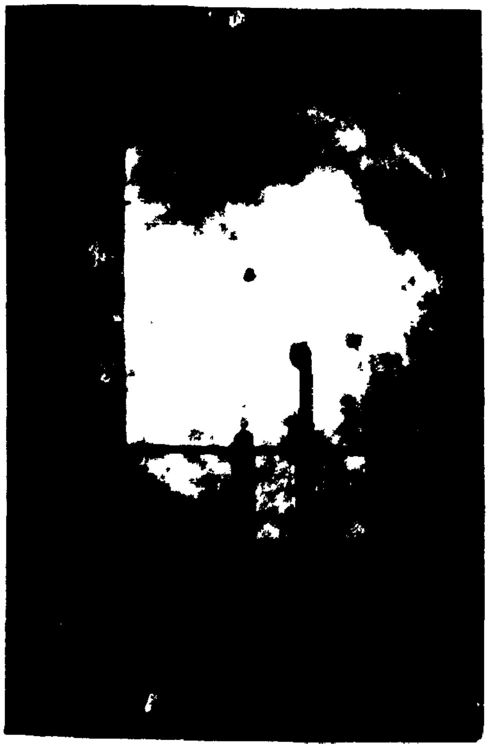

) Infinite fringe condition

Figure 6.10: (a) Finite fringe condition for the unheated model.
(b) Infinite fringe condition for the unheated model.

$81.4 \le Ra_c^* \le 5{,}930$

$0.069 \le t/b \le 0.2$

$4.73 \le L_c/b \le 13.68$

For these experiments, the channel-to-ambient temperature difference was held roughly constant ($T_s - T_0 \approx 18$ to 25 C°) and Rayleigh number was increased by widening the channel gap (2b). For each experiment, the channel wall spacing (2b) was set using a 2.54cm long jig made from standard aluminum and brass bar stock. Six jigs were used to obtain the following wall spacings: 2b = 17.4mm, 17.55mm, 25.4mm, 31.95mm, 38.15mm, 50.7mm. Using these jigs, the gap width could be set to within ±0.05mm.

The interferometer is very sensitive to building vibrations; high vibration levels cause poor quality interferograms. The main sources of vibration seem to be the activities of people in the building and automobile traffic. For this reason, all interferograms were taken at night between the hours of 11 p.m. and 5 a.m.. During these hours the vibration of the interferometer output was substantially reduced.

The following procedure was used for each experiment:

Initially, the tank that supplied water to the heat exchangers was filled. The water temperature was adjusted to be within 1C° of ambient temperature.

With the optical windows removed, the channel wall spacing (2b) was set by adjusting the threaded rod spacers at each corner of the model. The wall spacing was adjusted until it was the same as the appropriate jig over the entire channel area. Once the wall spacing was set, the dividing plate was centrally located between the channel walls using vernier callipers.

After the wall spacing and plate positioning were set, the optical windows were placed on the test section. The test section was then positioned near the centre of the interferometer test beam, and levelled. A plumb bob was used to set the channel walls parallel to the gravity vector. Alignment of the test beam with the channel was done by placing a white card in the beam, just beyond the test section, and rotating mirror I such that the beam and channel were parallel. Misalignment of the beam was easily detected because of reflections off the polished surfaces. Once alignment was obtained, the infinite fringe condition was regained by rotating beamsplitter H and mirror G.

In accordance with a study by Mehta and Black [73], the camera was focused at one third the distance from the exit plane of the test section to minimize refraction error. At this time the reference beam was blocked and a picture (scale photograph) of the unheated channel was taken at a camera shutter speed of 1/60th of a second. The film negative was examined with a travelling microscope to check alignment, uniformity of wall spacing, dividing plate positioning and scale factor. The test section was then ready for the experiment.

The power supplies for the walls and dividing plate were turned on and adjusted to heat each surface to $T_s - T_o \approx 21C^\circ$. A temperature difference of 21C° gives about seven fringe shifts. Generally, three or four power adjustments were required to get all three surfaces to the same average temperature. A period of 10 to 15 minutes was allowed for a new steady-state condition to be reached after each adjustment. Once the temperatures of the walls and the plate were the same and steady, the atmospheric pressure was measured using a mercurial barometer.

Next, the cooling water supply to the heat exchangers was turned on to cool the horizontal surfaces at the channel inlet. Although these surfaces cooled almost instantly, a time delay of about 5 minutes was allowed before proceeding with the experiment.

A photograph of the infinite fringe pattern was taken next. Slight rotation of mirror G was usually required to regain an infinite fringe condition prior to taking the photograph. The infinite fringe condition was set by ensuring, as closely as possible, that the destructive fringe closest to channel walls did not intersect the surface. All interferograms were taken at a camera shutter speed of 1/125th of a second.

Immediately after taking the infinite fringe interferogram, the finite fringe pattern was photographed. It is necessary for analysis that the finite fringes in the undisturbed field (i.e. in the unheated air near the channel inlet) be perpendicular to the channel walls. This condition was most easily achieved by rotating mirror G about the horizontal axis.

6.6 Interferogram Analysis

A detailed discussion of the fundamental theory and optical considerations of interferometry is given by Eckert and Goldstein [66]. A brief explanation is given here for completeness.

Interferometry utilizes the wave nature of light. The amplitude (A) of a monochromatic light wave in a homogeneous medium can be expressed as:

$$A = A_o \sin\frac{2\pi}{\lambda}(c\tau - z) \qquad (6.1)$$

where A_o is the peak amplitude, c the speed of light, τ the time, z the distance and λ the wavelength. Hence, the amplitude of the reference beam at a fixed point can be expressed as:

$$A_{ref} = A_{o_{ref}} \sin\frac{2\pi c\tau}{\lambda} \qquad (6.2)$$

Similarly, amplitude of the test beam at the same position is:

$$A_{test} = A_{o_{test}} \sin\left(\frac{2\pi c\tau}{\lambda} - \phi\right) \qquad (6.3)$$

where ϕ is the phase shift between the two beams because of the difference in the optical path lengths. Note that the phase shift ϕ is only a function of the distance (z) and is not a function of time.

Now consider these two beams recombining beyond the second beamsplitter (H). Since both beamsplitters cause fifty percent of the light to be transmitted and fifty percent to be reflected it may be assumed that $A_o = A_{oref} = A_{o\ test}$. The amplitude of the interferometer output is given by:

$$A = A_{test} + A_{ref} = A_o\left(\sin\left(\frac{2\pi c\tau}{\lambda} - \phi\right) + \sin\frac{2\pi c\tau}{\lambda}\right) \qquad (6.4)$$

From equation (6.4) it is evident that constructive interference will occur when $\phi/2\pi$ is an integer. Also, complete destructive interference will occur when $(\phi/2\pi)+\frac{1}{2}$ is an integer. It is these constructive and destructive interference fringes that can be calibrated to give the temperature field in the test beam.

The Mach-Zehnder interferometer integrates changes in the index of refraction along the light path. The integrated index of refraction (N) is called the optical path length (PL) and is defined by:

$$PL(x,y) = \int N(x,y)dz \tag{6.5}$$

where x,y are the traverse coordinates to the light path and z is the coordinate in the direction of the light beam. The fringe shift $\epsilon(x,y)$ is the difference in the optical path length between the test beam and the reference beam, expressed in terms of vacuum wavelengths (λ). Note that the refractive index of the test beam is constant and equal to that of the reference beam except over the heated length of the test section (Z_T). Therefore, the fringe shift is given by:

$$\epsilon(x,y) = \frac{\Delta PL(x,y)}{\lambda} = \frac{1}{\lambda} \int_0^{Z_T} (N(x,y) - N_{ref})dz \tag{6.6}$$

where N(x,y) is the refractive index of the test medium,

N_{ref} is the refractive index of the reference medium,

Z_T is the heated length of the test section in the direction of the light beam (z).

In the present study, the refractive index field is considered to be two-dimensional in the (x,y) plane (neglecting end effects). For this condition, equation (6.6) becomes:

$$\epsilon(x,y) = \frac{Z_T}{\lambda}(N(x,y) - N_{ref}) \tag{6.7}$$

The Lorentz-Lorenz equation [74] relates the index of refraction to density as follows:

$$\frac{N^2-1}{\rho(N^2+2)}=G(\lambda) \qquad (6.8)$$

where G(λ) is the specific refractivity of the test medium for a given wavelength of light. For air and a helium-neon laser (λ=0.6328x10^{-6}m), G=0.1504x10^{-3}m^3/kg. Since air has a refractive index very near unity (N=1.0002716 at 20°C, 1 atm [74]) equation (6.8) can be simplified to:

$$\frac{2(N-1)}{3\rho}=G \qquad (6.9)$$

In this study, the air density (ρ) was calculate using the ideal gas law:

$$\rho=\frac{P}{R_{air}T} \qquad (6.10)$$

Substituting equation (6.10) into (6.9) and solving for N gives:

$$N=\frac{3GP}{2R_{air}T}+1 \qquad (6.11)$$

Substitution of equation (6.11) into equation (6.7) yields a practical equation for determining the fringe shift $\epsilon(x,y)$ between two known temperatures:

$$\epsilon(x,y)=\frac{3GZ_Tp}{2R_{air}\lambda}\left(\frac{1}{T(x,y)}-\frac{1}{T_{ref}}\right) \qquad (6.12)$$

Solving equation (6.12) for T(x,y):

$$T(x,y)=\frac{T_{ref}}{\frac{2\epsilon(x,y)R_{air}\lambda T_{ref}}{3G\ Z_T\ p}+1} \qquad (6.13)$$

Using equation (6.13), the temperature at any location can be calculated for a known fringe shift relative to a known reference temperature. In the present study, the model surface temperature (T_s) was used as the reference temperature. However, the fractional fringe shift between the model surface and the first fringe is initially unknown. This fraction fringe shift was determined by extrapolation using the two constructive interference fringes closest to the model surface.

Interferograms were analyzed using a digital imaging system developed by the author. The sole function of the imaging system was to determine the spacing of destructive interference fringe centres at scans perpendicular to the model surface. Destructive interference fringes were used because they appeared narrower than the constructive fringes on the film negatives. For all experiments, only one half of the channel was scanned because of symmetry. A detailed description of the digital imaging system is given in Appendix B.

6.6.1 Calculation of the Local and Average Wall Nusselt Numbers

Finite fringe interferograms were analyzed to determine the wall local heat transfer coefficients. Finite fringe interferograms are less sensitive to vibrational disturbances and give more accurate results than infinite fringe interferograms. A full discussion of the relative merits of finite versus infinite fringe interferograms is given by Saidi [75].

Equating the heat transferred by convection to the heat transferred by conduction at the wall gives an expression for the local heat transfer coefficient:

$$h_{w,y} = \frac{k_s \left.\frac{dT}{dx}\right|_{x=b}}{T_s - T_o} \tag{6.14}$$

where k_s is the thermal conductivity of air evaluated at the wall temperature.

The wall local Nusselt number is defined by:

$$Nu_{w,y} = \frac{h_{w,y}\, b}{k_f} = \frac{k_s \left.\frac{dT}{dx}\right|_{x=b} b}{(T_s - T_o) k_f} \tag{6.15}$$

where k_f is the thermal conductivity of air evaluated at the film temperature, $T_f = (T_s + T_o)/2$.

Equation (6.15) was used to calculate the wall local convective coefficients. The temperature difference $(T_s - T_o)$ was calculated from the difference of the averaged wall and ambient thermocouples readings. The temperature gradients at the surface were evaluated by linearly extrapolating the optically determined temperature profiles obtained from scans perpendicular to the wall. That is, only the two destructive fringes closest to the wall were used to estimate the surface gradients. Linear extrapolation is recommended and has been used successfully by Eckert and Soehngen [76] for the vertical flat plate geometry. Also, Kuehn and Goldstein [77] have successfully used linear extrapolation to estimate the surface temperature gradients on surfaces with large radii of curvature. Typically, higher order extrapolation methods do not satisfy the condition that $d^2T/dx^2=0$ at the surface.

Local convective coefficients were measured at about 70–80 locations along the wall. The distance between measurements was decreased toward the channel inlet because of the rapid increase in the local heat transfer. Unfortunately, it is not possible to get local heat transfer coefficients all the way up to the leading edge of the channel (y=0). This problem has also been reported by Showole [78]. No scanning of the interferogram could be done at the inlet corner, so the leading edge heat transfer had to be estimated based on linear extrapolation using the two measurements closest to the leading edge. After linearly extrapolating the local Nusselt number distribution to y=0, the local coefficients were integrated using the trapezoidal rule to give the wall average Nusselt number. The contribution of the extrapolated portion of the local heat transfer distribution was typically about 3% of the total heat transfer from the wall. Hence, this correction was relatively small.

6.6.2 Calculation of the Local and Average Plate Nusselt Numbers

The plate local Nusselt number is defined by:

$$Nu_{p,y} = \frac{h_{p,y}\, b}{k_f} = \frac{-k_s \frac{dT}{dn}\Big|_s b}{(T_s - T_e)\, k_f} \qquad (6.16)$$

where $dT/dn|_s$ = the surface temperature gradient normal to the plate surface.

The interferograms were analyzed in three separate sections to determine the plate local heat transfer distribution (see Fig. 6.11). The curved leading edge (AB), the straight middle section (BC) and the upper curved section (CD), were each scanned separately.

Finite and infinite fringe interferograms were analyzed to determine the

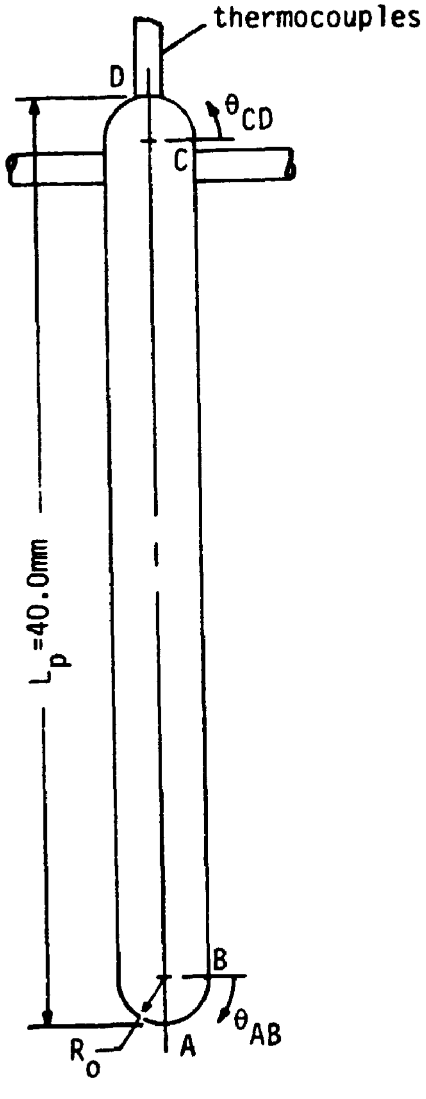
thermocouples
D
θ_{CD}
C
L_p=40.0mm
B
θ_{AB}
R_o
A

Wetted plate length $L_{p,wet}$=42.0mm

Figure 6.11. Sketch of the divider plate showing the three sections scanned, AB, BC, CD.

plate heat transfer distribution. For the present geometry, the finite fringes in the undisturbed field (ie. the unheated air at the inlet) must be perpendicular to the surface to be scanned. Since the finite fringes in the ambient air were set perpendicular to the channel walls, only the local heat transfer on the vertical middle section of the plate (BC) could determined from the finite fringe interferograms. Infinite fringe interferograms had to be used to calculate the local heat transfer on the curved leading and trailing edges (AB and CD).

For the middle section of the plate (BC), the analysis is the same as for the channel wall. The local Nusselt number was calculated using linear extrapolation based on the first two destructive interference fringe centres.

The bottom curved section of the plate (AB) was scanned at 15 degree increments for local heat transfer coefficients. However, the bottom section of the plate had a small radius of curvature, so the surface gradients ($dT/dr|_s$) were obtained using a straight line fit to the first two fringe temperatures versus the logarithm of radius:

$$\frac{dT}{dr}\bigg|_s = \frac{-(T_1-T_2)}{R_o \ln\left(\frac{r_2}{r_1}\right)} \qquad (6.17)$$

where R_o = radius of curvature of the bottom of the plate,

T_1,T_2 = temperatures of the first and second centres from the plate surface,

r_1, r_2 = first and second fringe radii.

Eckert and Soehngen [76] recommend logarithmic extrapolation when the radius of curvature is low. Since the fluid velocity is low near the surface the temperature field is conduction dominated, and logarithmic extrapolation reflects the nature of conduction in a cylindrical layer.

The local heat transfer from the top portion of the plate (CD) was calculated differently from the bottom surface (AB). Although the surface has a low radius of curvature, logarithmic extrapolation was not used because the fringes were far from the surface and well outside the conduction dominated region (see interferograms, Fig. 7.6 and 7.7). Instead, linear extrapolation based on the first two fringe temperatures was used. It should be noted that in this region, the local heat transfer is low and the fringes are widely spaced. The accuracy of the experimental local coefficients in this region is expected to be very poor. However, the contribution to the total plate heat transfer is small, so the accuracy of the plate average Nusselt number is not greatly affected.

Another problem encountered when measuring the local heat transfer on the top of the plate was the blockage caused by the thermocouple wires and lack of working beam height (see interferograms, Fig. 7.6 and 7.7). Where sufficient fringes were visible, the top of the plate was scanned at 15 degree increments. When integrating the local coefficients to get the plate average Nusselt number, it was assumed that the local heat transfer varied linearly from the last measured value (usually at $\theta_{CD}=60^\circ$ for $L_i/L_c=0$ and at $\theta_{CD}=0^\circ$ for $L_i/L_c=2/3$) to zero at the top of the plate ($\theta_{CD}=90^\circ$). Although this is a crude assumption, the heat transfer in this region is very low; hence, it does not significantly affect the accuracy of the plate average Nusselt number.

With the assumptions mentioned above, the plate average Nusselt number was calculated by integrating the local coefficients (using the trapezoidal rule) over the wetted length of one side of the plate. Note that the wetted length of one side of the plate is $L_{p,wet}$=42.0mm; whereas, the plate length in the y direction is L_p=40.0mm.

6.6.3 Calculation of the Channel Average Nusselt Number

The channel average Nusselt number (Nu_c) was calculated using the experimental wall and plate average Nusselt numbers as follows:

$$Nu_c = \frac{L_{p,wet}\, Nu_p + L_e\, Nu_w}{L_{p,wet} + L_e} = \frac{42.0 Nu_p + 120.0 Nu_w}{162.0} \qquad (6.18)$$

CHAPTER 7

PRESENTATION OF EXPERIMENTAL RESULTS

7.1 Introduction

Natural convection experiments were conducted for both the undivided and the divided isothermal channel geometries. A total of twelve finite fringe and twelve (12) infinite fringe interferograms were used for final analysis.

7.2 Experimental Results for the Undivided Channel

Initially, a single experiment was conducted *without* the presence of the dividing plate. This experiment was done for two reasons:

i) Verification of the experimental method prior to introducing the dividing plate into the channel.

ii) Comparison with the numerical results presented in Chapter 4.

An effort was made to achieve a channel Rayleigh number close to $Ra_c^*=91.625$, so that comparisons could be made with the numerical results of previous investigators [39,40] as well as the present numerical results. The infinite and finite fringe interferograms for this experiment are shown in Figure 7.1. The channel aspect ratio is $L_c/b=13.8$ and the Rayleigh number is $Ra_c^*=92.4$. Notice the cooling effect of the heat exchangers on the horizontal surfaces near the leading edge. In Figure 7.1(a), it can be seen that the air adjacent to horizontal surface is only slightly preheated prior to entering the channel. The preheating extends about 1.0cm back

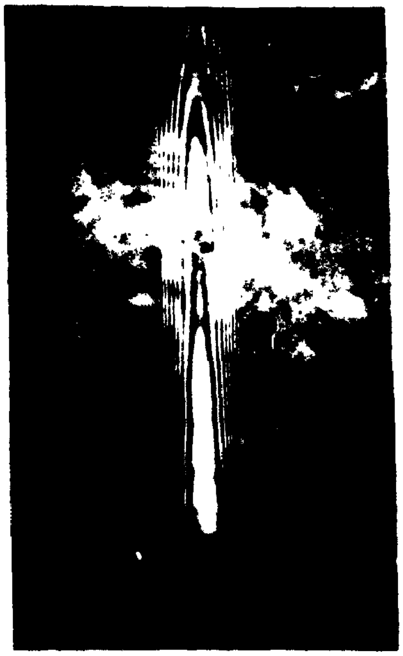

(a) infinite fringe interferogram

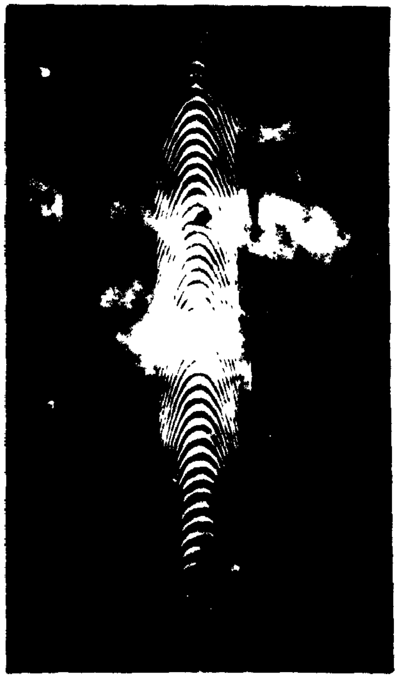

(b) finite fringe interferogram

Figure 7.1: (a) Infinite fringe and (b) finite fringe interferograms of the undivided channel for $Ra_c^*=92.4$, $L_c/b=13.8$.

from the leading edge and is largely mitigated by the presence of the heat exchangers.

Figure 7.2 shows a comparison of the experimental developing temperature profiles with those predicted by Nakamura et al. [40], Kettleborough [39] and the present elliptic solution. (This graph was previously presented in Chapter 4 without the experimental data). Near the channel inlet (y/L_c=1.12), the experimental results do not agree with any of the numerical solutions. This could be expected because of the slight difference in the temperature boundary conditions of the numerical and experimental models at the inlet. At y/L_c=3.59, the present elliptic solution agrees very closely with the experimental data; however, farther up the channel the agreement is not as close. Overall, the present elliptic solution is in better agreement with the experimental data than other solutions. Unfortunately, the agreement is not sufficiently close to settle unequivocally the question of which solution is correct. However, reverse flow draw into the channel from the channel exit predicted by Kettleborough was not seen in the experiment.

Figure 7.3 shows the local Nusselt number distribution along the channel wall compared with the present numerical prediction. The general trend of the local heat transfer distributions is very similar, but the experimental data are consistently lower than the elliptic solution, especially near the leading edge. The average Nusselt numbers compare as follows:

Experiment	Nu_c=1.684
Elliptic Solution	Nu_c=1.867 (diff.≈10%)
Elliptic Solution	Nu_{c2}=1.802 (diff.≈7%)

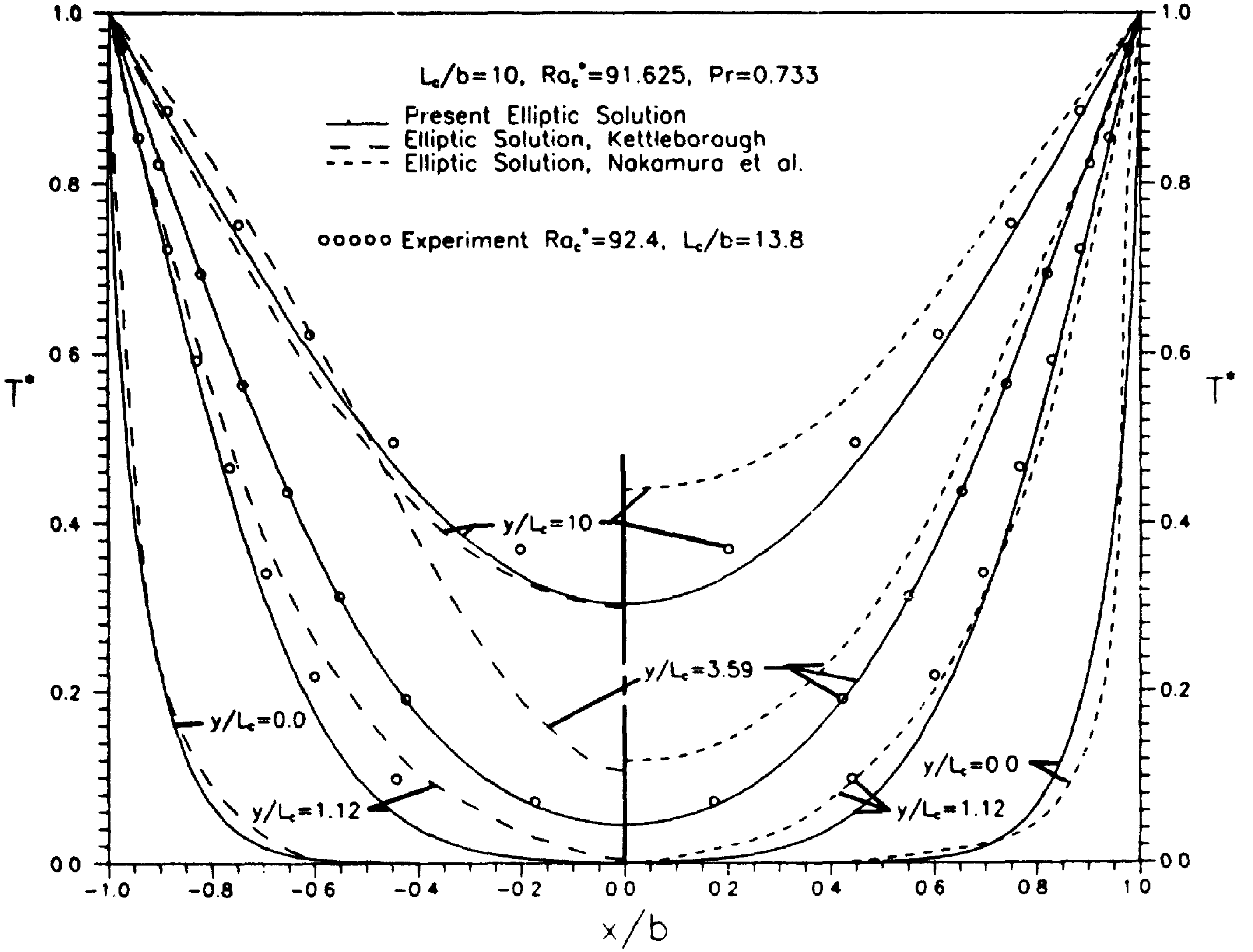

Figure 7.2: Comparison of the experimental temperature profiles for the undivided channel with the numerical results of Nakamura et al., Kettleborough, and the present solution.

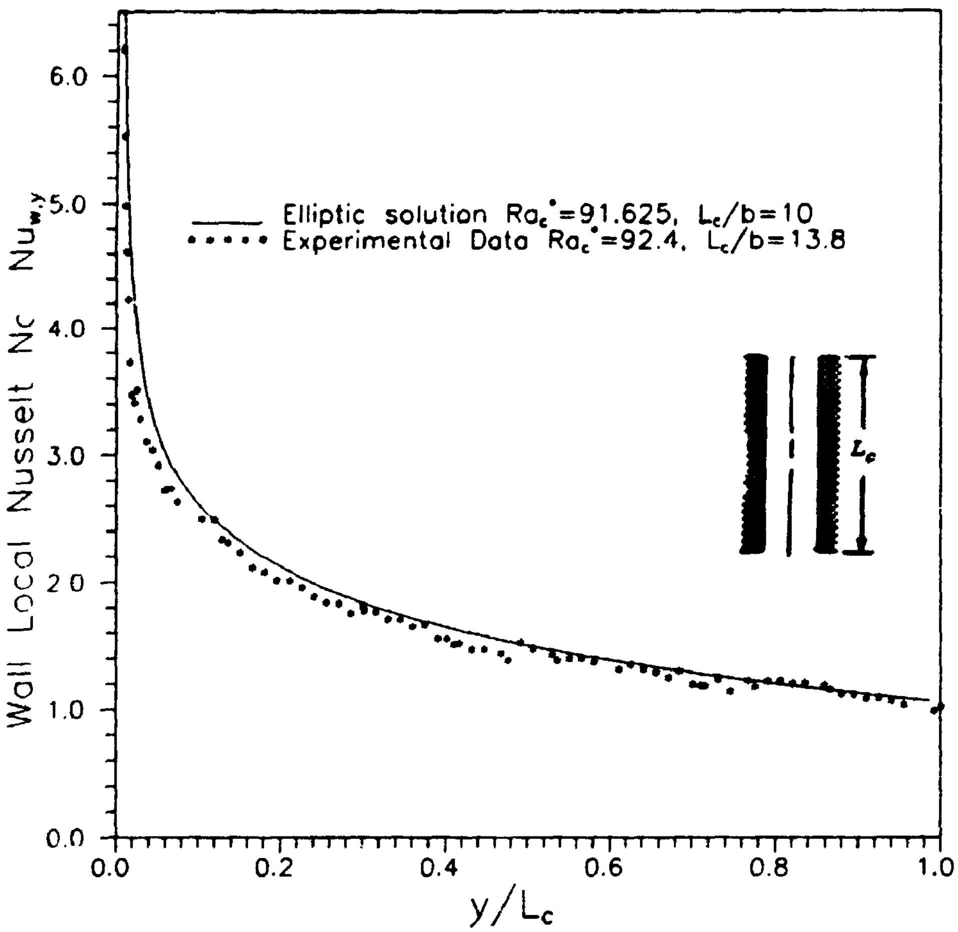

Figure 7.3: Comparison of the experimental and numerical (elliptic) wall local Nusselt number distributions for the undivided channel.

There are several possible reasons why the experimental data are slightly lower than the numerical data. First, it is not possible to get local heat transfer coefficients all the way up to the leading edge of the channel ($y/L_c=0$) using interferometry. No scanning of the interferogram could be done at the inlet corner, so the heat transfer had to be estimated by linear extrapolation (as discussed in Section 6.6.1). This has been estimated to cause the average Nusselt number to be about 2-3% low; however, no other reliable method exists. Also, as previously mentioned, heat exchangers were installed near the leading edge in order to improve the temperature boundary condition of the horizontal surfaces near the inlet. Despite the presence of the heat exchangers, the air is still slightly preheated when it enters the channel. As a result, the local heat transfer coefficients near the leading edge will be somewhat reduced. Yet another factor that could affect the experimental local Nusselt numbers is the temperature profile extrapolation method. As described in Section 6.6.1, fringe temperatures were linearly extrapolated at each "y" location to calculate the local temperature gradient. Although this method is generally preferred to higher order extrapolation, linear extrapolation will generally slightly underestimate the surface gradient. Regardless of these problems, agreement of overall heat transfer within 10% is sufficient for most engineering purposes.

7.3 Experimental Results for the Divided Channel

For the main set of experiments, interferograms were taken over the Rayleigh number range $81 \leq Ra_c^* \leq 5,930$, with the dividing plate located in the bottom ($L_1/L_c=0$) and top of the channel ($L_1/L_c=1-L_p/L_c=2/3$). For these experiments, the plate length ratio was fixed at $L_p/L_c=1/3$.

It is important to note that the surface-to-ambient temperature difference was held roughly constant ($T_s-T_0 \approx 18$ to 25 C°) and the experimental Rayleigh number was increased by widening the channel gap (2b). Since the channel length (L_c) and dividing plate thickness (2t) were fixed, the channel blockage ratio (t/b) and the channel aspect ratio (L_c/b) decrease with increasing Rayleigh number. The lower limit of Rayleigh number for the experiments was determined by allowing a maximum blockage of 20%. The limiting geometries for the experimental model are listed below:

Lowest Rayleigh number: $Ra_c^*=81.4$, $t/b=0.2$, $L_c/b=13.68$
Highest Rayleigh number: $Ra_c^*=5{,}930$, $t/b=0.069$, $L_c/b=4.73$

In contrast, the results from the elliptic solution are for fixed geometric ratios ($t/b=0$, 0.1, 0.2 and $L_c/b=15$) over the full range of Rayleigh number. This causes a slight difficulty when making comparisons with the experimental data. However, the average Nusselt numbers are almost independent of channel aspect ratio, so aspect ratio differences are not of much concern. Also, it was predicted numerically in Chapter 5 that blockage (t/b) has only a weak affect on average Nusselt numbers for moderate and high Rayleigh number. Hence, except at low Rayleigh number, slight differences in the channel blockage ratio (t/b) should not hinder the comparison of the numerical and experimental average Nusselt number data.

Figure 7.4 shows the comparison of an infinite fringe interferogram and the

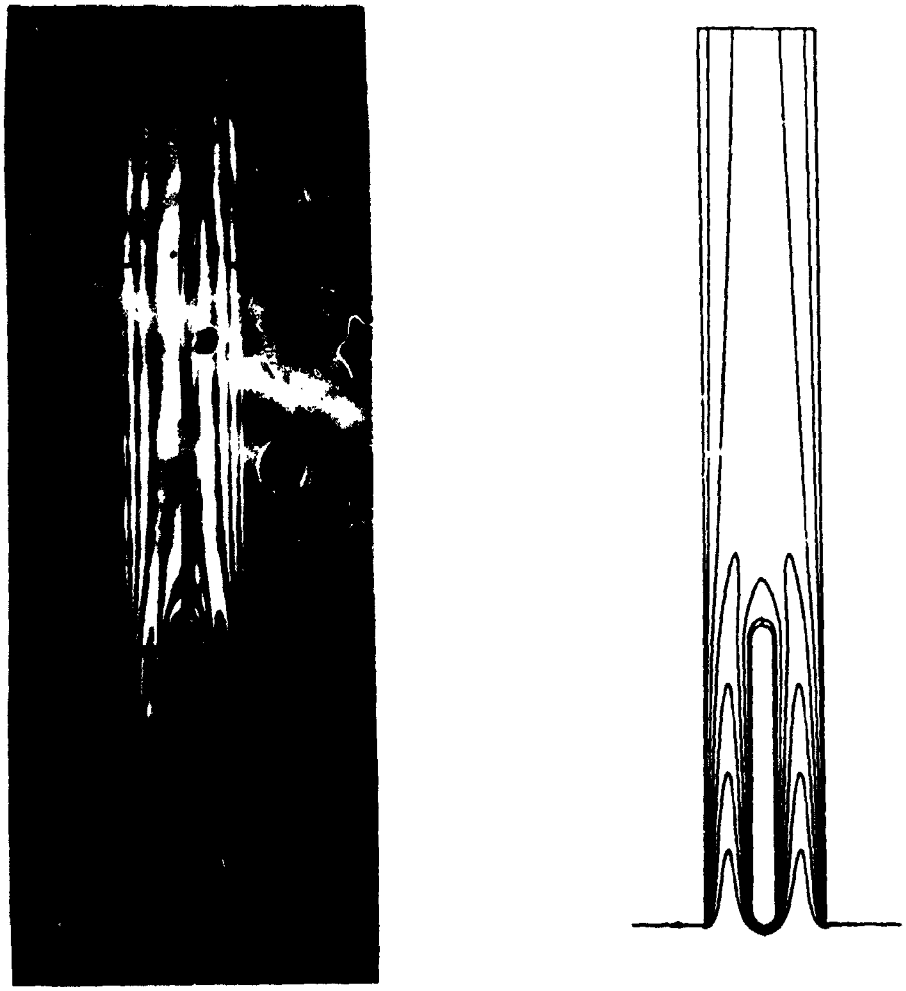

(a) infinite fringe interferogram

(b) numerical isotherm contours (elliptic)

Figure 7.4: Comparison of (a) an infinite fringe interferogram and (b) a numerical isotherm contour plot for $Ra_c^*=97.6$, $L_i/L_c=0$, $L_c/b=13.68$, $t/b=0.20$.

numerical isotherms at $Ra_c^*=97.6$, $L_i/L_c=0$. For this comparison, a finite element grid was used with exactly the same channel aspect ratio ($L_c/b=13.68$) and blockage ratio ($t/b=0.2$) as the experimental model. It can be seen in Fig. 7.4 that the temperature fields are qualitatively very similar, although some differences exist in the plume region above the plate.

Figures 7.5(a) and 7.5(b) show the comparison of the numerical and experimental local heat transfer distributions on the plate and channel walls for the case shown in Figure 7.4. As with the undivided channel data (see section 7.2), the largest differences occur near the leading edge of both the wall and plate. At the tip of the plate, the experimental local Nusselt number is about 20% lower than the numerical prediction. The average Nusselt numbers comparison is shown in Table 7.1. The overall heat transfer results are about 11% lower than the numerical predictions. Nevertheless, given the similarity of the general shape of the local Nusselt number distributions, the agreement is sufficiently close for most practical purposes.

Table 7.1: Experimental and numerical average Nusselt numbers for $Ra_c^*=97.56$, $L_p/L_c=1/3$, $t/b=0.2$, $L_c/b=13.68$.

	Experiment	Elliptic Solution	% diff.
Wall Nusselt Number Nu_w	1.44	1.60	11.1
Plate Nusselt Number Nu_p	3.13	3.48	11.2

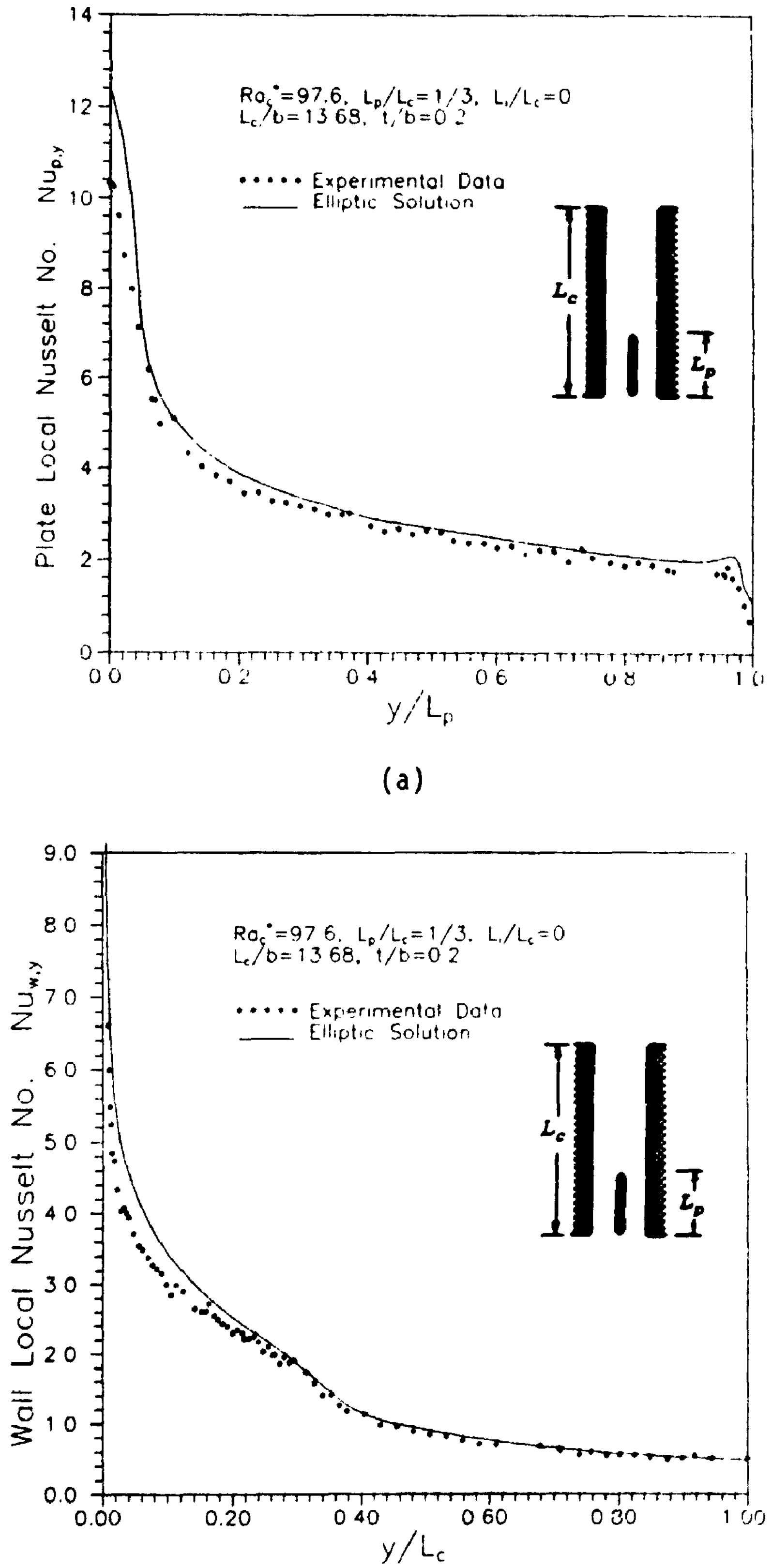

(a)

(b)

Figure 7.5: Comparison of the experimental and numerical (elliptic) local Nusselt number distributions for (a) the wall, (b) the plate. ($Ra_c^*=97.6$, $L_p/L_c=1/3$, $L_i/L_c=0$, $t/b=0.2$)

It is interesting that both the numerical and experimental data in Fig. 7.5(b) show a subtle change slope of the wall local Nusselt number at the end of the dividing plate. At $y/L_c \approx 1/3$, the wall local Nusselt number decreases at a slightly greater rate as the flow adjusts to the undivided portion of the channel. This effect was also seen and was discussed in Chapter 5 for a zero thickness plate (see Fig.s 5.8 and 5.17).

Figures 7.6 and 7.7 are interferograms of the divided channel with the plate located at the bottom ($L_i/L_c=0$) and top ($L_i/L_c=2/3$) of the channel. Figures 7.6(a),(b),(c) and Figures 7.7(a),(b),(c) are infinite fringe interferograms showing the influence of increasing Rayleigh number on the temperature field. Figure 7.6(d) is the finite fringe interferogram for the same experiment as Fig. 7.6(b). Similarly, Fig. 7.7(d) is the finite fringe interferogram corresponding to Fig. 7.7(b). For $L_i/L_c=0$ the thermal boundary-layers of the plate and wall merge close to the channel inlet at low Rayleigh number (see Fig. 7.6(a)). As would be expected, with increasing Rayleigh number the boundary-layers on the walls and plate gradually tend toward the appearance of boundary-layers on isolated plates.

Some of the interferograms shown in Fig.s 7.6 and 7.7 show slight asymmetry of the fringe patterns about the channel centre line. It should be noted that such minor asymmetry can easily result from an imperfect infinite fringe setting and is not necessarily caused by actual asymmetry in the temperature field.

The influence of dividing plate's vertical position on the temperature field

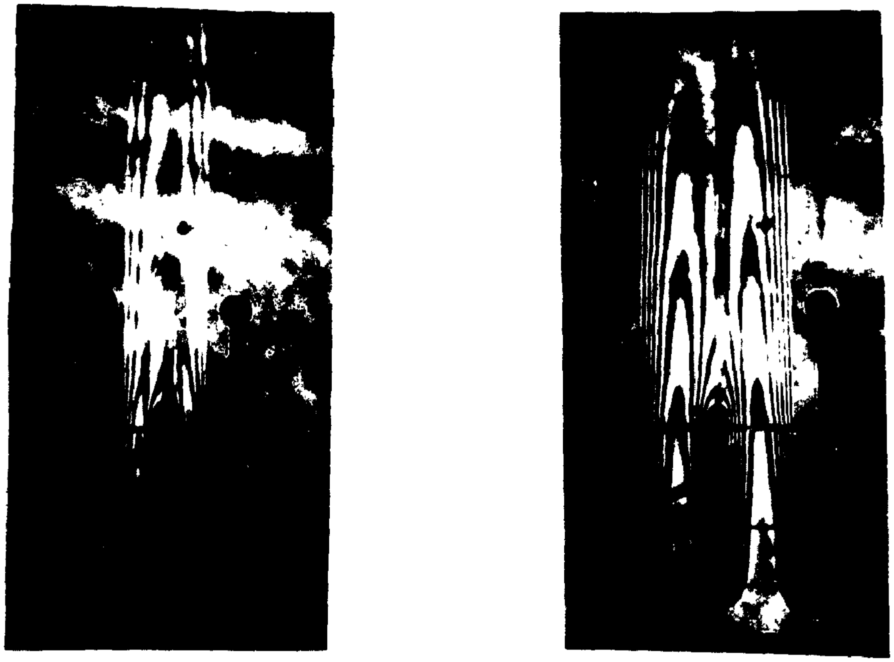

(a) $Ra_c^*=97.6$ (b) $Ra_c^*=874$

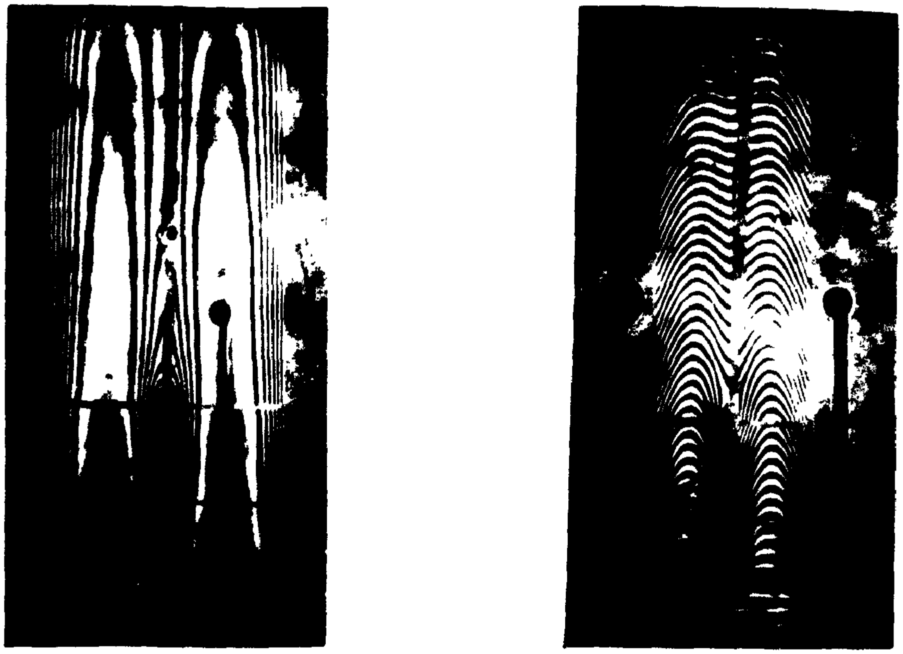

(c) $Ra_c^*=5,930$ (d) $Ra_c^*=874$

Figure 7.6: Interferograms showing the effect of increasing Rayleigh number with the plate located in the bottom of the channel, $L_i/L_c=0,(L_p/L_c=1/3)$.

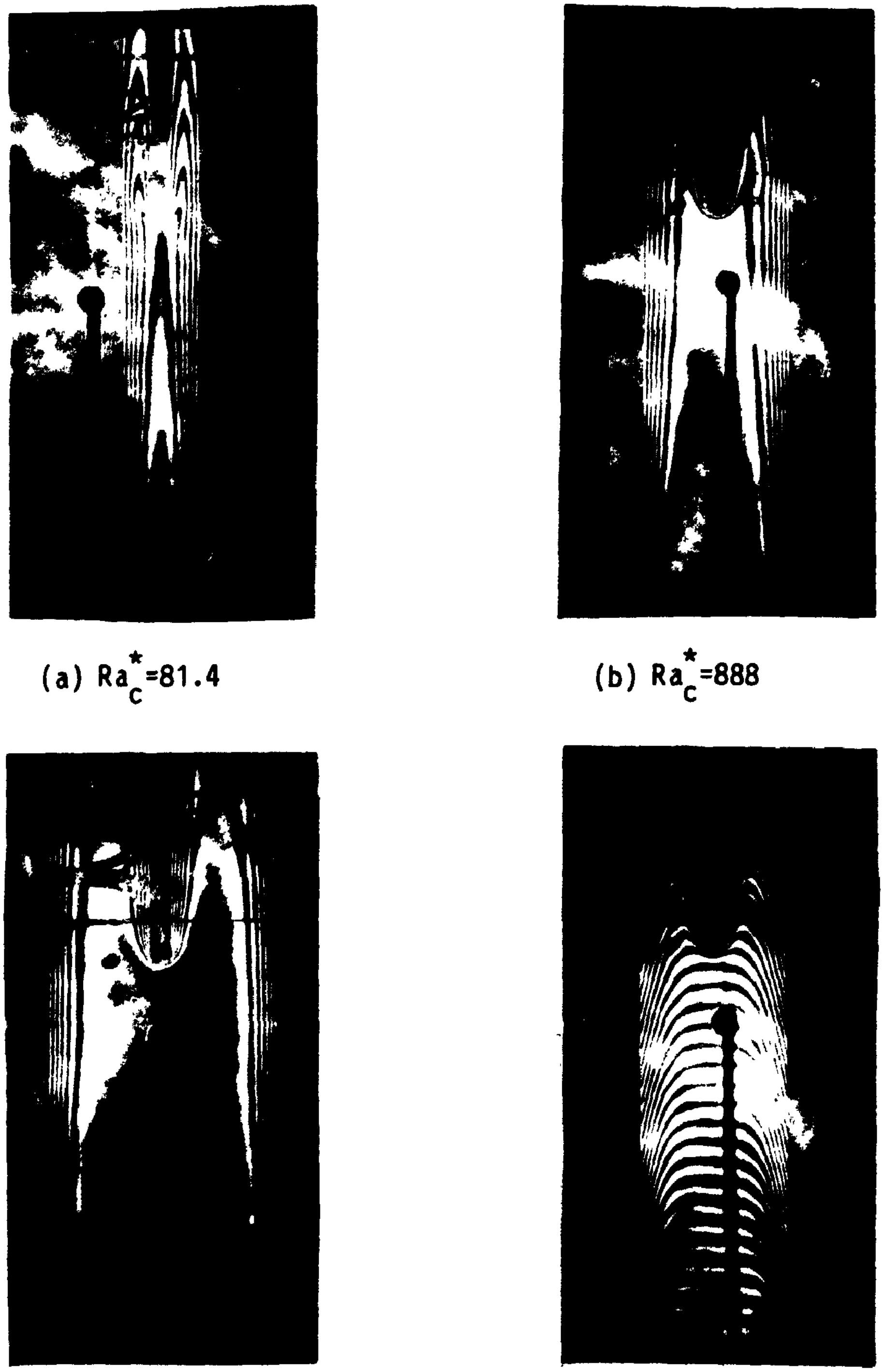

(a) $Ra_c^*=81.4$

(b) $Ra_c^*=888$

(c) $Ra_c^*=5,610$

(d) $Ra_c^*=888$

Figure 7.7: Interferograms showing the effect of increasing Rayleigh number with the plate located at the top of the channel, $L_i/L_c=2/3$, $(L_p/L_c=1/3)$.

is most striking at the lowest Rayleigh number. Comparing Figures 7.6(a) and 7.7(a) shows that the plate heat transfer is reduced when the plate is in the top of the channel largely because air is warmed by the walls before reaching the plate. Also, it is evident that the bulk air temperature in the middle and top portions of the channel is much higher when the plate is at the bottom. This, of course, causes an additional heat transfer enhancement because of the chimney effect.

Figures 7.8(a),(b) and 7.9(a),(b) show some of the experimental plate and wall local Nusselt number distributions. In general, the distributions are as expected and have been included primarily for completeness. It is interesting that when the plate is at the top of the channel (L_1/L_c=2/3), there is a local maximum in the wall heat transfer distribution near the location of the plate's leading edge, $y/L_c \approx 2/3$ (see Fig. 7.9(b)). The local maximum is caused by the presence of the plate and is quite pronounced at the lowest Ra_c^*. In fact, visual inspection of Fig. 7.7(a) shows that the interference fringes (isotherms) are pushed closer to the wall as the flow is diverted by the plate. Again, this effect was also seen and discussed in Chapter 5 for the numerical results with t/b=0 (see Fig. 5.17).

Unfortunately, it was not possible to achieve the experimental conditions needed to verify the inlet separation that was predicted numerically. High Rayleigh numbers and large channel aspect ratios cannot be attained simultaneously using the present experimental apparatus. This is a limitation of the interferometer, not the test model. Since the working height of the test beam is about 13cm, the channel length was limited to L_c=12cm. With this length fixed, large channel aspect ratios require small

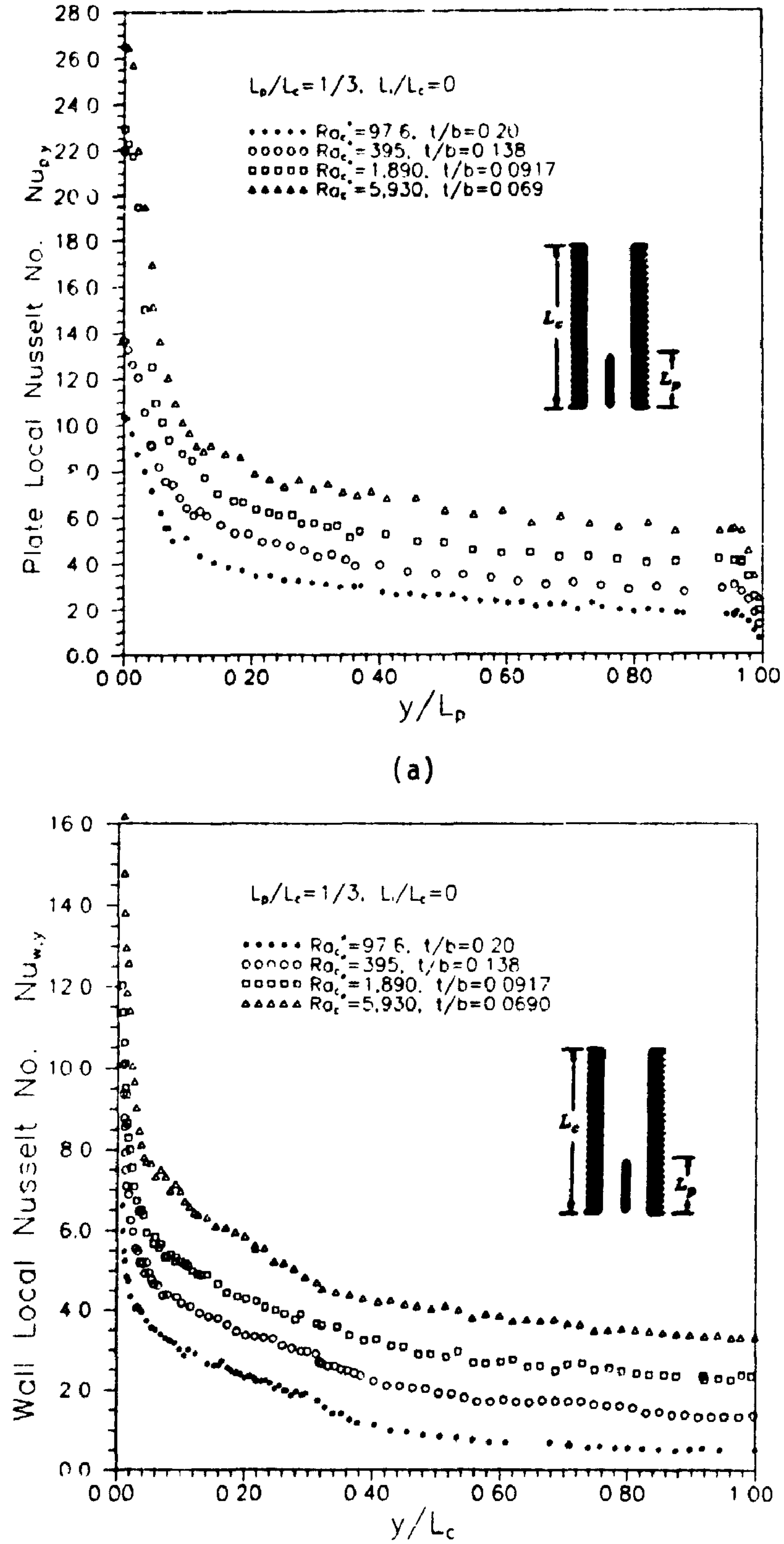

(a)

(b)

Figure 7.8: Experimental local Nusselt number distributions for (a) the plate and (b) the wall, for $L_p/L_c=1/3$, $L_i/L_c=0$.

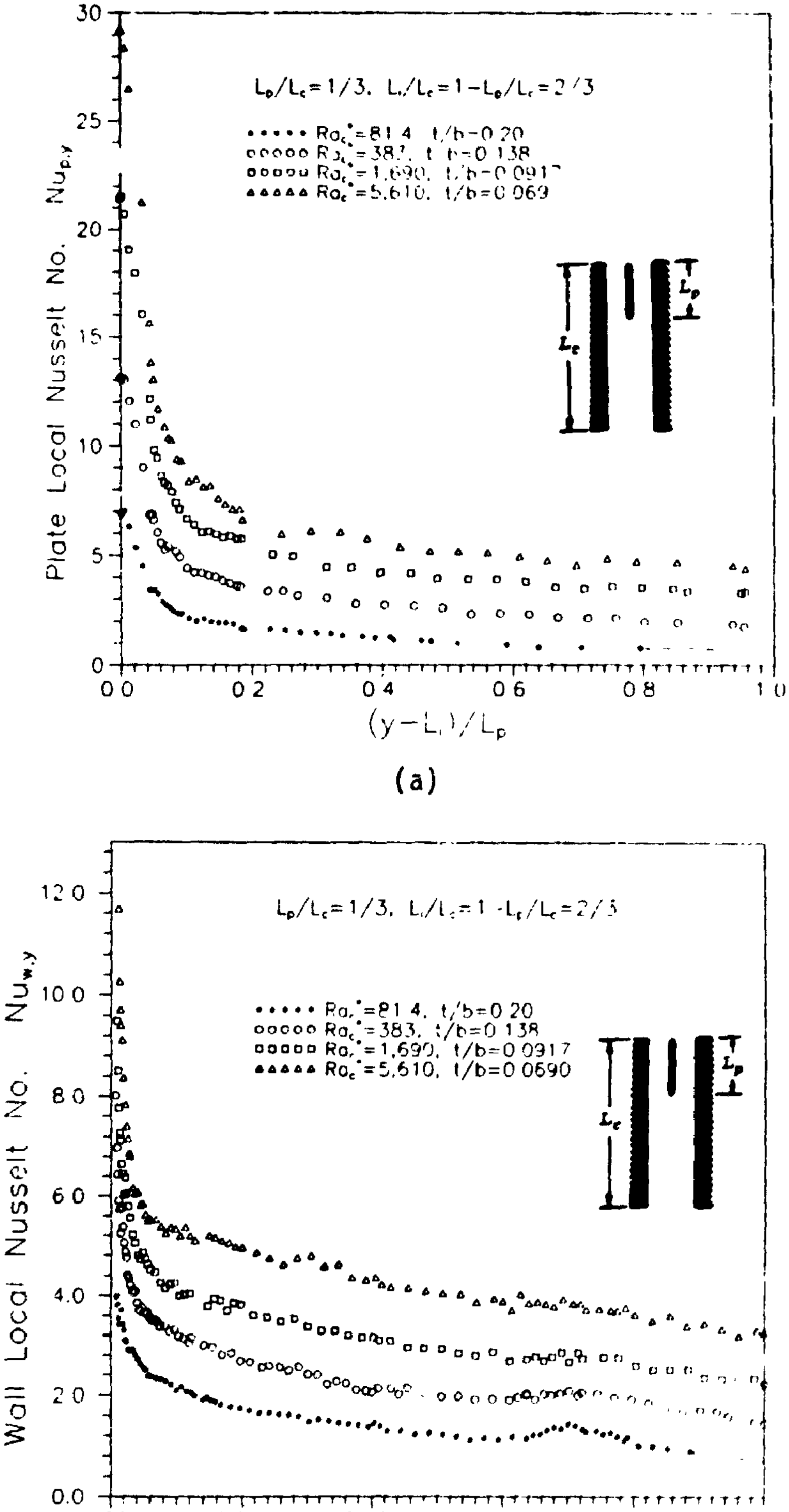

(a)

(b)

Figure 7.9: Experimental local Nusselt number distributions for (a) the plate and (b) the wall, for $L_p/L_c=1/3$, $L_i/L_c=2/3$.

gap widths (2b). Consequently, very high temperatures, which are not compatible with the present interferometric technique, are needed to get even moderate Rayleigh numbers (since $Ra_c^* \propto b^4$). For this reason, it was not feasible to verify leading edge separation and its effect on local heat transfer using the current experimental apparatus.[1]

The average Nusselt number data obtained by integrating the local distributions are given in Table 7.2. Note that for the interferogram shown in Figure 7.7 (a), there are insufficient full fringe shifts to determine the local heat transfer coefficient on the upper portion of the plate and wall. For these cases, the local distributions were linearly extrapolated (dashed lines in Fig. 7.9) in order to calculate average Nusselt numbers.

Figures 7.10 and 7.11 show a comparison of the experimental plate and wall average Nusselt numbers with the numerical predictions. When comparing the results it is important to realize that the blockage ratio for the experiments decreases from t/b=0.2 at the lowest Rayleigh number to t/b=0.069 at the highest Rayleigh number. At low Rayleigh number, the experimental data can be compared to the numerical data for t/b=0.2. At high Rayleigh number the effect of blockage is predicted to be small (see Fig.s 5.27-5.30), so the experimental data can be compared to the numerical results for t/b=0.

---

[1] It would be possible to achieve large channel aspect ratios at high Rayleigh number if the model was substantially longer than the working beam height. Such a model would have to be photographed in several sections. Because of the technical difficulties and reduction in accuracy associated with repositioning and realigning the model with the test beam, this option was not taken.

Table 7.2(a): Experimental average Nusselt number data for $L_p/L_c=1/3$, $L_i/L_c=0$ (bottom).

Ra_c^*	Ra_p^*	L_c/b	t/b	Pr	Nu_p	Nu_w	Nu_c
97.6	293	13.68	0.200	0.712	3.13	1.44	1.88
395	1185	9.45	0.138	0.713	4.43	2.55	3.04
874	2620	7.51	0.110	0.713	5.26	2.89	3.50
931	2790	7.51	0.110	0.713	5.43	2.86	3.53
1,890	5660	6.29	0.0917	0.713	6.11	3.48	4.16
5,930	17,790	4.73	0.0690	0.713	7.80	4.79	5.57

Table 7.2(b): Experimental average Nusselt number data for $L_p/L_c=1/3$, $L_i/L_c=1-L_p/L_c$ (top).

Ra_c^*	Ra_p^*	L_c/b	t/b	Pr	Nu_p	Nu_w	Nu_c
81.4	244	13.68	0.200	0.713	1.48	1.44	1.45
383	1150	9.45	0.138	0.713	3.23	2.37	2.59
888	2660	7.51	0.110	0.713	4.34	2.97	3.33
1,690	5670	6.29	0.0917	0.713	5.18	3.25	3.75
5,610	16,800	4.73	0.0690	0.713	6.82	4.48	5.09

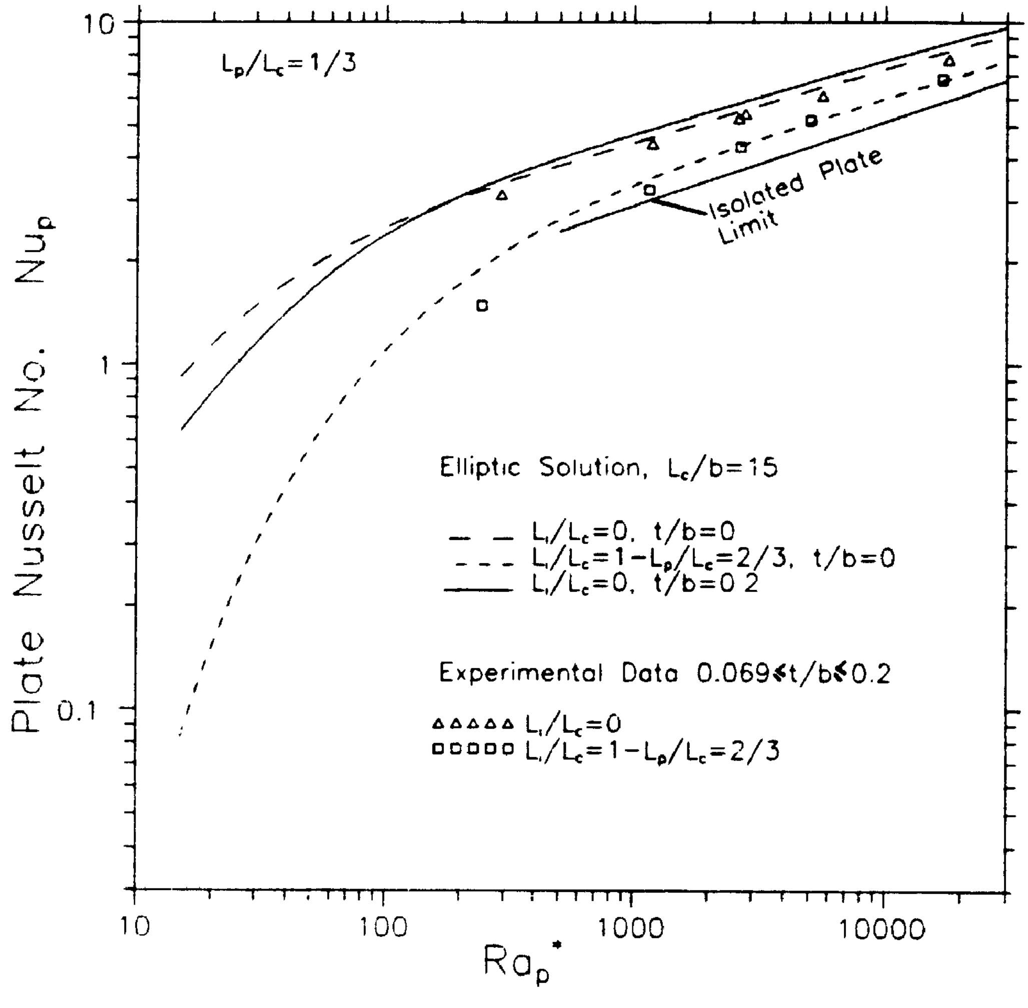

Figure 7.10: Comparison of the experimental and numerical plate average Nusselt numbers, $L_p/L_c=1/3$.

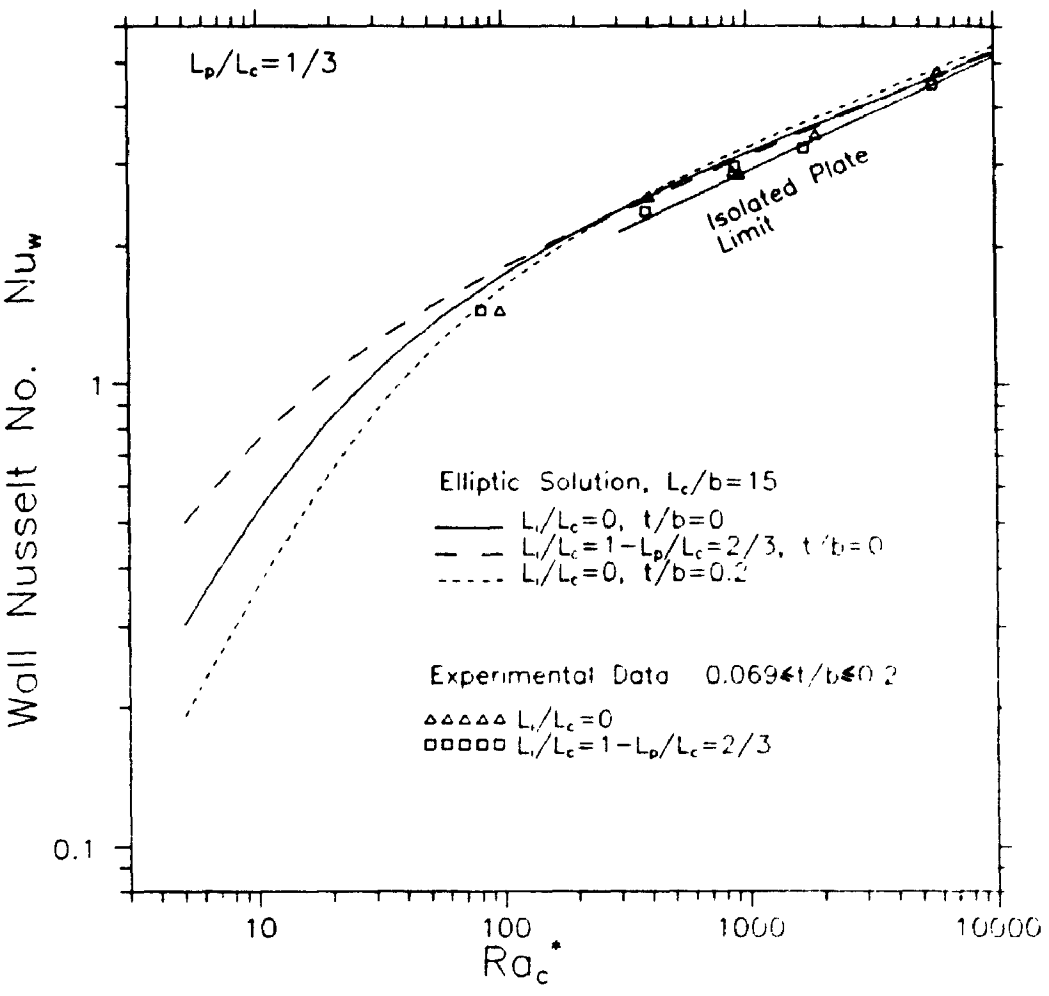

Figure 7.11: Comparison of the experimental and numerical wall average Nusselt numbers, $L_p/L_c=1/3$.

In Figure 7.10 it can be seen that the experimental plate Nusselt number trend is very similar to the numerical predictions. When the plate is at the top of the channel ($L_i/L_c=2/3$), the data are in excellent agreement with the numerical results (for $t/b=0$) at high Rayleigh number. At lower Rayleigh number the experimental data are slightly below the numerical results for $t/b=0$. To some extent, this may be caused by increasing blockage effects. When the plate is located in the bottom of the channel, the experimental data are about 10% lower than the numerical data at lowest Ra_c^* and about 6% lower at the highest Ra_c^*. From an engineering perspective, these differences are quite small; for most practical purposes, the experimental results validate the numerical prediction regarding the effect of plate position on plate average Nusselt number: positioning the plate higher in the channel reduces the heat transfer from the plate. This effect is most severe at lower Rayleigh numbers. For $L_p/L_c=1/3$, moving the plate from the top to the bottom of the channel causes the average Nusselt number of the plate to approximately double at $Ra_p^*\approx300$.

Figure 7.11 shows the comparison of numerical and experimental data for the wall average Nusselt number. Again, the trend of the experimental and numerical data is in fair agreement. In general, the experimental data are slightly lower than the numerical results. Nevertheless, the experimental data verify that the wall average Nusselt number is relatively insensitive to the plate position above $Ra_c^*\approx200$.

7.4 Reproducibility of the Experimental Data

To get an indication of the reproducibility of the experimental results, one experiment was repeated after a time lapse of several days. For this experiment, the plate was located at the bottom of the channel ($L_i/L_c=0$) and the channel aspect ratio was $L_c/b=7.51$. Prior to the reproducibility test, the interferometer was realigned and the beam parallelism was checked. Also, the channel gap width was reset and the dividing plate was repositioned. The results of these two experiments are shown below:

Experiment #1	$Ra_c^*=931$,	$Nu_w=2.86$	$Nu_p=5.43$
Experiment #2	$Ra_c^*=$[illegible],	$Nu_w=2.89$	$Nu_p=5.26$
	Adjusted difference:	2.6%	1.6%

The Rayleigh numbers for the two experiments differ slightly, so the Nusselt number difference has been adjusted, assuming $Nu=C(Ra^*)^{1/4}$. As can be seen from the data presented in the previous section, the local Nusselt number data typically have an experimental scatter of about ±5%. For this reason, the maximum difference in the local heat transfer values from the two experiments above was as much as 10%. However, typical differences in the local Nusselt numbers were much smaller. A detailed error analysis is given in Appendix F.

CHAPTER 8

DATA CORRELATION

8.1 Method of Data Correlation

Correlations are often more convenient for practical purposes than tabulated data. In this chapter, average Nusselt number correlations are presented for the dividing plate, channel wall and overall channel. These correlations include the effects of Rayleigh number (Ra^*), plate length ratio (L_p/L_c), plate position (L_i/L_c), and plate thickness (t/b).

Often, and in the present study, limiting closed form solutions exist for small and large values of the independent variable (see Chapter 3). However, solutions for intermediate values of the independent variable are not usually available in closed form. Churchill and Usagi [63] have devised a remarkably successful empirical method for obtaining correlation equations using the upper and lower limiting solutions. A brief description of the method is given below.

In the present study, the power of the independent variable (Ra^*) decreases at the higher limit. For so-called "decreasing dependency" of the Nusselt number on Rayleigh number, Churchill and Usagi propose a correlation of the following general form:

$$Nu = [(Nu_{Fully\ Dev.})^{-n} + (Nu_{Isol.\ Plate})^{-n}]^{-\frac{1}{n}} \tag{8.1}$$

where, $Nu_{Fully\ Dev.}$ is the closed form expression for fully developed conditions ($Ra^* \to 0$) and,

$Nu_{Isol.\ Plate}$ is the closed form expression for the isolated plate limit ($Ra^* \to \infty$).

In equation (8.1), the exponent (n) is arbitrary. This exponent is chosen to best fit experimental and numerical data for intermediate values of Ra^*.

8.2 Channel Average Nusselt Number Nu_c

The variation of the channel Nusselt number with Rayleigh number is not ideal for the application of the method of Churchill and Usagi. Ideally, the second derivative of the Nusselt number with respect to the Rayleigh number should not change sign. Unfortunately, the numerical results show that the isolated plate limit is approached from above (see Chapter 5). Hence, there is a change in the sign of the second derivative. Nevertheless, useful correlations sufficiently accurate for most purposes can be obtained.

There are three separate correlations for the channel Nusselt number: one for the plate in the bottom $L_i/L_c=0$, middle $L_i/L_c=(1-L_p/L_c)/2$, and top $L_i/L_c=1-L_p/L_c$ of the channel. Substituting expressions for the upper and lower asymptotic values (equations (3.14) and (3.30)) into equation (8.1) gives the general form of the correlations for the channel Nusselt number:

$$Nu_c=\left(\left(\frac{Ra_c^*}{3\left(4\left(\frac{L_\ell}{L_c}\right)^2\left(\frac{b}{b-t}\right)^3+4\frac{L_\ell}{L_c}\left(\frac{b}{b-t}\right)^3-\left(\frac{L_\ell}{L_c}\right)^2+1\right)}\right)^{-n}+\left(C Ra_c^{*\frac{1}{4}}\frac{\left(\frac{L_\ell}{L_c}\right)^{\frac{3}{4}}+1}{\frac{L_\ell}{L_c}+1}\right)^{-n}\right)^{-\frac{1}{n}} \tag{8.2}$$

Strictly, the constant "C" has the value of about C=0.515 for the isolated plate limit (Ostrach [49]). However, to compensate for the fact that the upper asymptotic limit is approached from above, "C" is treated as an arbitrary constant in equation (8.2). Hence, for each vertical plate position, both the constant "C" and the exponent "n" were determined numerically by minimizing the RMS percent error between the correlation and the data.

Table 8.1 gives tne values of C and n for each vertical plate position and the correlation statistics. A plot showing the effectiveness of the Nu_c correlation for $L_i/L_c=0$ is shown in Fig. 8.1. Note that the correlation (equation (8.2)) is a forty-five degree line in Fig. 8.1. Error limits of ±10% are shown to illustrate the fit of correlation to the data. Equation (8.2) fits *all* of the numerical and experimental data with a maximum error of about ±12% and a standard deviation of 4.6%.

8.3 Wall Average Nusselt Number Nu_w

Correlations for the wall average Nusselt number (Nu_w) were calculated using the same method as for the channel average Nusselt number. Substituting the expressions for the upper and lower asymptotic limits from Chapter 3 into equation (8.1) gives the general form of the correlations for

Table 8.1: Constants and statistics for the channel Nusselt number correlation equation 8.2.

Plate Position L_i/L_c	C	n	Number of Data	Standard Deviation	Maximum Error
0	0.626	1.63	116	4.6%	±12.1%
$(1-L_p/L_c)/2$	0.618	1.45	89	4.4%	±10.9%
$1-L_p/L_c$	0.595	1.42	95	5.0%	±15.0%

Table 8.2: Constants and statistics for the wall Nusselt number correlation equation 8.3.

Plate Position L_i/L_c	C_1	C_2	n	Number of Data	Standard Deviation	Maximum Error
0	0.588	6	1.48	84	6.2%	±17.0%
$(1-L_p/L_c)/2$	0.595	3	1.37	76	6.0%	±17.9%
$1-L_p/L_c$	0.583	3	1.53	82	4.9%	±13.0%

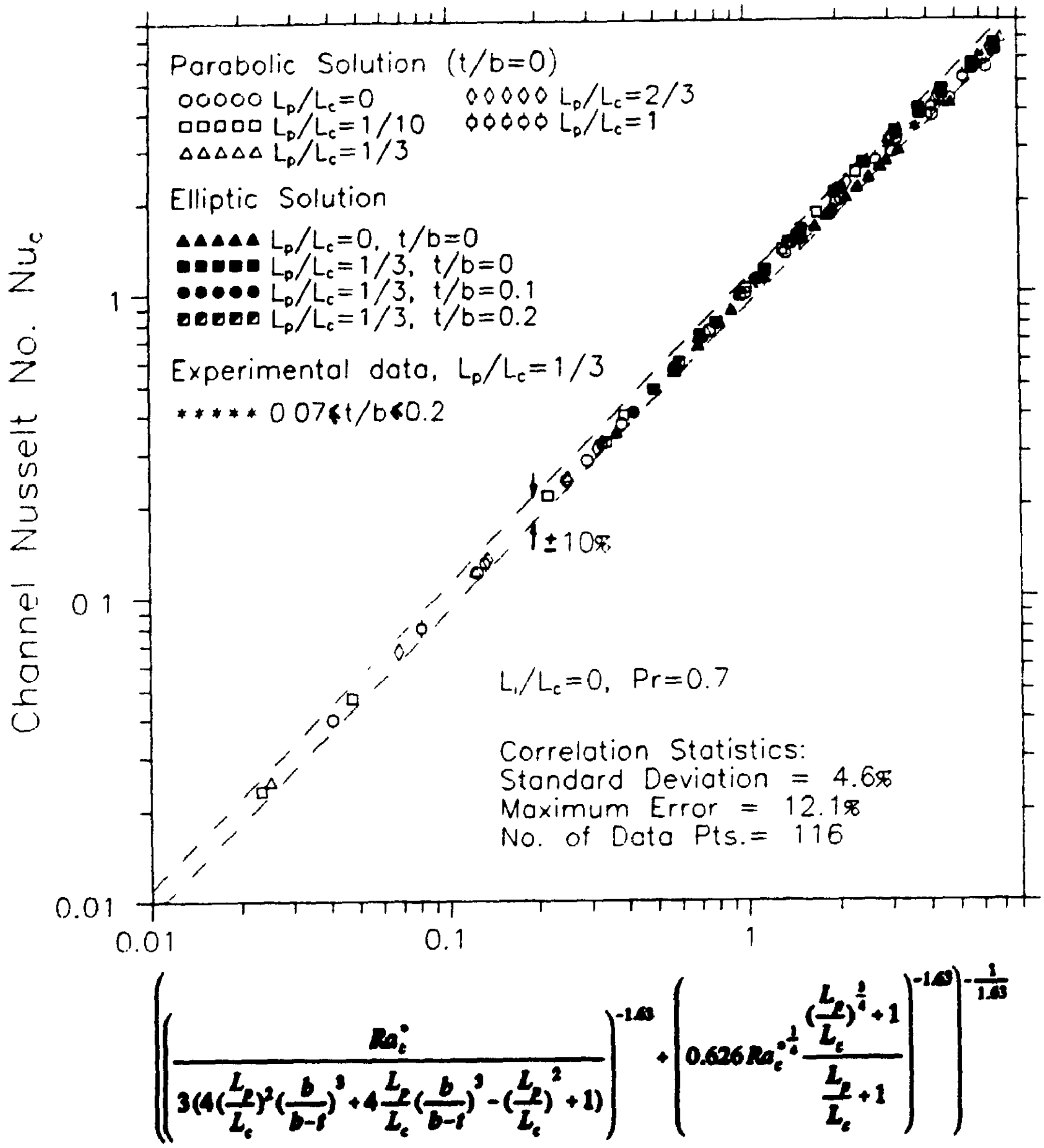

Figure 8.1: Correlation of the channel average Nusselt number (Nu_c) data for $L_i/L_c=0$.

the wall average Nusselt number:

$$Nu_w = \left(\left(\frac{Ra_c^*}{C_2\left(4\left(\frac{L_p}{L_c}\right)\left(\frac{b}{b-t}\right)^3 - \frac{L_p}{L_c} + 1\right)} \right)^{-n} + \left(C_1\, Ra_c^{*\frac{1}{4}} \right)^{-n} \right)^{-\frac{1}{n}} \qquad (8.3)$$

Table 8.2 gives the values of C_1, C_2 and n for each vertical plate position and the correlation statistics. The lower limiting asymptotic value of Nu_w depends upon the plate's vertical position: $C_2=6$ for $L_i/L_c=0$ (see equation (3.22)), and $C_2=3$ for $L_i/L_c>0$ (see equation (3.23)). Note that the correlation (equation (8.3)) should not be used for plate length ratios much less than $L_p/L_c=1/10$ when the plate is at the bottom of the channel ($L_i/L_c=0$); as discussed in Chapter 3, the lower limiting value for the wall Nusselt number (equation (3.22)) is not valid as $L_p/L_c \to 0$. Similarly, the correlation should not be used for plate length ratios much larger than $L_p/L_c=2/3$ when the plate is not at the bottom of the channel ($L_i/L_c>0$), because of the limitations of equation (3.23); as discussed in Chapter 3, equation (3.23) is not valid as $L_p/L_c \to 1$.

A correlation plot showing the Nu_w data for $L_i/L_c=0$ is shown in Fig. 8.2. Again, error limits of ±10% are shown to illustrate the fit of correlation to the numerical data. It can be seen from Table 8.2 that the Nu_w data do not correlate as well as the Nu_c data; equation (8.3) fits the numerical and experimental data with a maximum error of about ±17% and a standard deviation of 6.2%. The main reason for the poorer correlation statistics is the slightly larger difference between the parabolic and elliptic data, especially in the range $0.2 \le Nu_w \le 1.0$.

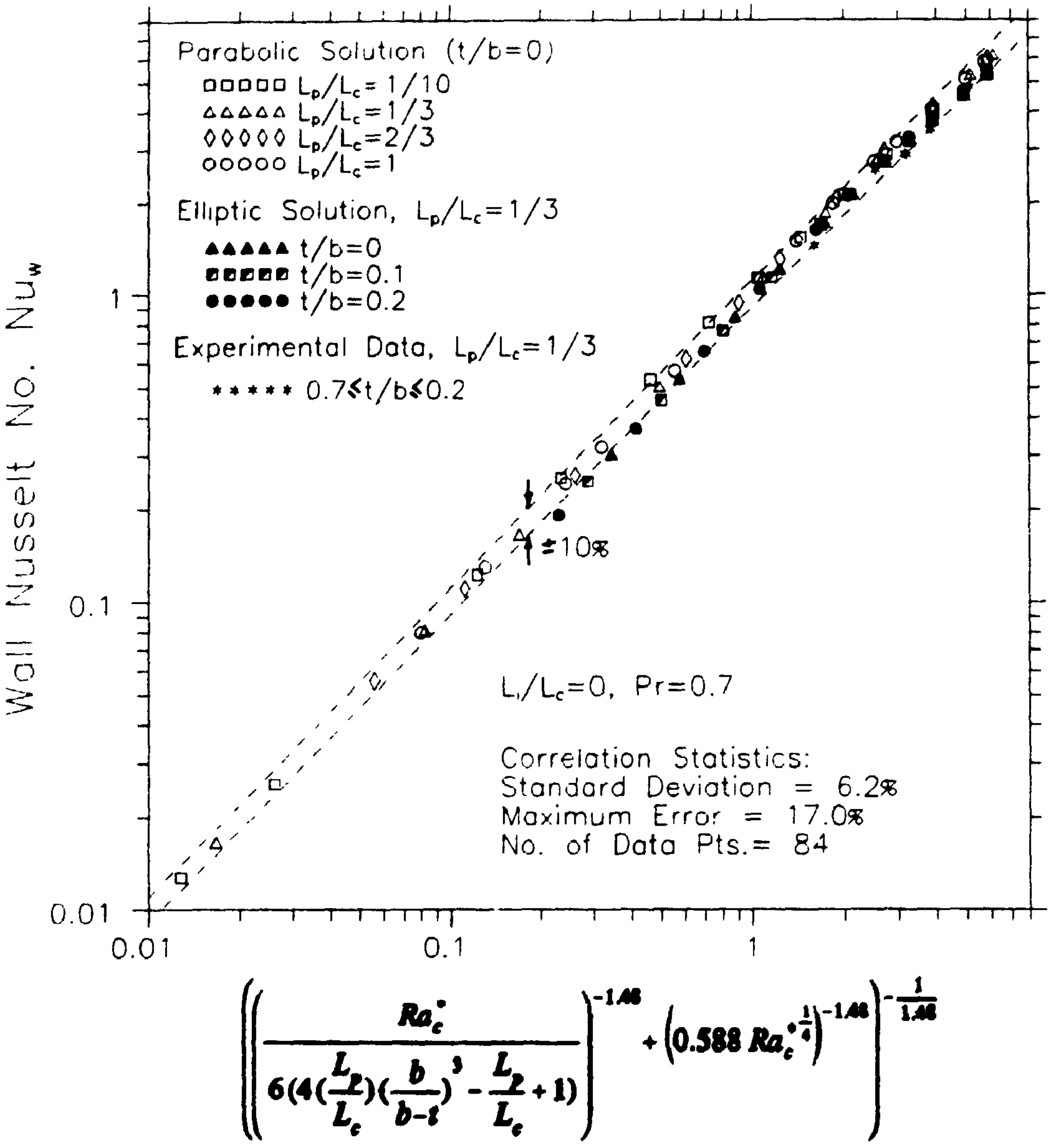

Figure 8.2: Correlation of the wall average Nusselt number (Nu_w) data for L_i/L_c=0.

8.4 Plate Average Nusselt Number Nu_p

Data correlation using the method of Churchill and Usagi is only possible when closed form expressions are available at both the upper and lower limits of Rayleigh number. When the plate is located at the channel inlet ($L_i/L_c=0$), a closed form expression exists in the limit as $Ra_p^* \to 0$ (equation (3.19)). However, for $L_i/L_c>0$ an equation for the lower limiting behaviour of Nu_p is not available. For this reason, a plate Nusselt number correlation is presented only for $L_i/L_c=0$. Fortunately, this is the channel configuration of most practical interest.

The correlation for the plate average Nusselt number for $L_i/L_c=0$ is:

$$Nu_p=\left(\left(\frac{Ra_p^*}{6(4(\frac{L_p}{L_c})(\frac{b}{b-t})^3-\frac{L_p}{L_c}+1)}\right)^{-2.01}+\left(0.632(\frac{L_p}{L_c})^{-0.189}Ra_p^{*\frac{1}{4}}\right)^{-2.01}\right)^{-\frac{1}{2.01}} \tag{8.4}$$

Notice that the upper asymptotic limit has been modified to include the effect of the plate length ratio L_p/L_c. The results presented in Chapter 5 show that the plate average Nusselt number depends strongly on plate length ratio (L_p/L_c) even at highest Rayleigh number considered in this study (see Fig. 5.4). A best fit power curve to the data from the parabolic solution at $Ra_p^*=10^4$ is shown in Fig. 8.3. At $Ra_p^*=10^4$ it was found that $Nu_p \propto (L_p/L_c)^{-0.189}$. Hence, the factor $(L_p/L_c)^{-0.189}$ was included in the expression for the upper limiting value in equation (8.4). Again, the constant C=0.632 and the exponent n=2.01 were determined by minimizing the RMS percent error between the data and the correlation.

A plot showing the effectiveness of the Nu_p correlation is shown in Fig.

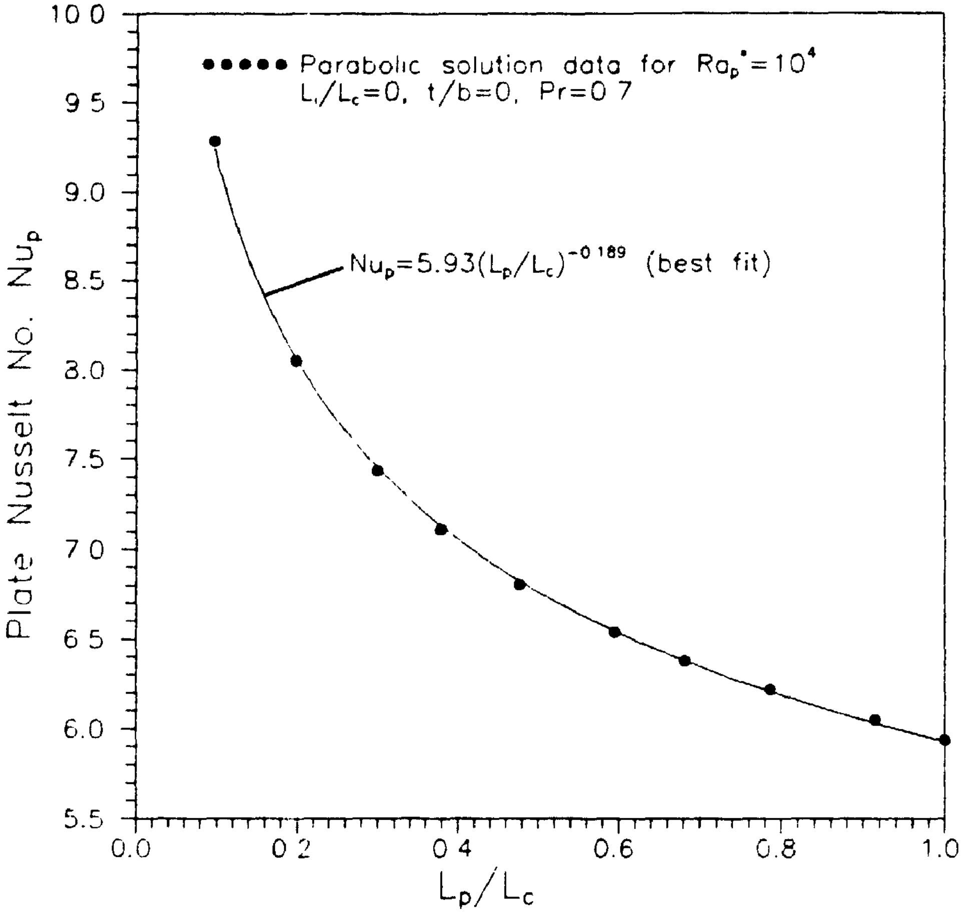

Figure 8.3: Variation of the plate average Nusselt number (Nu_p) with plate length ratio (L_p/L_c) at $Ra_p^*=10^4$ ($L_i/L_c=0$, $t/b=0$).

8.4. Equation (8.4) fits all of the experimental and numerical data with a maximum error of ±13% and a standard deviation of 6.2%. Considering the wide range of variables, the closeness of the fit is remarkable. The correlation (equation (8.4)) should not be used for plate length ratios much less than $L_p/L_c=1/10$ because of the limitation on the lower limiting expression; equation (3.19) is not valid as $L_p/L_c \rightarrow 0$.

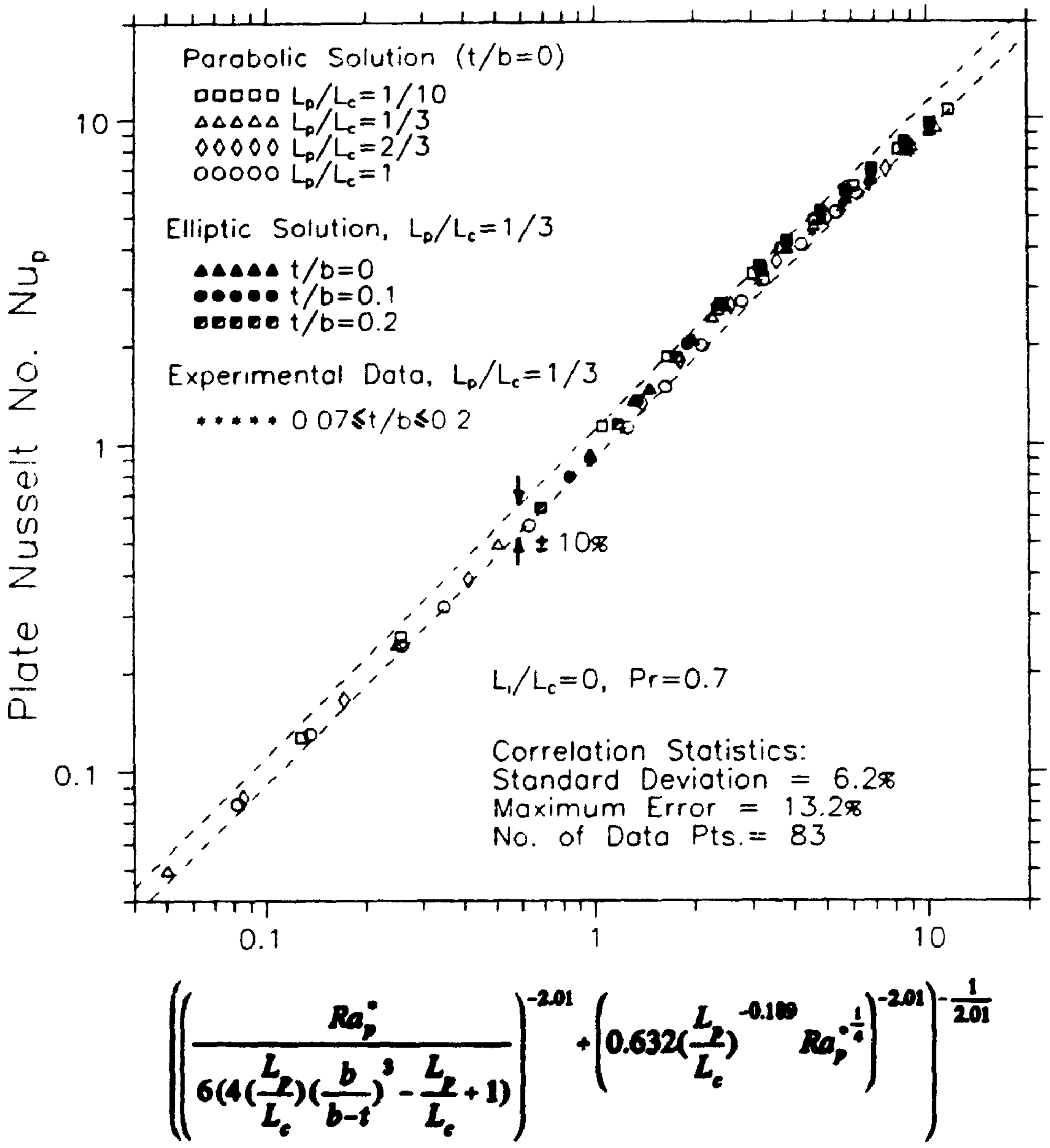

Figure 8.4: Correlation of the plate average Nusselt number (Nu_p) data for $L_i/L_c=0$.

CHAPTER 9

CONCLUSIONS AND RECOMMENDATIONS

9.1 Summary and Conclusions

A study has been conducted on natural convection in an undivided and divided vertical isothermal channel. For the divided channel, an isothermal plate at the same temperature as the channel walls was located on the channel centre line. Closed form expressions were derived for the limiting case of fully developed flow in the divided channel. The developing natural convection has been solved numerically. Solutions to both the full elliptic and boundary-layer forms of the Navier-Stokes and energy equations have been obtained for Pr=0.7 (air). For the elliptic solution, new inlet boundary conditions have been proposed that allow a smaller computational domain and more realistically represent the entrance flow than previous methods. To verify the numerical predictions, experimental local and average Nusselt number data were obtained using a Mach-Zehnder interferometer.

The study examined the effect of Rayleigh number (Ra_c^*, Ra_p^*), plate length ratio (L_p/L_c), vertical plate position (L_1/L_c) and plate thickness (t/b) on the free convective heat transfer from the channel walls, the dividing plate and the channel as a whole. The salient conclusions are summarized below:

i) Detailed comparisons of the parabolic (boundary-layer) and elliptic solutions show that an elliptic solution is necessary to get accurate local quantities, such as local heat transfer, near the channel entrance. However, global quantities predicted by the elliptic and parabolic solutions (such as total flow rate and average Nusselt numbers) are in good agreement.

ii) For the undivided channel (L_p=0), the present elliptic solution is not in agreement with previous elliptic solutions. The close agreement of the present elliptic and parabolic (boundary-layer) solutions casts doubt on the validity of the results of Nakamura et al. [40] and Kettleborough [39]. The present study did not find reverse flow drawn in from the channel exit as did Kettleborough. Also, the pressure distributions presented by Nakamura are suspect in light of the close agreement between the present elliptic and parabolic pressure distributions. The inlet pressure approximation ($p'=-\rho v_o^2/2$) commonly used in parabolic solutions is validated by the present elliptic solution.

iii) For both the undivided and divided channel geometries, the present elliptic solution predicts that fluid separation occurs at the channel inlet for sufficiently high Rayleigh number. The onset of separation was shown to correlate approximately with dimensional flow rate. Also, at high Rayleigh number, fluid separation was found to greatly reduce the local heat transfer on the channel wall near the channel entrance. To the author's knowledge, flow separation at the inlet has not been seen or predicted by any previous study of natural convection in vertical channels.

iv) The interferometric data validate the numerical predictions. Although the experimental average Nusselt numbers are slightly lower (typically

$\approx$10%) than the numerical predictions, the data trends are in close agreement. Also, the agreement of the experimental and numerical local Nusselt number distributions is close, except near the leading edge of the dividing plate and channel wall.

The following conclusions relate specifically to the divided channel geometry:

i) For a zero thickness dividing plate ($t/b=0$), the data from the parabolic solution verify the equations (derived in Chapter 3) for the fully developed Nusselt numbers. In all cases, the numerical data (for $t/b=0$) asymptotically approach these expressions at low Rayleigh number. Also, comparison with the data from the elliptic solution indicates that these expressions give reasonable estimates of the effect of finite plate thickness for $t/b \leq 0.2$. For $t/b>0.2$ the accuracy of these equations is uncertain.

ii) For the divided channel geometry, it was found that the heat transfer from the dividing plate could be significantly enhanced by the presence of the confining walls. For example, the experimental and numerical results show that the plate Nusselt number is about 50% higher than the isolate plate Nusselt number for $L_p/L_c=1/3$, $L_i/L_c=0$ at $Ra_p^* \approx 300$. Also, numerically it was found that for $L_p/L_c=1/10$ and $L_i/L_c=0$, the plate average Nusselt number was about two times higher than the isolate plate Nusselt number at $Ra_p^*=100$.

iii) The length of the confining walls greatly influences the heat transfer from the dividing plate, especially at low Rayleigh number. At low Rayleigh number, when the plate is at the bottom of the channel (L_i/L_c=0), extending the channel walls above the plate can increase the plate heat transfer by as much as a factor of four. At moderate values of Rayleigh number the enhancement decreases, but is still significant.

iv) Positioning the plate at the bottom of the channel (L_i/L_c=0) was found to give the highest average Nusselt number for the plate and channel as a whole over the full range of parameters studied experimentally and numerically. Lower plate positioning causes a greater chimney effect (i.e., more induced flow); this is in qualitative agreement with the findings of previous studies of natural convection from cylinders between confining walls [12,14,52].

v) The obverse of the above conclusion is that positioning the plate higher in the channel reduces the plate and channel average Nusselt number. In fact, at low Rayleigh number, plate average Nusselt number decreases to near zero as the plate is positioned higher in the channel. At high Rayleigh number, the plate Nusselt number is less dependent on the vertical location of the plate. For example, at $Ra_p^* \approx 6000$ with L_p/L_c=1/3, the experimental and numerically predicted Nusselt number for L_i/L_c=0 (plate at the channel inlet) is only about 20% higher than for $L_i/L_c=1-L_p/L_c=2/3$ (plate at the top of the channel).

vi) The wall average Nusselt number is highly dependent upon the vertical location of the plate at low Rayleigh number. In the fully developed limit, a short dividing plate located at the channel inlet reduces the wall average Nusselt number by about a factor of two, compared with the undivided channel. With increasing Rayleigh number, the wall average Nusselt number becomes almost independent of both the vertical plate position (L_i/L_c) and the plate length ratio (L_p/L_c). This is a very significant result: above $Ra_c^* \approx 200$ the heat transfer from the dividing plate is enhanced by the confining walls without reducing the heat transfer from the walls. Below $Ra_c^* \approx 200$ there is a trade-off between the dividing plate and channel walls.

vii) The effect of blockage caused by a finite thickness dividing plate ($t/b \leq 0.2$) is largest at low Rayleigh number and becomes insignificant at high Rayleigh number. At $Ra_c^*=5$, for $L_p/L_c=1/3$ and $L_i/L_c=0$, twenty percent blockage of the channel cross-section ($t/b=0.2$) causes about a thirty percent reduction in the plate and channel Nusselt numbers.

viii) Average Nusselt number correlations have been obtained for the dividing plate, the channel wall and the channel as a whole. These correlations include the effects of Rayleigh number (Ra^*), plate length ratio (L_p/L_c), plate position (L_i/L_c), and plate thickness (t/b).

9.2 Recommendations for Future Research

The following recommendations are made for future studies:

i) The present numerical study predicts that the flow separates at the channel inlet for sufficiently high Rayleigh number. Flow visualization needs to be done to verify this phenomenon. Possibly, with the use of a laser-Doppler velocimeter, the geometric and thermal conditions necessary for separation could be determined and compared to the numerical predictions. In addition, interferometry at the leading edge could be used to examine the adverse effect of separation on local heat transfer.

ii) The present full elliptic solution imposed derivative boundary conditions at the channel exit: $\partial T/\partial y=\partial u/\partial y=\partial v/\partial y=0$. These boundary conditions are not entirely correct. An improved method of handling the channel exit boundary conditions needs to be developed.

iii) The present study has shown the thermal behaviour of a divided channel with equal plate and channel wall temperatures. Uniform heat flux (UHF) conditions are more realistic for modelling printed circuit board geometries. For this reason, a similar study with UHF boundary conditions is needed. Other possible extensions to the present study could include a variety of boundary conditions. For example, symmetric *unequal* UHF conditions or the effect of adiabatic confining walls could be studied. Note that asymmetric boundary conditions are not compatible with the present boundary-layer solution method and would require a full elliptic solution of the flow in the entire channel.

iv) In the present study, the dividing plate location was fixed on the channel centre line. It would be of interest to see the effect of the horizontal plate location on the plate, wall and channel heat transfer.

v) In the present numerical studies, the flow in the channel was assumed to be laminar up to $Ra_c^* \leq 10^4$. At present, there is almost no information on the criteria for turbulent transition for natural convection in vertical channels. A comprehensive study of this problem is needed.

vi) In the literature, studies of the effect of angle of inclination [79] and surface roughness elements [80,81] have been conducted for the undivided UWT/UHF channel. Similar studies are logical extensions to the present research.

APPENDIX A

APPLICATION OF THE CFD CODE FIDAP

FIDAP [54] is a general purpose computational fluid dynamics (CFD) code for the simulation of incompressible viscous fluid flow with heat and mass transfer. FIDAP solves the full elliptic form of the Navier-Stokes and energy equations using the finite element method. Since the governing equations for fluid flow and heat transfer are partial differential equations, they must be first converted into a set of algebraic equations before they can be solved computationally. In the finite element method, the exact solution to the continuous problem is approximated within each element by a combination of interpolation (or trial) functions (usually polynomials). Element equations are derived using a residual method that is based on minimizing the residual after the trial solution is substituted into the governing differential equations. The element equations along with equations derived from the boundary conditions form a set of simultaneous equations that can be solved. Detailed description of the method used by FIDAP is given in the FIDAP Theoretical Manual [54].

There are many commercial CFD packages on the market. Some of the others include NEKTON [82] which uses a spectral element method, FLUENT [82] which uses a finite difference method, and 3D-FLUID [83] which uses a finite element method. FIDAP was used for the present study because of its availability at The University of Western Ontario Computing Centre.

Like most commercial packages, FIDAP has three modules: preprocessor, processor, and postprocessor. The preprocessing module is used first. In this module the flow characteristics are defined, the boundary conditions are specified, and the finite element mesh is generated. When preprocessing is complete, the processor module is used to solve the set of simultaneous algebraic equations. Finally, the postprocessing module is used to view the results. Although FIDAP solves the problem in primitive variables, derived quantities such as stream function contours can be viewed in the postprocessor.

In FIDAP, the problem is specified using an input file consisting of a list of commands. A sample FIDAP input file is given in this appendix. The finite element mesh produced by this file is shown in Fig. 2.5(b). In the input file, the computational domain is specified in both a logical and a physical plane. The physical plane has dimensionless X and Y coordinates and the logical plane has i,j indices as coordinates. Figure A.1 shows the logical and physical planes for the unexpanded mesh with a dividing plate located at the channel inlet ($t/b=0.2$, $L_p/L_c=1/3$, $L_i/L_c=0$). In the logical plane, the domain is divided into topological rectangles. "Keypoints" are defined at the corners of the rectangles in both the logical and physical planes.

The velocity and temperature field in the channel was initially solved at low Rayleigh number ($Ra_c^*=5$). Solutions for higher Rayleigh number were obtained using the solution vector from a previous calculation (at lower Rayleigh number) as the starting values for the unknown vector. At low Rayleigh number, this procedure reduces the number of iterations and cost of the calculations; at high Rayleigh number it is absolutely necessary in order to obtain convergence. In FIDAP, the *EXECUTION(RESTART) statement is used to specify that the "initial guess" is to be taken from a previous solution.

Local and average Nusselt numbers for the channel wall and dividing plate were obtained from FIDAP using the postprocessor command HEATFLUX. This command calculates the temperature gradient normal to a specified surface. These values are also used to compute the integrated heat transfer from the surface. Similarly, the total dimensionless flow rate through the channel was calculated using the command FLOWRATE.

The channel average Nusselt number (Nu_c) was calculated by integrating the total heat convected out of the top of the channel (see equation 2.40). There was no postprocessor command which would perform this task. Hence, a user-defined subroutine was written (in Fortran) to integrated the product ($V \cdot T^*$) at the channel exit using the trapezoidal rule. This subroutine was linked with the postprocessor module (FIPOST) and was executed through the postprocessor command LINE.

Sample FIDAP input file (for $Ra_c^*=100$, $t/b=0.2$, $L_p/L_c=1/3$, $L_1/L_c=0$, $Pr=0.7$)

```
/ TITLE CARD
*TITLE
FPIN104 T=0.2 RAC=100 LP=5 BOTTOM LC=15
*FIMESH(2-D,IMAX=9,JMAX=25)
/EXPANSION OF THE MESH
EXPI
1 0 17 0 39 0 61 0 109
EXPJ
1 0 49 0 69 0 91 0 103 0 117 0 169 0
205 0 217 0 239 0 261 0 313 0 337
/SPECIFICATION OF THE I,J,K INDICIES AND
/THE X,Y,Z CO-ORDS OF EACH KEY POINT IN
/THE LOGICAL PLANE.
POINT(CARTESIAN)
/#    I     J     K     X     Y
1     1     1     1     0.    -5.0
2     3     1     1     1.5  -4.7697
3     1     3     1     0.    -1.
4     3     3     1     0.42426  -1.0
5     5     1     1     1.5 -4.7697
6     7     1     1     3.5355 -3.5355
7     1     5     1     0.0  -0.4
8     3     5     1     0.42426 -0.22426
9     5     3     1     0.42426  -1.0
10    7     3     1     1.0  -1.0
11    9     3     1     3.5355 -3.5355
12    1     7     1     0.0  0.0
13    3     7     1     0.14142  0.058579
14    5     7     1     0.42426  -0.22426
15    7     7     1     1.0  -0.22426
16    9     7     1     4.918333 -0.9
50    5     5     1     0.42426  -0.22426
51    7     5     1     1.0  -0.22426
52    9     5     1     4.918333 -0.9
/ POINT 17 IS A REF. POINT (DOES NOT
/  EXIST IN  THE LOGICAL PLANE)
17    0      0     0     0.0  0.2
18    3      9     1     0.188562  0.13333
19    5      9     1     0.56568  0.0
20    7      9     1     1.0  0.0
21    9      9     1     5.0  0.0
22    3     11     1     0.2  0.2
23    5     11     1     0.6  0.2
24    7     11     1     1.0  0.2
25    3     13     1     0.2  2.5
26    5     13     1     0.6  2.5
27    7     13     1     1.0  2.5
28    3     15     1     0.2  4.8
29    5     15     1     0.6  4.8
30    7     15     1     1.0  4.8
31    3     17     1     0.14141  4.94142
32    5     17     1     0.42426  5.22426
33    7     17     1     1.0  5.22426
34    1     17     1     0.0  5.0
35    1     19     1     0.0  5.4
36    3     19     1     0.42426  5.22426
37    5     21     1     0.42426  6.0
38    7     21     1     1.0  6.0
39    1     21     1     0.0  6.0
40    3     21     1     0.42426  6.0
41    5     23     1     0.42426  10.0
42    7     23     1     1.0  10.0
43    1     23     1     0.0  10.0
44    3     23     1     0.42426  10.0
45    5     25     1     0.42426  15.0
46    7     25     1     1.0  15.0
47    1     25     1     0.0  15.0
48    3     25     1     0.42426  15.0
```

```
/  49 IS A REF. POINT
49    0     0     0   0  4.8
53    5     19    1   0.42426  5.22426
54    7     19    1   1.0  5.22426
LINE
/ DEFINE ALL HORIZONTAL LINES
3 4
9 10 4 4
10 11 5 3
50 51 4 4
51 52 5 3
13 14 4 3
14 15 4 4
15 16 5 3
18 19 4 3
19 20 4 4
20 21 5 3
22 23 4 3
23 24 4 4
25 26 4 3
26 27 4 4
28 29 4 3
29 30 4 4
31 32 4 3
32 33 4 4
53 54 4 4
37 38 4 4
39 40
41 42 4 4
43 44
45 46 4 4
47 48
/DEFINE ALL VERTICAL LINES
1 3 5 4
2 4 5 4
3 7 3 4
4 8 3 4
5 9 5 4
6 10 5 4
7 12 4 4
8 13 4 4
9 50 3 4
10 51 3 4
15 20 2 4
20 24
22 25 5 3
23 26 5 3
24 27 5 3
25 28 3 4
26 29 3 4
27 30 3 4
30 33
34 35 4 3
31 36 4 3
53 37 2 3
54 38 2 3
35 39 2 3
36 40 2 3
37 41 3 3
38 42 3 3
39 43 3 3
40 44 3 3
41 45
42 46
43 47
44 48
ARC
1 2 12
```

```
5 6 12
11 52 12
16 21 12 2 4
7 8 17
12 13 17
13 18 17
14 19 17 2 4
18 22 17
19 23 17
28 31 49
29 32 49
31 34 49
35 36 49
/DEFINE THE SURFACES
SURFACE
1 13
13 32
5 51
10 52
14 33
34 48
15 21
53 46
MERGE
2 4 5 9
4 8 9 50
13 8 13 14
10 6 10 11
31 36 31 32
53 37 36 40
37 41 40 44
41 45 44 48
14 15 50 51
15 16 51 52
53 54 32 33
/ SPECIFY TEMPERATURE B.C.'S
BCNODE(TEMPERATURE)
1 2 0.0
5 6 0.0
11 52 0.0
16 21 0.0
12 13 1.0
13 31 1.0
31 34 1.0
20 33 1.0
54 46 1.0
/ SPECIFY BOUNDARY CONDITIONS
/ FOR X-COMPONENT OF VELOCITY
BCNODE(UX,CONSTANT)
12 13 0.0
13 31 0.0
31 34 0.0
1 12 0.0
34 47 0.0
20 21 0.0
20 33 0.0
54 46 0.0
/ SPECIFY B.C.'S FOR Y-COMPONENT
/ OF VELOCITY
BCNODE(UY,CONSTANT)
12 13 0.0
13 31 0.0
31 34 0.0
20 21 0.0
20 33 0.0
54 46 0.0
/ ELEMENTS ARE NINE NODE QUADRILATERALS
ELEMENTS(QUAD,NODES=9,ALL)
/BOUNDARY ELEMENTS NEEDED TO SPECIFY
NORMAL
/ AND TANGENTIAL B.C.'S ON CURVED INLET
ELEMENTS(BOUNDARY,NODES=3,CRNS,CRNF)
1 2
5 6
11 52
16 21
/PLOT ELEMENTS
12 13
13 31
31 34
20 33
54 46
47 48
45 46
/ TANGENTIAL COMPONENT OF
/ VELOCITY =0 AT INLET
BCNODE(UX,CONSTANT)
1 2 0.0
5 6 0.0
11 52 0.0
16 21 0.0
/ NORMAL STRESS=0 AT INLET
BCFLUX(N,NODES=3)
1 2 0.0
5 6 0.0
11 52 0.0
16 21 0.0
END
/ PROBLEM DEFINITION
*PROBLEM(2-D,STEADY,NONLINEAR,
STRONGLY-CPLD)
/ RHO= GR**1/2 (SEE SCALING)
*DENSITY(CONSTANT=46.291)
*PRESSURE(PENALTY=1.E-8,DISCONTINUOUS)
*EXECUTION(RESTART)
/ CONVERGENCE CRITERIA AND
/ QUASI-NEWTON SOLVER
*SOLUTION(Q.N.=8,VELCONV=0.0001,
RESCONV=0.0001)
/TWO SUCCESIVE SUBSTITUTION
/ ITERATIONS FIRST
*STRATEGY(S.S.=2)
*DATAPRINT(NORMAL,PAGE,NODES=3,
ELEMENTS=1)
*PRINTOUT(ALL)
*POSTPROCESS(ALL)
*NODES(FIMESH)
*RENUMBER(PROFILE)
/ INITIAL GUESS FOR VELOCITY
*ICNODES(VELOCITY,STOKES)
/ MU=1 (SEE SCALING)
*VISCOSITY(SET=1,CONSTANT=1.0)
*BODYFORCE(CONSTANT)
0.,1.,0.
*ELEMENTS(GROUP=1,QUADRILATERAL,
NODES=9,FLUID,CONSISTENT,LINEAR,
LOCAL,FIMESH,MDENS=1,MVISC=1)
*ELEMENTS(SLIP,NODES=3,FIMESH)
*ELEMENTS(SLIP,NODES=3,FIMESH)
*ELEMENTS(SLIP,NODES=3,FIMESH)
*ELEMENTS(SLIP,NODES=3,FIMESH)
*ELEMENTS(PLOT,NODES=3,FIMESH)
*ELEMENTS(PLOT,NODES=3,FIMESH)
*ELEMENTS(PLOT,NODES=3,FIMESH)
*ELEMENTS(PLOT,NODES=3,FIMESH)
*ELEMENTS(PLOT,NODES=3,FIMESH)
*ELEMENTS(PLOT,NODES=3,FIMESH)
*ELEMENTS(PLOT,NODES=3,FIMESH)
/ CP=PRANDTL NUMBER (SEE SCALING)
*SPECIFICHEAT(CONSTANT=0.7)
/ BETA=1 (SEE SCALING)
*VOLUMEXPANSION(CONSTANT=1.,
REFTEMP=0,GRAVITY=1,THETA=0.)
*END
```

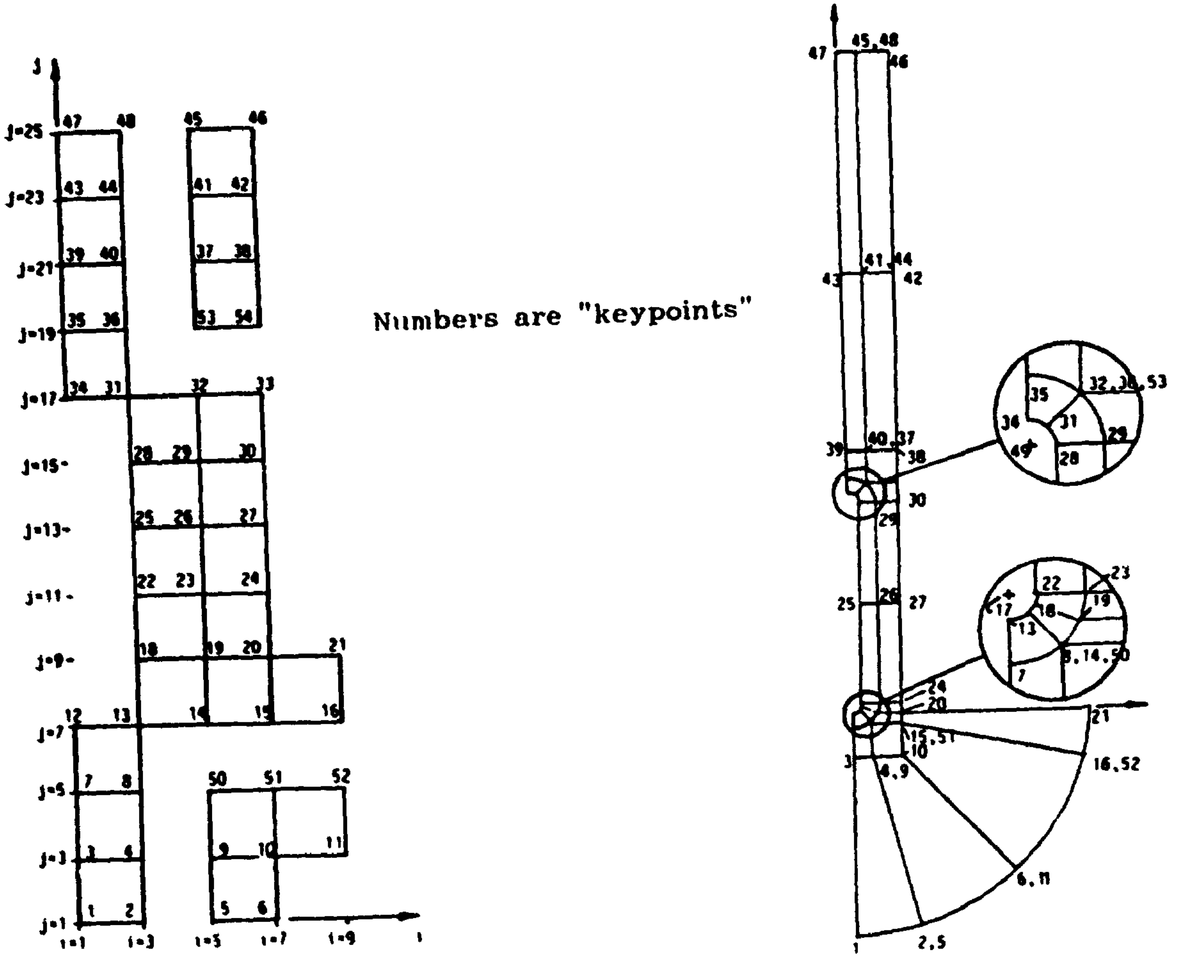
j
j=25
j=23
j=21
j=19
j=17
j=15
j=13
j=11
j=9
j=7
j=5
j=3
j=1
i=1
i=3
i=5
i=7
i=9
i
1
2
3
4
5
6
7
8
9
10
11
12
13
14
15
16
18
19
20
21
22
23
24
25
26
27
28
29
30
31
32
33
34
35
36
37
38
39
40
41
42
43
44
45
46
47
48
50
51
52
53
54
2,5
6,11
16,52
15,51
4,9
8,14,50
45,48
32,36,53
17
49

Numbers are "keypoints"

(a) Logical plane

(b) Physical plane (unexpanded F.E. mesh)

Figure A.1: (a) Logical and (b) physical planes for the divided channel finite element mesh (corresponding to the FIDAP input file listing).

APPENDIX B

A DIGITAL IMAGING SYSTEM FOR INTERFEROGRAM ANALYSIS

B.1 Introduction

Interferometry is widely used to analyze heat transfer and compressed fluid flows. Photographically recorded interference fringe patterns can be calibrated to yield the temperature or density fields; given the precise location of the fringe centres, local gradients of these properties can be calculated. In the past, interference fringe centres have commonly been located by eye using a travelling microscope or densitometer. Both of these methods are time consuming and subject to human error. This appendix describes the development of an IBM PC-based digital image processing system for finite and infinite fringe interferogram analysis. Image scanning to locate and record the centres of destructive interference fringes has been semi-automated. The present system reduces processing time and gives greater precision than standard manual methods.

Interferogram analysis by digital image processing has been used recently by several heat transfer researchers [84,85,86]. Problems of poor image resolution and low reliability/accuracy of the fringe centre detection algorithms have been reported. Hunter and Collins [85] found varying background light intensity to be a major problem. However, other "false fringes" can be produced by surface diffraction, imperfections in the optics or blemishes on the film. The simple algorithm presented here for analyzing interferograms largely overcomes these problems.

B.2 System Hardware

In the present system the interference patterns are recorded photographically using Polaroid Land Film (4"x5", type 55 positive/ negative). Film negatives are analyzed since they have higher resolution (160 lines/mm) than the positives.

The image processing system is shown schematically in Fig. B.1. A charged coupled device (CCD) camera (Cohu model 4815, 754 x 488 pixels) is mounted onto a variable magnification microscope (Bausch and Lomb MonoZoom-7) fitted with a 1.5X objective lens. The CCD camera supplies a video signal to a frame grabber board (Imaging Technology PCVISION) in an expansion slot of an IBM compatible (80286) personal computer. The digitized image is displayed on a colour monitor. Rather than capturing the entire interferogram at once, it is stored as many separate images. Each image is digitized and stored in 640 x 480 x 8 bit frame memory (256 grey levels). In this way, excellent image resolution is achieved.

The film negative is accurately positioned under the microscope with a precision X-Y rotating stage, fitted with micrometer adjustments. The stage has a 5.08cm diameter circular glass viewing area. A light table under the stage is used to illuminate the negative. It is worth noting that it is very easy to under or over illuminate the negative. For example, if too much light is supplied, the image is "washed out". That is, most of the pixel intensities are at their maximum value of 255, and the peaks of the

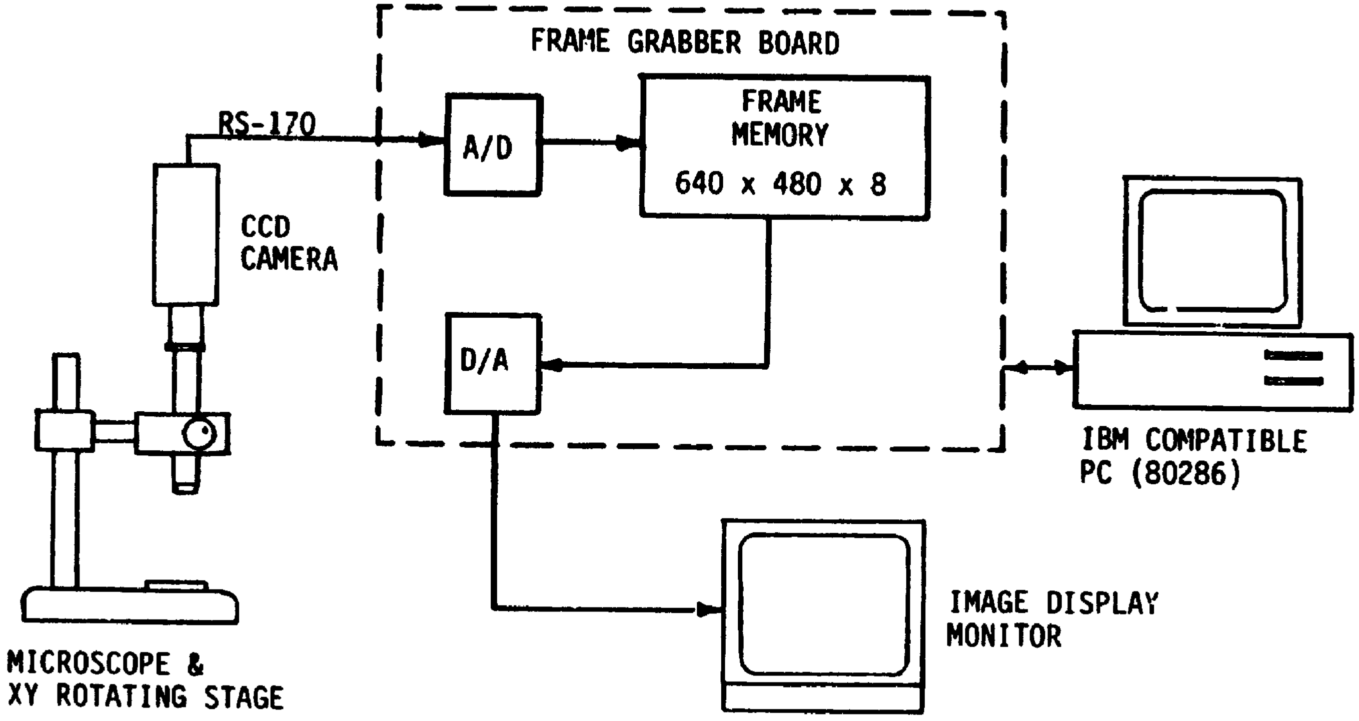
FRAME GRABBER BOARD
RS-170
A/D
FRAME
MEMORY
640 x 480 x 8
CCD
CAMERA
D/A
IBM COMPATIBLE
PC (80286)
MICROSCOPE &
XY ROTATING STAGE
IMAGE DISPLAY
MONITOR

Figure B.1: Schematic diagram of the image processing system.

destructive fringes are "clipped". To avoid this problem, all pixels with value 255 (white) are written to the image display monitor with the colour blue, rather than white. Similarly pixels with value 0 (black) are displayed as red on the monitor. In this way, maximum image contrast can be achieved while ensuring that the image is not being clipped.

The overall scale factor of the system is measured by placing a reticule under the travelling microscope. The reticule has a scale 10 mm long with 0.1 mm divisions. The scale factors are determined by placing the reticule in both the horizontal and vertical scanning positions and recording the number of pixels between a known distance on the reticule. It was found that the image in frame memory was slightly distorted since the horizontal and vertical scale factors differ by approximately 1%. However, this difference does not introduce errors into the results since vertical and horizontal distances are scaled appropriately in the fringe analysis software.

In the present heat transfer study, the fringes near the channel inlet were very closely spaced. In this region the zoom microscope was adjusted to its maximum magnification; the resulting horizontal scale factor was about 2.8 µm per pixel. Toward the top of the channel, the fringe spacing was much wider. In order to get sufficient fringes in the field of view, the magnification had to be reduced. Typically, the horizontal scale factor was about 4.9µm per pixel.

B.3 FRINGE ANALYSIS ALGORITHM

In an infinite fringe interferogram as shown in Fig. B.2(a), fringe centres can be calibrated as lines of constant temperature. However, surface temperature gradients (i.e., local heat transfer coefficients) are of primary interest in the present study. To measure the surface temperature gradient, first a temperature profile perpendicular to the model wall is obtained from the destructive interference fringe centres. The temperature profile is then extrapolated to the wall to obtain the surface gradient.

Menu-driven interactive software (in Microsoft C language) has been developed by the author that accurately locates the fringe centres in an image. The procedure is as follows: Initially, the interferogram image is aligned under the microscope (with the aid of software generated cross hairs) so that the model surface is vertical on the monitor as shown in Fig. B.2(a). Once the desired section of the interferogram has been captured into frame memory, a cursor is used to indicate the horizontal location of the wall on the interferogram. Then the user selects the start and end locations for each horizontal scan using the cursor. Figure B.2(b) shows the image after scanning has taken place at a vertical increment of five pixels. White lines are displayed at each scan so that the user can verify the scanning locations. The complete scan and data processing of one image takes about 30 seconds after the desired image has been captured.

A typical horizontal pixel intensity profile from frame memory is shown in Fig. B.3. The three primary peaks represent destructive interference fringes. The "noise" that is superimposed upon the interference pattern is produced by surface diffraction, blemishes on the film, and imperfections

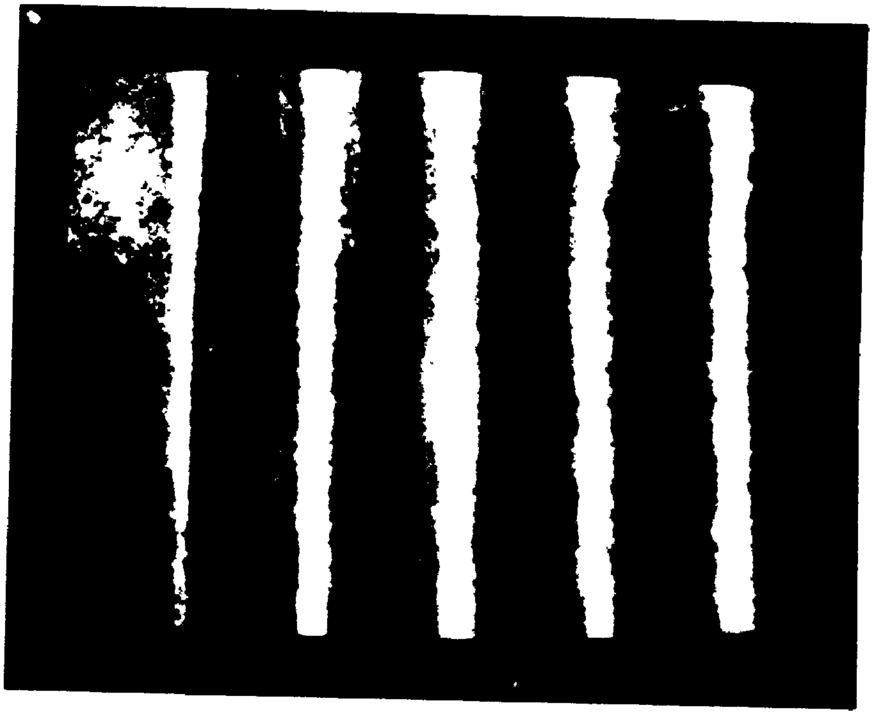

Figure B.2(a): Section of an infinite fringe interferogram displayed on the monitor.

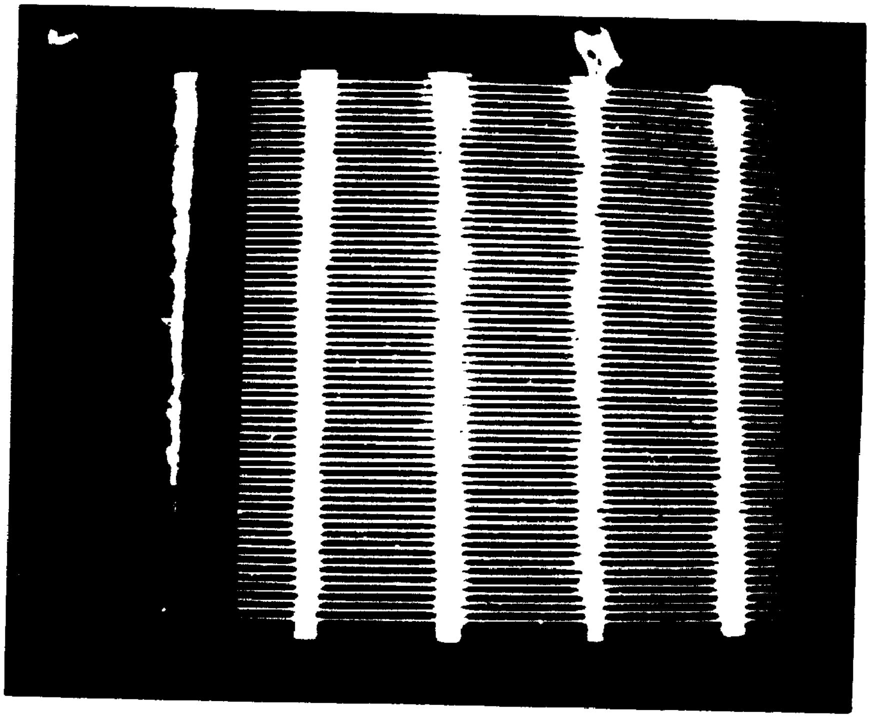

Figure B.2(b): Interferogram on the monitor showing the scanned locations.

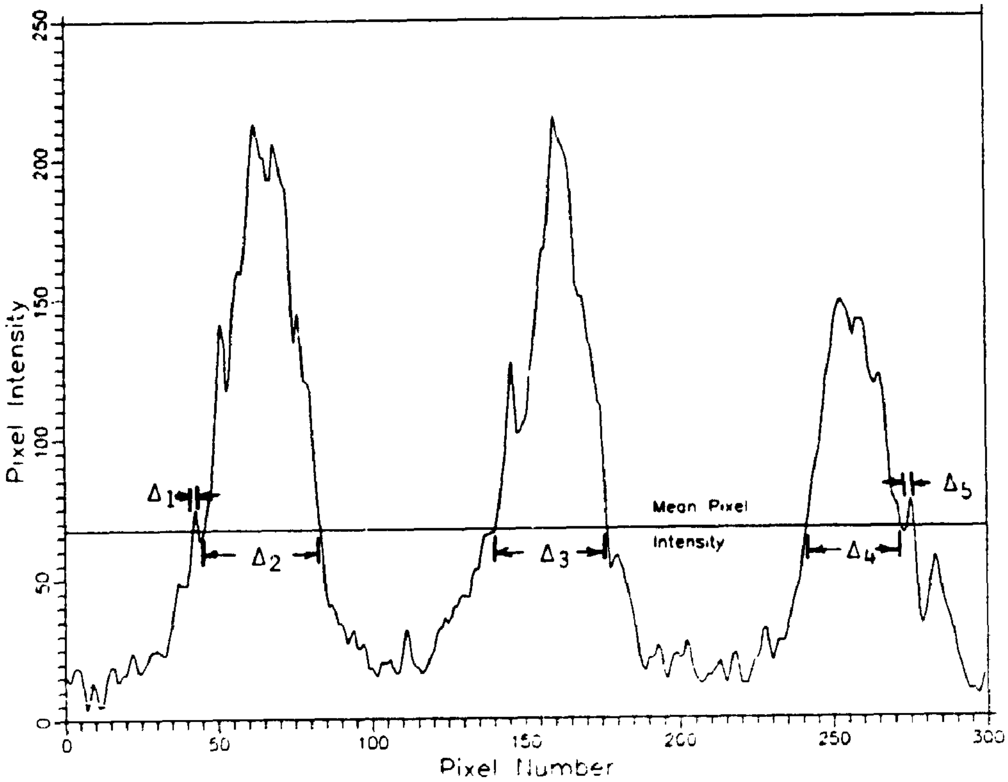

Figure B.3: A typical horizontal pixel intensity profile (showing three destructive fringe peaks).

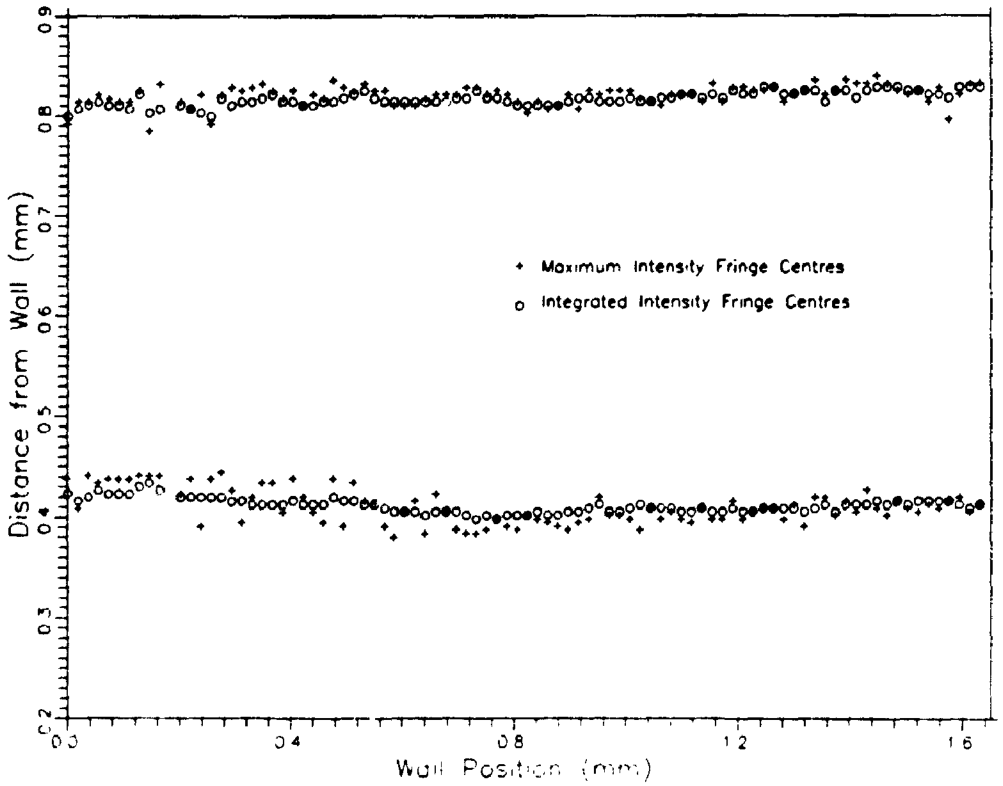

Figure B.4: Integrated intensity and maximum intensity fringe centre plot.

in the interferometer and digitizing optics. For each horizontal scan the following algorithm is used to extract the fringe centre locations.

First, the mean pixel intensity (I_m) for the scan is calculated. Next, the width of each peak (Δ_i) is calculated where it crosses the mean intensity line (see Fig. B.3). Each Δ_i represents a potential fringe. To eliminate the small noise "spikes" (Δ_1 and Δ_5 in Fig. B.3) the width of each Δ_i is compared to the largest spacing (Δ_{max}). If $\Delta_i < 0.2\ \Delta_{max}$ the "spike" is discarded as noise.

Once only valid fringe peaks remain, the intensity data in each Δ_i range are processed to yield the fringe centres. Two different techniques have been used:

i) *Maximum pixel intensity fringe centre:*

In the range Δ_i, the location of maximum pixel intensity is found. If the data are completely free of noise this is the ideal technique. Measured fringe spacings would not be in error by more than the width of one pixel.

ii) *Integrated intensity fringe centre:*

The integrated intensity fringe centre is found by locating the line that equally divides the area under each valid fringe peak. The area under the pixel intensity curve for a valid fringe peak is calculated numerically using the trapezoidal rule:

$A = \Sigma(I - I_m)$ summed over each pixel in the range Δ_i.

The fringe centre is taken to be the pixel location that corresponds to A/2.

This method is a modification of a method used by McKeen and Tarasuk [87,88] to extract fringe centres from the output of an automated scanning densitometer.

The mean intensity value fluctuates from one horizontal scan to another because of noise and changes in the background light intensity across the image. For this reason the sensitivity of the integrated intensity data to fluctuations in the mean intensity has been tested. The image shown in Fig. B.2 was analyzed with the mean intensity line arbitrarily shifted by ± 20%. The maximum change in any measured fringe spacing was 1.7%. The average difference was 0.18%.

It should also be noted that this algorithm can also be extended to measure half fringe shifts simply by repeating the analysis for the data under the mean intensity line. It is clear from Fig. B.3 that the *constructive* interference fringe peaks are not as well defined and the measured spacings will be less accurate. However, the ability to measure half fringe shifts could be very useful in regions where the fringe spacing is very large or where insufficient full fringe shifts exist.

B.4 RESULTS AND DISCUSSION

Figure B.4 shows a fringe centre plot of the first two fringes obtained from scanning the image at five pixel increments (approx 0.018mm) as shown in Fig. B.2(b). This is a much higher scan frequency than would be used in most actual applications. However, from this plot it is evident that the maximum intensity fringe centres exhibit substantially more scatter than the integrated intensity fringe centres. Also, in general, the maximum intensity fringe centres appear to be uniformly scattered on both sides of the integrated intensity centres. Hence, it may be concluded that the integrated intensity fringe centre detection algorithm is superior for analyzing "noisy" interferograms.

For the fringe closest to the wall, the large amount of scatter in the maximum intensity fringe centres is primarily caused by surface diffraction fringes. This will always be the case. Hence, even in a high quality interferogram, in which noise is kept to a minimum, the integrated intensity fringe centre method will likely give more accurate results for the first fringe. Based on these results, integrated fringe centres were used for the present heat transfer study.

More sophisticated methods of reducing noise in an image are available using image processing algorithms (see Baxes [89]). One method is to apply a low pass filter to the entire image with the appropriate cut-off frequency. Alternately, high frequency noise could be reduced using a median filter. However, in the present system, the computing power is insufficient to implement these imaging techniques. For example, with the present system (80286 with math co-processor) a median filtering operation with a 3X3 kernel takes about two to three minutes for each image. Also, it was found that a 3X3 kernel was insufficient to reduce the noise level in the image significantly. Much larger kernel sizes requiring greater computing power are needed.

Ten scans of the same location on an interferogram were made manually using a travelling microscope by two people experienced at fringe reading. The same process was then repeated using the imaging system. The manually measured fringe spacings differed by as much as 3%, whereas the imaging system gave the same fringe spacing with 0.2% in all cases.

B.5 Concluding Remarks

An IBM PC based digital image processing system has been developed for analyzing interferograms. An algorithm for detecting interference fringes has been implemented that is insensitive to noise in the image. Fringe centre data with a low amount of scatter can be obtained using an integrated intensity method.

APPENDIX C

Air Properties

With the exception of density (ρ), the properties of air were considered to be functions of temperature only. The temperature dependence of dynamic viscosity (μ), thermal conductivity (k) and specific heat was obtained from a comprehensive compilation of data by the Thermophysical Properties Research Centre, Purdue University [90,91,92]. Recommended values were given (at standard atmospheric pressure) based on the data of many independent researchers.

C.1 Dynamic Viscosity (μ)

The recommended data of Touloukian, Saxena and Hestermans [90] are shown in Fig. C.1. Linear interpolation between data points was used. From a scatter plot of data from many sources given in reference [90], the data are estimated to be accurate to ±0.5 percent.

C.2 Thermal Conductivity (k)

The recommended data of Touloukian, Liley and Saxena [91] are shown in Fig. C.2. Linear interpolation between data points was used. In the temperature range of the present study, the data are stated to be accurate to ±1.0 percent.

C.3 Specific Heat (C_p)

A third order best fit polynomial presented by Touloukian and Makita [92]

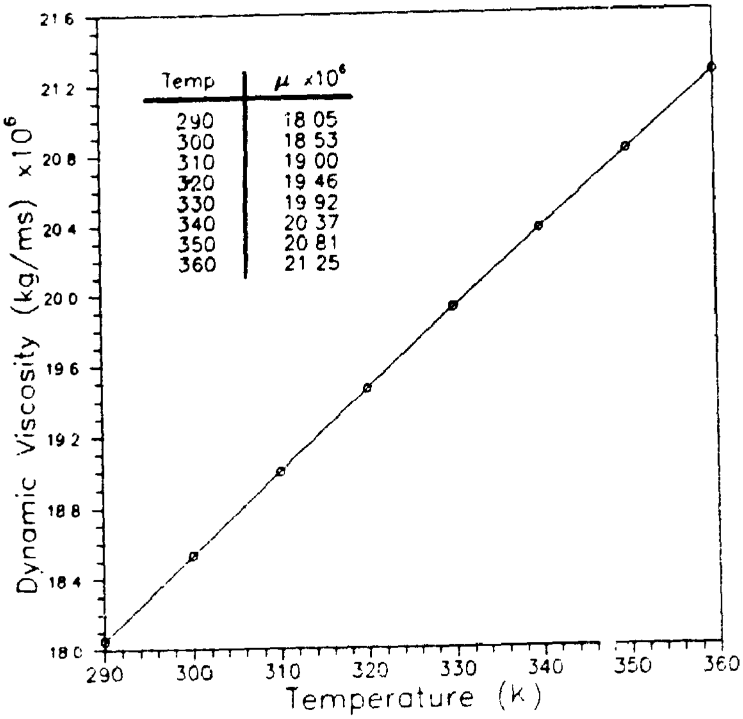

Temp	$\mu \times 10^6$
290	18.05
300	18.53
310	19.00
320	19.46
330	19.92
340	20.37
350	20.81
360	21.25

Figure C.1: Dynamic viscosity versus temperature for air.

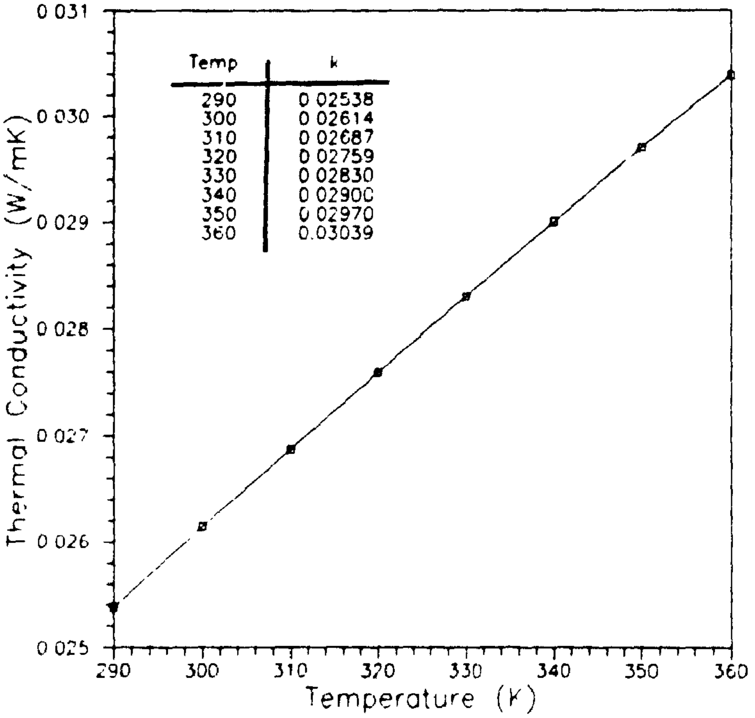

Temp	k
290	0.02538
300	0.02614
310	0.02687
320	0.02759
330	0.02830
340	0.02900
350	0.02970
360	0.03039

Figure C.2: Thermal conductivity versus temperature for air.

was used to calculate specific heat:

$$C_p(\mathrm{J/kg\ K}) = 1044.66 - 3.15967\times10^{-1}\ T + 7.07908\times10^{-4}\ T^2 - 2.7034\mathrm{E}{-7}\ T^3 \quad (T \text{ in } ^\circ\mathrm{K}) \tag{C.1}$$

Valid over temperature range $260\mathrm{K} \le T \le 610\mathrm{K}$.

From a scatter plot of data for C_p (at p=1 atm) given in reference [92], the data are estimated to be accurate to approximately ±0.25 percent.

C.4 Coefficient of Thermal Expansion (β)

The coefficient of thermal expansion for a fluid is defined as:

$$\beta = -\frac{1}{\rho}\left(\frac{\partial\rho}{\partial T}\right)_p \tag{C.2}$$

In this study, air was considered to behave as an ideal gas. The coefficient of thermal expansion can therefore be evaluated by,

$$\beta = \frac{1}{T} \tag{C.3}$$

where T is the absolute temperature.

C.5 Index of Refraction (N)

The index of refraction (N) is related to density (ρ) by the Lorentz-Lorenz equation [74],

$$\frac{(N^2-1)}{\rho(N^2+2)} = G(\lambda) \tag{C.4}$$

where $G(\lambda)$ is called the specific refractivity and is a function of both the substance and the light wavelength. For air and He-Ne laser ($\lambda=0.6328\times10^{-6}$m), $G=0.1504\times10^{-3}$ m^3/kg. Since air has a refractive index very close to unity, equation (C.4) can be simplified to:

$$\frac{2(N-1)}{3\rho} = G \tag{C.5}$$

Equation (C.5) is called the Gladstone-Dale equation [74].

C.6 Density (ρ)

The density of air was calculated using the ideal gas law.

APPENDIX D

TABULAR NUMERICAL DATA

D.1 Numerical Results from the Elliptic Solution

Table D.1. Numerical results from the elliptic solution (FIDAP) for the undivided channel (L_p/L_c=0).

Gr_b	L_c/b	Pr	Ra_c^*	R_i	Nu_{c2}	Nu_c	Q_o	T_b^*	# of nodes
100	10	0.733	7.33	5	0.8421	0.8833	1.3948	0.8675	9,753
1,250	10	0.733	91.62	5	1.8022	1.8671	1.4391	0.5006	9,753
7,000	10	0.7	490.0	5	2.6397	2.7250	1.2671	0.3672	9,753
8,000	10	0.7	560.0	5	2.7203	2.8074	1.2438	0.3605	9,753
9,000	10	0.7	630.0	5	2.7934	2.8820	1.2223	0.3550	9,753
10,000	10	0.7	700.0	5	2.8604	2.9504	1.2025	0.3505	9,753
50,000	10	0.7	3,500	5	4.1225	4.2340	0.8604	0.3144	9,753
100	17	0.7	4.118	5	0.6462	0.6718	1.7387	0.9384	10,347
1,000	17	0.7	41.18	5	1.4840	1.5240	1.9362	0.6045	10,347
2,000	17	0.7	82.35	5	1.7604	1.8060	1.9053	0.5147	10,347
3,000	17	0.7	123.5	5	1.9362	1.9854	1.8704	0.4706	10,347
5,000	17	0.7	205.9	5	2.1766	2.2309	1.8065	0.4241	10,347
10,000	17	0.7	411.8	5	2.5433	2.6053	1.6815	0.3763	10,347
50	24	0.7	1.458	5	0.3307	0.3483	1.6967	0.9954	10,033
100	24	0.7	2.917	5	0.5358	0.5546	1.9649	0.9677	14,369
106.7	24	0.7	3.112	5	0.5552	0.5763	1.9863	0.9629	10,033
200	24	0.7	5.833	5	0.7728	0.7970	2.1512	0.8982	10,033
500	24	0.7	14.58	5	1.1036	1.1328	2.2780	0.7625	10,033
1,000	24	0.7	29.17	5	1.3601	1.3902	2.3046	0.6540	14,369
2,000	24	0.7	58.33	5	1.6204	1.6597	2.2871	0.5564	10,033
2,500	24	0.7	72.92	5	1.7098	1.7513	2.2726	0.5284	10,033
3,000	24	0.7	87.50	5	1.7851	1.8284	2.2574	0.5070	10,033
5,000	24	0.7	145.8	5	2.0080	2.0573	2.1978	0.4539	10.033
10,000	24	0.7	291.7	5	2.3568	2.4046	2.0734	0.3976	14,369
Grid Tests (partial listing)									
10,000	24	0.7	291.7	3	2.346	2.4055	2.084	0.3958	8,465
10,000	24	0.7	291.7	4	2.346	2.4046	2.076	0.3971	9,249
10,000	24	0.7	291.7	5	2.345	2.4040	2.073	0.3978	10,033

Table D.2. Numerical results from the elliptic solution (FIDAP) for the divided channel, $L_p/L_c=1/3$, no blockage $t/b=0.0$, $L_c/b=15$, $Pr=0.7$, plate at the bottom of the channel $L_i/L_c=0$.

Ra_c^*	Nu_c	Nu_{c2}	Nu_w	Nu_p	Q_e	T_b^*	# of nodes	R_i
5	0.4820	0.4537	0.3008	0.9127	1.3339	0.9975	14,479	5
10	0.8020	0.7678	0.5317	1.4762	1.6053	0.9752	14,479	5
20	1.1934	1.1528	0.8454	2.0748	1.8070	0.9116	14,479	5
40	1.6152	1.5678	1.2073	2.6492	1.9341	0.8152	14,479	5
100	2.1978	2.1407	1.7248	3.3883	2.0144	0.6736	14,479	5
200	2.6620	2.5967	2.1365	3.9771	2.0248	0.5739	14,479	5
500	3.3257	3.2469	2.7078	4.8644	1.9866	0.4622	14,479	5
1,000	3.8848	3.7936	3.1738	5.6531	1.9244	0.3940	14,479	5
2,000	4.5155	4.4101	3.6933	6.5604	1.8342	0.3398	14,479	5
5,000	5.4975	5.3698	4.5088	7.9529	1.6693	0.2875	14,479	5
10,000	6.3823	6.2336	5.2589	9.1578	1.5109	0.2607	14,479	5
Grid Tests (partial listing)								
10	0.8035	0.7691	0.5329	1.4775	1.6091	0.9750	9,003	3
10	0.8018	0.7668	0.5310	1.4742	1.6054	0.9752	10,143	5
100	2.2007	2.1443	1.7275	3.3947	2.0215	0.6722	9,003	3
1,000	3.8875	3.8012	3.1710	5.6916	1.9340	0.3925	9,003	3
5,000	5.5035	5.3895	4.5046	8.0446	1.6822	0.2856	9,003	3
5,000	5.5000	5.3842	4.5041	8.0245	1.6698	0.2875	10,143	5
10,000	6.3856	6.2561	5.2580	9.2503	1.5115	0.2607	10,143	5
10,000	6.3895	6.2621	5.2568	9.2778	1.5269	0.2584	9,003	3

Table D.3. Numerical results from the elliptic solution (FIDAP) for the divided channel, $L_p/L_c=1/3$, no blockage $t/b=0.0$, $L_c/b=15$, $Pr=0.7$, plate in the middle of the channel, $L_1/L_c=(1-L_p/L_c)/2=1/3$.

Ra_c^*	Nu_c	Nu_{c2}	Nu_w	Nu_p	Q_e	T_b^*
5	0.4256	0.4072	0.4487	0.2647	1.1764	0.9989
10	0.7058	0.6760	0.6775	0.6[illegible]12	1.3964	0.9867
20	1.0786	1.0409	0.9674	1.2615	1.5811	0.9417
40	1.5097	1.4638	1.3034	1.9449	1.7148	0.8595
100	2.1154	2.0586	1.7866	2.8743	1.8107	0.7211
200	2.5840	2.5187	2.1709	3.5620	1.8296	0.6116
500	3.2353	3.1575	2.7156	4.4834	1.8001	0.4963
1,000	3.7809	3.6922	3.1748	5.2446	1.7438	0.4233
2,000	4.3982	4.2975	3.6969	6.0992	1.6582	0.3661
5,000	5.3531	5.2448	4.5270	7.3983	1.4968	0.3127
10,000	6.2369	6.1042	5.2968	8.5263	1.3422	0.2868

Table D.4. Numerical results from the elliptic solution (FIDAP) for the divided channel, $L_p/L_c=1/3$, no blockage $t/b=0.0$, $L_c/b=15$, $Pr=0.7$, plate at the top of the channel $L_1/L_c=1-L_p/L_c=2/3$.

Ra_c^*	Nu_c	Nu_{c2}	Nu_w	Nu_p	Q_e	T_b^*
5	0.4155	0.3953	0.4996	0.08244	1.1493	0.9989
10	0.6659	0.6408	0.7545	0.2997	1.3165	0.9881
20	0.9921	0.9611	1.0475	0.7017	1.4431	0.9496
40	1.3709	1.3333	1.3600	1.2532	1.5265	0.8772
100	1.9195	1.8724	1.7904	2.1182	1.5780	0.7514
200	2.3644	2.3095	2.1404	2.9167	1.5800	0.6536
500	3.0039	2.9374	2.6655	3.7530	1.5391	0.5391
1,000	3.5462	3.4697	3.1279	4.4952	1.4774	0.4688
2,000	4.1630	4.0758	3.6620	5.3171	1.3911	0.4132
5,000	5.1322	5.0300	4.5124	6.5829	1.2401	0.3613
10,000	6.0119	5.8994	5.2975	7.7049	1.1025	0.3367

Table D.5. Numerical results from the elliptic solution (FIDAP) for the divided channel, $L_p/L_c=1/3$, 10% blockage t/b=0.1, $L_c/b=15$, Pr=0.7, plate at the bottom of the channel $L_i/L_c=0$.

Ra_c^*	Nu_c	Nu_{c2}	Nu_w	Nu_p	Q_e	T_b^*
5	0.4050	0.3853	0.2457	0.7946	1.1251	0.9992
10	0.7063	0.6826	0.4528	1.3566	1.4020	0.9889
20	1.1085	1.0805	0.7606	2.0188	1.6320	0.9428
40	1.5607	1.52843	1.1373	2.6754	1.7902	0.8557
100	2.1887	2.1502	1.6891	3.5028	1.9058	0.7129
200	2.6837	2.6401	2.1299	4.1365	1.9393	0.6074
500	3.3810	3.3291	2.7373	5.0648	1.9293	0.4865
1,000	3.9601	3.9005	3.2255	5.8800	1.8872	0.4119
2,000	4.6051	4.5371	3.7610	6.8135	1.8154	0.3521
5,000	5.5974	5.5186	4.5909	8.2395	1.6701	0.2942
10,000	6.4829	6.3973	5.3505	9.4675	1.5215	0.2645

Table D.6. Numerical results from the elliptic solution (FIDAP) for the divided channel, $L_p/L_c=1/3$, 20% blockage t/b=0.2, $L_c/b=15$, Pr=0.7, plate at the bottom of the channel $L_i/L_c=0$.

Ra_c^*	Nu_c	Nu_{c2}	Nu_w	Nu_p	Q_e	T_b^*
5	0.3245	0.3067	0.1912	0.6379	0.9062	0.9997
10	0.5903	0.5683	0.3665	1.1471	1.1609	0.9967
20	0.9852	0.9589	0.6527	1.8372	1.4170	0.9705
40	1.4636	1.4329	1.0350	2.5742	1.6055	0.8998
100	2.1445	2.1075	1.6213	3.5027	1.7585	0.7613
200	2.6786	2.6365	2.0961	4.1867	1.8166	0.6509
500	3.4205	3.3703	2.7490	5.1528	1.8375	0.5197
1,000	4.0287	3.9706	3.2670	5.9891	1.8205	0.4369
2,000	4.6992	4.6319	3.8254	6.9458	1.7753	0.3695
5,000	5.7187	5.6386	4.6750	8.4031	1.6623	0.3037
10,000	6.6187	6.5298	5.4435	9.6465	1.5317	0.2697

D.2 Numerical Results from the Parabolic Solution (t/b=0)

Table D.7. Numerical results from the parabolic solution for the undivided channel $L_p/L_c=0$, Pr=0.7. (Note: the results for $L_p/L_c=1$ were obtained by rescaling the data for $L_p/L_c=0$)

Ra_c^*	Nu_c	Q_p	T_b^*
0.1235	3.975E-2	3.220E-1	1.0000
0.2062	6.496E-1	3.150E-1	1.0000
0.4023	0.1207	3.000E-1	1.0000
0.5491	0.1592	2.900E-1	1.0000
1.0856	0.2819	2.600E-1	0.9986
1.5502	0.3698	2.400E-1	0.9939
2.9066	0.5313	2.000E-1	0.9656
4.9658	0.7483	1.650E-1	0.9132
9.6900	0.9958	1.250E-1	0.8222
15.839	1.1809	1.000E-1	0.7455
25.224	1.3582	8.000E-2	0.6731
44.869	1.5848	6.000E-2	0.5887
123.76	2.0366	3.500E-2	0.4702
326.52	2.5587	2.000E-2	0.3918
576.85	2.9132	1.400E-2	0.3607
1115.5	3.3777	9.000E-3	0.3364
1973.5	3.8352	6.000E-3	0.3239
3406.3	4.3305	4.000E-3	0.3178
8349.6	5.2993	2.000E-3	0.3173
10225	5.5469	1.700E-3	0.3191

Table D.8. Numerical results from the parabolic solution for the divided channel (t/b=0), $L_p/L_c=2/3$ (nominal), Pr=0.7, plate at the bottom of the channel $L_i/L_c=0$.

Ra_c^*	L_p/L_c	Nu_c	Nu_p	Nu_w	Q_p	T_b^*
1.0324	0.6686	6.664E-2	8.315E-2	5.560E-2	1.077E-1	1.0000
2.1210	0.6700	0.1327	0.1654	0.1108	1.045E-1	1.0000
5.3059	0.6672	0.3089	0.3856	0.2575	9.706E-2	1.0000
15.316	0.6682	0.7328	0.9082	0.6155	8.050E-2	0.9914
28.289	0.6723	1.0973	1.3347	0.9376	6.765E-2	0.9589
50.828	0.6707	1.5022	1.7925	1.3075	5.516E-2	0.8951
151.11	0.6665	2.2972	2.6499	2.0621	3.480E-2	0.7280
502.92	0.6682	3.2081	3.6061	2.9422	933E-2	0.5505
2004.0	0.6656	4.4491	4.9381	4.1236	9.194E-3	0.4022
9998.4	0.6642	6.3558	6.9703	5.9476	3.420E-3	0.3093

Table D.9. Numerical results from the parabolic solution for the divided channel (t/b=0), L_p/L_c=1/3 (nominal), Pr=0.7, plate at the bottom of the channel L_i/L_c=0.

Ra_c^*	L_p/L_c	Nu_c	Nu_p	Nu_w	Q_p	T_b^*
0.2017	0.3338	2.490E-2	4.975E-2	1.661E-2	1.647E-1	1.0000
1.0279	0.3333	0.1217	0.2435	8.115E-2	1.579E-1	1.0000
2.2251	0.3350	0.2483	0.4945	0.1659	1.490E-1	1.0000
8.0904	0.3324	0.7166	1.3634	0.5016	1.200E-1	0.9834
30.335	0.3358	1.4655	2.4408	1.1379	7.612E-2	0.8479
102.59	0.3339	2.2458	3.4190	1.8540	4.409E-2	0.6623
405.74	0.3334	3.2414	4.6569	2.7695	2.205E-2	0.4830
1962.0	0.3346	4.6823	6.5113	4.0701	9.270E-3	0.3436
6013.7	0.3331	6.0032	8.2003	5.2713	4.694E-3	0.2835
11788	0.3334	6.9404	9.3532	6.1360	3.011E-3	0.2607

Table D.10. Numerical results from the parabolic solution for the divided channel (t/b=0), L_p/L_c=1/10 (nominal), Pr=0.7, plate at the bottom of the channel L_i/L_c=0.

Ra_c^*	L_p/L_c	Nu_c	Nu_p	Nu_w	Q_p	T_b^*
0.1007	0.1002	2.319E-2	1.273E-1	1.276E-2	2.533E-1	1.0000
0.2054	0.1000	4.679E-2	2.573E-1	2.573E-2	2.505E-1	1.0000
1.0333	0.1009	0.2155	1.1315	0.1231	2.297E-1	1.0000
2.1141	0.0997	0.3963	1.8444	0.2520	2.068E-1	0.9967
5.0577	0.0999	0.7227	2.6857	0.5266	1.641E-1	0.9580
10.169	0.0999	1.0358	3.3107	0.8086	1.271E-1	0.8817
21.210	0.1000	1.3894	3.9766	1.1307	9.288E-2	0.7759
50.135	0.0998	1.8334	4.8485	1.5325	6.209E-2	0.6478
151.26	0.1008	2.4865	6.1628	2.1161	3.565E-2	0.5076
502.76	0.0997	3.3456	7.9863	2.8827	1.871E-2	0.3912
2014.4	0.1005	4.6272	10.604	4.0267	8.501E-3	0.2973
10051	0.1003	6.6332	14.468	5.8477	3.124E-3	0.2325

Table D.11. Numerical results from the parabolic solution for the divided channel (t/b=0), L_p/L_c=1/100 (nominal), Pr=0.7, plate at the bottom of the channel L_i/L_c=0.

Ra_c^*	L_p/L_c	Nu_c	Nu_p	Nu_w	Q_p	T_b^*
0.01021	0.01005	3.264E-3	0.1640	1.648E-3	3.230E-1	1.0000
0.03118	0.01008	9.933E-2	0.4974	5.020E-3	3.218E-1	1.0000
0.10319	0.01001	3.245E-2	1.4874	1.789E-2	3.176E-1	1.0000
0.20148	0.01000	6.202E-2	2.3026	3.963E-2	3.111E-1	1.0000
1.0265	0.01000	0.2670	4.5180	0.2244	2.629E-1	0.9992
2.1096	0.00994	0.4585	5.7450	0.4060	2.226E-1	0.9861
5.0658	0.00999	0.7675	7.4230	0.7011	1.665E-1	0.9191
10.075	0.00998	1.0379	8.9198	0.9593	1.258E-1	0.8271
21.031	0.00991	1.3389	10.756	1.2456	9.002E-2	0.7143
50.153	0.01000	1.7177	13.152	1.6034	5.877E-2	0.5886
150.71	0.00990	2.2701	16.910	2.1252	3.300E-2	0.4610
504.80	0.00999	3.0296	21.624	2.8438	1.662E-2	0.3647
1989.1	0.00992	4.1646	28.308	3.9251	7.272E-3	0.2908
10078	0.01000	6.0623	38.102	5.7420	2.625E-3	0.2315

Table D.12. Numerical results from the parabolic solution for the divided channel (t/b=0), L_p/L_c=2/3 (nominal), Pr=0.7, plate in the middle of the channel $L_i/L_c=(1-L_p/L_c)/2$=1/6.

Ra_c^*	L_p/L_c	Nu_c	Nu_p	Nu_w	Q_p	T_b^*
0.2000	0.6667	1.315E-2	3.407E-8	2.219E-2	1.096E-1	1.0000
1.0001	0.6667	6.252E-2	3.934E-3	0.1025	1.042E-1	1.0000
2.1001	0.6667	0.1246	3.377E-2	0.1861	9.890E-2	1.0000
5.0011	0.6668	0.2705	0.1668	0.3341	9.017E-2	1.0000
10.002	0.6668	0.4845	0.4102	0.5365	8.080E-2	0.9992
21.004	0.6668	0.8467	0.8468	0.8517	6.818E-2	0.9855
50.010	0.6668	1.4164	1.5215	1.3499	5.155E-1	0.9158
150.03	0.6668	2.2170	2.4304	2.0700	3.260E-2	0.7555
500.11	0.6668	3.1327	3.4417	2.9231	1.818E-2	0.5742
2000.2	0.6667	4.3684	4.7541	4.0833	8.656E-3	0.4205
9998.5	0.6666	6.2841	6.7907	5.9191	3.217E-3	0.3256

Table D.13. Numerical results from the parabolic solution for the divided channel (t/b=0), $L_p/L_c=1/3$ (nominal), Pr=0.7, plate in the middle of the channel $L_i/L_c=(1-L_p/L_c)/2=1/3$.

Ra_c^*	L_p/L_c	Nu_c	Nu_p	Nu_w	Q_p	T_b^*
0.2000	0.3334	2.443E-2	1.839E-9	3.292E-2	1.628E-1	1.0000
1.0002	0.3334	0.1123	3.748E-3	0.1499	1.498E-1	1.0000
2.0999	0.3333	0.2155	4.877E-2	0.2726	1.368E-1	1.0000
5.0028	0.3335	0.4372	0.2922	0.4872	1.167E-1	0.9988
10.005	0.3335	0.7229	0.7188	0.7253	9.785E-1	0.9846
21.007	0.3334	1.1273	1.3595	1.0488	7.686E-2	0.9310
50.010	0.3334	1.6783	2.2179	1.4942	5.458E-2	0.8199
150.02	0.3334	2.4280	3.3224	2.1226	3.300E-2	0.6539
500.12	0.3334	3.3203	4.5190	2.9025	1.787E-2	0.4952
2000.0	0.3333	4.5832	6.1137	4.0365	8.279E-3	0.3691
9998.6	0.3333	6.5446	8.4945	5.8366	2.994E-2	0.2915

Table D.14. Numerical results from the parabolic solution for the divided channel (t/b=0), $L_p/L_c=1/10$ (nominal), Pr=0.7, plate in the middle of the channel $L_i/L_c=(1-L_p/L_c)/2=9/20$.

Ra_c^*	L_p/L_c	Nu_c	Nu_p	Nu_w	Q_p	T_b^*
0.2000	0.1000	4.474E-2	6.161E-8	4.977E-2	2.460E-1	1.0000
1.0001	0.1000	0.1947	2.199E-2	0.2138	2.142E-1	1.0000
2.1007	0.1000	0.3553	0.2006	0.3725	1.863E-1	0.9985
5.0018	0.1000	0.6502	0.8207	0.6334	1.467E-1	0.9746
10.003	0.1000	0.9547	1.5919	0.8893	1.146E-1	0.9163
21.004	0.1002	1.3229	2.5821	1.1926	8.430E-2	0.8218
50.013	0.1000	1.7933	3.8471	1.5792	5.669E-2	0.6957
150.02	0.1000	2.4509	5.4890	2.1329	3.280E-2	0.5479
499.45	0.0999	3.2872	7.2467	2.8636	1.715E-2	0.4220
1999.2	0.1000	4.5187	9.5370	3.9683	7.679E-3	0.3238
9993.6	0.0999	6.4638	12.856	5.7495	2.730E-3	0.2606

Table D.15. Numerical results from the parabolic solution for the divided channel (t/b=0), L_p/L_c=2/3 (nominal), Pr=0.7, plate in the top of the channel $L_i/L_c=1-L_p/L_c=1/3$.

Ra_c^*	L_p/L_c	Nu_c	Nu_p	Nu_w	Q_p	T_b^*
0.1999	0.6668	1.315E-2	8.449-13	2.219E-2	1.096E-1	1.0000
0.9997	0.6668	6.246E-2	2.302E-4	0.1050	1.041E-1	1.0000
2.0987	0.6669	0.1233	7.349E-3	0.2022	9.791E-2	1.0000
4.9874	0.6675	0.2605	7.530E-2	0.3862	8.709E-2	1.0000
10.012	0.6663	0.4581	0.2456	0.6020	7.628E-2	0.9994
21.006	0.6666	0.7866	0.5999	0.9157	6.311E-2	0.9888
50.006	0.6666	1.3140	1.2171	1.3832	4.711E-2	0.9295
150.03	0.6666	2.0873	2.1357	2.0537	2.967E-2	0.7815
500.09	0.6666	2.9942	3.1789	2.8669	1.653E-2	0.6036
1999.5	0.6668	4.2226	4.5061	4.0153	7.861E-3	0.4478
9989.7	0.6670	6.1336	6.5404	5.8401	2.928E-3	0.3496

Table D.16. Numerical results from the parabolic solution for the divided channel (t/b=0), L_p/L_c=1/3 (nominal), Pr=0.7, plate in the top of the channel $L_i/L_c=1-L_p/L_c=2/3$.

Ra_c^*	L_p/L_c	Nu_c	Nu_p	Nu_w	Q_p	T_b^*
0.2044	0.3335	2.496E-2	2.91E-14	3.367E-2	1.628E-1	1.0000
0.9974	0.3355	0.1118	7.877E-5	0.1507	1.496E-1	1.0000
2.0455	0.3335	0.2096	5.250E-3	0.2803	1.367E-1	1.0000
3.0286	0.3337	0.2881	2.294E-2	0.3797	1.269E-1	0.9999
5.0051	0.3340	0.4217	8.963E-2	0.5357	1.125E-1	0.9989
10.061	0.3340	0.6780	0.3217	0.7992	9.109E-2	0.9872
21.338	0.3321	1.0410	0.7815	1.1282	6.910E-2	0.9405
50.540	0.3332	1.5259	1.5027	1.5330	4.778E-2	0.8424
151.22	0.3329	2.2157	2.5840	2.0925	2.834E-2	0.6891
503.30	0.3301	3.0761	3.8140	2.8224	1.515E-2	0.5369
2003.8	0.3322	4.2988	5.3425	3.9247	6.892E-3	0.4147
10025	0.3350	6.2286	7.6657	5.6972	2.441E-3	0.3398

Table D.17. Numerical results from the parabolic solution for the divided channel (t/b=0), L_p/L_c=1/10 (nominal), Pr=0.7, plate in the top of the channel $L_1/L_c=1-L_p/L_c=9/10$.

Ra_c^*	L_p/L_c	Nu_c	Nu_p	Nu_w	Q_p	T_b^*
0.2000	0.1000	4.479E-2	3.13E-12	4.983E-2	2.463E-1	1.0000
1.0000	0.1001	0.1953	5.858E-4	0.2169	2.149E-1	1.0000
2.0998	0.1001	0.3536	2.430E-2	0.3893	1.856E-1	0.9984
4.9986	0.1003	0.6327	0.2403	0.6745	1.429E-1	0.9744
9.9948	0.1005	0.9123	0.6803	0.9370	1.094E-1	0.9182
21.000	0.1000	1.2454	1.4132	1.2276	7.884E-2	0.8275
50.019	0.0997	1.6685	2.5197	1.5793	5.179E-2	0.7083
150.10	0.0994	2.2750	4.1008	2.0867	2.909E-2	0.5729
500.11	0.0998	3.0555	5.6479	2.7835	1.460E-1	0.4603
2000.1	0.1000	4.1869	7.3684	3.8470	6.104E-3	0.3772
10001	0.0999	6.0317	10.324	5.5766	1.995E-3	0.3324

Table D.18. Numerical results from the parabolic solution for the divided channel (t/b=0). Special calculations made holding Ra_p^* constant and varying the plate length ratio L_p/L_c. The plate is at the bottom of the channel $L_i/L_c=0$, and $Pr=0.7$.

Ra_p^*	L_p/L_c	Nu_c	Nu_p	Nu_w	Q_p	T_b^*
0.1000	1.0000	4.161E-3	4.161E-3	4.161E-3	8.318E-2	1.0000
0.1000	0.9127	4.247E-3	4.450E-3	4.062E-3	8.900E-2	1.0000
0.1000	0.8099	4.341E-3	4.9850-3	3.928E-3	9.700E-2	1.0000
0.1000	0.7031	4.417E-3	5.350E-3	3.761E-3	1.070E-1	1.0000
0.1000	0.5682	4.457E-3	6.150E-3	3.495E-3	1.230E-1	1.0000
0.1000	0.4532	4.397E-3	7.050E-3	3.195E-3	1.410E-1	1.0000
0.1000	0.3555	4.222E-3	8.050E-3	2.862E-3	1.610E-1	1.0000
0.1000	0.2794	3.953E-3	9.050E-3	2.529E-3	1.810E-1	1.0000
0.1000	0.2078	3.527E-3	1.025E-2	2.130E-3	2.050E-1	1.0000
0.1000	0.09951	2.321E-3	1.282E-2	1.276E-3	2.564E-1	1.0000
100.00	1.0000	1.6650	1.6650	1.6650	3.764E-2	0.8846
100.00	0.8693	1.7041	1.8010	1.6199	4.200E-2	0.8725
100.00	0.8095	1.7085	1.8597	1.5862	4.400E-2	0.8680
100.00	0.7047	1.7055	1.9709	1.5185	4.800E-2	0.8595
100.00	0.5980	1.6865	2.0992	1.4396	5.300E-2	0.8503
100.00	0.4971	1.6489	2.2397	1.3553	5.900E-2	0.8417
100.00	0.4060	1.5923	2.3880	1.2692	6.600E-2	0.8354
100.00	0.3103	1.4989	2.5763	1.1645	7.600E-2	0.8327
100.00	0.2007	1.3232	2.8640	1.0139	9.400E-2	0.8420
100.00	0.09617	1.0120	3.3182	0.7902	1.300E-1	0.8873
10,006	1.0000	5.9369	5.9369	5.9369	3.322E-3	0.3573
10,000	0.9142	5.9452	6.0523	5.8472	3.600E-3	0.3458
10,000	0.7865	5.9018	6.2169	5.6539	4.000E-3	0.3351
10,000	0.6812	5.8382	6.3784	5.4701	4.400E-3	0.3275
10,000	0.5947	5.7607	6.5371	5.2990	4.800E-3	0.3218
10,000	0.4768	5.6024	6.8082	5.0275	5.500E-2	0.3155
10,000	0.3787	5.4010	7.1083	4.7545	6.300E-2	0.3121
10,000	0.2989	5.1649	7.4340	4.4866	7.200E-3	0.3117
10,000	0.1975	4.7072	8.0509	4.0469	9.000E-3	0.3172
10,000	0.09599	3.8920	9.2856	3.3743	1.300E-2	0.3418

APPENDIX E

TABULAR EXPERIMENTAL DATA

Table E.1. Experimental average Nusselt number and associated data (L_p/L_c=1/3, L_c=120.0mm, L_p=40.0mm , $L_{p,wet}$=42.0mm, 2t=3.5mm).

L_i/L_c	T_s (°C)	T_o (°C)	P_{atm} (mmHg)	2b mm	Ra_c^*	Nu_p	Nu_w	Nu_c
0	45.7	21.1	738.0	17.55	97.6	3.13	1.44	1.88
0	42.4	20.5	741.9	25.40	395	4.43	2.55	3.04
0	40.5	21.2	738.0	31.95	874	5.26	2.89	3.50
0	40.4	20.2	741.4	31.95	931	5.43	2.86	3.53
0	40.2	20.0	740.2	38.15	1,890	6.11	3.48	4.16
0	40.7	20.3	741.7	50.70	5,930	7.80	4.79	5.57
2/3	40.6	20.8	737.3	17.55	81.4	1.48	1.44	1.45
2/3	42.8	21.2	737.2	25.40	383	3.23	2.37	2.59
2/3	40.9	21.2	737.7	31.95	888	4.34	2.97	3.33
2/3	39.7	21.3	737.3	38.15	1,690	5.18	3.25	3.75
2/3	40.7	21.1	737.3	50.70	5,610	6.82	4.48	5.09
*	45.0	21.1	738.4	17.40	92.4	-	1.68	1.68

* Data for the undivided channel

APPENDIX F

EXPERIMENTAL ERROR ANALYSIS

F.1 Introduction

Numerous systematic (bias) and random sources of error are present in the experimental data. An attempt is made in this appendix to indicate the major sources of error. Also, uncertainty estimates are made for the primary measured and calculated quantities.

The single-sample uncertainty analysis of Kline and McClintock [93] has been used: consider that a result R of an experiment is to be calculated from n independent variables, x_1, x_2, ..., x_n. Let δx_1, δx_2, ..., δx_n be the random uncertainties in these quantities. The maximum uncertainty can be expressed as the sum:

$$\delta R_{max} \leq \left|\frac{\partial R}{\partial x_1}\delta x_1\right| + \left|\frac{\partial R}{\partial x_2}\delta x_2\right| + \ldots + \left|\frac{\partial R}{\partial x_n}\delta x_n\right| \qquad (F.1)$$

However, because of the random nature of the individual uncertainties, equation (F.1) will generally greatly overestimate the actual error.

Kline and McClintock [93] recommend calculating the root-sum-square uncertainty. That is, if the uncertainties in the independent variables are all given with the same odds, the uncertainty in the result (δR) is:

$$\delta R = \left(\left(\frac{\partial R}{\partial x_1}\delta x_1\right)^2 + \left(\frac{\partial R}{\partial x_2}\delta x_2\right)^2 + \ldots + \left(\frac{\partial R}{\partial x_n}\delta x_n\right)^2 \right)^{\frac{1}{2}} \qquad (F.2)$$

Note that the analysis is simplified for cases where R can be written as a product of terms, each raised to some power. If R is given by:

$$R = x_1^a x_2^b \ldots x_n^z \tag{F.3}$$

Then, the relative uncertainty can be calculated as:

$$\frac{\delta R}{R} = \left((a\frac{\delta x_1}{x_1})^2 + (b\frac{\delta x_2}{x_2})^2 + \ldots + (z\frac{\delta x_n}{x_n})^2 \right)^{\frac{1}{2}} \tag{F.4}$$

Equations (F.2) and (F.4) have been used for the present uncertainty analysis.

F.2 Uncertainty in the Rayleigh Number (Ra_c^*, Ra_p^*)

The accuracy of the calculated Rayleigh number depends upon the accuracy of the fluid properties, thermocouple readings, barometric pressure, and channel wall spacing. From these quantities, the channel Rayleigh number was calculated as follows:

$$Ra_c^* = \frac{g(T_s - T_o) b^4 p^2 C_p}{T_f^3 \mu k R_{air}{}^2 L_s} \tag{F.5}$$

The estimated uncertainty in each of the relevant quantities in equation (F.5) is given in Table F.1. Applying equation (F.4) gives:

$$\frac{\delta Ra_c^*}{Ra_c^*} = \left((2\frac{\delta p}{p})^2 + (4\frac{\delta b}{b})^2 + (\frac{\delta (T_s - T_o)}{(T_s - T_o)})^2 + (3\frac{\delta T_f}{T_f})^2 \right. \\ \left. + (\frac{\delta \mu}{\mu})^2 + (\frac{\delta C_p}{C_p})^2 + (\frac{\delta k}{k})^2 \right)^{\frac{1}{2}} \tag{F.6}$$

Evaluating equation (F.6) gives an uncertainty in the Rayleigh number (Ra_c^* or Ra_p^*) of ±2.6%.

Table F.1: Summary of the sources of uncertainty in the Rayleigh number

Quantity	Absolute Uncertainty	Max. Percent Uncertainty
Barometric Pressure (p)	±0.5mmHg	±0.07%
Measure Gap Width (2b)	±0.05 mm	±0.28%
Temperature Difference (T_s-T_o)	±0.4 C°	±2.0%
Film Temperature $T_f=(T_s+T_o)/2$	±0.4 C°	±0.13%
Dynamic Viscosity (μ)	-	±0.5
Specific Heat (C_p)	-	±0.25
Thermal conductivity (k)	-	±1.0

F.3 Uncertainty in the Heat Transfer Measurements

The interferometric technique is complex and has numerous sources of error. A discussion of the sources of uncertainty is given first. Then, an uncertainty analysis is performed to show how these errors propagate into the calculated local Nusselt numbers.

1) Refraction Error: As a ray of light passes through the test section, it is bent by density gradients normal to its path. In the present case, light rays close to the heated model surface are bent away from the surface. The error caused by this light refraction was minimized by focusing the camera at one third the distance from the exit plane of the channel, in accordance with a study by Mehta and Black [73]. Also, Kuehn [94] has shown that the additional light refraction caused by the optical windows is negligible.

2) Beam Divergence/Convergence Error: Collimation of the test beam was obtained using the procedure described in section 6.4. Before each set of experiments, the optics were examined to ensure collimation was maintained. For this reason, the error associated with beam convergence or divergence has been neglected.

3) End Effect Errors: Optical end effect errors are caused by the fact that the air is heated beyond the assumed optical length of the test section (Z_T=259.1mm). This extra partially heated length causes an additional fringe shift in the test beam. Hence, end effect errors cause the measured temperature gradient to be erroneously high. There are two sources of optical end effect errors in the present experiment:

i) A fringe shift error is caused by the formation of free convective boundary-layers on the exterior of optical windows. The external temperature of the windows was measured to be about 2C° above the ambient temperature. Modelling the windows as an isothermal vertical flat plate, the maximum additional fringe shift was estimated to be about $\Delta\epsilon \approx 0.04$. This is equivalent to an error in the effective optical length of about +1.5 mm.

ii) Thin foam pads were mounted on the walls at each end of the model to protect the optical windows. The foam pads caused the spacing of the optical windows to be slightly greater than the test section length. The resulting uncertainty in the optical length was estimated to be about +4mm.

Combining the above errors, the uncertainty in the effective optical length of the test section was estimated to be $Z_T = 259.1 + 5.5$mm. This source of error is always positive and is essentially constant for all experiments, i.e. a bias error.

4) Fringe Centre Location Error: The uncertainty in the measured fringe spacing $(x_2 - x_1)$ is a significant source of error in the interferogram analysis. The main source of error in measuring the fringe spacing is the "noise" in the interferograms. The noise comes from a wide variety of sources: optical imperfections, vibration, surface diffraction fringes, imperfections in the film, dirt/scratches on the negative, and the image digitizing system. For the purpose of the uncertainty analysis, all these sources of fringe noise will be grouped together. From an examination of the raw fringe spacing data, the noise level from all the above sources was about ±5%.

5) Scale Factor Error: The horizontal scale factor for the film negative was obtained by measuring the channel wall spacing on the negative. The error in this measurement causes an additional uncertainty in the fringe spacing of ±0.5%.

Given these estimates of the sources of error, an uncertainty analysis can now be performed for the calculated local Nusselt number. The experimental local Nusselt numbers are calculated as:

$$Nu_y = \frac{k_s\left(\frac{T_1-T_2}{x_2-x_1}\right)b}{k_f(T_s-T_o)} \qquad (F.7)$$

In equation (F.7), the local Nusselt number is given by a product of the following terms:

(T_1-T_2) is the optically measured temperature difference between the first and second fringes,

$(x_2-x_1)^{-1}$ is the first and second fringe spacing,

b is the half channel gap width,

$(T_s-T_o)^{-1}$ is the surface to ambient temperature difference,

k_s/k_f is the conductivity ratio of air at the surface and film temperatures.

The relative uncertainty in each of these terms is now estimated, so that the relative uncertainty in the local Nusselt number can be calculated as:

$$\frac{\delta Nu_y}{Nu_y} = \left(\left(\frac{\delta(T_s-T_o)}{T_s-T_o}\right)^2 + \left(\frac{\delta(T_1-T_2)}{T_1-T_2}\right)^2 + \left(\frac{\delta(x_1-x_2)}{x_1-x_2}\right)^2 + \left(\frac{\delta b}{b}\right)^2 \right)^{1/2} \qquad (F.8)$$

The uncertainty in the conductivity ratio (k_s/k_f) is assumed to be negligible. As previously given in Table F.1, the maximum uncertainty in the measured channel width is $\delta b/b=0.28\%$ and the uncertainty in the surface-to-ambient temperature difference (from thermocouples) is $\delta(T_s-T_o)/(T_s-T_o)=\pm2.0\%$. Also, as discussed above, the relative uncertainty in the fringe spacing is $\delta(x_1-x_2)/(x_1-x_2)=\pm5.5\%$.

The relative uncertainty in the fringe temperature difference is more difficult to determine. The optically determined temperature difference (T_1-T_2) is calculated as:

$$T_1-T_2=\frac{T_s}{\dfrac{2\epsilon_1 R_{air}\lambda T_s}{3GZ_Tp}+1}-\frac{T_s}{\dfrac{2(\epsilon_1+1)R_{air}\lambda T_s}{3GZ_Tp}+1} \qquad \text{(F.9)}$$

Note that ϵ_1 is the fractional fringe shift between the first fringe and the wall. It normally has any value between $0<\epsilon_1<1$ from scan to scan. For algebraic convenience, let $\epsilon_1=0$. Therefore, equation (F.9) simplifies to:

$$T_1-T_2=T_s-\frac{T_s}{\dfrac{2R_{air}\lambda T_s}{3GZ_Tp}+1} \qquad \text{(F.10)}$$

The variables in equation (F.10) that are subject to significant uncertainty are the surface temperature T_s (from thermocouples), the optical length of the model Z_T, and barometric pressure p. Hence, we differentiate equation (F.10) and evaluate the following terms for typical experimental conditions:

$$\frac{\partial(T_1-T_2)}{\partial T_s}\delta T_s=\frac{C_1T_s(C_1T_s+2)}{(C_1T_s+1)^2}\delta T_s=\pm0.004C^\circ \quad \textit{where} \quad C_1=\frac{2R_{air}\lambda}{3GZ_Tp} \qquad \text{(F.11)}$$

$$\frac{\partial(T_1-T_2)}{\partial p}\delta p=\frac{-C_2T_s^2}{(C_2T_s+p)^2}\delta p=\pm0.002C^\circ \quad \textit{where} \quad C_2=\frac{2R_{air}\lambda}{3GZ_T} \qquad \text{(F.12)}$$

$$\frac{\partial(T_1-T_2)}{\partial Z_T}\delta Z_T=\frac{-C_3T_s^2}{(C_3T_s+Z_T)^2}\delta Z_T=-0.065C^\circ \quad \textit{where} \quad C_3=\frac{2R_{air}\lambda}{3Gp} \qquad (F.13)$$

From these calculations it can be seen that the dominant source of error in the measured fringe temperature difference is due to the uncertainty in the effective optical length (Z_T). Note that this source of uncertainty is a bias error. That is, the optically measured fringed temperature difference will always be higher than the actual temperature difference. Expressed as a percent of the overall temperature difference ($T_1-T_2\approx3C^\circ$) the relative error is $\delta(T_1-T_2)/(T_1-T_2)\approx-2\%$.

The dominant random errors in the local Nusselt number are due to the uncertainty in the fringe spacing and the surface-to-ambient temperature difference. Combining the uncertainty in each of the terms using equation (F.8), gives the random uncertainty in the local Nusselt number of about ±6%. In addition, there is a bias error of about 2% due to the uncertainty in the optical length as discussed above.

The overall Nusselt number is determined by integrating the local Nusselt numbers. However, it was not possible to get local heat transfer coefficients all the way up to the leading edge of the channel ($y/L_c=0$) using interferometry. No scanning of the interferogram could be done at the inlet corner, so the heat transfer had to be estimated by linear extrapolation (as discussed in Section 6.6.1). This was estimated to cause the wall average Nusselt number to be an additional 2% low. The integration process averages the "noise" in the local Nusselt number data. For this reason, the uncertainty in the average Nusselt number is likely more accurate than the individual local Nusselt number data. As discussed in section 7.4, the average Nusselt number data were reproducible to within about 3%.

APPENDIX G

SAMPLE EXPERIMENTAL CALCULATIONS

To clarify the method of analysis used for the experimental data, a sample calculation is included below for the infinite and finite fringe interferogram shown in Fig. 7.6(b),(d) ($Ra_c^*=874$, $L_p/L_c=1/3$, $L_i/L_c=0$).

Test Section Specifications:

Channel Length $L_c= 120.0$mm

Dividing Plate Length $L_p= 40.0$mm

Length in the Test Beam Direction $Z_T= 259.1$mm

Channel Wall Spacing $2b= 31.95$mm

Plate Thickness $2t= 3.50$mm

Primary Test Data:

Atmospheric Pressure P= 738.0mmHg = 98.37kPa

Ambient Temperature $T_o= 21.2$°C= 294.35K

Average Surface Temperature $T_s= 40.5$°C= 313.65K

Wall Spacing on the Scale Photo Negative = 20.234mm

Channel Length on the Scale Photo Negative = 76.888mm

G.1 Calculation of the Rayleigh Number

The channel Rayleigh number is calculated as follows:

$$Ra_c^* = Gr\,Pr\,\frac{b}{L_c} = \frac{g\beta(T_s-T_o)b^4\rho^2 C_p}{\mu\, L_c\, k} \tag{G.1}$$

where all the air properties are evaluated at the film temperature, $T_f=(T_s+T_0)/2=$ 30.85°C= 304.0K.

Using the properties for air (in Appendix C) gives:

$$Ra_c^* = \frac{9.806m/s^2\,(19.3K)\,(0.015975m)^4\,(1.127kg/m^3)^2\,1006J/kgK}{304K\,(18.718x10^{-6}kg/ms)\,0.12m\,(0.02643W/mK)} = 874$$

G.2 Calculation of the Wall Local Nusselt Number

The analysis technique used to determine the local Nusselt numbers is presented in Chapter 6, section 6.6.1. A sample calculation for the wall at y/L_c=0.162 is given below.

First, the horizontal scale factor for the interferogram is calculated from the ratio of the actual wall spacing to the measured wall spacing on a scale photo negative:

$$\text{Horizontal Scale Factor} = \frac{31.95mm}{20.234mm} = 1.579$$

The locations of the destructive fringe centres on the film negative from a horizontal scan perpendicular to the wall are:

Wall Surface	1st Fringe	2nd Fringe	
0.0000	0.012365	0.028594	(inches)

Using the horizontal scale factor, the actual locations of the first and second destructive fringe centres are:

x_1=0.4959mm

x_2=1.1468mm

The fringe temperatures are obtained from equation (6.13):

$$T(x,y)=\frac{T_{ref}}{\frac{2\epsilon(x,y)R_{air}\lambda T_{ref}}{3G\ Z_T\ p}+1}$$

where $T_{ref}=T_s=313.65$ K

The fractional fringe shift between the wall and the first fringe (ϵ_1) is calculated by linear extrapolation as:

$$\epsilon_1=\frac{x_1}{x_2-x_1}=\frac{0.4959mm}{0.6509mm}=0.7619$$

Now the temperature of the first fringe centre (T_1) can be calculated:

$$T_1=\frac{313.65K}{\frac{2\,(0.7619)\,287J/kgK\,(6.328x10^{-7}m)\,313.65K}{3\,(0.1504x10^{-3}m^3/kg)\,0.2591m\,(98.37x10^3Pa)}+1}=311.300$$

Similarly, noting that $\epsilon_2=\epsilon_1+1$, the temperature of the second fringe is:

$$T_2=\frac{313.65K}{\frac{2\,(1.7619)\,287J/kgK\,(6.328x10^{-7}m)\,313.65K}{3\,(0.1504x10^{-3}m^3/kg)\,0.2591m\,(98.37x10^3Pa)}+1}=308.2[illegible]$$

Now, the wall local Nusselt number is calculated using equation (6.15):

$$Nu_{w,y}=\frac{h_{w,y}\ b}{k_f}=\frac{k_s\frac{dT}{dx}\big|_{x=b}\ b}{k_f(T_s-T_e)}$$

Using linear extrapolation to calculate the temperature gradient, for $y/L_c=0.162$:

$$Nu_{w,y}=\frac{0.02713\,W/mK\,(3.031\,K)\,0.015975\,m}{0.02643\,W/mK\,(0.6509x10^{-3}m)\,19.3\,K}=3.96$$

G.3 Calculation of the Plate Local Nusselt Number

For the straight section of the plate, the local Nusselt numbers are calculated using the same technique as for the wall. However, at the leading edge of the plate a slightly different method of analysis is used because of surface curvature effect (see Chapter 6, section 6.6.2). A sample calculation for the plate at $\theta_{AB}=30^\circ$ ($y/L_p=0.02187$) is given below.

The vertical scale factor for the interferogram is calculated from the ratio of the actual channel length to the measured channel length on a scale photo negative:

$$\textit{Vertical Scale Factor} = \frac{120.0\,mm}{76.888\,mm} = 1.561$$

Note that the vertical scale factor is slightly different from the horizontal scale factor. Hence, the scale factor for a scan at angle θ is determined from the horizontal scale factor (HS) and vertical scale factor (VS) as:

$$\textit{Scale Factor} = \sqrt{(HS\cos\theta)^2 + (VS\sin\theta)^2}$$

$$= \sqrt{(1.579\cos 30^\circ)^2 + (1.561\sin 30^\circ)^2} = 1.574$$

The locations of the destructive fringe centres on the film negative from a scan perpendicular to the plate surface are:

Wall Surface	1^{st} Fringe	2^{nd} Fringe	
0.0000	1.5456×10^{-3}	5.8512×10^{-3}	(inches)

Hence, the radii of the fringes relative to the centre of curvature of the plate is:

$r_1 = 1.5456\times10^{-3}$ in. (25.4mm/in) 1.5744 + 1.75mm = 1.812mm

$r_2 = 5.8512\times10^{-3}$ in. (25.4mm/in) 1.5744 + 1.75mm = 1.984mm

The fractional fringe shift between the wall and the first fringe is calculated by logarithmic extrapolation as:

$$\epsilon_1 = \frac{\ln(\frac{r_1}{R_o})}{\ln(\frac{r_2}{r_1})} = \frac{\ln(\frac{1.812}{1.75})}{\ln(\frac{1.984}{1.812})} = 0.384$$

Now the temperature of the first fringe centre (T_1) can be calculated from equation (6.13) as:

$$T_1 = \frac{313.65K}{\frac{2\,(0.384)\,287\,J/kgK\,(6.328x10^{-7}m)\,313.65K}{3\,(0.1504x10^{-3}m^3/kg)\,0.2591m\,(98.37x10^3Pa)} + 1} = 312.466$$

Noting that $\epsilon_2 = \epsilon_1 + 1$, the temperature of the second fringe is:

$$T_2 = \frac{313.65K}{\frac{2\,(1.384)\,287\,J/kgK\,(6.328x10^{-7}m)\,313.65K}{3\,(0.1504x10^{-3}m^3/kg)\,0.2591m\,(98.37x10^3Pa)} + 1} = 309.412$$

Equation (6.17) gives the temperature gradient at the plate surface:

$$\frac{dT}{dr}\Big|_{surface} = \frac{-(T_1 - T_2)}{R_o \ln(\frac{r_2}{r_1})} = \frac{-(312.466K - 309.412K)}{1.75x10^{-3}m \ln(\frac{1.984}{1.812})} = -19{,}222\,K/m$$

Now, the plate local Nusselt number is calculated as:

$$Nu_{py} = \frac{h_{py}\,b}{k_f} = \frac{-k_s \frac{dT}{dr}\big|_{surface}\,b}{k_f(T_s - T_o)} = \frac{0.0271\,W/mK\,(19{,}222\,K/m)\,0.015975m}{0.0264\,W/mK\,(19.3K)} = 16.3$$

REFERENCES

1. Elenbaas, W., "Heat Dissipation of Parallel Plates by Free Convection," Physica, vol. 9, no. 1, pp. 1-28, 1942.

2. Incropera, F.P., "Convection Heat Transfer in Electronic Equipment Cooling," ASME J. Heat Transfer, vol. 110, pp. 1097-1111, 1988.

3. Hannemann, R., Fox, L.R., Mahalingham, M., "Heat Transfer in Microelectronic Components," International Symposium on Cooling Technology for Electronic Equipment, Honolulu, HI, March 1987.

4. Fox, L.R., Sofia, J.W., Shine, M.C., "Investigation of Solder Fatigue Acceleration Factors," IEEE Trans. on Components, Hybrids and Manufacturing Technology, vol. CHMT-8, no. 2, pp. 275-282, 1985.

5. Raithby, G.D., Hollands, K.G.T., "A General Method of Obtaining Approximate Solutions to Laminar and Turbulent Free Convection Problems," *Advances in Heat Transfer*, Academic Press Inc., vol. 11, pp. 265-315, 1975.

6. Kaminski, D.A. (editor), *Heat Transfer Data Book*, General Electric Company - Corporate Research and Development, Schenectady, N.Y., 1984.

7. Ramanathan, S., Kumar, R., "Correlations for Natural Convection Between Heated Vertical Plates," ASME J. Heat Transfer, vol. 113, pp. 97-107, 1991.

8. Johnson, C.E., "Evaluation of Correlations for Natural Convection Cooling of Electronic Equipment," Heat Transfer Engineering, vol. 7, nos. 1-2, pp. 36-45, 1986.

9. Bar-Cohen, A., "Bounding Relations for Natural Convection Heat Transfer from Vertical Printed Circuit Boards," Proc. IEEE, vol. 73, no. 9, pp. 1388-1395, 1985.

10. Marsters, G.F., "Natural Convective Heat Transfer from a Horizontal Cylinder in the Presence of Nearby Walls," The Canadian Journal of Chemical Engineering, vol. 53, pp. 144-149, 1975.

11. Marsters, G.F., Paulus, G., "Effects of Confining Walls on Heat Transfer from a Vertical Array of Heated Horizontal Cylinders," Trans. CSME, vol. 1, no. 4, pp. 219-222, 1972.

12. Tokura, I., Saito, H., Kishinami, K., Muramoto, K., "An Experimental Study of Free Convection Heat Transfer From a Horizontal Cylinder in a Vertical Array Set in Free Space Between Parallel Walls," ASME J. Heat Transfer, vol. 105, pp. 102-107, 1983.

13. Yang, J., Wei, B., Zhao, Y., Chen, G., "An Experimental Study of Free Convection Heat Transfer from Horizontal Elliptical Tubes in a Vertical Array Between Parallel Walls," Proceedings of the First World Conference on Experimental Heat Transfer, Fluid Mechanics, and Thermodynamics, Dubrovnik, Yugoslavia, pp. 441-445, 1988.

14. Sparrow, E.M., Ansari, M.A., Stryker, P.C., Ruiz, R., "Enhanced Heat Transfer from a Horizontal Finned Tube Situated in Vertical Channel," ASME J. Heat Transfer, vol. 108, pp. 62-69, 1986.

15. Hannemann, R., "Physical Technology for VLSI Systems," Proc. IEEE International Conference on Computer Design, pp. 48-53, 1986.

16. Chu, R.C., Simons, R.E., Moran, K.P., "Design Considerations for Electronic Cooling Systems," International Symposium on Cooling Technology for Electronic Equipment, Honolulu, HI, March 1987.

17. Anderson, R., Kreith, F., "Natural Convection in Active and Passive Solar Thermal Systems," *Advances in Heat Transfer*, Academic Press Inc., New York, N.Y., vol. 18, pp. 1-79, 1987.

18. Akbari, H., Borgers, T.R., "Free Convective Laminar Flow within the Trombe Wall Channel," Solar Energy, vol. 22, pp. 165-174, 1979.

19. Ormiston, S.J., Raithby, G.D., Hollands, K.G.T., "Numerical Predictions of Natural Convection in a Trombe Wall System," Int. J. Heat Mass Transfer, vol. 29, no. 6, pp. 869-877, 1986.

20. Peterson, G.P., Ortega, A., "Thermal Control of Electronic Equipment and Devices," *Advances in Heat Transfer*, vol. 20, Academic Press Inc., New York, N.Y., pp. 181-314, 1990.

21. Gebhart, B., Jaluria, Y., Mahajan, R.L., Sammakia, B., *Buoyancy-Induced Flows and Transport*, Hemisphere Publishing Corp., New York, 1988.

22. Sparrow, E.M., Bahrami, P.A., "Experiments on Natural Convection from Vertical Parallel Plates with Either Open or Closed Edges," ASME J. Heat Transfer, vol. 102, pp. 221-227, 1980.

23. Bodoia, J.R., Osterle, J.F., "The Development of Free Convection Between Heated Vertical Plates," ASME J. Heat Transfer, vol. 84, pp. 40-44, 1962.

24. Currie, I.G., Newman, W.A., "Natural Convection Between Isothermal Vertical Surfaces," Fourth International Heat Transfer Conference, Paris-Versailles, paper NC2.7, vol. 4, pp. 1-8, 1970.

25. Aung, W., Fletcher, L.S., Sernas, V., "Developing Laminar Free Convection Between Vertical Flat Plates with Asymmetric Heating," Int. J. Heat Mass Transfer, vol. 15, pp. 2293-2308, 1972.

26. Miyatake, O., Fujii, T., "Natural Convective Heat Transfer Between Vertical Parallel Plates with Unequal Uniform Temperatures," Heat Transfer: Japanese Research, vol. 2, pp. 79-88, 1973.

27. Miyatake, O., Fujii, T., "Natural Convective Heat Transfer Between Vertical Parallel Plates with Unequal Heat Fluxes," Heat Transfer: Japanese Research, vol. 3, pp. 29-33, 1974.

28. Dalbert, A.-M., Penot, F., Peube, J.-L., "Convection Naturelle Laminaire Dans un Canal Vertical Chauffe a Flux Constant," Int J. Heat Mass Transfer, vol. 24, no. 9, pp. 1463-1473, 1981.

29. Sparrow, E.M., Chrysler, G.M., Azevedo, L.F., "Observed Flow Reversals and Measured-Predicted Nusselt Numbers for Natural Convection in a One-Sided Heated Vertical Channel," ASME J. Heat Transfer, vol. 106, pp. 325-332, 1984.

30. Miyatake, O., Fujii, T., "Free Convection Heat Transfer Between Vertical Parallel Plates - One Plate Isothermally Heated and the Other Thermally Insulated," Heat Transfer: Japanese Research, vol. 1, pp. 30-38, 1972.

31. Davis, L.P., Perona, J.J., "Development of Free Convection Flow of a Gas in a Heated Vertical Open Tube," Int. J. Heat Mass Transfer, vol. 14, pp. 889-903, 1971.

32. Pollard, A., Oosthuizen, P.H., "Free Convection Through Open-Ended Pipes," National Heat Transfer Conference, Seattle, Washington, ASME paper 83-HT-28, pp. 1-7, 1983.

33. Aihara, T., Maruyama, S., Choi, J.S., "Laminar Free Convection with Variable Fluid Properties in Vertical Ducts of Different Cross-Sectional Shapes," Proceedings of the Eighth International Heat Transfer Conference, New York, N.Y., pp. 1581-1586, 1986.

34. Aihara, T., "Effects of Inlet Boundary-Conditions on Numerical Solutions of Free Convection Between Vertical Parallel Plates," Report of the Institute of High Speed Mechanics, Tohoku University, Sendai, Japan, vol. 28, pp. 1-27, 1973.

35. Chappidi, P.R., Eno, B.E., "Natural Convection in a Heated Parallel Plate Vertical Channel; Influence of Inlet Conditions," Proceedings of the 1988 National Heat Transfer Conference, Houston, Texas, vol. 2, pp. 135-143, 1988.

36. Aihara, T., "Heat Transfer due to Natural Convection from Parallel Vertical Plates," Trans. JSME, vol. 29, pp. 903-909, 1963.

37. Kennard, R.B., "Temperature Distribution and Heat Flux in Air by Interferometry," *Temperature, Its Measurement and Control in Science and Industry*, Reinhold Publishing Corp., New York, N.Y., pp. 685-706, 1941.

38. Sparrow, E.M., Azevedo, L.F.A., "Vertical-Channel Natural Convection Spanning Between the Fully-Developed Limit and the Single-Plate Boundary-Layer Limit," Int. J. Heat Mass Transfer, vol. 28., no. 10, pp. 1847-1857, 1985.

39. Kettleborough, C.F., "Transient Laminar Free Convection Between Heated Vertical Plates Including Entrance Effects," Int. J. Heat Mass Transfer, vol. 15, pp. 883-896, 1972.

40. Nakamura, H., Asako, Y., Naitou, T., "Heat Transfer by Free Convection Between Two Parallel Flat Plates," Numerical Heat Transfer, vol. 5, pp. 95-106, 1982.

41. Aung, W., "Fully Developed Laminar Free Convection Between Vertical Plates Heated Asymmetrically," Int. J. Heat Mass Transfer, vol. 15, pp. 1577-1580, 1972.

42. Said, S.A.M., Krane, R.J., "An Analytical and Experimental Investigation of Natural Convection Heat Transfer in Vertical Channels with a Single Obstruction," Int. J. Heat Mass Transfer, vol. 33, no. 6, pp. 1121-1134, 1990.

43. Oosthuizen, P.H., "A Numerical Study of Laminar Free Convective Flow Through a Vertical Open Partially Heated Plane Duct," Fundamentals of Natural Convection - Electronic Equipment Cooling, ASME HTD, vol. 32, pp. 41-48, 1984.

44. Sobel, N., Landis, F., Mueller, W.K., "Natural Convection Heat Transfer in Short Vertical Channels Including the Effects of Stagger," Proceedings of the Third International Heat Transfer Conference, Chicago, Illinois, vol. 2, pp. 121-125, 1966.

45. Sparrow, E.M., Prakash, C., "Enhancement of Natural Convection Heat Transfer by a Staggered Array of Discrete Vertical Plates," ASME J. Heat Transfer, vol. 102, pp. 215-220, 1980.

46. Prakash, C., Sparrow, E.M., "Natural Convection Heat Transfer Performance Evaluations for Discrete - (In-line or Staggered) and Continuous-Plate Arrays," Numerical Heat Transfer, vol. 3, pp. 89-105, 1980.

47. Squire, H.B., Goldstein, S., *Modern Developments in Fluid Dynamics*, Oxford University Press, New York, N.Y., 1938.

48. Schmidt, E., Beckmann, W., "Das Temperatur- und Geschwindigkeitsfeld vor einer Warme abgebenden senkrechter Platte bei naturlicher Konvektion," Tech. Mech. u. Thermodynamik, Bd. 1, Nr. 10, pp. 341-349; cont., Bd. 1, Nr. 11, pp. 391-406, 1930.

49. Ostrach, S., "An Analysis of Laminar Free-Convection Flow and Heat Transfer about a Flat Plate Parallel to the Direction of the Generating Body Force," NACA Technical Report #1111, 1953.

50. Sparrow, E.M., Gregg, J.L., "Similar Solutions for Free Convection From a Nonisothermal Vertical Plate," Trans. ASME, vol. 80, pp. 379-386, 1958.

51. Gebhart, B., "External Natural Convection Flow," Applied Mechanics Reviews, vol. 22, pp. 691-701, 1969.

52. Sparrow, E.M., Souza Mendes, P., Ansari, M.A., Prata, A.T., "Duct-Flow Versus External-Flow Natural Convection at a Short, Wall-Attached Horizontal Cylinder," Int. J. Heat Mass Transfer, vol. 26, no. 6, pp. 881-889, 1983.

53. Schlichting, H., *Boundary-Layer Theory*, Seventh Edition, McGraw-Hill Book Company, New York, N.Y., 1979.

54. Fluid Dynamics International Inc., Evanston, Illinois, FIDAP V4.51, 1989.

55. Gray, D.D., Giorgini, A., "The Validity of the Boussinesq Approximation for Liquids and Gases," Int. J. Heat Mass Transfer, vol. 19, pp. 545-551, 1976.

56. Mihaljan, J.M., "A Rigorous Exposition of the Boussinesq Approximations Applicable to a Thin Layer of Fluid," Astrophys. J., vol. 136, pp. 1126-1133, 1962.

57. Kageyama M., Izumi, R., "Non-Steady Natural Heat Convection in a Nonparallel Plane Walled Channel," Trans. JSME, vol. 45, no. 393, pp. 682-693, 1979.

58. Hamel, G., "Spiralformige Bewegung zaher Flussigkeiten," Jahresber. Dt. Mathematiker-Vereinigung, vol. 25, pp. 34-60, 1916.

59. Millsaps, K., Pohlhausen, K., "Thermal Distributions in Jeffery-Hamel Flows Between Nonparallel Plane Walls", Jounrnal of Aeronautical Sciences, vol. 20, pp. 187-196, 1953.

60. Burnett, D.S., *Finite Element Analysis - From Concepts to Applications*, Addison-Wesley Publishing Company, Reading Massachusetts, 1987.

61. Tanda, G., "Natural Convection in Partially Heated Vertical Channels," Warme- und Stoffubertragung, vol. 23, pp. 307-312, 1988.

62. Symbolic Computation Group, Department of Computer Science, University of Waterloo, Waterloo, Ontario, MAPLE version 4.2, 1988.

63. Churchill, S.W., Usagi, R., "A General Expression for the Correlation of Rates of Transfer and Other Phenomena," AIChE Journal, vol. 18, no. 6, pp. 1121-1128, 1972.

64. Wirtz, R.A., Haag, T., "Effect of an Unheated Entry on Natural Convection Between Vertical Parallel Plates," Winter Annual Meeting of the ASME, Paper 85-WA/HT-14, Miami Beach, Florida, November, pp. 1-8, 1985.

65. Naylor, D., Floryan, J.M., Tarasuk, J.D., "A Numerical Study of Developing Free Convection Between Isothermal Vertical Plates," ASME J. of Heat Transfer, vol. 113, pp. 620-626, 1991.

66. Eckert, E.R.G, Goldstein, R.J., *Measurements in Heat Transfer*, Hemisphere Publishing Corp., 1976.

67. Franke, M.E., "Interferometric Measurements in Free Convection on a Vertical Plate with Temperature Variation in the Light-Beam Direction," Heat Transfer 1970, Proceedings of the Fourth International Heat Transfer Conference, paper NC1.2, vol. 4, pp. 1-12, 1970.

68. Yousef, W.W., Tarasuk, J.D., "An Interferometric Study of Combined Free and Forced Convection in a Horizontal Isothermal Tube," ASME J. Heat Transfer, vol. 103, no. 2, pp. 249-256, 1981.

69. Papple, M.L.C., Tarasuk, J.D., "Natural Convection about Vertical Cylinders - Including the Effects of a Variable Property Ambient Gas," ASME paper no. 85-HT-15, ASME Conference, Denver, Colorado, 1985.

70. Tarasuk, J.D., "The Theory, Design, and Operation of The University of Saskatchewan 8-inch Mirror Mach-Zehnder Interferometer," Technical Report C-3, Mechanical Engineering Department, University of Saskatchewan, June, 1968.

71. Papple, M.L.C., "Developing Laminar Natural Convective Flow in Inclined Square Ducts - A Preliminary Investigation," Ph.D. Thesis, The University of Western Ontario, London, Ontario, 1988.

72. Melles Griot Inc., *Optics Guide 5*, Suite 1000, 36 Antares Dr., Nepean, Ontario, 1991.

73. Mehta, J.M., Black, W.Z., "Errors Associated with Interferometric Measurement of Convective Heat Transfer Coefficients," Applied Optics, vol. 16, no. 6, pp. 1720-1726, 1977.

74. Hauf, W., Grigull, U., "Optical Methods in Heat Transfer," Advances in Heat Transfer, Academic Press Inc., New York, N.Y., vol. 6, pp. 133-366, 1970.

75. Saidi, N.N., "An Interferometric Study of Coupled Convective Heat Transfer in a Horizontal Flat Plate Enclosure," Ph.D. Thesis, The University of Western Ontario, London, Ontario, 1983.

76. Eckert, E.R.G., Soehngen, E.E., "Studies on Heat Transfer in Laminar Free Convection with the Zehnder-Mach Interferometer," United States Air Force, AF Technical Report 5747, 1948.

77. Kuehn, T.H., Goldstein, R.J., "An Experimental and Theoretical Study of Natural Convection in the Annulus Between Horizontal Concentric Cylinders," J. Fluid Mechanics, vol. 100, part 4, pp. 695-719, 1976.

78. Showole, R.A.A., "An Interferometric and Numerical Study of Free and Mixed Convective Heat Transfer From Open Rectangular, Semi-Cylindrical, and V-Shaped Isothermal Cavities," Ph.D. Thesis, The University of Western Ontario, London, Ontario, 1988.

79. Azevedo, L.F.A., Sparrow, E.M., "Natural Convection in Open-Ended Inclined Channels," ASME J. Heat Transfer, vol. 107, pp. 893-901, 1985.

80. Moffat, R.J., Ortega, A., "Buoyancy Induced Forced Convection," Heat Transfer in Electronic Equipment, AIAA/ASME Fourth Thermophysics and Heat Transfer Conference, Boston, Mass., pp. 135-144, 1986.

81. Ortega, A., Moffat, R.J., "Buoyancy Induced Convection in a Non-Uniformly Heated Array of Cubical Elements on a Vertical Channel Wall," Heat Transfer in Electronic Equipment, AIAA/ASME Fourth Thermophysics and Heat Transfer Conference, Boston, Mass., pp. 123-134, 1986.

82. Creare.x Inc., Box 71, Etna Rd. Hanover, N.H., NEKTON & FLUENT, 1990.

83. Engineering Mechanics Research Corporation, Box 696, Troy, M.I., 3D-FLUID, 1990.

84. Kato, S., Maruyama N., "Holographic Interferometry Measurements of the Three-Dimensional Temperature Field with Thermally Developing Flow in the Measuring Beam Direction," Proceedings of the First World Conference on Experimental Heat Transfer, Fluid Mechanics and Thermodynamics, Dubrovnik, Yugoslavia, pp. 425-432, 1988.

85. Hunter, J., Collins M.W., "Problems in using Holographic Interferometry to Resolve the Four-Dimensional Character of Turbulence. Part II: Image and Data Processing," Journal of Optical Sensors, vol. 1, no. 3, pp. 227-234, 1986.

86. Lehmann, G.L., "Experimental Investigation of Convective Heat Transfer in a Transitional Channel Flow with Periodic Cavity Induced Roughness," Ph.D. Thesis, Clarkson University, Potsdam, N.Y., 1985.

87. McKeen, W.J., "The Development of a Technique to Measure the Location of Fringes on an Interferogram," M.Eng. Thesis, The University of Western Ontario, London, Ontario, Canada, 1978.

88. McKeen, W.J., Tarasuk, J.D., "Accurate Method for Locating Fringes on an Interferogram," Review of Scientific Instruments, vol. 52, no. 8, pp. 1223-1225, 1981.

89. Baxes, G.A., *Digital Image Processing: A Practical Primer*, Englewood Cliffs, N.J., Prentice-Hall, 1984.

90. Touloukian, Y.S., Saxena, S.C., Hestermans, P., "Viscosity," Thermophysical Properties of Matter, vol. 11, Thermophysical Properties Research Centre (TPRC), Purdue University, Plenum Publishing Corp., 1975.

91. Touloukian, Y.S., Liley, P.E., Saxena, S.C., "Thermal Conductivity: Nonmetallic Liquids and Gases," Thermophysical Properties of Matter, vol. 3, Thermophysical Properties Research Centre (TPRC), Purdue University, Plenum Publishing Corp., 1970.

92. Touloukian, Y.S., Makita, T., "Specific Heat: Nonmetallic Liquids and Gases," Thermophysical Properties of Matter, vol. 6, Thermophysical Properties Research Centre (TPRC), Purdue University, Plenum Publishing Corp., 1970.

93. Kline, S.J., McClintock, F.A., "Describing Uncertainties in Single-Sample Experiments," Mechanical Engineering, vol. 75, pp. 3-8, 1953.

94. Kuehn, T.H., "Natural Convection in the Annulus Between Horizontal Circular Cylinders," Master of Science Thesis, The University of Minnesota, 1976.